Radiation-directed production of chemical reagents and petroleum additives from waste organic feedstocks

Arran George Plant

BSc, MSc

This thesis is submitted for the degree of Doctor of Philosophy

Department of Engineering, Lancaster University

February 2023

Declaration of Authorship

I, Arran George Plant. BSc, MSc, declare that this thesis titled, “Radiation-directed production of chemical reagents and petroleum additives from waste organic feedstocks” and the work presented in it are my own. I confirm that:

- This work was done wholly in candidature for a research degree at this University.
- No parts of this thesis have been previously submitted for a degree or any other qualification at this university for any other institution.
- Where I have consulted the published work of others, I have referenced their attribution.
- I have acknowledged all main sources of help.
- Where the thesis is based on work done jointly with others, I have made clear what was done by others and what I have contributed myself.

Signed:

Date:

Abstract

Nuclear cogeneration is the collation of co-processes that aims to improve the sustainability, overall efficiency, and profitability of nuclear power by producing alternative products alongside electricity. A range of existing cogeneration processes explores the use of waste stream process heat for a variety of processes including district heating and desalination. However, the direct application of under-utilized ionization energy has yet to be fully realized. This thesis is a study on the potential application of ionizing radiation from nuclear facilities towards the radiolytic production of organic chemicals derived from waste renewable feedstocks. Here we show that glycerol, a notable waste feedstock from biodiesel production can be converted into acetol (hydroxyacetone) or solketal which are textile and biofuel additives, respectively using ionizing radiation from a 250-kW research fission reactor. The radical-initiated chain reaction for hydroxyl acetone (acetol) production is optimised to produce the highest *G*-value (2.7 ± 0.4 μmol J^{-1}) and mass productivity (~1 %) to be reported in the available radiolysis literature. A previously unreported radiolytic product, solketal, which is a valuable biofuel additive is produced radiolytically using ternary glycerol, acetone, and water mixtures with *G*-values of 1.5 ± 0.2 μmol J^{-1} at 50 kGy. Empirical data showed a preference for low LET, low dose rate, γ-ray emissions such as those from spent fuel was found to be favourable for acetol and solketal production. Simulating three production scenarios with MCNP models for preferential solketal production found that a spent fuel facility consisting of ~1710 elements showed the largest production capacity at 57.4 ± 5.6 t $year^{-1}$ due to the high volume available to be irradiated. Extrapolating to a theoretical European production network involving ~180 equivalent SFP facilities based on relative reactor power, a total of $(1.3 \pm 0.1) \times 10^4$ t $year^{-1}$ of solketal could be produced, contributing to $(2.5 \pm 0.2) \times 10^8$ litres $year^{-1}$ to a (95% petroleum, 5% solketal) fuel blend. While this represents only ~0.3 % of total transport fuels consumed within the EU, it presents a pioneering process that could be feasible if *G*-values and mass productivities were improved upon.

Acknowledgements

The journey to complete this doctorate has been a long but ultimately rewarding one, the experiences and people involved have helped me grow as an individual into the person I am today. Firstly, I’d like to thank the Engineering and Physical Sciences Research Council (EPSRC) for providing me with the funds to undertake this PhD. I’d also like to thank my supervisors, Professor Malcolm Joyce, and Dr Vesna Najdanovic for offering me the opportunity to undertake this PhD. Their guidance and support over the years has been invaluable.

I would also like to thank those who collaborated with me, from the Jožef Stefan Institute: Anže Jazbec for the operation of the TRIGA reactor and the irradiation of numerous samples, Bor Kos for his expertise in MCNP modelling, and Luka Snoj for his dosimetry expertise and facilitating the collaboration. Additionally, thanks to Radojko Jaćimović for his INAA service. At Lancaster University, I’d like to thank Peter Jones for helping with numerous technical aspects of my projects as well as for being a jovial, approachable character. Additionally, I’d like to thank Jess Fisher, Jonathan Gates, Ashley Jones, and Armin Y. Kanani as well as every technician who assisted over the years. I’d also like to thank Chris Tumilson for his collaboration on another project which is not described in this thesis. From the chemistry department, I’d like to thank David Rochester and Geoffrey Akien for the training, their time, and their analysis expertise.

Furthermore, whilst they may not have been directly involved with any of my research, all the friends made along the way made my time during my PhD significantly more enjoyable, fulfilling, and memorable.

I'd like to thank my parents who have always been there encouraging me to achieve my best and have always been there to support me. Last but certainly not least, thank you to my partner, Joanna who has kindly, patiently listened to my occasional evening ramblings about my work and who is a constant joy to be around. Our conversations have kept me mostly sane during the writing of this thesis.

List of Publications and Conferences

Publications:

- Published journal article on 17/09/2021 in *Nature Communications Chemistry*.
  - Plant, A.G., Kos, B., Jazbec, A. *et al.* Nuclear-driven production of renewable fuel additives from waste organics. *Commun Chem* **4,** 132 (2021). https://doi.org/10.1038/s42004-021-00572-5
- Published conference paper on 20/01/2020 from Advancements in Nuclear Instrumentation Measurement Methods and their Applications (ANIMMA), 2019.
  - Arran George Plant, Vesna Najdanovic-Visak, Malcolm J. Joyce, Luka Snoj and Anže Jazbec. Producing Useful Chemicals Using a Nuclear Reactor. *EPJ Web Conf.*, 225 (2020) 09003 DOI: https://doi.org/10.1051/epjconf/202022509003

List of International Conferences Attended:

- The 29th International Conference on Nuclear Energy for New Europe (NENE), 2020, Portorož, Slovenia. (Remotely Attended with an Oral Presentation)
- International Conference on Advancements in Nuclear Instrumentation Measurement Methods and their Applications (ANIMMA), 2019. Portorož, Slovenia. (Attended with an Oral Presentation)
- 7th Conference on Carbon Dioxide as Feedstock for Fuels, Chemistry and Polymers, 2018, Cologne, Germany. (Attended)
- The 27th International Conference on Nuclear Energy for New Europe (NENE), 2018, Portorož, Slovenia. (Attended with an Oral Presentation)

List of National and Departmental Conferences Attended:

- Engineering Postgraduate Research Conference, 2019, Lancaster, UK. (Attended with an Oral Presentation and awarded 2nd Prize in the year)
- Universities Nuclear Technology Forum (UNTF), 2018, Lancaster, UK. (Attended with an Oral Presentation and awarded top presentation)
- Engineering Postgraduate Research Conference, 2018, Lancaster, UK. (Attended with an Oral Presentation)
- Engineering Postgraduate Research Conference, 2017, Lancaster, UK. (Attended with an Oral Presentation and awarded 1st Prize in the year)

Table of Contents

ABSTRACT .... **II**

ACKNOWLEDGEMENTS .... **III**

LIST OF PUBLICATIONS AND CONFERENCES .... **IV**

TABLE OF CONTENTS .... **V**

LIST OF FIGURES .... **VIII**

LIST OF TABLES .... **XVI**

LIST OF ABBREVIATIONS .... **XIX**

1 INTRODUCTION **1**

1.1 List of Chapters 3

2 BACKGROUND: NUCLEAR COGENERATION AND RADIATION CHEMISTRY **4**

2.1 Nuclear Power: Essential and In Decline 4
2.2 Nuclear Cogeneration 6
  2.2.1 Nuclear Cogeneration of Chemicals 9
2.3 Biochemicals and Biofuels 10
  2.3.1 Biodiesel, Glycerol Market, and Wider Valorisation Research 12
2.4 The Nuclear-Biorefinery Concept 17
2.5 Radiation Chemistry 19
2.6 Types of Ionizing Radiations: Direct and Indirect 21
2.7 Radiation Interactions 23
  2.7.1 Electron Interactions 23
  2.7.2 Neutron Interactions 24
  2.7.3 Gamma (γ)-ray Interactions 28
2.8 Linear Energy Transfer (LET) and Stopping Power 30
2.9 Radiolysis Timeframes and Mechanisms 32
2.10 Fundamental Dose Definitions and Approximations 38
2.11 Dosimetry Techniques: Analytical and Simulations 42
2.12 Radiation Chemistry and Analytical Techniques 44
  2.12.1 Radiation Chemical Yield, G-Value 44

2.12.2 Molar Yield and Mass Productivity *47*
2.12.3 Chemical Analytical Techniques *48*
2.13 Radiolysis Literature Review 49
2.13.1 Industrial Applications *49*
2.13.2 Liquid Compounds and Aqueous Solutions *50*
2.13.3 Liquid Aliphatic Alcohols *51*
2.13.4 Ethylene Glycol, $C_2H_6O_2$ *53*
2.13.5 Glycerol, $C_3H_8O_3$ *54*
2.13.6 Variable Parameters *56*
2.14 Research Questions 62

3 MATERIALS AND METHODS 63

3.1 Chemicals – Organic Solutes 63
3.2 Radiation Vessels 63
3.2.1 Axial Compression Testing *66*
3.2.2 Internal Pressure Calculations *67*
3.3 Sample Preparation before Irradiations and Leak Testing Protocol 68
3.4 Radiation Sources 69
3.4.1 Californium-252, Lancaster University, UK *69*
3.4.2 250 kW TRIGA Fission Reactor, JSI Slovenia. *72*
3.4.3 Radiation Sample Plans and Variables *78*
3.5 Sample Work-up and Gas Chromatography-Mass Spectrometry Analysis at Lancaster, UK. 80
3.5.1 Dilution Method *80*
3.5.2 Gas Chromatography Methodology *80*
3.6 Radiation Chemical Yield (*G*-value) and Mass Productivity Calculations 83
3.7 Modelling, Economic and Feasibility 85
3.7.1 Scaling Up for a European Production Network *88*

4 RESULTS 90

4.1 Research with Californium-252 90
4.2 JSI 250 kW Reactor 94
4.3 Vial Appearance, Compression Testing, and Leaks 102
4.3.1 Axial Compression Analysis *103*
4.3.2 Leaking and Mass Change Analysis *107*
4.4 INAA and γ-ray Spectroscopy 109
4.5 Ethylene Glycol 110
4.5.1 Radiolysis Products: Qualitative *110*
4.5.2 Quantitative Analysis *113*
4.5.3 Dose Rate *124*
4.6 Glycerol 127
4.6.1 Radiolysis Products: Qualitative *127*
4.6.2 Quantitative Analysis *130*
4.6.3 Ternary Mixtures *143*
4.7 Production Calculations with MCNP models 148
4.8 Expansion to Europe-based Nuclear Facilities 150

5 DISCUSSION 152

5.1 Induced Radioactivity 152
5.2 Dependence on Absorbed Dose 153
5.3 Dependence on Vial Types and Vessel Materials 154
5.4 Dependence on Radiation Type and Dose Rate 155
5.5 Dependence on Solute Concentration and Mixtures 156
5.6 Radiolysis Mechanisms – Direct Action 158
  5.6.1 Ethylene Glycol 158
  5.6.2 Glycerol 160
5.7 Production Calculations, Feasibility and Comparisons 167
5.8 Immediate Suitability of Nuclear Cogeneration 169

6 CONCLUSIONS 171

6.1 Future Work 173

7 REFERENCES 174

8 APPENDIX A: SUPPORTING FIGURES AND TABLES 202

8.1 Tabulated Literature data on Alcohols, Ethylene glycol and Glycerol 208
8.2 Tabulated Experimental Radiolysis Data (Plant A. G.) of Ethylene Glycol and Glycerol samples 211
  8.2.1 Concentration Tables 211
  8.2.2 G-value and Mass Productivity % Tables 218
  8.2.3 INAA Radionuclide data of Neat Samples 226
  8.2.4 Pressure Calculations, Calibration Curves, and Chromatograms 227
8.3 MS Fragments Patterns of unidentifiable peaks 233
8.4 European NPPs by country with projected solketal production 234

List of Figures

Figure 1: Heat-derived cogeneration products and NPP coolant outlet temperature ranges in $^{\circ}$C. Co-products are listed by minimum required temperatures [1]. The maximum coolant temperature percentages per reactor type have been displayed against the 443 currently operational reactors worldwide (as of 2020) [7]. Possible future Gen IV reactor designs have been included. *Gen III reactors type percentages are similar to current Gen II NPPs. [10, 47] 8

Figure 2: Biodiesel or FAME (Fatty acid methyl ester) production reaction scheme with glycerol by-product. R: alkyl chain with varying saturation and lengths. This reaction can be catalysed by a strong base such as KOH. 12

Figure 3: a Worldwide crude glycerol product by source [90]. b Applications of only refined glycerol in 2015, showing 25% by mass for low-value uses [84]. 13

Figure 4: Thermochemical reaction schemes and associated catalysts, temperatures and pressures for: a acetol [107, 108] and, b solketal production [110, 111]. 16

Figure 5: A basic diagram of processes within a a nuclear facility and b a biochemical plant. c the neutron + γ-ray nuclear biorefinery concept, displaying the holistic sharing of resources. 18

Figure 6: A diagram showing the fluence, ϕ of a monoenergetic particle field, dN, through a cross-section, dA of a defined sphere volume, dV around point, P. [127] 22

Figure 7: General diagram representation of increasing LET leading to spur distribution alterations along the irradiation tracks (adapted from [147]). 30

Figure 8: Radiolysis of water and reactive species involved with a generalized timescale. Radiolytic and analytical techniques for monitoring during those generalized timescales are also shown (Adapted from [120]and [154]). 32

Figure 9: In-depth schematic of radiation interactions of low and high-LET irradiations: Smaller energetic volumes = spurs, and larger energetic volumes = blobs. Secondary particles (i.e., electrons or protons) are displayed for higher-LET irradiations 33

Figure 10: Absorbed Dose and KERMA vs liquid medium depth [175]. Showing the Build-up region ($\beta<1$) where $K_c>D$ and the TCPE region ($\beta\approx1$) where $K_c \approx D$. 40

Figure 11: Diagram of the principal operation of an ionization chamber. The ion current measured is directly related to the fluence of the incident particles or waves 42

Figure 12: Absorbed dose vs a concentration and b G-value plots showing the simplified example trends for primary (blue), secondary (red), and tertiary (green) molecular products. Extrapolation of trends to zero dose G-values indicates primary and secondary molecular products with >0 and ≈0 values, respectively [215]. 46

Figure 13: Bespoke axial compression mount and piston (designed with Armin Y. Kanani). a bottom vial holder, b a BS vial inserted into the vial holder, and c showing the mount with the top piston. 66

Figure 14: Filled irradiation vessels. a 20 ml Borosilicate vials example (Aluminium/Silicone septa has blue caps) b 5 ml Polypropylene cryogenic vials. c a large array of irradiated polypropylene vials. 68

Figure 15: a The steel cubic tank filled with water showing the ^{252}Cf source holder, the support frame, and the hydraulic system showing the safe and exposed positions. b Organic samples setup situated to the closest cubic face of the tank as to the ^{252}Cf exposed position: BS vials containing neat ethylene glycol or glycerol and corresponding bulk bottles for the ^{252}Cf exposures. 70

Figure 16: a A schematic of the TRIGA Reactor Core: showing the large triangular channel (TriC) indicated by the red arrow. b CAD schematic of the reactor showing the TriC access pipe (red arrow) used for *G*-value determination and the surrounding carousel facility (indicated by the blue arrow) used for INAA testing. Images were used with permission from Anže Jazbec [291]. 73

Figure 17: a Top view of the 250 kW TRIGA pool reactor at JSI (2018). The red arrow indicates the larger Triangular Irradiation Channel (TriC) access port for samples. b Organic vials being lowered into the TriC access port (Dr Anže Jazbec pictured). c diagram of the polypropylene (PP) and the borosilicate vessels (BS) used......... 74

Figure 18: Shimadzu TQ-8040 triple-quadrupole GC-MS with AOC 6000 autosampler. a Headspace heated agitator. b GC oven. c Mass spectrometer with vacuum pump. 82

Figure 19: A schematic diagram of the sample work-up quantities for irradiated viscous samples. M, Mass and V, Volume. Subscripts defining the volume or mass partition of the: 1 total irradiated sample, 2 extracted irradiated sample, and 3 the diluted sample. 84

Figure 20: 250 kW TRIGA reactor and MCNP model at JSI, Slovenia modified by B. Kos. a Top view photo of the JSI pool reactor, with the red arrow showing the Triangular (TriC) channel. b Equivalent spatial MCNP model of the JSI reactor. c MCNP top-view of JSI reactor showing possible radiation positions. Images kindly provided by B. Kos. 86

Figure 21: Spatial Images of the Krško PWR MCNP model, modified by B. Kos. The red arrow indicates the organic-carrying pipes (totalling 50) within the steel reactor containment vessel, travelling the vertical dimension of the containment vessel. a and b segmented cross-sections of the reactor with the red arrow indicating an organic-carrying pipe. c vertical cross-section showing sections for organic-carrying pipes. 86

Figure 22: Krško Spent Fuel Pool (SFP) 5 × 2 model developed by Bor Kos. a and b spent fuel element cross-section: blue circles= Ur fuel rods, purple circles = absorbing rods. c Top-view of the MCNP Model expansion to a 5 × 2 matrix. d Isometric Spatial MCNP Spent Fuel Pool (SFP) facility model with a 5 × 2 grid of spent fuel elements. Orange pipe and red arrows indicate the organic-liquid carrying pipes. 87

Figure 23: Scaling up of the 5 × 2 fuel element SFP model by Plant A. G. a 5 × 2 matrix model b extrapolation to a 30 × 57 matrix of fuel elements with 10 organic-carrying pipes (blue) in between each row of elements, giving a total of 560 pipes. Spent fuel elements are described by the squares with the pipes 88

Figure 24: The locations of the 180 operational nuclear reactors within continental Europe by country. The number of operational reactors in each country was obtained from [305], Last accessed 11/03/21]. The area of each circle is proportional to the number of reactors in each case. Grey indicates countries outside geographical Europe and black indicates countries within Europe with no commercial nuclear capacity. Base map altered from ©MapRoom, modified by Plant A. G., Table A20 lists the reactor numbers by country with their respective total electrical capacity. 89

Figure 25: Total ion chromatogram (TIC) of the ^{252}Cf-irradiated, ~25-day semi-continuous exposure, ~0.037 Gy ethylene glycol sample 1 (black) using the headspace sampling method. No new detectable analytes between the unirradiated sample (pink) and blank (blue). 92

Figure 26: Vial observations after high dose (>20 kGy) irradiations. a Discolouration of borosilicate vials due to increasing mixed-field absorbed dose from left to right. b Deformation of PP vials during high dose rate (6.54 kGy min.$^{-1}$) mixed-field irradiations when touching adjacent BS vials. BS crimp caps are made of steel with either a PTFE/ silicone (yellow top) or aluminium/ silicone (blue top) septa...... 103

Figure 27: Axial compression force vs time plots of empty, capped a round-bottomed (RB) and b flat-bottomed headspace vials. Unirradiated BS vials are either shown with yellow (PTFE/Silicone) or blue (Aluminium/Silicone) crimp caps. In a and b the compression of two 100 kGy γ-ray irradiated vials with the corresponding caps are shown by the green plots.. 104

Figure 28: Axial compression force vs time plots of empty, uncapped a round-bottomed (RB) and b flat-bottomed headspace vials. 105

Figure 29: Total Ion Chromatograms of liquid-injected irradiated neat ethylene glycol samples, diluted in ethanol post-irradiation and compared against unirradiated controls and solvent TICs. Samples irradiated in the TriC of the JSI reactor. Black line= 50 kGy irradiated glycerol sample of the specified irradiation type with identified peak labels. Pink = unirradiated glycerol control sample, Blue = ethanol solvent. a only γ rays and b mixed-field neutron + γ rays. 111

Figure 30: Concentration of acetaldehyde for the specified dose for γ-ray (green) and neutron + γ-ray (red) irradiations of neat ethylene glycol using the JSI reactor and quantified using a GC-MS. a Polypropylene vials (PP). b Borosilicate vials with Al/Si septa (BS). Y-axis error bars derive from the relative standard deviation from calibration curves with the x-axis indicating the deviation in dose. The data are available in Appendix A, Table A4 and Table A5. 114

Figure 31: Radiation chemical yields (*G*-value) and mass productivity values of acetaldehyde for the specified dose for γ-ray (green) and neutron + γ-ray (red) irradiations of neat ethylene glycol. a Polypropylene vials (Squares and circles).

b Borosilicate vials with Al/Si septa (Triangles). c and d Mass productivity percentages of acetaldehyde in PP and BS vials, respectively. Error bars indicate the combination of instrumental, calibration and dose errors for *G*-values. Data tabulated in Appendix A, Table A11 and Table A12. *G*-value references quoted are from Barker with 0.4 wt.% glycerol [210] and Pikaev with samples of 6.2 wt.% [244]. 116

Figure 32: Concentration of methanol for the specified dose for γ-ray (green) and neutron + γ-ray (red) irradiations of neat ethylene glycol. a Polypropylene vials (PP). b Borosilicate vials with Al/Si septa (BS). Y-axis error bars derive from the relative standard deviation from calibration curves with the x-axis indicating the deviation in dose. The data are available in Appendix A, Table A4 and Table A5. 118

Figure 33: Radiation chemical yields (*G*-value) and mass production % values of methanol for the specified dose for γ-ray (green) and neutron + γ-ray (red) irradiations of neat ethylene glycol. a *G*-values with polypropylene vials (PP). b *G*-values with borosilicate vials (BS) with Al/Si septa. c and d Mass productivity percentages for polypropylene and borosilicate vials, respectively. Error bars indicate the combination of instrumental, calibration and dose errors for both values. Datasets can be found in Appendix A, Table A11 and Table A12. *G*-value references for methanol at 298K and 443K quoted are from a report by Vetrov with an undefined dose [277]. 119

Figure 34: Concentration of ethyl acetate for the specified dose for γ-ray of neat ethylene glycol. From Polypropylene vials (PP, square) and borosilicate vials with Al/Si septa (BS, triangle). No peaks were detected from neutron + γ-ray irradiations. Y-axis error bars derive from the relative standard deviation from calibration curves with the x-axis indicating the deviation in dose. The data are available in Appendix A, Table A4 and Table A5........ 121

Figure 35: Radiation chemical yields (*G*-value) and mass productivity of ethyl acetate for the specified dose for γ-ray (green) irradiations of neat ethylene glycol. a γ-ray for polypropylene vials (Squares) and borosilicate vials with Al/Si septa (Triangles). b Mass productivity percentages. Error bars indicate the relative combination of instrumental, calibration and dose errors for both sets of values. The full dataset can be found in Appendix A, Table A11 and Table A12........ 121

Figure 36: Concentration of acetic acid for the specified dose for γ-ray (green) of neat ethylene glycol. From Polypropylene vials (PP, square) and borosilicate vials with Al/Si septa (BS, triangle). No acetic acid peaks were detected from neutron + γ-ray irradiations. Y-axis error bars derive from the relative standard deviation from calibration curves with the x-axis indicating the deviation in dose. The data are available in Appendix A, Table A4 and Table A5. 122

Figure 37: Radiation chemical yields (*G*-value) and mass productivity of acetic acid for the specified dose for γ-ray (green) irradiations of neat ethylene glycol. a γ-ray for polypropylene vials (squares) and borosilicate vials with Al/Si septa (triangles). b Mass productivity percentages. Error bars indicate the relative combination of instrumental, calibration and dose errors for both sets of values. Full datasets can be found in Appendix A, Table A11 and Table A12........ 123

Figure 38: Concentration and radiation chemical yields (*G*-value) as a function of neutron + γ-ray dose rate. From neat ethylene glycol samples, a and b display the concentration data for acetaldehyde and methanol, respectively. c and d display the *G*-value for acetaldehyde and methanol, respectively. All samples were irradiated with a total dose of 50 kGy. Error bars indicate the relative combination of instrumental, calibration, and dose errors for *G*-values with concentration errors deriving from calibration curve standard deviations. The datasets are available in Appendix A, Table A4 and Table A11. 125

Figure 39: Total Ion Chromatograms of liquid-injected irradiated neat glycerol samples within PP vials, diluted in ethanol post-irradiation and compared against unirradiated controls and solvent TICs. Black line = 50 kGy irradiated glycerol sample of the specified irradiation type with identified peak labels. Pink = unirradiated glycerol control sample, Blue = Ethanol. a γ-ray only and, b mixed field neutron + γ-ray irradiations. 127

Figure 40: Concentration of radiolytic acetol for the specified absorbed dose for γ-ray (green) and neutron + γ-ray (red) irradiations of neat glycerol. a Polypropylene vial, PP (circles and squares). b Borosilicate vials, BS with Al/Si septa (triangles). The data are available in Appendix A, Table A6 and Table A7. 131

Figure 41: Radiation chemical yields (*G*-value) and mass productivities of acetol for the specified dose for γ-ray only (green) and neutron + γ-ray (red/orange) irradiations of neat glycerol. γ-ray only dose rate ~40 Gy min. $^{-1}$ and neutron + γ-ray dose rate of 1.64 to 6.5 kGy min. $^{-1}$ a *G*-values with polypropylene vials (squares and circles). b *G*-values with borosilicate vials with Al/Si septa (triangles). c and d mass productivity of PP and BS vials, respectively for the two irradiation types. The data are available in Appendix A, Table A13 and Table A14..................................... 133

Figure 42: Concentration of radiolytic solketal for the specified absorbed dose for γ-ray only (green) and neutron + γ-ray (red) irradiations of neat glycerol. a Polypropylene vials (Squares). b Borosilicate vials with Al/Si septa (Triangles) as radiation vessels. The data are available in Appendix A, Table A8 and Table A9.......................... 134

Figure 43: *G*-values and mass productivity of solketal from varying the absorbed dose for γ-ray (green) and neutron + γ-ray (red) irradiations of neat glycerol. a Polypropylene vial (squares), b Borosilicate vials with Al/Si septa (triangles), c and d mass productivity of PP and BS vials, respectively for the two irradiation types. The full dataset is available in Appendix A, Table A13 and Table A14........................... 135

Figure 44: Concentration and *G*-values as a function of neutron + γ-ray dose rate. From neat glycerol sample for; Concentrations of a acetol and b solketal with corresponding *G*-values of c acetol and d solketal. All samples were irradiated with a total absorbed dose of 50 kGy. The data are available in Appendix A, Table A6 and Table A13.. 136

Figure 45: Concentration of radiolytic acetol and solketal for the specified absorbed dose for γ-ray only (a and b) and neutron + γ-ray (c and d) irradiations of binary mixtures in PP vials. Different mixtures are as follows: neat glycerol (black squares), glycerol-aqueous mixtures based on wt.%: 70% glycerol (red circles), 63% glycerol (blue upward triangles) and 50% glycerol (green downward triangles). a acetol and b

solketal concentrations from γ-ray only irradiations. c acetol and d solketal concentrations from neutron + γ-ray irradiations. The data are available in Appendix A, Table A8 and Table A9 (Produced by Plant A. G). 138

Figure 46: *G*-values and mass productivities of acetol and solketal from aqueous glycerol mixtures of varying concentrations with delayed γ-ray only absorbed doses with a and b from acetol and solketal *G*-values respectively, c, and d, acetol and solketal mass productivity percentages respectively. Different mixtures are as follows: neat glycerol (black squares), glycerol-aqueous mixtures based on wt.%: 70% glycerol (red circles), 63% glycerol (blue upward triangles) and 50% glycerol (green downward triangles). The data are available in Table A15. (Produced by Plant A. G). 139

Figure 47: *G*-values and mass productivities of acetol and solketal from varying aqueous glycerol mixtures of varying concentration with mixed neutron + γ-ray absorbed doses; a acetol *G*-values and, b and solketal *G*-values respectively. c and d show acetol and solketal mass productivities, respectively. Different mixtures are as follows: Neat glycerol (black squares), glycerol-aqueous mixtures based on wt.%: 70% glycerol (red circles), 63% glycerol (blue upward triangles) and 50% glycerol (green downward triangles). The data are available in Table A16. 140

Figure 48: Concentration of acetol and solketal from ternary glycerol mixtures (samples 108 to 116 in Table 18) for 50 kGy of either γ-ray only or mixed-field neutron + γ-ray irradiated, compared against irradiated neat samples and unirradiated ternary mixtures. The indicated ternary mixtures containing glycerol, acetone and water have the following compositions in wt.%: i) 46, 28, 26; ii) 34, 34, 32; and iii) 26, 48, 26, respectively. Error bars represent the relative standard deviation from the calibration curves for each analyte, combined with any dilution work-up errors. Data are available in Appendix A, Table A10. 143

Figure 49: *G*-value and % molar yield of acetol and solketal from ternary (samples 108 to 116 in Table 18) and binary (67, 55, 61 from Table 16 and 29, 17, 23 from Table 15) glycerol mixtures for 50 kGy of either γ-ray only or mixed-field neutron + γ-ray irradiated samples. a *G*-values from γ-ray only irradiated samples with an average dose rate of 40 Gy min. $^{-1}$. b *G*-values from mixed-field neutron + γ-ray irradiated samples with a dose rate of 3260 Gy min. $^{-1}$. c % molar yields for only γ-ray irradiations. d % molar yields of mixed-field and unirradiated control samples. The indicated ternary mixtures containing glycerol, acetone and water have the following compositions in wt.%: i) 46, 28, 26; ii) 34, 34, 32; and iii) 26, 48, 26, respectively. (Data are available in Appendix A, Table A17. Error bars represent the combined relative errors from instrumental and dose uncertainties for each sample. Reference data [3] (Ref) for acetol used in a, used N_2O-saturated aqueous glycerol samples with a γ-ray dose and dose rate of 1.4 kGy and 8 Gy min. $^{-1}$, respectively. 145

Figure 50: Ternary plots of radiation chemical yields (*G*-value) in μmol J^{-1} for samples of varying starting mixtures containing mass fractions of glycerol, acetone, and water of 50 kGy γ-ray only dose. *G*-values of, a acetol and, b solketal have been displayed with corresponding values for mass productivities in c and d, respectively. All mixtures within PP vials that have been irradiated with 50 kGy γ-ray only dose in the TriC. The 7 data points are indicated by black dots. A linear colour gradient is used for both *G*-value and mass productivity plots. 146

Figure 51: a Concentration and b *G*-values of acetic acid from the ternary (glycerol + acetone + water) mixtures using only γ-ray and neutron + γ-ray irradiations. Samples have been either irradiated with 50 kGy γ-ray only irradiations with an average dose rate of 40 Gy min^{-1} or 50 kGy neutron + γ-ray mixed field irradiations with dose rates of 3260 Gy min^{-1} 147

Figure 52: Max production values of acetol and solketal in t year^{-1} using the Krško reactor (50 organic pipes) and the Krško spent fuel pool (~1710 organic pipes) models and highest yielding mixtures. Mix 1= binary aqueous glycerol mixture (data from sample 67) and Mix 2 = ternary glycerol, acetone, and water mixture (data from sample 109). 149

Figure 53: A map of continental Europe showing acetol and solketal maximum production capacity per country (for ternary glycerol, water, acetone mixture of (46, 26, 28 wt.%, sample 109) based on the country's total net electricity capacity GW(e) output. Acetol=orange, solketal=turquoise with the areas of the circles being directly proportional to production values. Top 4: France, European Russia, Ukraine, and the UK. Base map altered from ©MapRoom. Table A20 in Appendix A lists the potential acetol and solketal production for each country. 150

Figure 54: The expanded proposed physical and physicochemical mechanisms involved up to ~10^{-4} s for the radiolysis of neat ethylene glycol. a Direct ionization. b Fragmentation of the radical cation. c Initiating H-abstraction for acetaldehyde production. d Acid-catalysed chain reaction. e Radical propagation while forming acetaldehyde. Mechanisms have been deduced from the general radiolysis literature for a and b, the chain rearrangement mechanisms for c, d and e have been expanded upon by Plant A. G. from the previous literature [244, 246]. 159

Figure 55: Proposed physical and physicochemical initial mechanisms from the direct action of irradiations upon pure neat glycerol (by Plant A. G.). a Direct ionization. b Ion fragmentations resulting in most C-C or C-O scissions. c and d Ion dissociation reactions form acidic glycerol cations with either radicals or carbonyl species. e clustering and stabilization of acidic glycerol. f, Neutralization of acidic glycerol via solvated electrons. Since H-dissociation could occur at any hydroxyl carbon of glycerol. (R_1 and R_2 = $-CH_2OH$ for α-carbon or -H and $–CHOH-CH_2OH$ for β-carbon species, respectively.) Physical and physicochemical mechanisms have been deduced from generalized literature by Plant A. G. 160

Figure 56: Subsequent proposed radiation-directed, diffusion-controlled reactions up to 10^{-4}s. Radical-directed reactions a-c. a Intraspur radical conversion to the more stable hydroxy radical. b C-H scission dominated by α-hydrogen abstraction. Reactions c to e is the expanded mechanism for acetol production [3]. c Hydrogen abstraction at the weaker α-C-H bond. d Acid-catalysed chain re-arrangement via an acidified species. e α-H-abstraction and α-hydroxy radical regeneration f, Direct action on water producing reactive species such as H_3O^+. g Acid-catalysed ketalization reaction scheme for solketal. (R_1 and R_2 = $-CH_2OH$ for α-carbon or H and $–CHOH-CH_2OH$ for β-carbon radicals, respectively.) The chain rearrangement mechanism has been expanded upon by Plant A. G. from previous literature [3]. 162

Figure 57: Proposed conflicting reactions affecting acetol production (by Plant A. G): a to e are interspur radical combinations reactions promoted by the overlapping of spurs with high LET and high dose rates. f reduction of acetol via e_{solv}^{-}. g neutralization of the hydronium ion. h superoxide anion formation. i hydroperoxy ($HO_2^{\bullet -}$) radical formation. j peroxyl radical ($RO_2^{\bullet}$) formation. k radical combination of peroxyl radicals for aldehyde formation). Physicochemical and chemical mechanisms have been deduced from generalized literature by Plant A. G......... 165

Figure 58: A basic process schematic of the proposed nuclear cogeneration process with the spent fuel pool design (dry cask storage also remains plausible) to produce acetol and solketal. 167

List of Tables

Table 1: Types of electron interactions with a light nuclei molecule (e.g., methanol), b and a are the parameters shown in Figure A3. 24

Table 2: Types of neutron interactions with a light nuclei molecule (e.g., methanol) and the primary transient species produced. 25

Table 3: Types of gamma interactions with a light nuclei molecule (e.g., methanol) and the primary transient species formed. 29

Table 4: LET of various radiation types in water, a) [147, 148], b) [149]. 31

Table 5: Primary reactions of e_{solv}^{-}, $^{\bullet}$OH. And $^{\bullet}$H. showing redox equations and potentials, E_o where n is the charge of the ion. Example reactions are also given [158]. 35

Table 6: The main radiolysis (physical and physicochemical) reactions of pure methanol, compiled from the available literature [168]. 36

Table 7: Relative absorbed dose (Bragg curve) into H_2O from epithermal neutrons and ^{60}Co γ rays. [178, 179] 40

Table 8: Bond scission likelihood percentages for aliphatic alcohols [114]. 52

Table 9: Californium-252 commissioning and in-use specifications 70

Table 10: Neutron Flux Specifications of the Triangular Irradiation Channel (TriC). 73

Table 11: Mass compositions of the glycerol mixtures irradiated with the indicated doses from the JSI TRIGA reactor using both operational and shutdown irradiation modes. 79

Table 12: Analyte standard concentrations for the calibration curve range. Full examples of the calibration curves are given in Figure A6 and Figure A7. 83

Table 13: Organic sample list for Cf^{252} irradiations for samples shown in Figure 15. 90

Table 14: Peak identification and vapour pressure of impurities within ethylene glycol. 93

Table 15: List of samples irradiated with neutrons + γ rays from the JSI reactor (in the TriC): containing either neat glycerol, neat ethylene glycol or binary aqueous glycerol mixtures in PP vials. Aqueous binary mixtures glycerol wt.%: Mix. 1: 63% Mix. 2: 50% Mix. 3: 70%. 95

Table 16: List of samples irradiated with γ rays only from the JSI reactor (in the TriC) containing either: neat glycerol, neat ethylene glycol or binary glycerol mixtures in PP vials. Unirradiated control samples are also listed. Aqueous binary mixtures glycerol wt. %: Mix. 1: 63% Mix. 2: 50% Mix. 3: 70%. 97

Table 17: List of organic samples irradiated with either neutron + γ – rays or γ – rays only from the JSI reactor (in the TriC) containing either neat glycerol or neat ethylene glycol within BS vials with Aluminium/Silicone septa. 99

Table 18: List of analysed organic samples irradiated with either neutron + γ rays or γ rays only from the JSI reactor (in the TriC). Organic samples are ternary glycerol: acetone: water mixtures within PP vials. 101

Table 19: Organic neat samples for instrumental neutron activation analysis (INAA). These samples were irradiated in the JSI carousel facility. 101

Table 20: Axial compression sample list. Rounded or flat-bottomed, empty, unirradiated BS vials capped with either Aluminium/Silicone or PTFE/Silicone septa with crimp caps are listed. Two 100 kGy γ-ray irradiated BS vials were compressed for comparison. Vial failure forces and pressures have been included. 102

Table 21: Axial compression force and pressure analysis of the borosilicate (BS), headspace rounded or flat-bottomed vials. Vials were capped with either aluminium/silicone (Al/Si), PTFE/Silicone (PTFE/Si) septa crimp caps or left uncapped. Two 100 kGy γ-ray irradiated vials were also compressed as listed in the table. 106

Table 22: Mass change analysis of BS and PP vials for leak identification. Vial mass data was used from Table 15 to Table 18. 108

Table 23: Induced radioactivity of detectable radioisotopes and their decay: Neat glycerol and ethylene glycol were irradiated with a mixed-field absorbed dose of a total of 520 kGy (270 kGy from thermal neutrons and 250 kGy from γ rays) producing the following activation products. 109

Table 24: Ethylene Glycol Radiolysis Products List: Products from either mixed-field neutron + γ-ray or only γ-ray from neat ethylene glycol. A similarity % match of >90% to an analyte was considered suitable for standard confirmation. 112

Table 25: Unidentified analyte peaks from neat ethylene glycol radiolysis listing main EI fragments. Full EI fragment patterns are shown in Appendix A, Figure A12...... 113

Table 26: Zero dose *G*-values for radiolytic products from neat ethylene glycol via extrapolation. 124

Table 27: Qualitative radiolysis products of glycerol from either mixed-field neutron + γ-ray or only γ-ray irradiation using liquid sampling GC-MS. Displayed products are for γ-ray absorbed doses above 20 kGy. Molecule similarity comparison against the NIST11 MS spectrum patterns, products were confirmed with analytical standards where applicable. 128

Table 28: Unidentified large analyte peaks from neat glycerol radiolysis. EI fragment patterns are shown in Appendix A, Figure A13. 129

Table 29: Extrapolation to *zero dose G*-values of acetol and solketal from glycerol samples in polypropylene (PP) vials.. 141

Table 30: Scale-up values for each MCNP scenario showing the maximum production capacity per year of acetol and solketal. Starting mixtures of i) binary glycerol, water composition (70, 30 wt.%) and ii) ternary glycerol, acetone, and water composition (46, 28, 26 wt.%). 148

Table 31: Expansion and impact values of the cogeneration Europe network for EU fuel blends. Extrapolated by total power output from 688 MWe Krško NPP to 180 reactors producing a total power output of 159.3 GW. 151

Table 32: Previously explored radiation-chemical processes in literature and *G*-values. 168

List of Abbreviations

Abbreviations	Full Name
Acetol	1-Hydroxypropan-2-one
BDE	Bond Dissociation Energy
BS	Borosilicate
BWR	Boiling Water Reactor
EI	Electron Ionization
EROI	Energy Return on Investment
Ethylene Glycol	1,2-Ethanedol
FAME	Fatty Acid Methyl Ester
FBR	Fast Breeder Reactor
GC-MS	Gas Chromatography Mass Spectrometry
GCR	Gas-Cooled Reactor
GHG	Greenhouse Gases
Glycerol	Propane-1,2,3-triol
GWP	Global Warming Potential
HPGe	High Purity Geranium
HPLC	High-Performance Liquid Chromatography
HS	Headspace
HSGC-MS	Headspace Gas Chromatography-Mass Spectrometry
IR	Infrared
INAA	Instrumental Neutron Activation Analysis
IAEA	International Atomic Energy Agency
ICRU	International Commission on Radiation Units and Measurement
IEA	International Energy Agency
IC or FCs	Ionization or Fission Chambers
JANIS	Java-based Nuclear Data Information System
JSI	Jožef Stefan Institute
KERMA	Kinetic Energy per unit Mass
LCA	Life Cycle Assessment
LCOE	Levelized Cost of Energy
LWGR	Light Water Graphite Reactor
LET	Linear Energy Transfer
LOD	Limit of Detection
MCNP	Monte Carlo N-Particle Transport
MP	Mass Productivity
MSR	Molten Salt Reactor
NPP	Nuclear Power Plant
OECD	Organisation for Economic Co-operation and Development
PP	Polypropylene
PHWR	Pressurized Water Reactor
PWR	Pressurized Heavy-Water Reactor

Abbreviations continued.

RED	Renewable Energy Directive
SPME	Solid-phase Microextraction
SCWR	Supercritical-Water-Cooled Reactor
SOMO	Singularly Occupied Molecular Orbital
SFP	Spent Fuel Pool
Solketal	(2,2-Dimethyl-1,3-dioxolan-4-yl) methanol
TIC	Total Ion Chromatogram
TriC	Triangular Irradiation Channel
TRIGA	Training, Research, Isotope, General Atomics
VALCOE	Value-added Levelized Cost of Energy
VHTR	Very-High-Temperature Reactor

1 Introduction

Nuclear cogeneration or co-production is the proposed strategy where alongside the production of electricity from nuclear power, a co-product is generated which is typically heat-derived [1]. The resulting co-products aim to decarbonise the industry and introduce better flexibility into nuclear energy generation. One alternative cogeneration system is to incorporate the synthesis of valuable chemicals from the under-utilized sources of ionizing energy from fission processes [2].

The research reported in this thesis is a study of the reactions and mechanisms within liquid polyol feedstocks using ionizing radiation. It studies the optimisation of these radiolytic reactions towards synthesising biofuel additives, textile reagents, or chemical intermediates for pharmaceutical solvents. A theoretical extrapolation of these reactions towards an industrial European production network using spent fuel as a catalytic source is detailed.

Several motivations prompted this research: firstly, there is a notable lack of salient radiation chemistry literature exploring variable radiation and sample parameters for the irradiation of glycerol. Furthermore, the radical chain reaction observed in the previous literature [3] has not been substantially optimised, especially with the significance of glycerol as a renewable organic feedstock to make sustainable chemicals. Additionally, in radiolysis literature, the lack of recent neutronic-related irradiations presents an opportunity to re-examine the previous conclusions reached and to highlight the possible use of spent fuel as a beneficial source of ionizing radiation. Finally, the radiation chemistry literature that focuses on scaling up radiolytic processes to industrial scales to solve current issues with renewable chemical supplies is limited.

The system proposed in this work details the utilization of ionizing energy from critical fission processes or spent nuclear fuel in a greater, more advantageous capacity than current methods. This work aligns with the recent foci on nuclear cogeneration strategies which aim to improve nuclear power’s flexibility, economic viability, and environmental performance [1, 4]. Newly proposed in this work is the combination of a nuclear cogeneration process with waste organic feedstocks, which results in the synthesis of sustainable bio-derived organic compounds. The cogeneration of chemicals offers a relativity valuable product when compared against electricity or other co-products such as hydrogen gas or desalinated water [5]. Additionally, the cogeneration of renewable bio-derived chemicals would alleviate the global reliance on petrochemically derived compounds.

While the current cogeneration policies mainly focus on utilizing low-temperature processes which are widely applicable for most NPPs (nuclear power plants), these processes would not present a suitable increase in the value proposition for nuclear power [5, 6]. Additionally, higher temperature processes such as hydrogen production, oil recovery or steel manufacturing do not apply to the majority (~96%) of current or proposed worldwide nuclear reactors [1, 7]. Consequently, this work presents a potentially profitable nuclear cogeneration process that is independent of any temperature requirements.

As shown in this research, numerous ethylene glycol and glycerol samples were irradiated with ionizing fields from a 250 kW, research fission reactor. The radiolytic products were analysed with gas chromatography-mass spectrometry techniques and assessed regarding the values of radiation chemical yield (*G*-value) and mass productivity. We have shown that the acid-catalysed radical chain reaction forming acetol is promoted by irradiating highly concentrated glycerol mixtures with low LET γ-ray irradiations at low dose rates. Additionally, similar conditions are beneficial for the newly reported radiolytic process to form solketal. These optimal conditions align with the potential use of spent nuclear fuel as a future catalytic resource, bringing a notable use to materials that are otherwise treated as costly wastes. Many spent fuel facilities within Europe possess numerous quantities of these under-utilized sources of ionization energy. In this work, particle transport code models of a representative spent fuel facility have been designed to calculate the maximum production capacity of acetol or solketal via radiolytic synthesis using such a spent fuel array. An expansion to 180 equivalent facilities throughout geographical Europe could theoretically yield production capacities of ~1.3 kt year^{-1} of biofuel additives. These additives could contribute to the bio-proportion of modern transport fuel blends and alleviate the reliance on petrochemicals.

1.1 List of Chapters

Chapter 2 presents the current state of nuclear power, nuclear cogeneration processes, and how these could be blended with the biodiesel industry to produce valuable chemicals using waste materials and under-utilized irradiation. It also covers the scientific background of radiation chemistry, primary interactions, radiation factors, and key radiolysis values. The available radiolysis literature regarding alcohols and polyols are reviewed as to their radiation and sample parameters.

Chapter 3 details the materials and methodologies used in the irradiation of ethylene glycol and glycerol-based samples using a fission reactor and their analysis. Additionally, it details the potential irradiation facilities via MCNP simulations which are then used to scale up a radiolysis process for a theoretical Europe production network.

Chapter 4 displays the results from the analysis of irradiated ethylene glycol and glycerol samples, showing *G*-values and mass productivities against several variable irradiation and sample parameters. The extrapolation and simulation results of the expansion of the radiolytic process are also given.

Chapter 5 discusses the data presented in Chapter 4, the projected trends from varying irradiation and sample parameters. Aspects of induced radioactivity, the efficacy of neutrons and radiolytic reaction mechanisms are discussed. Additionally, the expansion to a European production network utilizing spent fuel facilities is evaluated for the solketal production process.

Appendix A shows tabulated radiolytic data from the literature on alcohols and polyols and their dependence on variable parameters. Additionally, it shows the radiolytic data obtained from this research which is tabulated for comparisons to the literature. INAA data, vial pressure calculations, calibration curves, mass fragment patterns of unidentified peaks, supporting chromatograms, and the data used to show the European extrapolation of the solketal production process are also listed.

2 Background: Nuclear Cogeneration and Radiation Chemistry

In this chapter, the case for nuclear power and the current vision of nuclear cogeneration is presented, expanding on the potential for chemical production from ionizing energy. The field of radiation chemistry is explored with a focus on methodologies, reaction mechanisms, and energy transfer for the irradiation and analysis of liquid alcohol and polyol compounds. Finally, an in-depth exploration of radiolysis literature, concentrating on final product radiation chemical yields (*G*-values) is described.

2.1 Nuclear Power: Essential and In Decline

Since the first controlled, self-sustaining, nuclear chain reaction from a crude pile reactor at the University of Chicago in 1942 [8], mankind has been intrigued with harnessing the power of sustained nuclear fission. The operation of the Chicago Pile (CP-1) proved nuclear power's feasibility to generate electricity. During the following decades of the 1950s, 1960s and 1970s, Gen I & II nuclear reactors were constructed worldwide to provide for the ever-increasing demand for electricity. However, in recent years, nuclear power has seen a stasis in terms of operational reactors worldwide with the number oscillating between 415 and 450 since 1989 [9]. This stasis has resulted in a decline in terms of its share of the total global power when compared against all other power generation systems; showing a decrease in total % global energy output dropping from 6.7% since 2000 to 5.1% in 2018 [10, 11].

With the world's ever-increasing population, increasing energy demands and the looming problems associated with climate change which are linked to the global output of greenhouse gases (GHG) such as $CO_{2,}$ there is a concerning trend with the type of recently constructed power generation systems. Data indicates that coal and natural gas power plants have been increasing relative to other types of power generation systems which is also expected to continue until 2040 [12]. Coal and natural gas are amongst the worst electricity generation methods that produce relatively high CO_2 emissions, with a world median of 820 and 490 g CO_2-eq kWh^{-1}, respectively [13]. For comparison, low carbon footprint methods such as wind and nuclear produce 11 and 12 gCO_2-eq kWh^{-1}, respectively. For future net zero GHG emission goals [14] to be achieved, nuclear power will need to be part of the future zero-carbon scenario as a stable, reliable, firm, low-carbon supply of electricity [15], especially to keep future electricity costs low. Despite the importance of nuclear power, and its future power capacity projected to be relatively lower, this poses the question: why is nuclear power gradually declining relative to other methods? The answer can be explained by both economic and political factors being unfavourable towards nuclear power [16].

Politically, there are many complex factors for the relative decline of nuclear power which have resulted in drastic government changes in energy policy against nuclear power [17-22]. These changes contributed to an increased reliance on coal and natural gas, subsequently increasing GHG emissions and cumulative worldwide mortalities [23]. Changes in policies were mainly fuelled by public anxieties due to health and safety concerns [24], focusing on low-probability, high-impact events with additional concerns about spent fuel management. Despite these notable concerns, nuclear power appears to be safer than all fossil fuel alternatives in terms of related deaths [25, 26], as shown by Figure A1 in Appendix A. Despite the complex political factors, the main reason for the decline of nuclear power should be down to its economic viability.

Economically, nuclear power's decline can be partially attributed to its profitability when compared with other types of low CO_2 power generation methods such as wind and solar. According to the recent Value-Adjusted Levelized Cost of Electricity metric (VALCOE), the cost of electricity from new nuclear plant builds in 2040 within the EU are projected to be more expensive at 115 USD $MWhr^{-1}$ and 80 USD $MWhr^{-1}$ for both wind and solar systems [12, 17]. This VALCOE metric considers a system's initial costs and its lifetime revenue as well as the value of the electricity within its sector in terms of energy, capacity, and flexibility [27]. Additional economic metrics such as the LCOE and ROI put nuclear power less favourably [12]. Other metrics such as the Energy Return on Investment (EROI) metric [28] have shown nuclear power in a competitive light to renewables [29, 30], although there is variation between different studies and sources [31].

Other than these value metrics, additional factors make the nuclear industry less appealing than other power generation methods. The main drawback of nuclear power is the high capital costs involved in planning and construction followed by lengthy construction times [32]. Globally, an NPP takes a median of 7.7 years from planning to commissioning [33] which is a significant timescale to wait before the initial capital investments are seeing a return in profits. As an extreme example, a new 3200 MW NPP (Hinkley Point C, UK) requires a projected building cost of £22.9bn [34] and will take 13-15 years to build. In contrast, the recently constructed 2200 MW natural gas-fired power plant (Pembroke B, UK) took 4 years to build at a cheaper cost of £800m [34] and produces the same product of electricity. Despite these disadvantages, nuclear power offers low running costs due to lower uranium and enrichment prices which are less vulnerable to inflation when compared against fossil fuel alternatives [35]. Additionally, as a stable firm source of electricity, nuclear power can produce electricity to the grid in all conditions, unlike intermittent renewables.

However, one way to make nuclear power a more attractive alternative to other low-carbon methods is to improve its profitability. There are limited ways to do this, but cogeneration or co-production has been the focus of much interest from the nuclear industry and recent research [36-38]. Co-production expands the range of applications for nuclear power other than electricity would increase the value proposition of nuclear power, appealing to potential investors.

2.2 Nuclear Cogeneration

Nuclear cogeneration or co-production is the proposed concept where there is the simultaneous production of electricity and heat (or heat-related product) from a nuclear reactor [4], consequently using energy from a fission process more efficiently than is currently utilized in NPP operations. For standard operating, in-operation boiling or pressurized water reactors (BWRs or PWRs), approximately 33% of the energy produced from the reactor is harnessed just to produce electricity [39]. These efficiencies can be improved by utilizing different NPP types such as advanced gas-cooled reactors (AGR) (<42%) or molten salt reactors (MSR) (≈50%) [40], although modern MSR reactor designs still yet to field an operational commercial reactor to date [10]. The remaining percentage of lost energy is mostly rejected in the form of heated water to the environment as a waste product. Lower-temperature wastewater (200-300 ^{o}C) can be utilized for premises heating [1], while higher-temperature (>350 ^{o}C) wastewater can be used for hydrogen generation, direct air capture and many more applications [41]. These options provide additional possible revenue streams for different applications – alongside the normal production of electricity for nuclear reactors [4]. One of the benefits of cogeneration would be the natural increase in the flexibility of an NPP, giving the option of choosing to prioritize between electricity production during peak demand periods or focussing on other processes which have less variable daily demand. This increase in flexibility of the end-product would be factored into the VALCOE metric, improving the profitability metric of nuclear power if cogeneration processes are implemented.

Since most of the energy from an NPP is lost as heat, this explains the focus of cogeneration projects in utilizing low-temperature heated water for additional applications. According to the IAEA, as of 2017, 34 cogeneration projects were currently implemented, the majority of 19 being focussing on district heating, 11 on the desalination of water, and 4 on heating steam for industrial processes [1, 42]. Figure 1 shows more thermo-related co-products and their required process temperatures, alongside the outlet temperature ranges of coolants in operational and future NPP designs.

While the large variety of co-products listed in Figure 1 would have the potential to increase the flexibility of an NPP, it does not technically make it significantly more profitable. There are a few problems in using the excess heat from an NPP with these processes. The first problem is the limitation on outlet coolant temperatures which is required for higher temperature cogeneration processes from current Gen II and Gen III NPPs. Most operational reactors are limited to a low coolant outlet temperature below 340 °C, corresponding to 96.1% of the worldwide operational Gen II reactors based on PWR designs. By design and operation, PWRs are limited to maximum coolant temperatures of 345 °C to prevent the coolant from boiling which would impede the heat transfer properties of the system. Other water-based coolant reactors such as boiling water reactors (BWRs) also have this coolant temperature limitation. Additionally, the trend for under-construction, Gen III NPPs is shifting towards more PWR-based reactors due to their advantages in power output stability, ease of operation and safety. The second problem for thermo-related co-production is the value of the products generated. For the most common lower-temperature coproducts (<300 °C), despite the success of heating projects, new studies have found that other lower-temperature applications such as water desalination and electrolytic hydrogen production are just as profitable as the corresponding electricity that would normally be produced [5, 43-46], not significantly improving the value prospect of nuclear power.

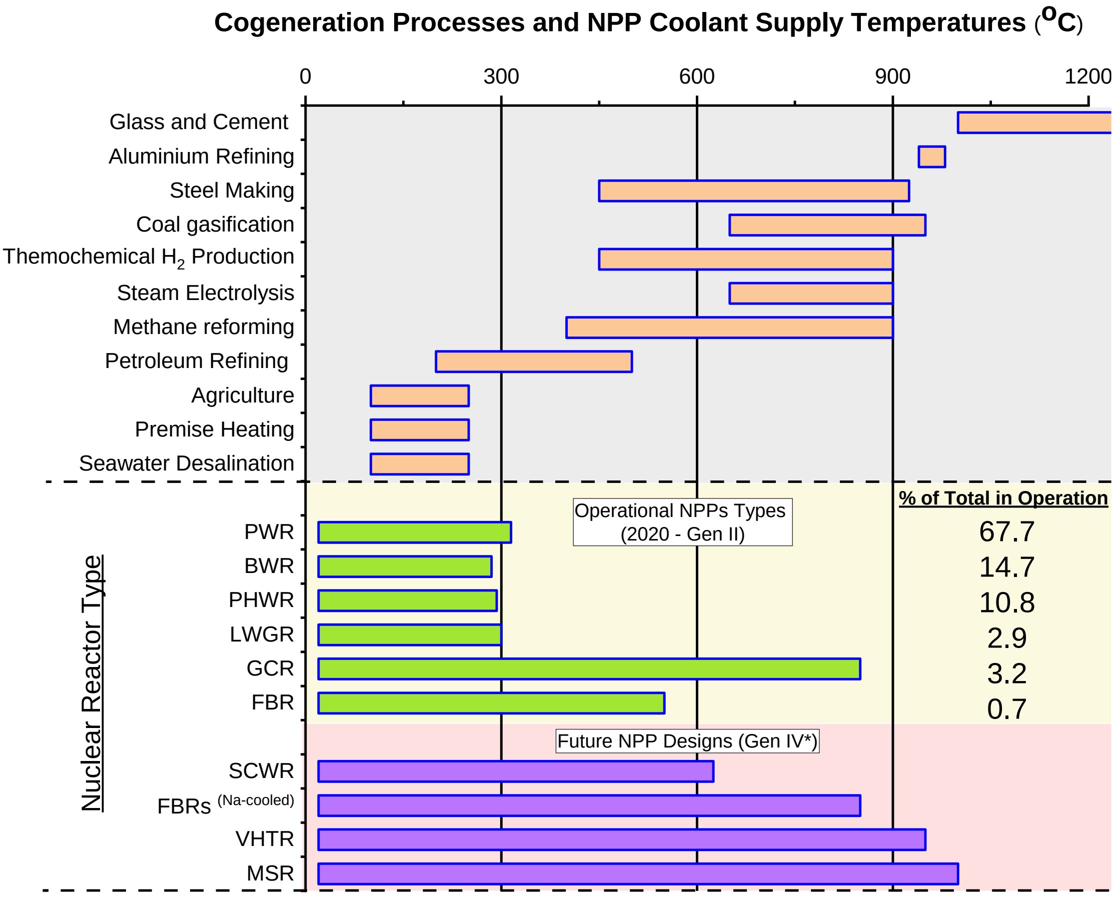

Figure 1: Heat-derived cogeneration products and NPP coolant outlet temperature ranges in °C. Co-products are listed by minimum required temperatures [1]. The maximum coolant temperature percentages per reactor type have been displayed against the 443 currently operational reactors worldwide (as of 2020) [7]. Possible future Gen IV reactor designs have been included. *Gen III reactors type percentages are similar to current Gen II NPPs. [10, 47]

For high-temperature heat-derived co-processes such as methane reforming and steam electrolysis, the applications of these are looking unlikely due to future reliance on low-temperature PWR designs. To significantly impact nuclear power's profitability, higher valued co-products are required. Therefore, exploring further in detail the cogeneration of coproducts that do not depend on thermal methods would be advantageous to the industry. The highest-value coproduct that could be produced from a nuclear reaction are radioactive isotopes. However, the most useful nuclear-derived radioisotope is ^{99m}Tc (readily produced from ^{99}Mo) and is utilized in niche medical imaging applications but has limited demand [48, 49], making scale-up processes unviable.

2.2.1 Nuclear Cogeneration of Chemicals

Another valuable co-product that could be synthesised from nuclear reactors are commodity chemicals. As the main co-product, commodity chemicals can offer a higher relative value product, estimated between 10^3 and 10^6 \$ mol^{-1} of depending on the product formed. This is compared against electricity which is only valued between 10^{-3} to 10^2 \$ mol^{-1} per cost of the corresponding fuel or source [5, 6]. The concept of producing chemicals using nuclear reactors has been initially explored in the 1950s and ’60s [2, 50, 51], although there have been scarce similar recent studies. Alongside heat, ionizing radiation is also emitted from fission events. This ionizing energy is currently utilised inefficiently, transforming this unique energy into thermal energy which has fundamental losses in energy conversion as defined by the second law of thermodynamics. However, valuable commodity chemicals could also be synthesised from this under-utilised ionizing radiation [5]. This ionizing energy can initiate unique reactions compared to traditional thermochemical methods. These unique radiation-chemical reactions can generally be referred to as radiolysis when ionizing radiation interacts with gaseous or liquid media. Radiolysis is where free radicals (generally a species with a singularly unpaired valence electron), ions, free electrons or neutral species are generated from the cleavage (dissociation) of chemical bonds from the ionizing radiation [52]. The specific concept of using ionizing fields from a nuclear reactor for chemical synthesis has been mentioned in older texts [2, 53]. This system is referred to as a neutron-gamma chemonuclear reactor.

Utilizing this ionizing energy for more purposes could elucidate more profitable cogeneration processes for the nuclear power industry, compared with conventional hydrogen production or desalination [5, 6]. From fission processes, it is estimated that 12% of all liberated energy is carried by neutrons and γ rays [2], with considerable γ-ray energy losses occurring in the reflectors and shielding. It is estimated that 3% to 3.5% of the total fission energy could be feasibly utilized for organic media deposition (as a γ-ray cogeneration process), with theorised minimal product activation given suitable purification techniques [2]. Additionally, the ionization energy emitted from decaying radioactive isotopes such as ^{90}Sr, ^{129}I, and ^{137}Cs within spent nuclear fuel rods is almost completely wasted [54]. With a dose rate of approximately 200 Gy hr^{-1} after a 1-year cooling period [55], these discarded sources of ionizing energy could be useful for radiolysis-driven applications.

Radiolysis-derived chemicals from ionization energy offer several advantages over the proposed traditional thermochemical cogeneration methods. Firstly, chemicals can be produced irrespective of reactor temperatures meaning that all reactors, including common PWRs, can be utilized for radiation chemical synthesis via the use of ionizing radiation. The second reason is the possibility of unique reactions compared to traditional thermochemical processes. Exploring the cogeneration definition [4] to expand upon ionizing radiation as a source of energy to produce chemicals could be important to the future of nuclear power and climate change mitigation. There have been several suggested chemonuclear systems [2] involving ionizing fission irradiations which include nitrogen dioxide [56], carbon dioxide cracking [57], ethylene glycol [58], phenol [59] and hydrazine [60]. However, one successful industrial example of radiation-induced chemical synthesis is the production of ethyl bromide (bromoethane) in 1963 [61]. The Dow Chemical Company developed a process to produce ethyl bromide via the use of high energy gamma (γ) irradiation to catalyse the addition reaction between ethylene and hydrogen bromide, as per equation (1). This promising process, yielded large quantities of ethyl bromide (400 tonnes per year), achieving maximum radiation chemical yields or G-values (see chapter 2.12.1) of ≈ 10^3 -10^4 μmol J^{-1} for liquid systems.

$$C_2H_4 + HBr \rightarrow C_2H_5Br \tag{1}$$

Used as a lead scavenger in transport fuels, the demand for ethyl bromide fell as leaded fuels were phased out in the 1960s and '70s before the Dow process was no longer required. Recently, no large-scale, notable industrial synthetic processes have utilized radiation chemistry like Dow's process. Exploring the idea of nuclear-chemical systems, a further possible advantage in terms of sustainability both economically and environmentally would be introducing a renewable feedstock element into a chemonuclear system.

2.3 Biochemicals and Biofuels

Nearly 12% of all worldwide oil production is currently directed towards the synthesis of petrochemicals [62], with 55% of oil towards transport fuels in 2010 [63]. Platform chemicals and fuels such as ethanol, ethylene, benzene, and methanol, among many more are mainly supplied through these petrochemical methods. Since the 1990s, due to the forecast dwindling petroleum resources and future climate change, there has been a growing focus on sustainable, renewable chemicals that are not petrochemically derived [64]. As of 2019, 3% of the total EU market for the top 10 key chemicals were bio-based, producing 4.7 Mt year^{-1}, with a forecast annual growth rate of 3.6% [65]. While biochemicals are currently considered to have a small share in chemical production, opportunities and new EU policies are expected to promote growth.

For biofuels, an increased world volume output between 2008 and 2018, with an increase of 67% and 300% for bioethanol and biodiesel, respectively has been observed [66]. According to BP and OECD (Organisation for Economic Co-operation and Development) countries, biofuel contribution is expected to increase from 3.4% in 2019 to 7% of the consumption of all worldwide transport fuels by 2030 [11]. Currently enforced, EU policies have included a standard 6% volume proportion of renewable additives in petroleum fuels [67] such as bioethanol. Additionally, this renewable proportion is expected to increase to 20% by 2030 [68, 69] as more sustainable transport fuel solutions are required. Bioethanol and biodiesel are the two most common biofuels, each with their specific advantages compared with their petrochemical counterparts [70]. While there is a noticeable shift in the transport energy philosophy from liquid-based fuels to electrical systems powered by the grid [71]. This shift would mean greater demands on national electrical systems, which mainly rely on high-CO_2 fossil fuel methods. This supports the case for nuclear cogeneration and alternative biofuels as an invaluable alternative to negate short-term global CO_2 output.

Despite the benefits of biochemical and biofuel industries, in recent years their environmental sustainability and economic viability have been in question [72]. Environmentally, biofuel sustainability has been assessed through life cycle assessments (LCAs) which assess the global warming potential (GWP) [72] and environmental factors for each fuel, taking into account criteria such as GHG emissions, water security, land use and fossil fuel usage. Based on these LCAs [73-75], only one first-generation feedstock of palm oil achieves a 60% GWP reduction, as defined by the EU’s Renewable Energy Directive (RED) target [73]. The second-generation, non-food feedstocks perform better within these LCAs, with bioethanol and biodiesel but their GWP remain variable depending on the specific process. The environmental sustainability of biofuels can be improved to meet EU targets and become competitive. Economically, biochemical sustainability depends on several factors such as feedstock type supply, oil prices and final biochemical prices. As of 2015, second-generation biofuels were not considered competitive due to low oil prices [76-78]. In a 2021 report focussing on the US market

[79], 100% pure biodiesel (B100) cost more at 3.18 \$ gallon^{-1}, whereas pure petroleum and 20% biodiesel blends cost less at 2.32 \$ gallon^{-1} and 2.42 \$ gallon^{-1}, respectively. Therefore, biofuels still require improvements both in terms of environmental sustainability and economic viability if they are to replace petroleum-based transport fuels.

2.3.1 Biodiesel, Glycerol Market, and Wider Valorisation Research

Focussing on the biodiesel reaction as indicated by Figure 2, the process involves the processing of rich fatty acid (lipid) feedstocks from vegetable oils such as soy or rapeseed. The long alkyl chains are liberated from the bulky lipid structure through an alcohol (typically methanol) and a strong base. However, this produces ~10% by mass of the unavoidable by-product, glycerol (1, 2, 3-propanetriol) [80].

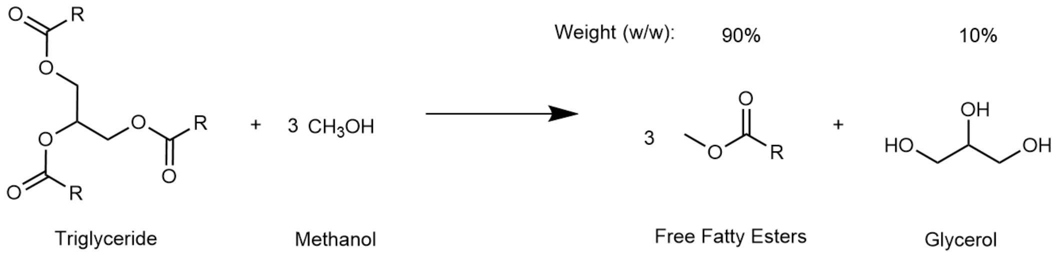

Figure 2: Biodiesel or FAME (Fatty acid methyl ester) production reaction scheme with glycerol by-product. R: alkyl chain with varying saturation and lengths. This reaction can be catalysed by a strong base such as KOH.

Worldwide, this large supply of the by-product glycerol has gathered much attention for the focus of research, mostly as a renewable chemical feedstock. Glycerol is a viscous, dense, non-toxic liquid that can be derived from natural or petrochemical feedstocks. As a dense, viscous and high boiling point liquid [81] introduces a challenge for refining processes, resulting in increased processing costs [82]. To avoid confusion, expressions including glycerin or glycerine are often used to describe commercial diluted aqueous solutions (<95 wt.% glycerol) but the pure form, glycerol will be referred to in this research. With increased biodiesel production, glycerol production has also risen, with biodiesel-derived glycerol production from OECD countries at ≈450 kt year^{-1} in 2005, rising to 2200 kt year^{-1} in 2017 [83]. Since the market saturation in 2005 [84, 85], the price of glycerol has been low but steadily rising. Historically, glycerol has been unusable in high-value applications [86, 87] with thousands of tonnes of crude being disposed of at negative prices in 2014 [88]. As of 2017 in the EU, crude and refined glycerol is at 200-300 € per tonne [89] and 500-700 € per tonne (pre-pandemic), respectively. The increase in popularity of the biodiesel industry has consequently yielded more global refined and crude glycerol, with the majority (≈ 70% in 2015) now deriving from biodiesel, as shown in Figure 3a.

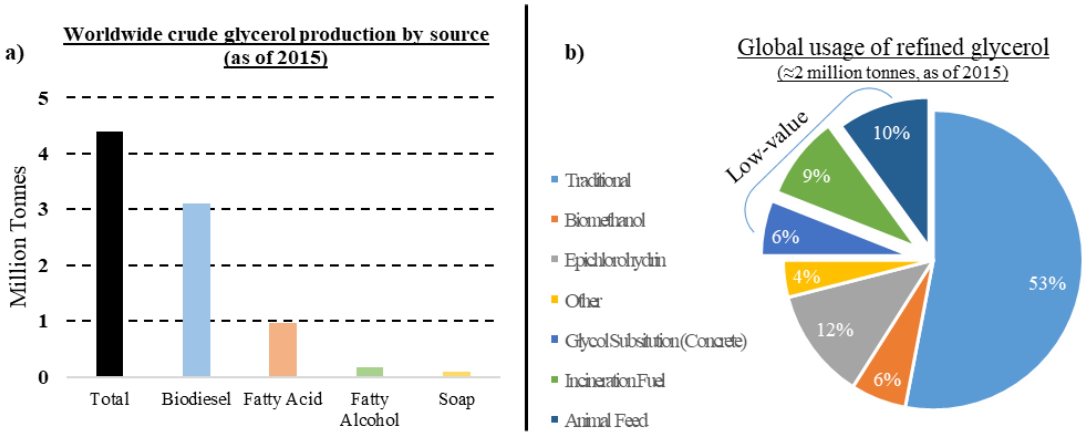

Figure 3: a Worldwide crude glycerol product by source [90]. **b** Applications of only refined glycerol in 2015, showing 25% by mass for low-value uses [84].

Higher-value traditional uses of refined glycerol include pharmaceutical formulations, food use and tobacco products. As of 2015, these higher-value traditional uses composed 53% of all supply. Other more recent higher-value applications such as the production of epichlorohydrin and bio-methanol make up a combined 22% of refined glycerol demand as of 2015, as shown by Figure 3b. The remaining 25% of refined global glycerol demand is mostly wasted in low-value applications such as animal feed, concrete additives, and incineration. Of the remaining unrefined crude glycerol, this will additionally get wasted for similar low-value applications.

Since 2005, a large growth of research has focussed on alternative uses and processes for valorising glycerol [91, 92]. For the conversion of glycerol, many useful derivatives have been identified, as shown in Appendix A, Figure A2 [92, 93]. Some of these derivatives such as epichlorohydrin [94, 95] have been recently developed and have been scaled up to worldwide industrial production [84]. Even with these new applications, glycerol still represents a significant sustainability issue for the future of biodiesel production and yet also at the same time a huge opportunity for the synthesis of valuable chemicals.

The different strategies used to synthesise these chemical derivatives include esterification, hydrogenolysis, gas reforming, and selective oxidation among many more [93]. Catalysts are normally employed in such processes to initiate a reaction, improve reaction rates, and increase product selectivity. The traditional thermochemical catalytic techniques can be generally grouped into two categories, homogeneous and heterogeneous catalysis. The distinction between the two depends on the state of the catalyst compared with the reactants, homogeneous is where the reactants are in the same phase (i.e., liquid-liquid) whereas heterogeneous catalysts operate and exist in a different phase (usually as a solid) compared to the reactants (usually a gas or liquid). There are general advantages and disadvantages associated with both catalytic methods [96, 97].

For specific glycerol conversion research, examples of homogeneous catalysts are simple basic or acidic compounds, organometallic complexes, or utilizing bacteria through biotechnological routes. Organometallic complexes specifically use expensive metals such as iridium (Ir-I, Ir-III) and ruthenium (Ru-II) as the central coordination ions for selective oxidations [98, 99] of glycerol. Heterogeneous examples can include the additional use of other expensive platinum (Pt), gold (Au), rhodium (Rh) and tungsten (W) metals in solid-supported catalysts to specifically initiate hydrogenolysis [100], steam reforming and oxidation [92], among many other processes.

One of the common disadvantages of both catalytic types is the use of these expensive metals, although research into cheaper alternatives like copper (Cu), iron (Fe) and Nickel (Ni) are being explored [100]. Another disadvantage of these traditional catalytic is the extensive separation techniques needed to remove the catalyst from the reactant mixture (homogeneous) [101] which typically destroys the catalyst itself. This is normally an advantage to heterogeneous catalysts but their reuse ability is additionally harmed through deactivation or poisoning mechanisms [102, 103].

Radiation-directed catalysis on the other hand can avoid some of the disadvantages of traditional catalytic methods. Radiation catalysis requires irradiating materials with an external ionizing source and avoids the traditional catalytic requirements for: a) catalyst separation as radiation sources can be isolated from the chemical system, b) purchase of expensive catalytic metals as radiolysis can be achieved through co-production through a reactor or waste nuclear energy sources, c) high process temperatures, d) traditional catalytic deactivation as nuclear spent fuel slowly deactivates over several years whilst emitting useful ionizing radiation.

Radiation-directed catalysis could also provide new mechanistic advantages compared with traditional thermochemical techniques; ionizing radiation could provide targeted energy transfer to break specific chemical bonds. Currently, there appears to be little available literature that explores the use of ionizing radiation for the transformation of glycerol. The radiolysis literature that is available for glycerol, similar polyols and alcohols is discussed in chapters 2.13.5, 2.13.4 and 2.13.3, respectively.

Highlighting several chemicals from glycerol, acetol (hydroxyacetone) is one valuable radiolytic product which could potentially show high radiation chemical yields due to a radical chain reaction observed in polyols [3]. While not yet industrialised as an isolated chemical from glycerol, acetol could be used as a reagent in dye production [104] and is usually synthesised as an intermediate to produce other valuable commodity chemicals such as 1,2-propandiol and 2,3-butanediol [105] which have a large global market [106]. 1,2-propanediol is widely used in pharmaceutical manufacturing as a solvent for drugs insoluble in water, as a stabilizing agent, or used as a plasticizer. Acetol as an intermediate can be synthesised thermochemically via the catalytic dehydration reaction of glycerol which requires temperatures of above 200 °C and typically with an acidic catalyst such as H_2SO_4 or acidic zeolites [106], as shown in Figure 4a. Literature has shown that acetol production can be directed by Cu-based heterogeneous catalysis at elevated temperatures and pressures [107]. Recent research has shown using a copper-magnesium fluoride catalyst in a gas-solid phase process at 260 °C and at atmospheric pressures produces an acetol yield of 46.5% with a selectivity of ~55% [108]. However, using irradiation in this dehydration process could replace the need for heterogeneous catalysts and elevated temperatures required for the dehydration of glycerol to the intermediate, acetol.

Solketal ((2,2-Dimethyl-1,3-dioxolan-4-yl)methanol) is an additional derivative from glycerol and is oxygenate fuel additive which has possible future applications within aviation fuels, automotive fuels, or as a green solvent [109]. Solketal can be synthesised via the ketalization reaction with acetone which typically requires an acidic catalyst, similar to acetol production as indicated by Figure 4b. Previous research has shown this reaction can be achieved through a variety of solid catalysts such as resins, silicates, and zeolites at elevated temperatures and pressures [110, 111]. Although, recent reports have reported using the acidic resin catalyst, Amberlyst-35 to produce solketal at ambient temperatures and pressures with a yield of 60% [111]. Figure 4 defines the reaction schemes for the chemical synthesis of acetol and solketal observed in research.

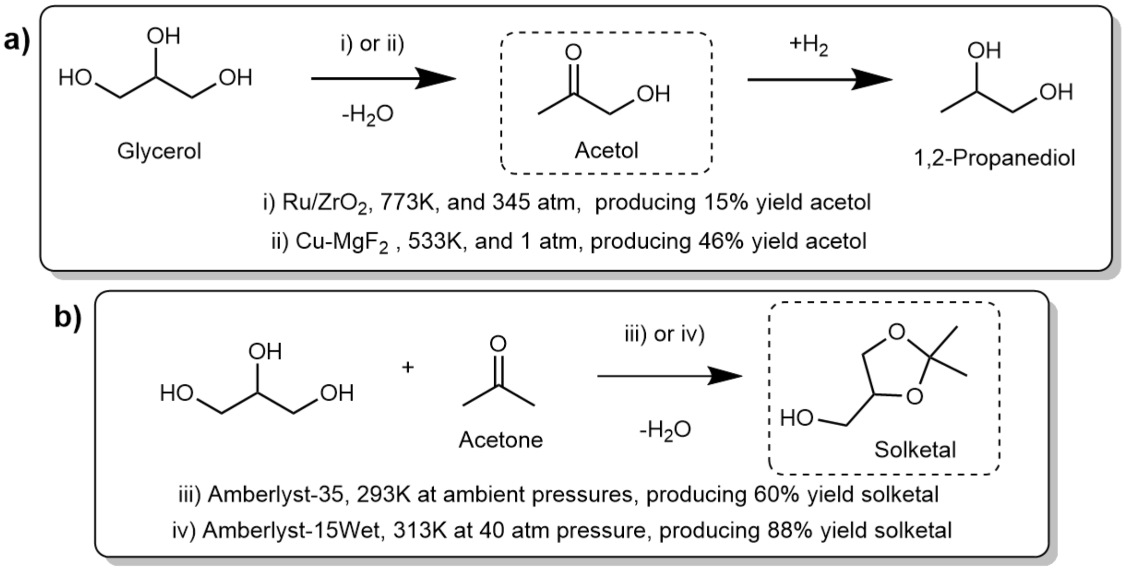

Figure 4: Thermochemical reaction schemes and associated catalysts, temperatures and pressures for: **a** acetol [107, 108] and, **b** solketal production [110, 111].

While the conditions for the thermochemical solketal processes are reasonable with high yields over several hours, the acidic resin catalysts can cost ~£2000 tonne^{-1} [112]. While in an industrial scale context this could be an acceptable cost, resins could potentially be replaced by the under-utilized catalytic ionization energy from NPPs or spent nuclear fuel.

2.4 The Nuclear-Biorefinery Concept

The concept presented in this research is the combination of the nuclear and biodiesel industries for the holistic, beneficial sharing of waste resources, improving the cases for economic viability and environmental sustainability for both. Nuclear power emits poorly utilized ionization radiation (especially in the case of spent nuclear fuel pools) that could be used for chemical transformations. Concurrently, the growing biodiesel industry produces glycerol as a waste by-product which has an appealing potential to be utilized as a platform chemical for the co-production synthesis of useful chemicals. It can be rationalised that the concept of a radiolysis-based nuclear-biorefinery can offer significant benefits industrially as well as environmentally. For the nuclear industry, the benefits are as follows:

a. Direct utilization of the ionization energy from NPPs or spent fuel pools (SFP).
b. A versatile nuclear co-production option that is available to all types of NPPs, irrespective of maximum outlet coolant temperatures.
c. A useful chemical co-product utilizing minimal radiation processing costs.
d. Onsite-chemical refining and processing facility.

Additionally, the benefits for the biochemical industry are as follows:

a. Transformation of waste organic by-products using unique radiation-induced chemical transformations.
b. Lower cost, on-site electricity and steam supply needed for refining.
c. Synthesis of an additional valuable bio-derived chemical.

Figure 5a and b show how the nuclear and biochemical industries operate separately. Figure 5c visually displays the concept and how the industry-specific resources could interact together. The research presented in this thesis offers an advancement in the concept of a nuclear-biorefinery plant than previously seen for other processes [2]. This innovative, integrated concept aims to improve environmental sustainability and the economic feasibility of nuclear and biofuel industries. The following sections will explore ionizing radiation mechanisms and further topics that are all included in the field of radiation chemistry.

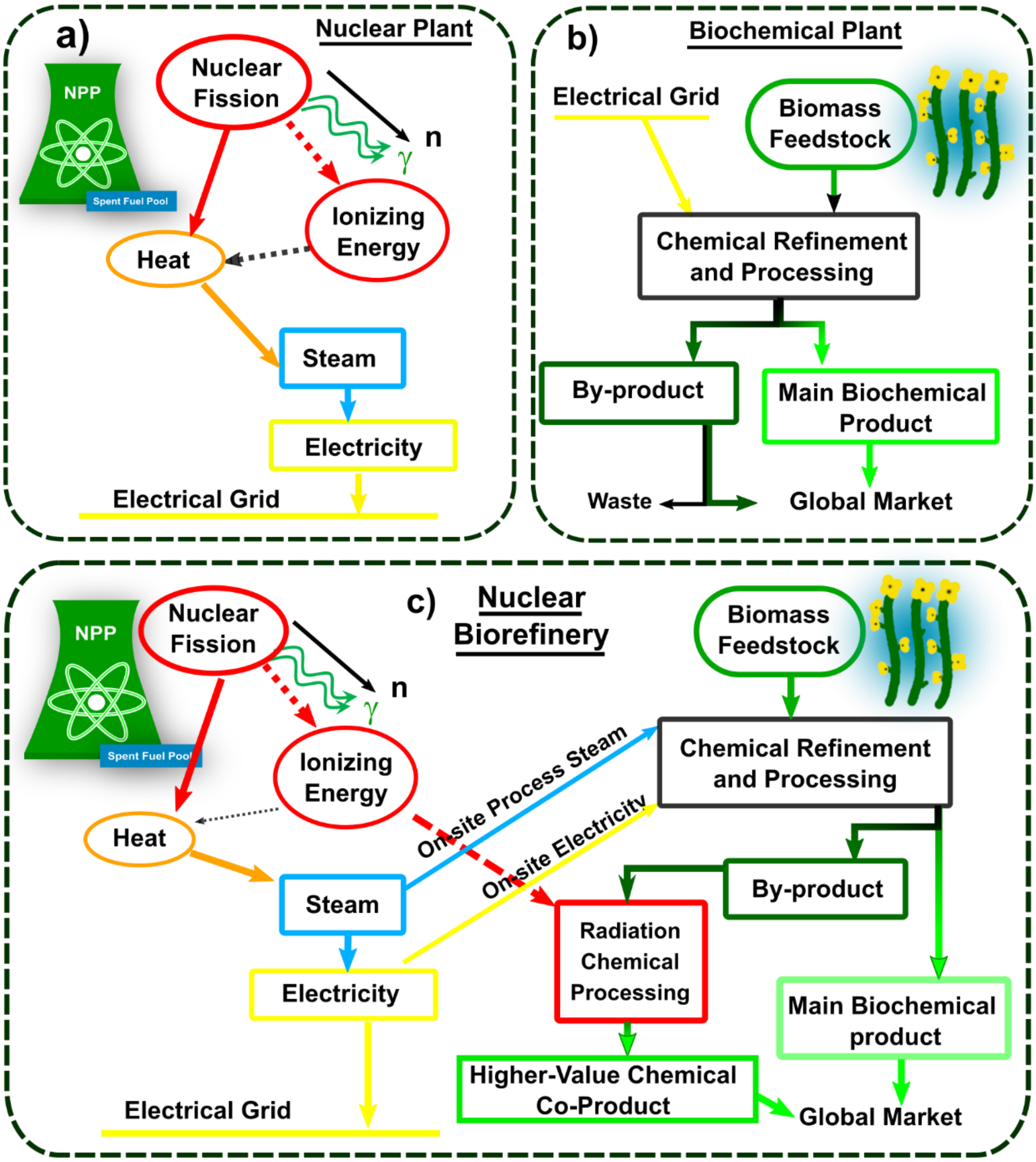

Figure 5: A basic diagram of processes within **a** a nuclear facility and **b** a biochemical plant. **c** the neutron + γ-ray nuclear biorefinery concept, displaying the holistic sharing of resources.

To offer an example of incorporating a biodiesel process with a nuclear power plant, the main biochemical product from a rapeseed oil feedstock would be biodiesel. The by-product of the biodiesel process, glycerol could be converted into valuable chemicals using ionizing irradiation from an active NPP core or its spent fuel. Chemicals such as acetol or solketal in this example are valuable radiolytic products and can be sold as well as biodiesel.

2.5 Radiation Chemistry

Radiation chemistry is simply the study of chemical reactions that are initiated by high-energy ionizing radiation, the field came into realization during the 1940s when it was first termed by Burton in 1942 [113] which separated it from the radiochemistry field. In the subsequent decades, considerable research was directed at the empirical chemical effects of varying types of radiations on diverse types of materials. A worthy note is that radiation chemistry should also be carefully distinguished from radiation damage which concerns the structural changes in solid-state materials as opposed to the chemical transformations [114].

Ionizing radiation can consist of both particles and waves which causes the ejection of electrons from a bound state of a target nuclei. The observable chemical effects often depend on multiple factors such as: the type of radiation, the rate of energy transfer through a material (linear energy transfer, LET), and the state and composition of the sample amongst many other factors. For organic materials, chemical bonds can cleave via radical or ionic mechanisms, producing reactive free radicals (unpaired valence electron species) or charged species [115]. These reactive species are typically highly chemically reactive but may only exist for a very short-lived period ($< 10^{-4}$ s). Free radicals can be generated through other non-specific methods such as heat, electrolysis and most relevantly to this project, ionizing radiation.

The synthesis and lifetime of these reactive ions and radicals (and consequently the stable molecular products) often depend on many factors of the radiation, as well as the irradiated sample. The direct interaction with ionizing radiation produces electrons (e^-) and radical cations of the molecular species ($M^{+\bullet}$) [116-118]. Alongside ionization, excitation of the target molecule to higher energy states (M^*) can also produce radicals from the target molecule if the energy of the incident radiation is not sufficient to ionize. The evolution of these initial reactive components (e^-, $M^{+\bullet}$, M^*) which are referred to as *transients* in the literature are formed within $\sim 10^{-12}$ s which leads to the synthesis of many ions, radicals, and molecular products through numerous reactions as time progresses. Despite e^-, $M^{+\bullet}$ and M^* being the first detectable species from radiolysis, the chemical species formed after 10^{-6} s of a radiation interaction are often referred to as the *primary radiolysis products* in the literature [118, 119]. For the radiolysis of H_2O, the primary radiolysis products are e_{aq}^-, $H^\bullet$, $HO^\bullet$, $HO_2^\bullet$, OH^-, H_3O^+, H_2 and H_2O_2 (a mixture of radicals, ions, and molecular products) [120]. It is at the $\sim 10^{-6}$ s timeframe where chemical processes start to dominate over physical with these *primary* species triggering multiple reactions with i) each other, ii) the bulk material, or iii) dissolved solutes. More stable *molecular* products are soon generated after the reactive species (also transients) have neutralized (by ~10^{-4} s). For H_2O radiolysis the stable molecular products are H_2, O_2, H_2O_2, and H_2O, as shown in Figure 8. In this work, these stable molecular products formed directly after the resolution of primary reactive species are going to be referred to as primary molecular species, due to the quick resolution of the kinetics and the foci in this work on stable molecular products. Under the continuous absorption of irradiation energy, stable primary molecular species are continuously formed, and they can react with the newly generated reactive species to form secondary molecular products. Consequently, the reactions with these secondary products can form tertiary products etc., creating a non-adiabatic system [118]. The reality of the reaction kinetics is often more complex with numerous reactions triggering the synthesis of multiple products to form an overall kinetic system that evolves with time [118].

Due to numerous reactions that occur from a single radiolysis event, the kinetics of radiolytic species are often simplified into reactions with a single rate constant and align adequately with classical chemical kinetics theory [118, 121, 122]. The generation of primary molecular species mostly obeys rapid pseudo-first-order kinetics, where $[B]=k_{pri}[A]$. Where [B] is the concentration of a primary molecular species, [A] is the primary transient species and k_{pri} is the rate of the pseudo-first-order reaction. Further reactive species and molecular products typically obey second-order kinetics if they depend on the concentration of a primary molecular species, where $[C]=k_{sec}[B][A]$ where [C] is the concentration of secondary species, and k_{sec} is the rate of the second-order reaction. However, these reactions are normally exceedingly quick (within 10^{-4} s) and the rates become less important as a system reaches a steady state system under continued irradiation for large, absorbed doses [118]. Whilst techniques such as pulse radiolysis are used to determine these fast physicochemical reactions, for longer exposures the measurement of the stable molecular product concentrations remains the best research tool to determine likely kinetic dependences [118]. The concentration of primary and secondary products and their dependences on dose are described further in chapter 2.12.1.

The following sections in this chapter expand on the aspects of radiation chemistry such as: radiation types, radiation fields (2.6 and 2.7), energy depositions (2.8) radiolysis reaction timeframes and mechanisms (2.9), dosimetry definitions (2.10), dosimetry methodologies (2.11), radiation chemistry parameters and measurement techniques (2.12) as well as the stable molecular products from the radiolysis of alcohols (2.13).

2.6 Types of Ionizing Radiations: Direct and Indirect

Ionizing radiation can exist in several different types, being a particle (alpha, beta, neutrons etc.) or a high-energy wave (γ or x rays). However, the first important factor to consider is how these different ionizing radiations primarily interact with media. Ionizing radiation has traditionally been categorized into two different groups of *directly* or *indirectly* ionizing radiation, as defined by the ICRU [123-125]. However, this categorization has the potential to be misunderstood because all particles of sufficient energy can ionize matter *directly*. A clarification of the definition is to distinguish between the method of *energy transfer* to the medium which occurs *directly* or *indirectly,* based on the type of particle [126].

Firstly, *directly* ionizing radiation (or *direct energy transfer*) types are charged particles (β^-, H^+, etc.) that deliver their energy to matter through coulombic interactions with the orbital electrons of target atoms. This results in persistent energy transfer events and ionization throughout the material along the irradiation track of the primary ionizing particle. Contrasting, *indirectly* ionizing radiation (or *indirect energy transfer*) types are uncharged particles (neutrons) or photons (γ rays or x-rays) which firstly transfer their energy to charged particles (i.e., electrons or protons) in the matter through which they pass, in relatively few interactions compared with direct types [126]. The resulting charged particles then deliver the vast quantity of energy as per the *directly ionizing method*. Therefore, neutrons and γ rays are considered *indirectly ionizing* or *indirect energy transfer* irradiation types as they deposit their energy through a two-step process which depends on the particle type [125-127]. The specific two-step processes from neutrons and γ-rays are covered in chapters 2.7.2 and 2.7.3, respectively.

Radiation Fields & Fluences

To understand the application of ionizing fields, it needs to be first defined. An ionizing field is often defined as a particle or energy fluence depending on the type of radiation. For a mono-energetic particle fluence, it is the sum of the number of particles (neutrons etc.) through a spherical area as defined by equation (2):

$$\phi = \frac{dN}{dA} \qquad (2)$$

Where the number of particles, *dN* incident to the cross-sectional area, *dA* of a sphere at a particular point, P, as per Figure 6. The particle fluence, ϕ with a unit of the number of particles per square meter, m^{-2}.

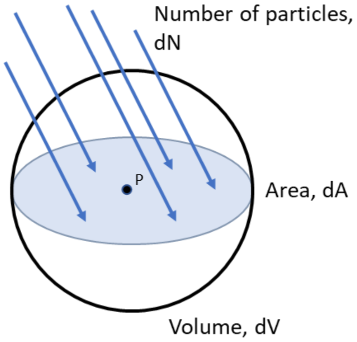

Figure 6: A diagram showing the fluence, ϕ of a monoenergetic particle field, *dN*, through a cross-section, *dA* of a defined sphere volume, *dV* around point, P. [127]

Similar to particle fluence, a wave fluence (γ-rays, x-rays etc.) can be defined as the energy of a wave, *dE* incident to the cross-sectional area of a sphere, *dA* as indicated by equation (3):

$$\psi = \frac{dE}{dA} \tag{3}$$

Where energy fluence, ψ is given in a unit of $J\ m^{-2}$.

Once the fluence of a wave or particle field has been determined through calculations and/or empirical measurements, it can then be used to determine the energy imparted to a sample. Depending on the specific type of irradiation, the incident energy, the sample, and the specific calculation method for energy deposition into the sample, the calculated energy imparted can vary. The energy imparted into a material is typically defined as KERMA (k̲inetic e̲nergy imparted per ma̲s̲s̲) which can be approximated to adsorbed dose, *D*. The definitions for KERMA, absorbed dose, and their approximations are explored in detail in chapter 2.10. From the energy fluence from photons, the absorbed dose may be approximated using equation (42) and the particle fluence for neutrons may be approximated using equation (43). Several methods to determine the absorbed dose into a sample from irradiations are covered in detail in chapter 2.11. Specific ionizing radiations that are relevant for nuclear fission are described as to their properties in chapter 2.7.

2.7 Radiation Interactions

Neutrons and γ rays are the most applicable radiation types derived from fission processes for radiation chemistry methods. However, the definition of ionization is to produce energetic electrons from bound sample nuclei via incident radiation waves or particles. Since all forms of ionizing radiations (neutron and γ rays included) produce some distribution of low-energy electrons [128], it is therefore important to discuss the primary interactions of electrons with low-Z, liquid organic materials (using methanol as an example).

2.7.1 Electron Interactions

As a charged particle, high-energy electrons typically have short penetration depths within liquid samples due to their consistent coulombic interactions, 0.141 mm for 100 keV monoenergetic electrons in water-like tissue [129]. As an electron travels through a medium, its electric field will interact with the electron fields of the target atom. Electrons can transfer energy into a medium through either collision or radiative interactions depending on the impact parameter b *vs* the atomic radius a, as shown in Figure A3 [124]. Soft collisions occur when an electron passes near a nucleus (b >> a), causing a low excitation or a higher-energy ionization of the target, as listed by equations (4) and (5), respectively in Table 1. Hard or knock-on collisions occur when an electron passes even closer to a nucleus ($b \approx a$), imparting significant energy to a single-bound electron, as per equation (6). These electrons are emitted with a large kinetic energy and are often referred to as delta (δ) rays. Elastic scattering of the incident electron may also occur during head-on collisions with the target nuclei ($b \ll a$), emitting an x-ray photon, termed bremsstrahlung as per equation (7). Soft collisions are the most probable interactions, accounting for ~50% of the energy transferred from electron irradiations.

The direct ionization of high energy electrons on organic molecules forms molecular radical cations (often denoted as $M^{\bullet +}$), as studied in the mass spectrometry electron ionization (EI) techniques [52]. Whilst the denotation of the radical (•) is only occasionally used in the wider literature, it is useful to denote this for radiolytic reaction schemes as it can give useful information on the localisation of the radical and the charge for any proceeding reactions. After ionization, the radical cations can undergo varied fragmentation mechanisms which can trigger a variety of bond scissions and are often specific to the target molecule involved, these are explored in chapter 2.9. Additionally, the dissociation of excited molecules (M^*) can also occur which is also explored in chapter 2.9. Table 1 lists the types of electron interactions and transient species produced with methanol as an example target molecule.

Table 1: Types of electron interactions with a light nuclei molecule (e.g., methanol), b and a are the parameters shown in Figure A3.

Type, condition	Reaction	Equation
Soft collisions, (b>>a)	$e^- + CH_3OH \rightarrow CH_3OH^*$ $e^- + CH_3OH \rightarrow CH_3OH^{+\bullet} + e^-$	(4) and (5)
Hard Collisions, (b ≈*a)*	$e^- + CH_3OH \rightarrow CH_3OH^{+\bullet} + e^-$	(6)
Elastic Scattering (b<<a)	$e^- + CH_3OH \rightarrow CH_3OH^{+\bullet} + e^- + \gamma$	(7)

Once an electron (primary or δ-ray) has lost sufficient energy towards its ionization threshold (for water the threshold is 12.61 eV), it will spend the rest of its energy on vibrational and rotational excitation of the liquid molecules [130]. In aqueous or liquid solutions, the low-energy electron becomes a solvated species, e_{solv}^- where it can trigger chemical transformations rather than excitations or ionizations. The electron-nuclei interactions may serve as the basis of knowledge for further discussions on other types of irradiations; this is because all ionizing radiation types will produce energetic electrons through primary or secondary energy transfer processes.

2.7.2 Neutron Interactions

Since incident neutrons are uncharged particles, they interact with nuclei via three possible methods: elastic scattering, inelastic scattering or neutron capture [131] with their likelihood dependent on the kinetic energy of the neutron and the target nucleus. Inelastic scatting collisions (n, n’) of neutrons produce an excited target nucleus where the overall kinetic energy is not conserved, as listed by equation (8). Elastic scattering collisions (n, n) are where the overall kinetic energy is conserved, and the bound target nucleus recoil and ejects from its bound molecule, depending on the energy of the incident neutron and the proton number of the target nucleus [132]. Elastic scattering leaves its target nucleus in its ground state with this scattering mode being the dominating mechanism for energy transfer of light target nucleus (H, C, O) as listed by equation (9). For fast neutrons (>0.5 MeV), they can elastically collide with an H-atom and they can deposit their energy in a single, high-energy event [132]. These secondary charged particles (probably recoil protons from H-rich, low-Z materials) can interact coulombically and ionize many surrounding molecules along their recoil track as shown in Figure A4. A single, fast, 2 MeV neutron will interact an average of 19 times with a water sample before absorption into a nucleus [133]. These 19 primary interactions would produce a corresponding number of energetic protons with varying energy. Consequently, these secondary particles will ionize or excite hundreds of adjacent molecules, ejecting lower-energy electrons, and producing ions and radicals. The final possible interaction of a neutron is via absorption into a target nucleus through thermal capture which occurs with low-energy thermal neutrons (<0.025 eV). Thermal neutron capture (n,γ) produces an activated nucleus and emits a photon of discrete energy (depending on the target nuclei), as shown by equation (10). Table 2 lists the primary physical reactions that occur with neutrons and the species that are formed using methanol as an example.

Table 2: Types of neutron interactions with a light nuclei molecule (e.g., methanol) and the primary transient species produced.

Type, Required Incident Energy	**Reaction**	**Equation**
Inelastic (n, n'), >6.5 MeV	$n + CH_3OH \rightarrow n' + CH_3OH^*$	(8)
Elastic (n, n), >10 eV	$n + CH_3OH \rightarrow CH_3O^- + H^+ + n$	(9)
Capture (n,γ), ~0.025eV	$n + CH_3OH \rightarrow CH_3OD + \gamma$	(10)

In terms of the primary interaction, multiple factors can determine how probable an energetic particle or wave will interact with a stationary target nucleus. These factors include both the masses and charge of the incident and target nucleus, the energy of the projectile particle and the molecular structure of the target. These factors can be grouped and expressed as a single hypothetical probability factor to describe the likelihood of an interaction, which is termed the *microscopic* cross-sectional [132]. This parameter, σ is the apparent size of the target for the bombarding radiation but can be thought of as a measure of the probability of a certain interaction. Thus, the larger the area, the larger the interaction probability. The term *microscopic* is used because it describes the interaction with a single nucleus, the term *macroscopic* is used when considering the bulk matter with a larger volume.

For microscopic cross-sections, the unit of measurement is typically denoted as σ which is called a barn, is not an SI unit, but where:

$$1 \text{ barn}, \sigma = 10^{-24} \text{ cm}^2.$$

As typical cross-sections are between 10^{-27} and 10^{-31} cm^2 for most interactions, the barn was adopted to remove the need to deal with small numbers regularly. The probability of each type of interaction (thermal capture, elastic scattering etc.) occurring can be described through its cross-section (e.g., $\sigma_\gamma, \sigma_{se}$ *etc.*), and these can be combined to give the total microscopic cross-section, σ_T [134].

$$\sigma_T = \sigma_a + \sigma_{se} + \sigma_{si}$$

Where σ_a, σ_{se}, and σ_{si} are the absorption, elastic scattering, and inelastic scattering cross sections, respectively. These values cannot be calculated or predicted entirely on nuclear theory so are determined experimentally for each specific interaction. As the interaction probability is dependent primarily on energy and the target nucleus, the areas are tabulated and plotted as a function of neutron energy in terms of million electron volts (MeV) for each nucleus. For example, the total cross-section for the three most relevant isotopes for organic materials, hydrogen, carbon and oxygen is shown in Figure A5 [135]. Figure A5 shows the higher probability that an incident neutron will interact with a hydrogen atom than any of the other light isotopes shown for energies up to 0.5 MeV (≈ fast neutrons). This illustrates that coupled with a high threshold of transferable energy per interaction (on average 50% of the incident energy) [132, 133], neutron interactions with hydrogen-rich materials need to be highlighted. The relatively large cross-sections for these nuclei and correspondingly high-energy transfer for hydrogen explain the use of high-density hydrocarbons such as polymeric composites for neutron shielding in nuclear environments [136]. For the neutron energies emitted from ^{235}U fission (approximately <8 MeV), the only scattering mechanism possible for target H, C, and O nuclei are through elastic scattering interactions [137].

Typically for photonuclear interactions such as for γ rays, cross-sections are given in milli-barns for higher energies (5 MeV) and tend to zero for lower energies of approximately 1 MeV, meaning with mixed-field neutron and γ-ray irradiation sources with comparable fluences, the energy deposited into organic molecules from neutrons could be greater than the energy from γ rays. From a mixed-field fission source, ~65% of the total dose will be from neutrons and ~35% from γ rays.

Molecular Dependence on Neutron Interactions

For molecular liquid materials, the target molecular structure can be an important factor for primary interactions depending on the energy of the incident neutron. However, for intermediate and fast neutrons, molecular chemical bonding is unimportant as the interaction with individual nuclei dominates [138]. The molecular structure of the target becomes more important with slow incident neutrons (<10 eV). As the kinetic energy of the neutron approaches the molecular binding energy of the molecule, B_m, the cross-sectional area of the molecule increases relative to its nuclei within and increases the probability of scattering interactions. For example, an incident slow neutron of 0.1 eV colliding with H_2O would have a sum of cross-sectional areas of the individual nuclei of ~43 barns but ~68 barns for H_2O as a single molecule [138]. A slow neutron that interacts may excite one or multiple rotational, vibrational, or translational modes within the target molecule. The surrounding medium may also impede these activations, i.e., intramolecular hydrogen bonding would restrict rotational modes as seen in water and polyols such as glycerol [139]. However, at these low neutron energies (<10 eV), the decay of these excited modes emits one or several photons but of a maximum wavelength of UV light (~250 nm) which is non-ionizing. Therefore, the significance of high molecular cross-sections for slow neutron interactions is insignificant compared with higher energy interactions. Fast and intermediate neutrons (300 eV to 8 MeV) would produce recoil protons from the elastic collisions of light nuclei, with intermediate neutrons producing lower energy recoil protons. The strength of chemical bonds for hydrocarbons is in the region of ~4 eV so any intermediate elastic scattering has sufficient energy to potentially heterolytically cleave hydride (X-H) bonds to produce recoil protons. For alcohols such as methanol, there would be negligible influence on the probability of the elastic scattering upon from the type of the hydride chemical bond (either O-H or C-H).

For neutron capture as shown by equation (8), the likely nuclei to activate is hydrogen due to a higher cross-sectional area for neutron capture than the other light nuclei. For equation (9), elastic collisions can produce recoil atoms as long as sufficient energy is transferred to the target nuclei. For the anion that remains e.g. CH_3O^-, it is thought to undergo either: a) further fragmentation or dissociation to smaller species through physicochemical radical and ionic mechanisms or b) be neutralized through recombination reactions. However, the role of this primary anion in the complex physicochemical kinetic system is insignificant to the numerous ionization events which are produced from the recoil proton and secondary electrons. As mentioned previously, the recoil proton acts like a charged particle by initiating multiple low-energy ionization and excitation events along its radiation track in the bulk material. Equation (10) lists the inelastic scattering reaction on methanol but this is highly unlikely with fission neutrons and is treated as insignificant in this work.

2.7.3 Gamma (γ)-ray Interactions

It is still important to discuss the mechanisms of primary γ-ray interactions as they feature prominently in the radiolysis literature and serve as a reference point for the efficacy of neutrons or mixed-field neutron and γ-ray irradiations from a reactor or pile. A pile refers to the earliest version of a nuclear reactor in which piles of graphite-uranium bricks were used to achieve criticality [8, 140], in which some of the earliest radiolytic studies were performed. Like neutrons, γ rays ionize matter through *indirect energy transfer* methods. For most γ-ray energies, the primary γ–ray interactions are with atomically-bound electrons. The categories of these interactions depend on the incident energy of the γ ray in which three different types of interactions can occur [141]: a) photoelectric absorption, b) Compton scattering, and c) pair production.

Photoelectric absorption is the process where a γ ray will lose all its energy to overcome the binding energy of an electron, as per equation (11). However, this process is only significant with lower γ energies below 0.1 MeV [142]. In contrast, the following two processes are more significant for higher photon energies and lighter atomic target nuclei [133]. Compton scattering is typically the most dominant energy absorption process for photon energies in the range of 100 keV to 10 MeV. This process occurs when a higher-energy incident photon is deflected and partially donates some of its energy to a comparatively weakly bound electron, as per equation (12). This ejected energetic electron leaves behind a positive ion and undergoes higher-order interactions within the material as it loses energy. Pair production occurs when a photon transforms all its energy into creating an electron-positron pair as per equation (13); this is only possible within the vicinity of a strong electromagnetic field such as that of a nearby nucleus. This third process is possible for γ-ray energies above 1.022 MeV, which is equivalent to the rest masses of the electron-positron pair. The nucleus itself receives very little of this energy and any remaining energy from the γ ray is given to the generated pair in the form of kinetic energy. Table 3 lists the primary physical reactions that occur with γ rays of various energies and how that changes the types of primary radiolytic species formed, using methanol as an example.

Table 3: Types of gamma interactions with a light nuclei molecule (e.g., methanol) and the primary transient species formed.

Type, Required Incident Energy	Reaction	Equation
Photoelectric, <0.1 MeV	$\gamma + CH_3OH \rightarrow \; CH_3OH^*$	(11)
Compton Scattering, 0.1 MeV to 10 MeV	$\gamma + CH_3OH \rightarrow CH_3OH^+ + e^- + \gamma$	(12)
Pair Production, >1.022 MeV	$\gamma + CH_3OH \rightarrow CH_3OH + e^- + e^+$	(13)

Radioactive sources yield higher energies of γ rays such as from ^{60}Co (1.17 and 1.33 MeV) and fission (0.2 to 8 MeV continuous range) are observed. This would increase the relative probability of Compton scattering and pair production as the main types of interactions. Similarly, for lower-Z nuclei such as carbon-12, the probability of Compton scattering dominates over the two other mechanisms [143]. In all high-energy irradiations, fast-moving electrons are ejected from bound states from target nuclei, which cause subsequent secondary ionizations throughout a given sample under exposure. This ejection of secondary electrons has similarities to neutron interactions, where electrons are also produced via secondary and tertiary ionization steps.

From Compton scattering, the molecular cations (e.g. CH_3OH^+) can interact during the physicochemical timescale stages with molecules of the bulk solution. As shown by equation (24) in chapter 2.9, the cation can trigger the formation of multiple radicals. A neutralization reaction can also occur between the molecular cation and a solvated electron as shown by equation (22), where this will produce a molecule with an excited state.

From pair production, the ejected electron (e^-) will cause further excitations and ionizations dependent on its kinetic energy, eventually solvating into the bulk liquid at lower energies. The positron (e^+) will repel its closest positive nucleus and will attract towards a nearby electron where they will annihilate to produce a high-energy (≥1.02 MeV) photon.

While the primary irradiation interactions are well understood, the subsequent secondary physical and physicochemical interactions can be complex. Different irradiations produce different patterns of energy deposition in a material along their irradiation tracks and consequently produce different radiolytic effects. These differences in energy deposition are described in the following chapter.

2.8 Linear Energy Transfer (LET) and Stopping Power

Linear energy transfer (LET) is an average, generalized quantity that can be quoted to quantify the energy deposition profile of irradiations and allows comparison between different radiation types [144].

LET is the energy deposited per unit of distance travelled within the material by the radiation, typically given in the units of keV μm^{-1}. In irradiating a liquid sample such as H_2O, energy is deposited at points along an irradiation track creating energetic volumes called *spurs, blobs, or tracks* depending on the size of the volume generated [145, 146]. Higher-LET irradiations tend to transfer energy in higher-energy events and more frequently, condensing spurs along the irradiation track. As a result, high-LET irradiations have smaller penetration depths. Contrastingly, lower-LET irradiations have typically lower-energy interactions and the spurs are more separated along the irradiation track, typically giving longer relative penetration depths as shown in Figure 7.

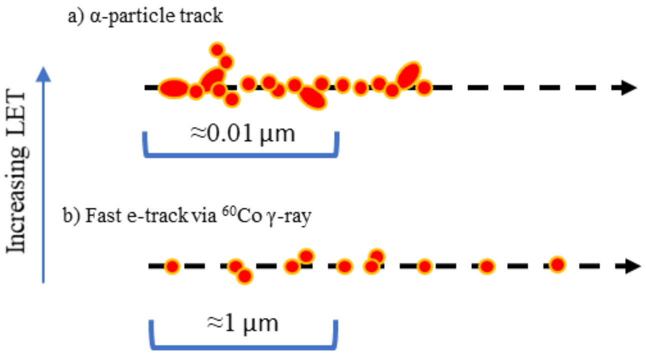

Figure 7: General diagram representation of increasing LET leading to spur distribution alterations along the irradiation tracks (adapted from [147]).

LET can only be applied to charged particles such as α and β^- particles due to consistent ionization of the sample along the track via coulombic interactions. However, an approximation needs to be described to contrast against uncharged, *indirect energy transfer* irradiations such as γ rays and neutrons. This is due to LET being evaluated from the secondary electrons (delta rays) that are generated as a result of the irregular ionizations. However, the energy of these electrons is closely correlated with the incident energy of the γ ray with a similar case made neutrons. Table 4 shows LET values for different radiation types in water.

Table 4: LET of various radiation types in water, a) [147, 148], b) [149].

Radiation Type	**LET** (keV µm^{-1})
Theoretical Minimum for Any Particle	0.22 [a]
20 MeV betatron X-rays	0.28 [a]
^{60}Co γ rays	0.42 [a], 0.2 [b]
200 keV X-rays	2.8 [a]
12 MeV protons	10 [a]
Neutrons (D, Be)	23 [a]
Polonium α-particles	150 [a]

γ-ray irradiations are generally considered low-LET irradiations with 1.1 and 1.3 MeV γ rays from ^{60}Co giving a LET of 0.2 or 0.42 keV µm^{-1} depending on the source. In comparison with charged particles, due to constant strong electromagnetic interactions LET values are larger which also generally results in shorter penetration depths.

For neutrons, being uncharged particles, their energy deposition is not described completely by LET. Instead, the value of mass stopping power is often quoted which is linked very closely with LET. Mass stopping power is a measure of energy lost in a distance per unit density, given in units MeV cm^{2} g^{-1}. There are two main differences between LET and mass stopping power; the first is that density is considered, but assuming the density of the media is 1 g cm^{-3} (water), a value for stopping power can be given in MeV cm^{-1}. To finally equate the two values of LET and mass stopping power, the second difference between them is the loss of energy via fast secondary electrons or electromagnetic radiation. Fast electrons escaping the vicinity of the track can result in some discrepancies in energy deposition, although this loss is practically negligible in terms of LET. For charged particles, the loss of energy from the track via electromagnetic radiation is termed Bremsstrahlung from the term braking radiation and is often more significant [150]. Since both γ-ray and neutron radiations are uncharged, secondary electromagnetic waves and particles are mostly contained within the main irradiation track due to interactions at deeper penetration depths, causing relatively small radiative losses (<1 %) with low-Z materials. Therefore, the values for mass stopping power and LET can be compared directly, assuming a constant density [151].

2.9 Radiolysis Timeframes and Mechanisms

Primary Interactions (Physical Stage)

After the initial deposition of energy from an incident particle or wave, the specific physical and physicochemical processes that follow in organic matter can be very complex, varied, and difficult to isolate. Since the conception of radiation chemistry, one of the main limitations of the field has been the inability to isolate the early-stage physical radiolysis events and the primary species involved due to the very short timescales [152]. This limitation did not alter significantly in the following decades with researchers striving for even picosecond optical spectroscopy resolutions (10^{-12} s) in the 1970s to elucidate primary radiolysis events [153]. For example, of the context of timeframes involved and interactions from a single irradiation event, Figure 8 shows stages, reactive species, timescales, and techniques required for mechanistic elucidation with low-LET radiation with water. The currently accepted theory of primary ionization events for lower-LET irradiation into water and other liquid hydrocarbons is the creation of excited states or solvent hole pairs [115]. For H_2O, lower-energy interactions produce excited solvent states, H_2O^*, alongside higher-energy ionizations which generate solvent cation-electron pairs, H_2O^+ and e^- [120]. Here, the radical cation species ($H_2O^{+\bullet}$) is a precursor.

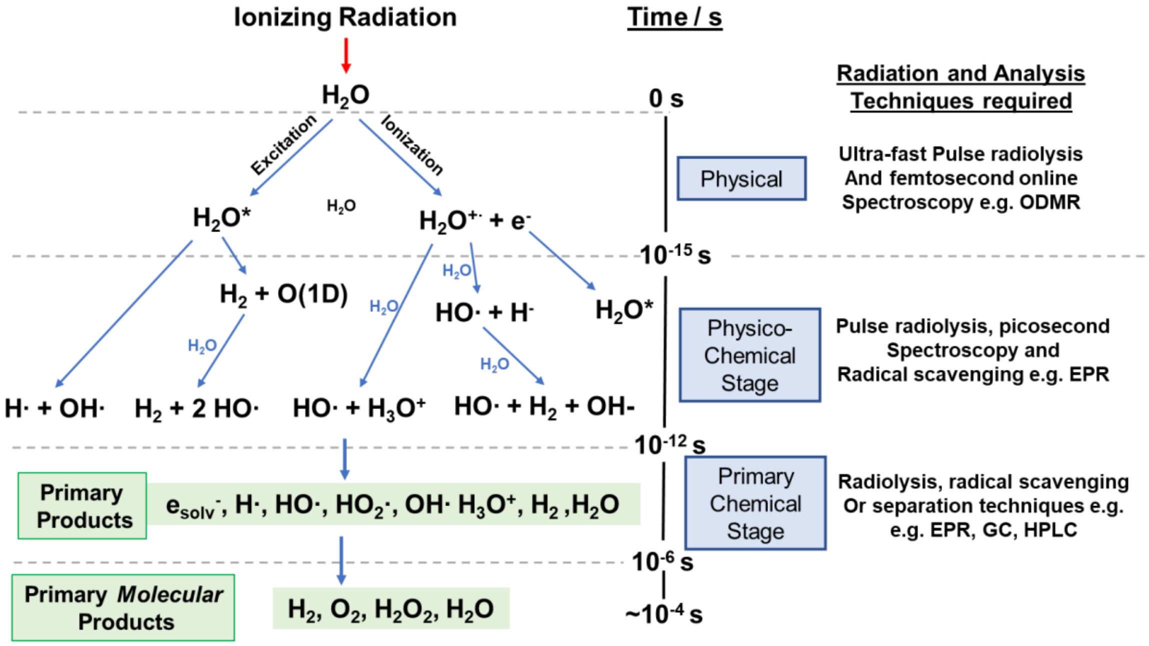

Figure 8: Radiolysis of water and reactive species involved with a generalized timescale. Radiolytic and analytical techniques for monitoring during those generalized timescales are also shown (Adapted from [120]and [154]).

Physicochemical and Chemical Stages

While, historically, the kinetics at timescales less than 10^{-15} s have been difficult to study for most materials, some accepted theories expand into the physicochemical stage (10^{-15} s to 10^{-12} s) of the radiolysis of aqueous and organic liquids. The reactive components such as cations, electrons, and radicals that are generated are all situated within a short-lived energetic volume which is referred to as *spurs*, *blobs*, or *short tracks* depending on its relative size and energy [145]. *Spurs* are small energetic volumes (<100 eV) in which one or several pairs of reactive species will be formed [146]. *Blobs* occur with higher-LET irradiations where a larger energetic volume (≈100 eV to 5 keV) is generated, in which many of these reactive species are produced. *Short tracks* are longer, higher-energy volumes (500-5000eV) comprised of overlapped spurs which are caused by charged species that have branched off from the main irradiation track. These energetic volumes and the reactive species within will change depending on the irradiation type, its corresponding LET and the organic sample irradiated. Figure 9 displays typical primary radiation interactions along its main track into organic or aqueous media [155].

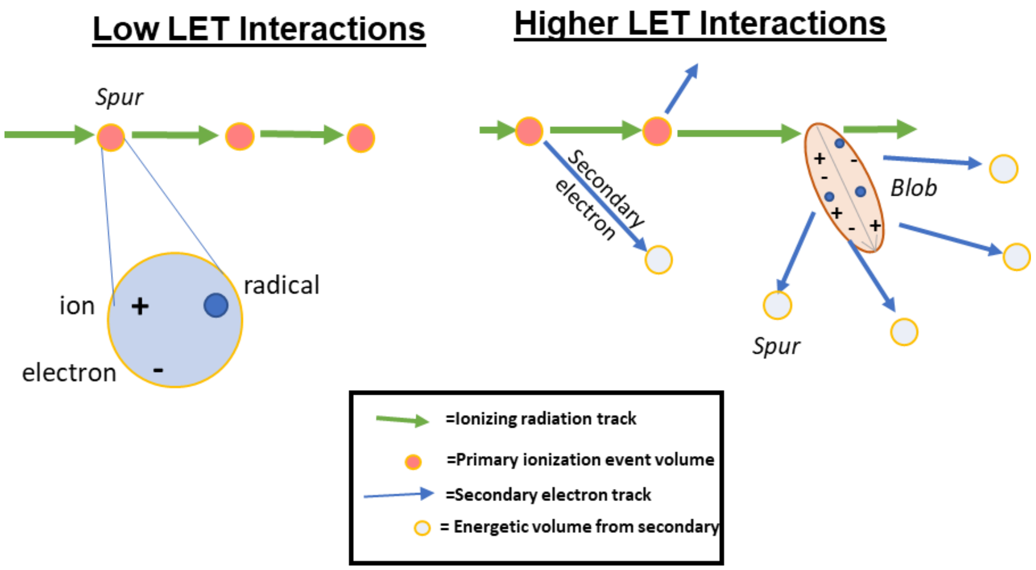

Figure 9: In-depth schematic of radiation interactions of low and high-LET irradiations: Smaller energetic volumes = spurs, and larger energetic volumes = blobs. Secondary particles (i.e., electrons or protons) are displayed for higher-LET irradiations.

The electrons, cations, or radicals (transients) will either recombine with other transients within the volume or they may diffuse into bulk solution if they possess sufficient energy. The diffusion of various species from the energetic volumes will allow various diffusion-controlled chemical reactions to occur after ~10^{-12} s. It is quoted in the literature that only 5% of species will escape recombination processes [115], although the spur diffusion theory [156, 157] of the transient species is dependent on multiple factors such as LET, viscosity, temperature and other bulk species. Given sufficient energy from the primary interaction, the ejection of a secondary particle (typically an electron or a proton for fast incident neutrons) is expected. This secondary particle will traverse the solution to cause secondary ionization events where further radicals, electrons, and cations are generated. Similar to before, these reactive particles have the potential to diffuse and interact with the bulk for a short period until they are neutralized.

The primary chemical processes start to occur between the sub-picosecond ($<10^{-12}$ s) and millisecond ($<10^{-4}$ s) timescales in which stable molecular products start to be generated. Many different complex reactions can occur during this time, for even a simple molecule such as pure H_2O, there are 34 individual known reactions that may occur from a single γ-ray radiolysis exposure [158]. Early radiolysis studies in the 1950s, 1960s and 1970s focussed mainly on final product yields and detecting selected intermediates at a time which gave only a glimpse towards the suggested primary kinetic mechanisms, with over 3500 reactions tabulated for various aqueous solutions [158]. Currently, only a small selection of chemicals in non-polar alkanes [115] and polar H_2O [120] has been elucidated so far in terms of the primary reaction kinetics, intermediates, and final molecular products. For the pioneering radiolytic studies, the radiation parameters often varied significantly between different studies of the same organic solute, which include but are not limited to radiation type, LET, absorbed dose and dose rate. While the sample parameters also varied significantly depending on the focus which could include saturated gases, added radical scavengers, solute concentration, solvent, and sample work-up methods with their subsequent analytical methods.

In terms of the radiolysis of H_2O and aqueous samples, the main reactive species that are responsible for indirect chemical changes in solutes are the solvated electron, e_{solv}^{-}, the hydroxyl radical, $^{\bullet}OH$ and the hydrogen atom (or radical), which is denoted as either H or $H^{\bullet}$ in radiolysis literature [120, 158, 159]. The solvated electron is a strongly reducing species that can interact with species and molecules that contain low-lying vacant orbitals such as in H^{+} or from halogenated organics [160, 161]. The hydroxyl radical is a highly reactive, oxidizing species and typically abstracts hydrogen atoms from C-H bonds within compounds containing electron-withdrawing heteroatoms such as oxygen in alcohols, aldehydes, organic acids, or nitrogen in amines. Finally, the hydrogen atom is a reducing species, similarly to e_{solv}^{-} but reacts with organic compounds more like $^{\bullet}OH$ radicals, via H-abstractions [158]. Generalised reactions, as well as specific reactions with alkanes or alcohols, have been given in Table 5, along with their related redox potentials. The numerous possible reactions and kinetics of aqueous systems can be found in relevant literature [158, 162, 163]. However, it is important to note that as solute concentrations increase beyond 10% wt.%, direct action upon the dissolved solute will become more prevalent [159], as opposed to indirect interactions from these three main species.

Table 5: Primary reactions of e_{solv}^{-}, $^{\bullet}OH$. And $^{\bullet}H$. showing redox equations and potentials, E_o where n is the charge of the ion. Example reactions are also given [158].

$General:\ e^{-}_{solv} + S^{n} \rightarrow S^{n-1}\ ,\quad E_o(SRP) = -2.9V$	(14) and
$For\ alkanes:\ e^{-}_{solv} + RX \rightarrow RX^{-} \rightarrow R^{\bullet} + X^{-}$	(15)
$General:\ HO^{\bullet} + S^{n} \rightarrow S^{n+1} + OH^{-}\ ,\quad E_o(SOP) = 2.7\ V\ or\ 1.8\ V$	(16) and
$For\ alcohols:\ HO^{\bullet} + CH_3OH \rightarrow H_2O + {}^{\bullet}CH_2OH$	(17)
$General:\ H^{\bullet} + RH \rightarrow R^{\bullet} + H_2\ ,\quad E_o(SRP) = -2.3V$	(18) and
$For\ alcohols:\ H^{\bullet} + CH_3OH \rightarrow {}^{\bullet}CH_2OH + H_2$	(19)

In terms of longer timeframe mechanisms ($>10^{-4}$s), if the sample is of biological origin, then biochemical and biological effects can occur hours or days after the initial irradiation event. Cell death from irradiations is believed to be due to breakages in the backbone of DNA strands (either single or double-strand breakages) [164, 165], mostly caused by the reactive oxygen species, $^{\bullet}OH$ and H_2O_2 or by the direct action of the DNA molecules to form its reactive radical cation, $DNA^{+\bullet}$ [166]. These DNA breakages cause cascade effects, preventing DNA replication mechanisms from functioning correctly, leading to acute and long-term effects of radiation [154, 167].

Direct radiolysis of concentrated alcohol systems: Methanol Case Study

Whilst the direct effects of radiation on H_2O have been extensively studied and reported, the physical, physicochemical, and chemical reactions upon other neat compounds are less frequently studied. For alcohols specifically, there are a small number of reports which focus on the primary radical, ionic, and chemical reactions from methanol radiolysis [168-170].

The radiolytic reactions of pure methanol from the available literature are listed in Table 6. The initial excitation and ionization reactions from methanol are shown by equations (20) and (21), respectively where they occur within the physical timeframe. The early femtosecond physical stages of radiolysis are similar to H_2O or any liquid in which there is the generation of excited molecular states, molecular cations, and electrons. From the excited molecular state of methanol, CH_3OH^* the two possibilities are to emit a photon relative to the energy of the excited state or for a bond to be homolytically cleaved. Ionization produces the methanol molecular cation, CH_3OH^+ and an electron which will ionize molecules further but eventually become a solvated electron, e_{solv}^- once sufficient energy has been lost.

Table 6: The main radiolysis (physical and physicochemical) reactions of pure methanol, compiled from the available literature [168].

$Excitation: CH_3OH \rightsquigarrow CH_3OH^* \rightarrow H^\bullet + CH_3O^\bullet$ or ${}^\bullet CH_2OH$		(20)
$Ionization: CH_3OH$	$\rightarrow CH_3OH^+ + e_{solv}^-$	(21)
$CH_3OH^+ + e_{solv}^-$	$\rightarrow CH_3OH^*$	(22)
$CH_3O^\bullet + CH_3OH$	$\rightarrow {}^\bullet CH_2OH + CH_3OH$	(23)
$CH_3OH + CH_3OH^+$	$\rightarrow CH_3OH_2^+ + CH_3O^\bullet$ or ${}^\bullet CH_2OH$	(24)
$CH_3OH + e_{solv}^-$	$\rightarrow CH_3O^- + H^\bullet$	(25)
$CH_3OH + H^\bullet$	$\rightarrow H_2 + CH_3O^\bullet$ or ${}^\bullet CH_2OH$	(26)
$CH_3OH_2^+ + e_{solv}^-$	$\rightarrow H^\bullet + CH_3OH$	(27)
$CH_3OH_2^+ + e_{solv}^-$	$\rightarrow H_2 + CH_3O^\bullet$ or ${}^\bullet CH_2OH$	(28)
$CH_3OH_2^+ + e_{solv}^-$	$\rightarrow {}^\bullet CH_3 + H_2O$	(29)
$2\,{}^\bullet CH_2OH$	$\rightarrow CH_3OH + HCHO$	(30)
$2\,{}^\bullet CH_2OH$	$\rightarrow (CH_2OH)_2$	(31)
$2\,CH_3O^\bullet$	$\rightarrow CH_3OH + HCHO$	(32)
$CH_3O^\bullet + {}^\bullet CH_2OH$	$\rightarrow CH_3OH + HCHO$	(33)
${}^\bullet CH_3 + H^\bullet$	$\rightarrow CH_4$	(34)

Equation (24) lists the interaction of the ionized species with the bulk methanol, producing primary radicals and ions. The two main molecular radicals from methanol are the hydroxy (${}^\bullet$C-O) or alkoxyl (C-O${}^\bullet$) radicals from equations (20), (23), (24), (26) and (28). Whilst the oxygen-centred alkoxyl radical is formed with a kinetic preference from equations (20) and (24), it is rapidly converted to the more thermodynamically stable, carbon-centred hydroxyl radical over time. Further studies with other alcohols have also arrived at the same conclusion with the initial hydroxy-alkyl preference [171]. This preference for the hydroxy radical indicates the initial cleave of the O-H bond, as opposed to the C-H bond which is contrary to expectations based on bond dissociation energy estimates (O-H being the stronger bond). The initial preference of the alkoxyl radicals is thought to be influenced by the oxygen atom's ability to kinetically stabilise a radical (or singularly occupied molecular orbital, SOMO) due to its larger electron cloud relative to the adjacent carbon atom. The conversion to the hydroxy radicals as described by equation (23) is due to several factors which make the carbon-centred radical more thermodynamically stable. Firstly, the weaker electronegative atoms are better long-term stabilizers (thermodynamically). Secondly, the lone electron pairs of the adjacent oxygen atom stabilize and reduces the energy state of the carbon-centred radical. A similar preference in the alkoxyl radical formation and conversion to the hydroxy radical over time is expected from the radiolysis of ethylene glycol and glycerol samples. For larger-chained alcohols with increasing in C-C bonds as alpha substitution increases, the stability of the alpha carbon-centred hydroxy radical would increase, allowing them to exist for a longer duration and increase formaldehyde and dimer yields.

The hydrogen atom, $H^\bullet$ is also produced as a primary radical from methanol via equation (20) and preferentially forms hydroxyl radicals through secondary abstractions of the bulk methanol as shown by equation (26). Herein, carbon-centred radical becomes higher yielding which can promote aldehyde and dimer formation further as listed by equations (30) and (31). Equations (27) to (34) list the transient-transient reactions that may occur between two reactive species which typically occur within the physicochemical stages. As mentioned in the literature, the reaction between two transient species is unlikely for low dose rates and low LET exposures [168]. However, for high dose rates and high LET irradiations such as that from neutronic NPP environments, these transient-transient reactions (including recombination reactions) possibly become more likely due to increased intraspur reactions and larger blob sizes. For high LET, mixed-field neutron + γ-ray radiolysis, it is predicted that this could lead to higher yields or aldehydes or dimers than seen for low LET radiolysis in literature. From the literature, the primary *molecular* products from methanol radiolysis are reported as H_2, $(CH_2OH)_2$, CH_2O, CH_4, and CO [169]. H_2 is produced as the highest-yielding radiolytic product which is expected from all hydrocarbons. Formaldehyde and the methanol dimer (ethylene glycol) are the second and third most yielding. A similar distribution of product yields is expected from ethylene glycol and glycerol which are discussed in chapters 2.13.4 and 2.13.5, respectively.

2.10 Fundamental Dose Definitions and Approximations

Dosimetry is an important technique for the quantitative determination of energy deposited into a sample from ionizing fields. Dosimetry calculations are utilized routinely for calculating the dose in a human body for radiation protection monitoring purposes, but the technique can equally be used to determine the energy (or absorbed dose) into any solid, chemical, or biological sample. This energy can be responsible for any physical, chemical, or biological effects within matter and is required to determine radiolytic quantities such as *G*-values, as described in chapter 2.12.1.

Three main different fundamental dose quantities can be defined for different applications: i) absorbed dose, *D*, ii) ambient dose, *H* and iii) effective dose, *E*. Each of these has its unique calculation method depending on its purpose and sample type.

Fundamental Dose Quantities and Approximates

Absorbed dose, *D* is a non-stochastic physical dose quantity that can be applied to both direct and indirect types of ionizing radiation [172] and any type of sample: solids, polymers, liquids, gases, humans etc. The absorbed dose, *D* can be simply defined as the mean energy imparted per unit mass and this can be described by equation (35):

$$D = \frac{d\epsilon}{dm} \tag{35}$$

Where the mean energy imparted is ε and *m* is the mass of the material. The SI unit for the absorbed dose is given in J kg^{-1} or Grays, Gy. However, calculating the absorbed dose from *indirect* radiation such as neutrons or γ rays requires further specification due to their indirect nature of energy transfer.

For photon and neutron interactions, the quantity KERMA, *K* is often used to estimate the incident energy into a sample [173]. KERMA. KERMA is defined as the sum of the kinetic energies transferred to the material or to the secondary particles (electrons etc.) from the uncharged ionizing radiation divided by the mass of the material, as per the following equation:

$$K = \frac{d\bar{E}_{tr}}{dm} \tag{36}$$

where E_{tr} is the energy transferred along the photon's irradiation track length in the material and dm is the mass of the sample.

KERMA is given in the same SI units as absorbed dose, Grays, *Gy*. Whilst identical units, KERMA is not strictly equivalent to the absorbed dose. The main difference between KERMA and absorbed dose is that KERMA only describes the energy transferred at the primary point event. Absorbed dose considers the total energy absorbed into the sample which includes secondary energy transfer processes; herein lies the difference between the two quantities. For the indirect irradiation of liquids, secondary energy transfer processes are important as the secondary particles will further disperse energy into the sample, initiating further chemical reactions.

The difference in the quantity between D and KERMA arises if secondary particles such as photons or electrons escape out of the sample, meaning that a KERMA calculation may exceed the absorbed dose. These radiative emissions which escape a sample are typically electromagnetic (photon) radiative energy losses that are referred to as bremsstrahlung. KERMA can therefore then be split up into two components, *collision* and *radiative* KERMA as shown by the following equation,

$$K = K_c + K_r \tag{37}$$

where K_c and K_r refer to collision and radiative interactions respectively. For the KERMA collision approximation, the following equation can be utilized:

$$K = K_c(1 - \bar{g}) \tag{38}$$

where $\bar{g}$ is the fraction of radiative losses. The radiative fraction is heavily dependent on the materials considered; higher values of $\bar{g}$ is expected for higher Z (proton number) materials. For example, ^{60}Co γ rays incident to air and water result in radiative losses of 0.32% and 0.39%, respectively. For neutron irradiations, recoil protons and electrons are the prominent secondary particles and the radiative losses here will be negligible ($K_r \approx 0$) so it can be assumed that $K = K_c$ [124].

KERMA-Absorbed Dose Approximation

Since most radiative losses occur at the edge of a sample (known as the build-up region), in a large enough depth of material, KERMA and the absorbed dose may be considered roughly equivalent. This can be described by the transient charged particle equilibrium (TCPE) region of a sample [127, 174], as shown in Figure 10. This TCPE region describes when all radiative components (K_r) are contained within the sample.

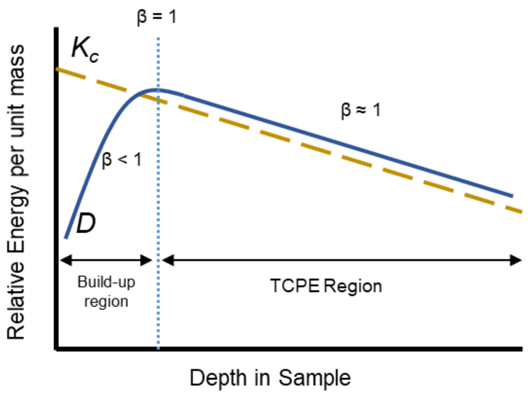

Figure 10: Absorbed Dose and KERMA vs liquid medium depth [175]. Showing the Build-up region (β<1) where $K_c>D$ and the TCPE region (β≈1) where $K_c\approx D$.

The TCPE region shows how KERMA and absorbed dose converge and both fall with increased sample depth, due to neutron or γ-ray attenuation through the material. The ratio, β between absorbed dose, D to KERMA, K, can be described by the following equation,

$$\beta = \frac{D}{K} \tag{39}$$

For materials with low-Z (proton number) compositions, such as water and hydrocarbons, and with sufficient depth, it can also be assumed that $\beta = 1$ [176] with an uncertainty of 1% [177]. This means collision KERMA, K_c can be approximated to the absorbed dose, D for samples most examples of organic media (where $Z < 16$). For specific types of irradiations used in this research, Table 7 describes a relative dose profile for neutrons and γ-ray irradiation from ^{60}Co radiation into water.

Table 7: Relative absorbed dose (Bragg curve) into H_2O from epithermal neutrons and ^{60}Co γ rays [178, 179].

Depth into water (cm)		0.1	0.5	1	1.5	2	5	10
Relative Absorbed Dose (to Max)	**Neutrons**	1	1	1	0.92	0.83	0.5	0.17
	^{60}Co γ rays	0.6	0.85	0.98	0.95	0.96	0.85	0.7

Within 2 cm of a low-Z sample, the absorbed dose profiles are similar for epithermal neutrons and ^{60}Co γ rays but differ significantly beyond 2 cm [178, 179]. For indirect mono-energetic radiation, relating fluence, KERMA and absorbed dose can be further specified for either the photon or the particle fluence using equations (40) and (41), respectively, with previous approximations [172],

$$Photons : D \approx K = \psi \left(\frac{\mu_{tr}}{\rho}\right) \tag{40}$$

$$Neutrons : D \approx K = \phi \left(\frac{\mu_{en}}{\rho}\right) \cdot \bar{E}r \tag{41}$$

Where μ_{tr}/ρ is the mass-energy transfer coefficient, E_r is the energy of the mono-energetic wave or particle. Where Φ and Ψ are particle fluence and energy fluence, respectively as per equations (2) and (3. Both equations can be generalized through the summation and integration of the wave or particle energy range of the spectrum or for individual discrete values. For simplicity, researchers have combined the mass-energy transfer coefficient with the energy of the particle to result in a singular (kerma) coefficient for a specific interaction which results in the following equations for particles and photons, respectively [180]:

$$Photons : D \approx K = \psi \cdot k_{\psi}(E) \tag{42}$$

$$Neutrons : D \approx K = \phi \cdot k_{\phi}(E) \tag{43}$$

Where $k_{\psi}(E)$ is the photon energy fluence-to-kerma conversion coefficient $k_{\phi}(E)$ is the neutron fluence-to-kerma conversion coefficient. Both kerma factors are weighted for each stochastic interaction based on the energy of the incoming uncharged particle or wave and the target element or molecule. Fluence-to-kerma (or absorbed dose) conversion factors are experimentally determined using cross-sectional areas and are tabulated in the units of Gy cm^2 [181, 182], allowing basic neutron dosimetry calculations or more intricate calculations using **M**onte **C**arlo **N**-**P**article transport (MCNP) models. Models crafted using the MCNP code can tally up the KERMA for each neutron-target elemental interaction of a defined sample and output the total KERMA to the user. Equation (43) is utilized for neutron dose calculation methods for a ^{252}Cf radioactive source in chapter 3.4.1 and a more complex calculation method using MCNP transport codes and dose simulations for a fission reactor in chapter 3.4.2.

For biological samples, equivalent *(H)* and effective *(E)* doses (given in Sieverts, Sv) are important quantities for the determination of biological doses to organs and humans, respectively which are required for radiation protection purposes. Absorbed dose is converted into equivalent dose by multiplying by the specific radiation weighting factor (*Wr*) for an organ (e.g. skin) due to different radiation types having different effects. The equivalent dose is converted to effective dose by multiplying by the tissue weighting factor (*Wt*) due to different organs' sensitivity to radiation. The effective dose is then summed up for each organ of the whole body. These latter dose quantities are utilized only in a periphery aspect within radiation safety assessments to facilitate this research and will not be described further.

2.11 Dosimetry Techniques: Analytical and Simulations

Many methods exist to analyse and quantify the absorbed dose from a radiation field in a sample [183]. These broad methods include organic detectors, solid state detectors, ionization chambers, calorimeters and chemical or radical dosimeters in addition to mathematical modelling [184]. However, only three different methods will be mentioned here for the relevance of the radiation fields and sample types utilized in this research: ionization chambers, chemical dosimeters, and mathematical modelling.

Gas Detectors: Ionization or Fission Chamber

One of the primary standard methods of dosimetry to quantify charged particles and γ rays is using an Ionization Chamber (IC). This chamber is filled with a gas mixture (typically N_2 or Ar), across which an electric field is applied. The ions generated from radiation-gas interactions are collected using this electric field, allowing quantitative dose determination from the charge-related output signal. Figure 11 is a basic diagram of an ionization chamber. A Fission Chamber (FC) is a variant for the detection and quantification of neutron flux due to the uncharged nature of neutrons. Typically, a fissile isotope (such as ^{235}U) is often used to sensitise a chamber to neutrons, yielding high-energy charged fragments that ionize the gas.

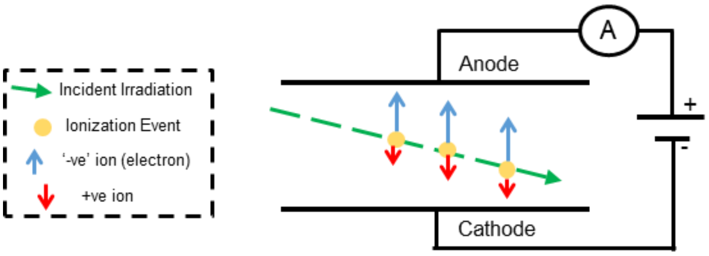

Figure 11: Diagram of the principal operation of an ionization chamber. The ion current measured is directly related to the fluence of the incident particles or waves.

A combination of ICs or FCs and MCNP code techniques can accurately define ionizing fields and sample dose through the process of modelling through empirical measurements, validations and standardizations [125]. The energy deposition profile within ionization chambers is also advantageous as it aligns well with the projected absorbed dose, removing the need for the KERMA-absorbed dose approximation in this case. ICs and FCs are primary standard dosimeters in established use in large nuclear facilities such as research or commercial NPPs and are maintained by national standard laboratories. ICs allow accurate quantification of radiation fields, with instant readouts which allow quick corrections of reactor fields which are closely calibrated to the reactor power. The signal uncertainties involved for ICs or FCs are typically only ± 2% [185].

Chemical Dosimetry

Historically, one of the most used methods for dosimetry was to irradiate a material for a well-known radiolytic reaction, measure the related product concentrations and determine the absorbed dose through known *G*-values trends (see 2.12.1). However, chemical systems often have maximum absorbed dose limitations, for example, Fricke, ceric sulphate, and red Perspex systems all have absorbed dose limitations of 0.4 kGy [186], 50 kGy and 50 kGy [187], respectively. In the literature, there are also concerns about chemical systems' applicability for neutron fields and nuclear reactor dosimetry [188]; difficulties arise specifically for determining dose independently of the neutron energy spectrum and distinguishing between neutron and γ-ray doses. Exceeding these parameters often causes non-linearity in the dosimeter response, increasing absorbed dose uncertainties. Due to the limitations of NPP environments, chemical dosimetry was not conducted but dosimetry relied on a verified simulation model via MCNP methodologies.

Monte Carlo N-particle (MCNP) Dosimetry

The **M**onte **C**arlo **N**-**P**article (MCNP) transport code is a versatile, general-purpose code that can be applied to simulate neutrons, photons (γ or x-ray) or electron transport, their interactions and physical parameters [189]. This code allows the simulation and tracking of individual particles in a continuous energy range, for a user-specified geometry of materials [190]. MCNP simulation methods can be utilized for radiotherapy [191], radiation shielding and nuclear fission and fusion reactor [190, 192, 193] purposes, to name a few.

Not commonly reported as a dosimetry technique in the literature for liquid organic samples in pre-1990 radiolysis, MCNP simulations can provide quick and accurate dose calculations. This is without the requirement for constant empirical measurements which can often be expensive and time-consuming to perform [194], especially for critical nuclear fission reactor environments. The MCNP simulations for nuclear environments are often validated against empirical measurements [195], usually from IC or FC detectors [196] for consistency. KERMA values from photons and neutrons can often be determined accurately from MCNP models for a wide array of different materials, including liquid systems such as water [197] and solid polymers. Specifically, for nuclear reactor operations, the dose accuracy of a validated MCNP model with supporting measurements from IC or FCs is in the range of ±10% [198, 199].

As shown by studies of simulated values for neutron or γ-ray KERMA compared with values of absorbed dose, *D* shows an excellent alignment for a standard ICRU sphere with only relative differences between 1.1 and 9.3% across the fission energy range [200]. The only notable difference where the relative differences are severe is at extremely high γ-ray energy ranges (>4 MeV) which for nuclear reactors represents a relatively low proportion of the γ-ray fluence [201]. Since KERMA values and absorbed doses are given in the SI unit of J kg^{-1}, the total energy into an irradiated sample in J can be determined by factoring in the mass of the organic sample in kg. This fundamental determination of energy is then utilized for the calculation of radiation chemical yields or *G*-values for analytes, as discussed in chapter 2.12.1. The verified MCNP model for reactor dosimetry used in this research is described in chapter 3.4.2.1.

2.12 Radiation Chemistry and Analytical Techniques

This section describes the physical quantities and formula used to define the feasibility of radiolytic processes in which *G*-value, molar yield and mass productivity are defined. The chemical analytical technique used for quantifying complex radiolytic mixtures, gas chromatography (GC) is also described.

2.12.1 Radiation Chemical Yield, *G*-Value

A radiation chemical yield or *G*-value is often quoted to quantitatively show the energy efficiency for the synthesis of a product via radiolysis. The yield of species such as short-lived ions, free radicals or stable chemical products can be described by this *G*-value, which measures the quantity of the species generated per unit of energy deposited. Historically, it has also been defined as the number of molecules formed or destroyed per 100 electronvolts ($100eV^{-1}$) of absorbed energy in a sample. Although, with the International System of Units (SI), a modern notation of micromoles per joule ($\mu mol\ J^{-1}$) is preferred. To compare the molecular *G*-values quoted in the resident literature against more recent publications, a factor of 1 molecule per 100eV to 0.1036 µmol J^{-1} is used, as shown by equation (44).

$$Radiation\ chemical\ Yield, G = 1\frac{molecules}{100eV} = 0.1036\frac{\mu mol}{Joule} \tag{44}$$

This *G*-value can vary significantly, dependent on the desired species, radiation parameters, starting material and several other factors. *Simple radiolysis* reactions typically involve the radiolysis of liquid-aqueous samples where *G*-values tend to range between 0.01 and 1 µmol J^{-1} for ambient temperatures and pressures. However, *G*-values depend on a multitude of radiation and sample factors, as described in chapter 2.13. For most simple reactions, the focus of literature tends to be towards the transient species from aqueous samples (e_{solv}^-, $^{\bullet}OH$, and $^{\bullet}H$) and their reactions. The radiolysis of only H_2O is thoroughly elucidated and offers good examples of simple radiolysis processes. The production of H_2 gas, the most common gas to arise from water radiolysis, has a mean *G*-value of 0.046 µmol J^{-1} [202, 203]. As with other radiolytic products, the generation of H_2 from organic mixtures is strongly altered by the solute involved and other sample and radiation parameters [203, 204], i.e., ranging from ~0.31 µmol J^{-1} from hexane to ~0.003 µmol J^{-1} from polystyrene using γ-ray radiolysis [204].

A zero-dose *G*-value is often quoted in the radiolysis literature [169, 205]. This corresponds to where *G*-values from an absorbed dose-*G*-value relationship may be extrapolated towards a dose of zero and its *G*-value estimated, usually larger than the measured *G*-values quoted in the paper. While not completely useful for radiation-chemical processing (as a zero-dose value would be impractical and potentially misleading), it can be used to compare against results in the prior art. For the highest *G*-value processes, mechanisms typically involve chain reactions; this is where the radicals or ions generated via radiolysis interact as a catalyst with an expected bond or molecule. This catalytic radical/ion then gets regenerated as a process of radical rearrangement which also produces the desired product or change in chemical structure. Chain reactions have been observed for chemically reactive substances, such as unsaturated hydrocarbon-halogen systems [61] and alcohols [206] and due to their rapid kinetics, produce high concentrations of primary, stable molecular products.

Stable Primary, Secondary and Tertiary Molecular Products

For stable molecular products, a typical plot reported in the literature is shown in Figure 12 where the absorbed dose (kGy) is plotted against concentration or *G*-value, which can show key characteristics of the radiolytic molecular products. If a product is formed because of radiolytic interactions, its concentration will increase relative to the absorbed dose [3, 121, 207-212], as per Figure 12a. Contrastingly, there are also reports where dissolved solutes are decomposed by radiolytic reactions where their concentrations decrease with absorbed dose [213, 214]. However, if a radiolytic molecular species is formed as a primary molecular product, it only relies on the resolution of a primary ionic or radical species from radiolysis. From the absorbed dose plot, the typical *G*-value trend for a primary molecular species will decrease with an increased absorbed dose. This is intuitive since the *G*-value for a radiolytic product would be directly dependent on the gradient of the dose-concentration graph. Secondary molecular species typically rely on the generation of a primary molecular species and will gradually increase *G*-value with absorbed dose, as shown in Figure 12b. Tertiary or higher-order molecular products will typically increase at slower rates.

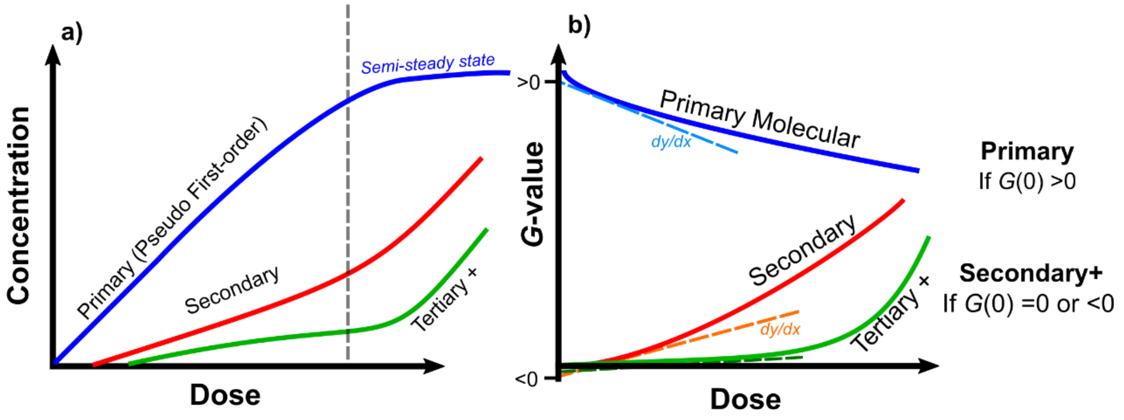

Figure 12: Absorbed dose vs **a** concentration and **b** *G*-value plots showing the simplified example trends for primary (blue), secondary (red), and tertiary (green) molecular products. Extrapolation of trends to zero dose *G*-values indicates primary and secondary molecular products with >0 and ≈0 values, respectively [215].

In literature, the y-axis intercept with a species' dose trend is referred to as the *zero-dose G*-value. The zero-dose *G*-value for primary molecular products is positive and is often higher than the *G*-values determined for a specific dose. For secondary products, extrapolation to zero-dose shows *G*-values close to zero or negative as shown in Figure 12. The absorbed dose vs *G*-value response (and the zero dose *G*-value) of a radiolytic compound can signify if a product is a primary molecular species or a second molecular species. Here, a primary molecular product is generated directly from radiolytic, short-term ($<10^{-4}$ s) radical, ionic, or chemical processes. A secondary (or higher order) molecular product depends on the concentration of a primary molecular species to be produced. Secondary and tertiary molecular species are often observed from larger absorbed dose irradiations when concentrations have built up to detectable levels. A secondary radiolytic product is identified as increasing in *G*-value with absorbed dose and its zero dose *G*-value is often close to 0 µmol J^{-1}. An example of the concentration vs absorbed dose plot can be found in the literature for the radiolysis of 4-chlorobenozic acid (*Fig. 10 in* [215]). Where 4-chloro-3-hydroxybenzoicacid (4-Cl3OHBzA) is a primary molecular product and benzoic acid appears to be a secondary product. There are several more examples in the literature of *G*-value's dependency on absorbed dose (or irradiation time) for primary molecular species [216, 217].

To determine *G*-values, two quantities need to be accurately calculated or measured: a) the quantity of the radiolysis product in question, usually measured in moles, and b) the total energy into the organic sample, measured in Joules. Common quantitative analysis techniques of mixtures- are described in chapter 2.12.3. The energy absorbed by a sample is determined by dosimetry techniques, described in chapter 2.11.

2.12.2 Molar Yield and Mass Productivity

To compare radiolytic processes against thermochemical synthetic mechanisms, a quantity such as a molar yield % or mass productivity (MP) % [218] is required. Percentage molar yield is a measure of the number of moles of the desired product against the theoretical maximum number of moles that could be yielded from the starting moles of the reagents, as indicated by equation (45), as a percentage. The mass productivity metric normally given as a ratio but described by equation (46), has been defined for green chemistry applications to evaluate resource utilization, waste production, and process sustainability [219].

$$Molar\ Yield\ \% = \frac{Moles\ of\ Product}{Max.\ Theoretical\ Moles} \times 100\% \tag{45}$$

$$Mass\ Productivity\ \% = \frac{actual\ mass\ of\ desired\ radiolytic\ product}{\begin{array}{c}Total\ mass\ of\ all\ reaction\ reagents\\ and\ solvents\end{array}} \times 100\% \tag{46}$$

The previously stated *G*-values only consider the transformation of the solute, without consideration of other reagents in the sample. A similar point is also made here for molar yield %; since much of the radiolysis literature concerns the irradiation of heavily diluted aqueous samples, molar yield percentages would be a misleading indicator of the effectiveness of a radiolytic process for industrial purposes, since only a tiny proportion of the mixture is converted but this would still indicate high molar yields. To assess radiolytic processes for scaling up feasibility accurately, Mass Productivity (MP) % is a more robust measure as it considers the total mass of the irradiated sample. This is especially useful for two reasons: when the energy into the sample (dose rate) would be a limiting factor for process throughput as a suitable absorbed dose will need to be reached, superior mass productivity would show a more efficient utilization of the radiated energy over time. Secondly, mass productivity percentages highlight the use of excess solvents in a process and improving this MP value would have knock-on economic benefits in terms of downstream separating, purifying, and recycling costs for a process.

2.12.3 Chemical Analytical Techniques

For the identification of stable radiolytic products within organic liquid samples, chromatography techniques such as gas chromatography-mass spectrometry (GC-MS) can be utilized [220]. Since radiolysis is likely to cause the formation of several different products, with multiple compounds often with similar functional groups, a complex mixture is often formed. Chromatography techniques allow the separation and isolation of various products from such complex mixtures. After GC separation, radiolysis products can be identified as to their structure through mass spectrometry (MS) techniques. The analytes can be electrically ionized (EI), fragmenting into smaller organic ions where they are quantified to collect a mass fragment pattern that indicates the original structure of the analyte. The EI fragmentation patterns are then compared against a database of known compounds. In the radiolysis literature, a hurdle for the detection and accurate quantification of gaseous or volatile radiolysis products has been in the steps required for sample workup [221]. Dilutions and derivatizations can cause losses, reducing the quantitative accuracy of volatiles. However, headspace (HS) sampling techniques can be applied to determine volatiles and dissolved gases in liquid samples. Provided a fully sealed sample-irradiation vial can be used, direct sampling of a volatile-rich gas phase could be achieved without sample workup processes. Other different sampling techniques can be used with GC-MS such as standard liquid injection or solid-phase microextraction (SPME) injection for analysing volatiles from solid matrices.

Other analytical techniques were explored as to their applicability such as infrared (IR) spectroscopy and HPLC (High-Performance Liquid Chromatography). IR spectroscopy was not utilized due to limitations in its sensitivity and high limits of detection (LOD) for this specific application. For routine IR analysis, high limits of detection (LOD) of ~0.1% are shown for most analytes within other solvents [222]. Additionally, only limited qualitative information could be extracted from IR analysis such as chemical bond type. HPLC was not explored as it operated a similar analytical capability and function as to GC analysis. However, HPLC lacks the analytical screening sensitivity for volatiles which are prevalent within alcohol radiolysis literature. The decision was to singularly develop methodologies of the powerful GC-MS analytical technique which can be time-consuming but process a large array of samples.

2.13 Radiolysis Literature Review

The section provides an overview of the fields of study and applications of radiolysis. The general radiolysis kinetics of water, organics and aliphatic alcohols will be explored with a focus on radiolytic products. Polyols and glycerol are discussed in detail.

2.13.1 Industrial Applications

Industrially, several processes utilize ionization radiation to achieve desired chemical or physical effects in materials, including: flue gas purification [223], polymerization [224], sterilization and food irradiation [225]. Kinetic and mechanistic studies focussing on short reaction timescales are also still prominent in recent reports [226]. For the radiolytic chemical synthesis using NPPs or ionizing sources, historically there has been an initial research exploration into the radiolytic production of several compounds [53], including ethylene glycol [50], nitrogen dioxide [56], hydrazine [60] and phenols [59]. However, only rarely have radiolytic processes been implemented industrially for chemical synthesis, as previously described in chapter 2.2.1. One of the reasons for the lack of nuclear radiolytic processes has been the uneconomic viability of importing feedstocks, e.g., methane [227]. This would be a key advantage of the nuclear-biorefinery concept: the availability to convert on-site waste feedstocks such as glycerol.

Despite the focus on radiolysis research into reaction kinetics, there has been a recent resurgence of research that focuses on final product yields for the proposal of radiolytic chemical synthesis and decomposing waste compounds at industrial scales. These papers include decomposing CO_2 [228] and the halogenation of ethylene [5, 6]. However, these studies are focused on theoretical analysis using known reactions and data from prior art whilst there has been little recent empirical radiolysis research into the discovery of new reactions of organic materials for radiolytic conversion applications. The following section provides an overview of the existing scope and data for the radiolysis of organic compounds.

2.13.2 Liquid Compounds and Aqueous Solutions

Several reviews and books, for example by Swallow [147], Hummel [229], and Butler [230], explore the radiolysis of a wide range of organic compounds. Only a few compounds have been considered extensively, such as hydrocarbons [115, 231] and aromatics [232]. Water and aqueous solutions have been considered extensively in terms of the reaction kinetics involving reactive intermediates and final stable product *G*-values [120, 233]. For brevity, the current focus is on aqueous media and alcohols.

In the majority of studies, either irradiating pure compounds or diluted solutes in aqueous solutions has been the focus for many radiation chemistry researchers [234]. There are several reasons for the foci on aqueous samples:

a) Water radiolysis has well-characterised physicochemical kinetics and chemical products across radiation parameters compared to other compounds. Consequently, producing aqueous radicals and ions of predictable quantities and reactivities allows easier prediction of solute interactions.
b) Water is the solvent that is most common to biological organisms, so elucidating the reaction mechanisms is relevant to fields such as radiation protection [235], radioactive waste management [234], radiotherapy [236], food science [237], and sewage treatment [238].

Some of the goals of aqueous radiolysis have been to promote the prevalence of a specific radical and its corresponding mechanisms [238], but at the cost of preventing others which may be desirable in some cases. Most of the kinetics within aqueous samples are generally due to the three main reactive species, the solvated electron, e_{solv}^{-} the hydroxyl radical, $^{\bullet}OH$, and the hydrogen atom, $^{\bullet}H$, as mentioned previously in chapter 2.9.

For example, the addition of scavengers, such as N_2O gas, reacts with the e_{solv}^- species in aqueous samples, generating $^{\bullet}OH$ radicals which promote oxidizing processes [239]. When considering the radiation-induced chemical conversion of solutes, they are typically of concentrations of <1% wt.% in aqueous systems [159]. The majority of the energy is transferred to aqueous molecules, limiting energy transfer directly to the solute. Radiation processing of dilute aqueous samples introduces two problems: i) the production of stable water radiolysis products, such as H_2 and H_2O_2, are not particularly valuable or desired, ii) energetic aqueous species undergoing higher rates of recombination, in which the solute is not affected and iii) lower mass productivity for dilute solutions, compared with concentrated solutions.

Increasing the solute concentration beyond the scope of that reported in most of the radiolysis literature (<1% wt.% of solutes in water), would yield higher mass productivities. However, for brevity, the focus of the literature is narrowed to directly relevant materials and nuclear processes which considers the following aspects:

a) The final radiolysis product yields (not yields of radicals, ions, intermediates etc.) of glycerol and similar alcohol-related compounds.
b) Mechanisms for the synthesis of important stable products.
c) The radiolysis arising from the two penetrating radiations from nuclear fission, γ rays and neutrons, and corresponding dependences on *G*-values.

2.13.3 Liquid Aliphatic Alcohols

For alcohol-related compounds specifically, there are historical collated datasets and reviews published by Baxendale [169], Freeman [114, 240], and Swallow [147] for a range of diluted solutions and pure alcoholic liquids. There has been a recent revisiting of the literature regarding the radiolysis of ethanol [241]. The following alcohols appear in radiolysis literature: methanol, ethanol, propan-1-ol, propan-2-ol, n-butyl alcohol, isobutyl, n-octyl and n-decyl [147]. Appendix A, Table A1 lists several aliphatic alcohols, their main stable products from radiolysis, related *G*-values and key experimental parameters given in the literature.

It appears no matter the radiation type or conditions, the two major effects upon alcohols [147] are: a) the loss of a hydrogen bond (C-H scission) on an α-carbon atom to form α-hydroxy radicals or b) H loss via O-H scissions where the oxidation of C-O hydroxy groups into C=O carbonyl groups to produce aldehydes or ketones. Further oxidations and reactions have also been seen to occur to form carboxyl groups (COOH), hemiacetals (if applicable) and alcohol dimers (glycols). As alkyl chains are increased, the probability of C-C bond scission increases, increasing yields for alkane products such as CH_4 and C_2H_6. Table 8 shows the probability of various bond scissions for short alkyl chain alcohols.

Table 8: Bond scission likelihood percentages for aliphatic alcohols [114].

	Bond Scission Likelihood% from radiolysis			
Solute/Alcohol	C-C	C-O	C-H	O-H
Methanol	~	10	90	
Ethanol	10	10	80	
1-Propanol	35	5	60	
2-Propanol	30	10	60	

Across the alcohol radiolysis literature, some common products and chemical moieties are observed. As from all starting hydrocarbon solutes, the radiolytic product of H_2 gas has shown to be the highest yielding, stable radiolysis product amongst all C-H-containing compounds. However, since hydrogen is comparable to electricity production in terms of profitability [16], hydrogen would not make a suitable radiolytic product for scaling up industrially. Other gaseous products such as CO and CH_4 generally show inferior *G*-values across the short-chain alcohols but increase with longer alkyl chain lengths. However, most of these reactions typically have lower *G*-values of less than 0.16 μmol J^{-1}. The yields of carbonyls appear to be the second-highest among radiolytic products for short alcohols, with dimers typically the third most yielding. The formation of carbonyls and dimers typically occurs through ionic or radical interactions shown by the reactions previously given in Table 6. However, these reactions are a simplification due to the multitude of different mechanisms that can occur.

The radiolysis of alcohol mixtures has also been reported in the literature recently [242, 243], with alcohol-formaldehyde systems producing ethylene glycol at *G*-values of 14.4 μmol J^{-1} at elevated temperatures of 473 K. As reported in the literature, a carefully selected mixture, rather than a binary alcohol-aqueous solution may achieve improved *G*-values of certain products.

2.13.4 Ethylene Glycol, $C_2H_6O_2$

The simplest, stable polyol, ethylene glycol (ethane-1,2-diol) was the focus of several radiolysis studies by Barker [210], Pikaev [244], and Schulte-Frohlinde [245]. As in other reports, variable parameters such as dose, dose rate, solute concentration, pH, and gaseous environment are all explored with ethylene glycol. Appendix A, Table A2 displays the available *G*-values for various radiolytic products from ethylene glycol.

Further reports focus on the possible reaction mechanisms to various radiolytic products [246]. In terms of the likely radiolytic reactions from ethylene glycol, an increased number of hydroxyl groups compared against aliphatic alcohol literature, O-H bond scissions will be more probable. As per the data in Appendix A, Table A2, most reports have utilized γ rays with comparable *G*-values across the radiolytic products. Compared with aliphatic alcohols, there is a relative reduction in the *G*-values for H_2 for ethylene glycol; this could be explained by fewer weaker C-H bonds for abstraction and increased intermolecular linkages (hydrogen bonding) between molecules. Depending on the parameters, the highest *G*-values are generally seen for acetaldehyde, glycolaldehyde, formaldehyde and ethylene glycol's dimer. In higher dose studies (≈100 kGy) [210], formic and acetic acid are formed alongside an acetal, 2-methyl-1,3-dioxolane for higher yields of 0.38, 0.78 and 1.65 μmol J^{-1} respectively.

Reports have suggested a chain reaction for the radiolytic synthesis of the primary aldehyde, acetaldehyde, and higher *G*-values of 18.13 μmol J^{-1} have been reported depending on the parameters [245, 246]. One previous study has reported a yield of $\sim 2 \times 10^4$ μmol J^{-1} of acetaldehyde from pure ethylene glycol [247]. However, acetaldehyde was not measured directly in this study but its cyclic acetal, 2-methyl-1,3-dioxolane was quantified. Additionally, reports on ethylene glycol have not replicated these exceptionally high yields for acetaldehyde or its acetal, and the results have not been reproduced. Additionally, with potential chemical effects altering the *G*-values and the lack of specific methods, *G*-values from this report have been omitted. Although, an important factor for the high yields could be the irradiation of a pure solute, rather than heavily diluted samples. Similar studies [210, 245, 248] on ethylene glycol have reported more conservative yields of acetaldehyde of 0.24 and 0.12 μmol J^{-1}. Wider applications of acetaldehyde mainly use it as an intermediate chemical for the production of acetic acid and acetate esters [249]. Despite the high *G*-values reported for acetaldehyde, the reported mass productivity is low at 0.006%, indicating the poor utilization of ethylene glycol as a resource.

2.13.5 Glycerol, $C_3H_8O_3$

For glycerol, the radiolysis literature is sparse, with only a small collection of articles that quote *G*-values for final stable products from aqueous solutions [3, 250]. Despite the number of articles being small, they do cover the effect of changing some variables, including dose rate, temperature, and glycerol concentrations in aqueous samples. However, these *G*-value data from glycerol mostly derive from a single article by Baugh [3] describing the use of a ^{60}Co γ-source to expose aqueous glycerol samples to doses ranging between 1442 Gy and 3124 Gy and dose rates 1.7 Gy min^{-1} and 8 Gy min^{-1}. Other articles reporting *G*-values of stable products include an article by Moore [251]. The available *G*-values for glycerol radiolysis, radiation and sample parameters are listed in Appendix A, Table A3.

One of the most prominent glycerol-radiolysis products is the carbonyl, acetol (1-Hydroxypropan-2-one). Acetol displays one of the highest *G*-values quoted across multiple parameters, which is consistent compared to data for the simpler alcohols as discussed previously. A *G*-value for acetol of 0.23 μmol J^{-1} was determined for aqueous samples of 4.6 wt.% glycerol, a dose of 3124 Gy, a dose rate of 1.7 Gy min^{-1} and saturated with N_2O gas. Similarly to acetaldehyde from ethylene glycol, the higher yield for acetol was suggested to be a chain reaction mechanism involving hydroxyalkyl radicals (-CHOH-ĊHO-) and carbonyl-conjugated radicals (-ĊHO-CO-) [3]. This potentially high-yielding reaction has not been fully explored in terms of the many radiation and sample parameters that could promote it and serves as a research area to explore for glycerol radiolysis.

The *G*-values from these aldehydes increase significantly with glycerol concentration respective to other radiolytic products, like those from ethylene glycol. The radicals responsible for acetol and 3-hydroxypropanal undergo an acid-catalysed water elimination reaction, analogous to the similar mechanism from ethylene glycol [252, 253]. All other commonly detected main products display inferior yields compared with acetol, with glyceraldehyde being the third-most yielding radiolysis component across various parameters (<0.09 μmol J^{-1}). Also quoted in the literature, there are only two detectable stable products from O_2-present environments [250], suggesting a favourable parameter for product selectivity. These radiolytic products are glyceraldehyde and dihydroxyacetone, as shown in Appendix A, Table A3 [250]. In terms of gaseous radiolytic products, there is no available data for H_2, CO, or CH_4, perhaps due to gaseous sample losses during the sample work-up and the choice of analytical methods.

Acetol is an important intermediate chemical used in the chemical synthesis of propylene glycol, propionaldehyde, acetone and furan derivatives [104]. Acetol is also a reducing dye in the textile industry but its current high cost of production limits its potential for further applications [254]. Developing a process for acetol synthesis from waste resources (glycerol and ionizing energy) could yield a cost-effective industrial solution. In the literature, no high-level *G*-values (>1 μmol J^{-1}) have been reported for the synthesis of a corresponding carbonyl from glycerol, as was acetaldehyde from ethylene glycol. Based on the high *G*-values, this could be acetol due to its corresponding chain reaction mechanism and presents a potential area to research further to maximise *G*-values. Mass productivity values for acetol specifically only reached a maximum of 0.0053% in previous work [3].

There appears to be no literature exploring the direct radiolysis mechanisms and corresponding *G*-values of radiolytic species from glycerol, but there has been literature exploring the indirect radiolytic mechanisms of products from glycerol in aqueous mixtures [3, 246]. Further mechanisms which additionally expand on the literature have been devised in this work and have been proposed in chapter 5.6.2 with illustrations in Figure 55, Figure 56, and Figure 57.

All of the glycerol radiolysis studies reported to date were conducted before the glycerol market glut of 2005. The assumed motivation here is the curiosity of studying the mechanistic effects and final product yields. The perspective of glycerol being utilized as a waste chemical feedstock for radiolysis conversion may not have been realised. A study investigating the conversion of glycerol using high doses, dose rates, and higher glycerol solute weight percentages to determine its feasibility for industrial applications has not yet been conducted.

2.13.6 Variable Parameters

This section explores the variable parameters involved in radiolysis literature, observed effects and applicability to glycerol radiolysis. The following radiation parameters are discussed in order: i) radiation type and LET, ii) absorbed dose, and iii) dose rate. Followed by the variable sample parameters: iv) solute and solute concentration, v) gaseous environment, vi) pH and other additives, and vii) temperature.

2.13.6.1 Radiation Parameters

i) Radiation Type and LET: For radiation types, most radiolysis literature features γ-ray only irradiations to determine *G*-values. Other, more sparsely-featured radiation types are accelerated electrons (β^-), X-rays, fast ions (e.g., H^+, α) and mixed-field neutrons + γ rays. γ-ray irradiations are normally conducted using radioactive sources such ^{60}Co, whereas charged particle irradiations are typically achieved through particle accelerators (H^+), or via fission sources. Mixed-field neutron and γ-ray irradiations have been conducted with a stack or pile of radioactive sources, although the available literature regarding glycerol is not available or limited, as are most solutes. Only a few older reports focus on utilizing nuclear radiation (neutron + γ-ray) for radiation-induced chemical synthesis [50, 53, 255], although this perspective to use nuclear reactors for radiation-induced chemical synthesis has not been revisited since for empirical research. Most materials research for mixed-field irradiations has been for decomposition studies for coolant and dosimetry applications. Examples include the decomposition of oxalic acid [256], cyclohexane [257], polyethylene [140] and terphenyl [258] among more [259]. Several references suggest the reason for the lack of available literature from mixed-field or neutron radiolysis is due to possible neutron activation mechanisms for radionuclide production [147, 260, 261]; for this reason, neutrons have potentially been overlooked since the 1960s as a potential source for energy to catalyse chemical transformations. Additionally, the value proposition of utilizing ionizing radiation from decaying spent fuel rods remains unexplored [147]. The literature raises some important unanswered research questions about neutron radiolysis: does neutron radiolysis cause significant activation of organic compounds? Can it be quantified? Are activation levels sufficient to prevent the implementation of an industrial process? Do *G*-values from mixed-field neutron + γ-ray irradiations of glycerol differ significantly from other types of irradiations?

Depending on the radiation type and the incident energies involved, the transfer of energy throughout the medium will be different but can be generalised to LET values, as described in chapter 2.8. In the literature, the final product yields of higher-LET irradiations to organics are often difficult to predict due to the complex interactions between excited states and intermediates [204]. For alcohols and polyols specifically, the differences in *G*-values between different types of radiations to produce H_2 gas from methanol and ethanol are observed, as shown in Table A1. There is a notable increase in H_2 *G*-values from 0.5 to 1 μmol J^{-1} from pile to 84 MeV recoil fragments for comparable variable parameters. Lower alcohol-dimer *G*-values for higher-LET irradiations are observed for alcohols. However, *G*-values from neutronic-related irradiations have not been explored for glycerol or ethylene glycol which presents a research opportunity.

ii) Absorbed Dose, D: The literature concerning γ-ray irradiations quote relatively low absorbed doses (typically < 1 kGy) which can be explained by several reasons:

a) Limited maximum dose rates of irradiation equipment causing practical experimental limitations (primarily for ^{60}Co γ-ray irradiators).
b) To avoid radiolytic transformation of primary stable products to secondary order products with higher doses, reducing corresponding primary product *G*-values.
c) Suggested greater proportional effects with dilute solutions at lower doses [147].

For dose types such as pile, α and β^- irradiations, higher absorbed doses are observed for alcohol solutes of methanol, ethanol and ethylene glycol as shown in Table A1. Across the literature for organics, increasing absorbed dose is reported to decrease *G*-values of primary radiolytic products [147, 262], as seen for the most common radiolytic product, H_2. This may be explained by increased radiolytic interactions with these primary products as concentrations increase. For ethanol, as shown by Table A1, an increase in absorbed doses from 1.6 Gy to 16,000 Gy is shown to decrease in *G*-values of H_2 and acetaldehyde from 0.6 to 0.43 μmol J^{-1} and 0.38 to 0.21 μmol J^{-1}, respectively.

For ethylene glycol, in studies exploring higher doses (~100 kGy) [210], more secondary products are reported such as carboxylic acids when compared to lower-dose studies. Further, [244] lower absorbed doses between 32 Gy and 417 Gy (as shown by Table A2) show a decline in acetaldehyde and formaldehyde production from 5.39 to 2.49 μmol J^{-1} and 0.36 to 0.11 μmol J^{-1}, respectively, with increased dose. For glycerol, lower absorbed doses of either 1.4 kGy or 3.1 kGy have only been studied from the available literature as shown in Table A3 [3]. Dependencies on radiation parameters are difficult to evidence for most of the radiolytic products from glycerol due to the limited data, except for an inverse relationship with the dose rate for *G*-values of glyceraldehyde.

Many articles report extrapolated *G*-value data for a low-dose condition or *zero-dose* condition to quote *G*-values [3, 169, 205], as described in chapter 2.12.1. This may give inaccurate insights into the radiolysis efficiencies for higher dose processes. Since *G*-values typically decrease with increased absorbed dose and, additionally, since higher doses are required for efficient resource conversion, utilizing zero dose *G*-value data would not present an accurate case for industrial scaling up and would inflate the calculated production values. However, for a general comparison with changes in other variable parameters and the literature, the zero-dose value may be a useful metric.

iii) Dose Rate: Depending on the solutes involved, and the desired reaction, chain reactions may propagate at certain ranges of dose rates. Examples include amines [263, 264] and aromatic hydrocarbons [147]. Whereas some radiolytic products from systems are seemingly unaffected by changes in dose rate such as some alcohols [207] and some monomers [265], dose-rate dependencies are variable depending on the system (and radiation type). Even for some alcohol systems in the presence of O_2, some product *G*-values are linked to being dose-rate dependent [211, 266], so revealed dependencies are entirely dependent on the dose rate range explored for that specific system. Due to the significant use of γ-ray irradiators, lower dose rates (<500 Gy min. $^{-1}$) are reported in most of the radiolysis literature. Higher dose rates (>1000 Gy min. $^{-1}$) are often achieved using higher-LET radiations such as from α or H^+ ions.

Lower γ-ray dose rates have been observed more commonly for the radiolysis of ethylene glycol and glycerol of less than 433 Gy min.$^{-1}$ and 72.1 Gy min^{-1}, respectively. From ethylene glycol, increasing dose rates have been shown to decrease *G*-values of acetaldehyde and formaldehyde [244], from 18.13 to 13.99 μmol J^{-1} and 0.5 to 0.3 μmol J^{-1} using γ-ray dose rates 12 and 433 Gy min^{-1}, respectively. However, for glycerol, an increase in dose rate has shown a *G*-value increase of glyceraldehyde, of 0.06 to 0.12 μmol J^{-1} from 1.7 to 72.1 Gy min.$^{-1}$, respectively. Higher dose rates have not been explored for glycerol radiolysis and present another research opportunity.

2.13.6.2 Sample Parameters

iv) Solute, Solute Concentrations and Mixtures: Across all organic solutes, irradiated chemicals are usually dissolved in dilute aqueous samples, only ranging up to a maximum solute concentration of 10% wt.% [159]. Significant focus has been given to these low concentrations to date with higher concentrations with pure solutes irradiated occasionally. The low solute concentrations are designed to limit direct ionization upon the solute, causing the reactive water radiolysis species, e_{solv}^{-}, $^{\bullet}OH$, and $^{\bullet}H$ to be the vehicles for chemical transformations of the solute, allowing mechanistic control. A higher proportional effect on many solutes is also observed for very low concentrations showing higher *G*-values than with higher solute concentrations [159, 267]. However, low concentrations could be counterproductive in terms of glycerol conversion and mass productivity values compared with direct radiolysis of purer mixtures. Several studies have shown favourable *G*-values for certain radiolytic products with increasing solute (glycerol) concentrations in water, with increases in acetol and 3-hydroxypropanal *G*-values, as shown in Table A3 which is contrary to conventional thinking for most dilute samples. In other works, the highest *G*-values are reported to arise from chain reactions that focus on either pure compounds or reagent mixtures [61, 162], with industrial success resulting from chain reactions based on radical propagation mechanisms. A similar approach for high wt.% solutes and selected mixtures should be given to maximise mass productivity percentages. For binary mixtures, there has been a small number of systems explored which were methanol [206], ethanol [268-270], and aromatic-based [271]. Although, very little additional literature is available on other organic mixtures.

v) Gaseous Phase: The composition of the gaseous phase inside a sample has been a variable parameter in previous works which include the study of aerated (O_2 present), deaerated (vacuum), nitrogen-rich, and N_2O-saturated samples. The alteration of the gas phase can alter the chemical mechanisms within aqueous samples since the main reactive species from water radiolysis are e_{solv}^{-}, $^{\bullet}OH$ and $^{\bullet}H$, gases can be introduced to react with specific species, minimizing or promoting their respective effects. For ethanol specifically, dissolved O_2 gas has been seen to increase *G*-values of stable product yields, such as acetaldehyde (where $G = 0.62$ μmol J^{-1} [147]), with other alcohols showing similar increases in product *G*-values with O_2 gas for other carbonyls.

A sample saturated with N_2O gas scavenges the solvated electrons (preventing reduction mechanisms), as shown by equation (47) and $^{\bullet}H$ radicals as per equation (48)

[272]. Around 90% of the $^{\bullet}$OH radicals are produced with the remaining reactive species of an N_2O-saturated mixture being 10% of $^{\bullet}$H radicals [245]. The mechanistic benefit here is to prioritize H-abstraction, specifically from the weaker C-H bonds for the generation of alkyl radicals as opposed to abstraction from O-H bonds.

$$e_{aq}^{-} + N_2O \rightarrow {}^{\bullet}OH + N_2 \tag{47}$$

$$^{\bullet}H + N_2O \rightarrow {}^{\bullet}OH + N_2 \tag{48}$$

The saturation of N_2O has been a factor to result in higher *G*-values of carbonyl products such as acetaldehyde from ethylene glycol [244]. Whilst important for isolating mechanisms, N_2O scavenging could limit potential mechanisms. This could be beneficial to glycerol radiolysis. For N_2O environments, the additional processes of vacuum drying and gas sparging could result in costly, lengthier process times if applied to glycerol, especially with its thicker viscosity. An air-present sample would be most easily applicable to an industrial process due to its simplicity. Although, the gas additive would offer a potential parameter to vary to increase selectivity and specific product *G*-values.

vi) Additives: Together with other parameters, a pH additive has been used previously to attempt to control reaction mechanisms. However, the influence of pH on aqueous samples and solutes is uncertain [273], as there are inconsistencies between some of the reports. Historically, acidic, or oxidizing environments were achieved using H_2SO_4, typically in the concentration range of 0.01 M to 0.4 M, giving a pH of 1.7 to 0.46. H_2SO_4 (chosen due to the HSO_4^- ion thought to be non-intervening in radiolytic mechanisms). It is hypothesised that acidic environments were supposed to protect $^{\bullet}$OH radicals, capture e_{solv}^{-} and produce $^{\bullet}$H species [273] as per equation (49). The same oxidizing effect has also been achieved with the addition of H_2O_2.

$$e_{aq}^{-} + H^{+} \rightarrow H^{\bullet} \tag{49}$$

Alkaline additives such as KOH or MeOH in the concentration ~0.1M are occasionally utilized to create a reducing environment [274], increasing pH up to 14, scavenging $^{\bullet}$OH radicals whilst only slowly reacting with $^{\bullet}$H and e_{solv}^{-}. Reports on alkaline solutions and the related primary and radical yields are generally scarce which is where some inconsistencies remain to make quantification interpretations difficult [273]. It is claimed for pH ranges from 4 to 11 in aqueous solutions, the primary and radical *G*-values tend to be independent of pH and display similar yields seen for neutral solutions. However, the yields from extreme pH values are still not clear. Contrasting acidic solutions, using alkaline solutions, aims to consume all $^{\bullet}$OH radicals [273], generating oxide radical anions ($O^{\bullet -}$) as the main oxidizing species as shown by equation (50). Subsequent reactions with $O^{\bullet -}$ depends on the solute but with alcohols, $O^{\bullet -}$ is likely to reduce the hydroxyl group to a carbonyl group.

$$HO^{\bullet} + HO^{-} \rightarrow O^{\bullet -} + H_2O \qquad (50)$$

There is little final product *G*-value data in varying pH for glycerol specifically, with neutral samples studied more often. On the other hand, data on ethylene glycol [244] shows a *G*-value preference for glycolaldehyde of 0.15 μmol J^{-1} at a neutral pH of 6, compared against a pH of 13.7 with glycolaldehyde not registered and formaldehyde at a high of 0.46 μmol J^{-1}. Similarly, with gaseous additives, pH additives would introduce another complexity into radiation-chemical processing, but varying pH additives could present as a potential parameter to improve *G*-values.

vii) Temperature: In water, the effect of temperature has been shown to affect the measurable yields of primary reactive components [275]. These changes in concentrations of primary species likely alter the solute-aqueous chemical reactions in the physicochemical timeframe (10^{-12} s to 10^{-4} s) from an ionization event. However, it is noted that some chemical reactions can take place before these reactive species have a chance to diffuse ($<10^{-12}$ s). Despite these differences, in the measurable final stable *G*-values from water, there are only small variations in these yields (±10%) from 0 °C to 60 °C [276], as with most other organics [162]. Temperature-dependent trends in *G*-values may be measurable at higher temperatures in which thermal-assisted radical dissociation to form decomposition products increases the observed *G*-values, rather than relying solely on direct radiolytic effects. In the literature on alcohols, the radiolysis of methanol [114] and ethanol [240] in their gaseous phase at higher temperatures showed improved product *G*-values compared with lower-temperature samples.

For ethylene glycol and glycerol, temperature studies from Baugh have shown a mostly independent relationship between *G*-values for all stable radiolytic products, with no clear dependences in glycerol from 0 °C to 60 °C. However, elevated temperatures of 170 °C for ethylene glycol do see higher methanol yields of 0.72 μmol J^{-1} compared with 0.56 μmol J^{-1} at room temperature [277]. For simplicity, the radiolysis of liquid samples at ambient temperatures or normal reactor temperatures will be investigated first.

2.14 Research Questions

In this chapter, the problems associated with the nuclear and biodiesel industries have been explored with an innovative nuclear-biorefinery concept proposed to address these problems. The lack of mixed-field neutron + γ-ray or neutron-related radiolysis prior art has been highlighted which has raised some areas worthy of further consideration. Furthermore, the prior art often considers only very dilute solutions (<1% wt.%) to improve *G*-values without consideration of production-level processes. This is the case for glycerol, where very few reports exist for optimising *G*-values for high wt.% solute mixtures, with molar yield % and mass productivity values not currently considered to evaluate the scope of coupled radiation-chemical production systems.

Therefore, the parameters chosen to be explored in this research for glycerol radiolysis are radiation types (and corresponding LET), absorbed dose, dose rate, solute concentration, binary and tertiary mixtures, and gaseous environment for glycerol. To compare against the findings of prior reports for ethylene glycol and the high *G*-values of acetaldehyde reported, neat samples of ethylene glycol have also been irradiated with the following parameters: radiation type, absorbed dose and dose rate.

The following questions are posed here which this research aims to answer:

1) Are neutronic-related irradiations effective for the radiation-induced chemical processing of organic materials?
2) Why are there relatively few reports on specifically neutron irradiations?
    - Is this a radioactivity or regulation issue?
3) Can the *G*-values of products from glycerol as stated in previous literature be improved upon using specific parameters? Are there any unreported products?
4) Could a scaled-up radiolysis-directed process be used to evaluate the industrial-scale feasibility of a nuclear-biorefinery process?
5) What is the applicability of using under-utilized nuclear (spent fuel storage) facilities across Europe for radiation-induced chemical processing?
    - Will these processes improve the economic viability of nuclear cogeneration?

3 Materials and Methods

The following chapter describes the chemicals, equipment, and methodologies involved in this research. The initial sections describe the chemicals and irradiation sample vessels, the radiation sources, the dosimetry calculations, and the methodologies used in this research. Irradiation sample plans for solutes are described with varying parameters of radiation type, absorbed dose, dose rate, solute concentration, mixtures, and gaseous environment. Scale-up production capacity and feasibility calculations utilizing spatial MCNP models of a commercial NPP and spent fuel pool are also described.

3.1 Chemicals – Organic Solutes

For solutes to be irradiated, glycerol (>99.5 wt.%, Honeywell), acetone (99.8 wt.%, Fisher Scientific) and ethylene glycol (>99% wt.%, Scientific Lab Supplies, SLS) were used. Ultra-pure water was used from a Milli-Q Direct purification system. Chemical analytical standards for acetol (95 wt.%), acetic acid (99.9 wt.%), 2-butanol (99.9 wt.%), acetaldehyde, ethyl acetate, methanol, glycolaldehyde dimer were purchased from Sigma Aldrich. Ethanol and propan-1-ol used for the pre-chemical dilution of samples were also purchased from Sigma Aldrich. Solketal standard (98 wt.%) was purchased from Alfa Aesar. Chemicals were used without further treatment.

3.2 Radiation Vessels

For radiation vessels, there are several design requirements to assess the suitability of vessels for radiolysis vessel applications.

The first requirement was the good retention of volatile compounds produced from the organic sample under testing. In the literature, the radiolysis of hydrocarbons consistently produces gases such as H_2, CO and CO_2 as well as volatile components such as formates and aldehydes for oxygen-containing compounds. Therefore, a radiation vessel needed to be sealed with a theoretically zero leak potential that could also withstand significant internal pressure increases due to the gases generated for accurate analyte quantification. Due to hydrogen being the most prominent gas produced in terms of *G*-values from hydrocarbons, data from the prior art were used to calculate potential increases in vessel pressure. A headspace volume to organic liquid volume partition ratio of 4:1 was used to account for a maximum pressure increase of 1 bar for up to ~100 kGy irradiations. This is important because leaking vials could have contaminated in-core reactor positions with organic material, with no feasible way of cleaning. Leaking vials would have also reduced the accuracy of concentration and *G*-value determination of volatiles.

In previous radiation testing involving glycerol, one of the problems was the retention of volatile radiation-chemical products such as formaldehyde and acetaldehyde. However, the detection of such products after the chemical work-up and sample preparation steps has not been reported in previous glycerol radiolysis literature [3]. Therefore, the second requirement for a vessel was exploring the option of sampling directly from the irradiation vessel to detect and quantify these volatile components accurately. Two different vial options were chosen for organic radiolysis vessels:

1) 20 ml Rounded bottom, borosilicate headspace GC crimp-capped vials (Phenomenex) with an aluminium-coated silicon septum (Sigma Aldrich, Part Number: Z292052).
2) 5 ml Polypropylene cryogenic vials with a sealed external thread cap (Manufactured by Argos Technologies and purchased from Cole-Parmer, Part Number: WZ-04395-69)

The crimp-capped borosilicate (BS) vials with a septum offered the ability to sample directly from the vial by the GC headspace autosampler, without opening the vial and losing volatiles. The polypropylene (PP) cryogenic vials were also selected as alternative irradiation vessels. These polymer vials were quoted to be stable up to a temperature of 121°C, have a leak-proof seal and with it able to withstand an internal pressure of 95 kPa. These vials were mostly an ideal alternative but lacked the option of a septum to allow direct sampling for GC analysis. However, it was thought that these vials would be superior for longer-term storage and analyte leak prevention. These PP vials are also a more comparable composition (hydrocarbons) and density (ρ=0.9 g cm^{-3}) to the organic samples (ρ≈1 g cm^{-3}) as opposed to the borosilicate vials (ρ=2.2 g cm^{-3}), this was preferable to ensure uniform dose deposition across the sample [278, 279]. No polypropylene degradation analysis to measure residual volatiles was done in this work. However, the literature on polypropylene radiolysis is significant [280, 281]. High-dose

(500 kGy) exposures of isotactic polypropylene within the presence of oxygen show that the four main gaseous products from GC analysis were H_2, CH_4, CO and CO_2 with *G*-values of 0.3, 0.01, 0.26, and 0.11 µmol J^{-1}, respectively [281]. Most other gaseous products were chained hydrocarbon products (e.g., butane and heptane) below 0.01 µmol J^{-1}. Further volatile analysis of 24.4 kGy ^{60}Co γ-ray irradiated PP lists 18 low-molecular weight products at *trace* concentrations [280], including 2-propanone (acetone), acetic acid, 3-methyl-2-cyclopenten-1-one, and 2,4-dimethylheptane and 1,3-bis-(1,1-dimethylethyl)-benzene [282], although most of the *G*-values were not determined due to analytical difficulties [280]. Whilst some of these PP degradation products may add or interfere with the products from glycol radiolysis (i.e., acetone and acetic acid), a comparison between the PP and BS vials may highlight any significant anomalies from polypropylene degradation. Although, the concentrations and *G*-values produced from PP volatiles are thought to be low.

After initial exposures with neutronic mixed-field irradiations with the BS vials, the presence of boron within the glass was theorised to be responsible for a discrepancy in the total calculated absorbed dose. This was due to ^{10}B being an excellent thermal neutron absorber and would absorb a significant proportion of the neutron dose compared with the organic phase. As discussed in the following chapter 4.3, a significant heating effect caused seal breaks and consequently the loss of volatile components. Due to borosilicate glass being composed of a network of mostly silicon and boron linked via covalent -O- bridges, there would not be any carbon-based volatiles produced from BS radiolysis.

Several other requirements for the ideal irradiation vessel are: i) for the vessels to be chemically unreactive to the starting reagent or any formed products and ii) the vessel does not interact significantly with neutrons to avoid nuclide activation. Materials such as metals, glasses and plastics are all damaged by ionizing radiation to some degree [283]. In similar recent studies [121], headspace vials were also used as radiation vessels for liquid water samples for volatile quantification. However, due to the recorded effects on borosilicate glass under irradiations, its physical hardness increases over time due to embrittlement [284] and could present vessel stability issues for high-dose (~100 kGy) irradiations. Hence, the physical strength of the BS vials was evaluated before conducting irradiations with organic samples.

3.2.1 Axial Compression Testing

Empty, capped unirradiated and irradiated vials were tested as to their capacity to withstand an axial compressive force until failure. This was accomplished using a Zwick-Roell Z020 axial compressor and a bespoke stainless-steel mount and piston as shown in Figure 13.

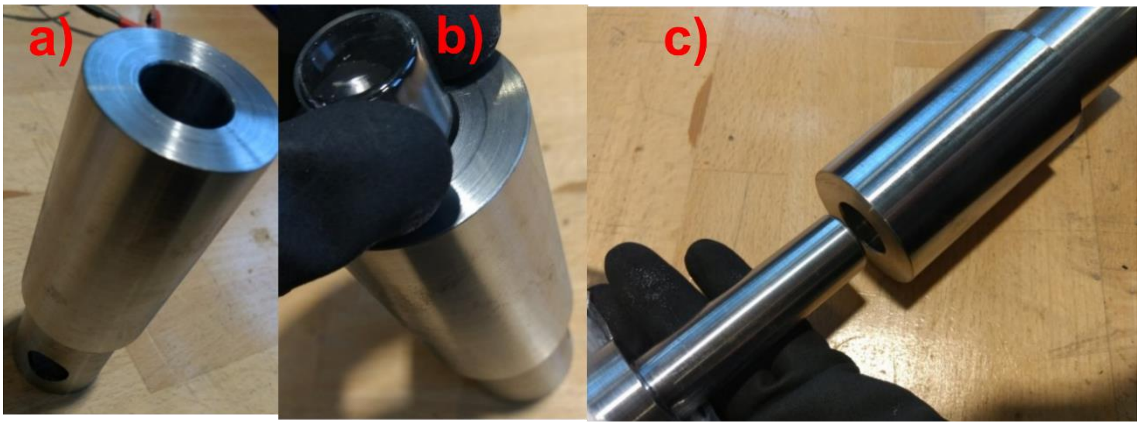

Figure 13: Bespoke axial compression mount and piston (designed with Armin Y. Kanani). **a** bottom vial holder, **b** a BS vial inserted into the vial holder, and c showing the mount with the top piston.

The stainless-steel holder and piston were affixed to the bottom and top of the axial compressor, respectively with a BS vial situated in the holder for compression. A flexible plastic guarding was then secured to both the holder and the piston using rubber bands to contain any possible glass shards or dust from escaping the holder. The piston was manually lowered to just above the vial. The axial compressor was then programmed to lower the piston at 0.025 mm min^{-1} into the holder to compress the held vial. The force (in N) upon the vial was then measured over time until the failure point of the vial, as indicated by the sudden drop of force or the audible cracking of glass. After compression, the piston was then retracted, and the holder was thoroughly cleaned for the next vial. 13 empty, capped unirradiated BS vials were tested as to their failure force and 2 empty, capped 100 kGy irradiated vials were tested. The empty, γ-ray only irradiated vials were irradiated in the TriC position of the JSI reactor (as detailed in chapter 3.4.3) whilst in shutdown mode. Rounded bottom and flat bottom BS vials were compressed to provide an assessment of the strength of differently shaped vials. 10 uncapped BS vials were also compressed to remove the cap as a variable. The axial pressure (in N cm^{-2}) upon each vial can also be calculated by dividing the failure force by the surface area of the bottom of the vial. The flat and rounded-bottomed vials had an area of 4.15 cm^2 and 0.74 cm^2, respectively. Table 20 in chapter 4.2 lists the different vials compressed with their compression results. These results showed no significant statistical differences between the compression force required to crush the irradiated borosilicate vials, compared with the unirradiated vials. While this method did not test the integrity of the cap seal, it did show that the BS vials could withstand minor stresses whilst being extracted from the TriC reactor position or parcel transport. Therefore, the irradiation of organic samples could proceed.

3.2.2 Internal Pressure Calculations

When introducing an organic sample into a vessel, a suitable headspace was given of approximately a 4:1 ratio of headspace-volume-to-organic-phase to account for internal pressure increases. The internal pressure increases across the absorbed dose range (20, 40, 50, 60, 80, and 100 kGy) were estimated by extrapolating from the sum of G-values for all the main gaseous components (H_2 (G 0.43), CO (0.01), CH_4 (0.06), C_2H_4 (0.01), C_2H_6 (0.02) and CH_2O (0.19)) from ethanol (G-value sum = ~0.74 µmol J^{-1}) [240], as shown in Appendix A, Table A19. For example, the maximum 100 kGy doses would generate 373 µmoles of the main gaseous compounds. Using the ideal gas equation as per equation (51), a fully sealed vessel at 25 °C would generate an internal pressure of 57.8 kPa (0.57 atm.) above atmospheric, and if the vessel was heated to 100 °C would generate an internal pressure of 97.9 kPa (0.966 atm.) which is comparable to the pressure rating of the PP vials. The ideal gas equation used as follows:

$$P = \frac{\left(n_b + n_{gas}\right) * R * T}{V_{gas}} \tag{51}$$

Where P is the internal pressure in the vial, n_b is the moles of the gas phase before irradiation, n_{gas} is the moles of estimated gas produced from the irradiation of the organic sample, R is the universal gas constant, T is temperature, and V_{gas} is the volume of the headspace gaseous phase.

Due to the volume differences of the vials, a lower mass of organics was required for the smaller PP vialed samples, but the ratio between the liquid organic to the gaseous headspace remained the same. Figure 14 shows the vial types used in this research.

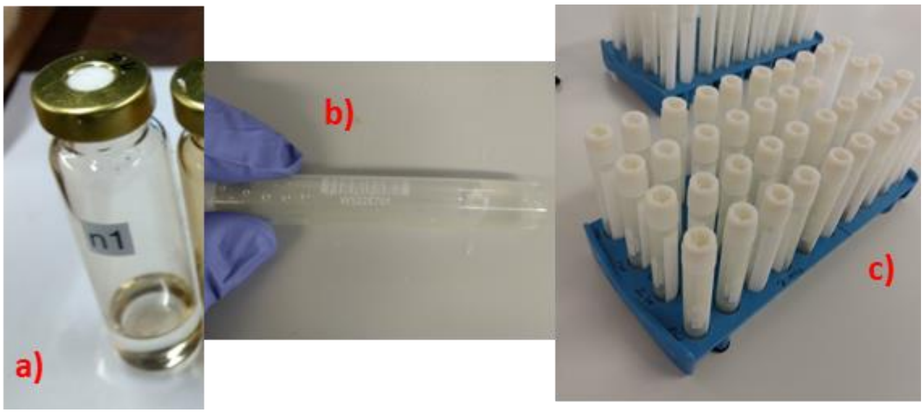

Figure 14: Filled irradiation vessels. **a** 20 ml Borosilicate vials example (Aluminium/Silicone septa has blue caps) **b** 5 ml Polypropylene cryogenic vials. **c** a large array of irradiated polypropylene vials.

3.3 Sample Preparation before Irradiations and Leak Testing Protocol

Organic samples had different preparation methods depending on the desired solute, mixture, and gaseous capping environment. For neat ethylene glycol and glycerol liquids, samples were either dispensed into the vials, within an MBraun UNIlab Pro nitrogen-pressurized glovebox, or in a regular fume cupboard with an N_2 line connected to the headspace vial to limit the concentration of both O_2 and H_2O within the neat, irradiated samples and prevent possible side reactions. Reagent bottles for the pressurized glovebox were opened within the glovebox and left to stand for 24 hours. During sample preparation, the concentrations of O_2 and H_2O were measured in the N_2-glovebox to be <0.5 ppm and 0.7 ppm, respectively, at an N_2 overpressure of 4.2 mbar. Due to the unsuitability of aqueous-based mixtures within the pressurized nitrogen glovebox, binary and ternary mixtures were capped within an air-present atmosphere. Binary and ternary mixtures were mixed within volumetric flasks and capped within an N_2-promoted headspace. The various sample parameters explored in the sample plans are detailed in chapter 3.4.3.

To determine if the samples had leaked, the mass of the organic and total vial mass was recorded before being shipped off to be irradiated by the JSI reactor. The total mass of the vial was then recorded after the irradiations once returned to Lancaster. The difference in the total vial mass could then be attributed to the change or loss of the organic phase within the vials. Based on the statistical variance in the mass changes, a leak of a vial could be highlighted. A leaked vial was identified if the change in the total mass of the vial was above 1% of the mass relative to the starting organic sample. The vial mass data has been given as part of the sample lists in Table 15 to Table 18 in chapter 4.2.

3.4 Radiation Sources

3.4.1 Californium-252, Lancaster University, UK

Preliminary irradiation research began with the californium-252 sealed source at Lancaster University. ^{252}Cf disintegrates via either alpha decay (96.9 % of the time) or through spontaneous fission (3.1% of the time). From spontaneous fission, daughter fission fragments are produced alongside an average of 3.7 energetic neutrons and 8.38 γ rays with an average energy of 2 MeV and 1.2 MeV, respectively. ^{252}Cf can fragment into a variety of daughter nuclei with varying weights [285]. Often a heavy and a light fragment are produced in pairs with atomic numbers of ~140 and ~110, respectively. Example spontaneous fission equations with different daughter nuclei are given as follows:

$$^{252}\mathrm{Cf} \rightarrow {}^{140}\mathrm{Xe} + {}^{108}\mathrm{Ru} + 4n + Q \tag{52}$$

$$^{252}\mathrm{Cf} \rightarrow {}^{140}\mathrm{Cs} + {}^{109}\mathrm{Tc} + 3n + Q \tag{53}$$

The unstable daughter nuclei from spontaneous fission e.g. ^{140}Xe, ^{108}Ru, ^{109}Tc and ^{140}Cs all decay via a series of rapid β^- emissions until stable nuclei are reached (e.g. ^{108}Pd or ^{139}La) [285]. The fluence of neutron and γ-ray emissions reduces over time relative to logarithmic decay of an effective half-life of 2.65 years. Extrapolating from the commissioning specifications for the ^{252}Cf source, the current activity, neutron fluence and γ-ray fluence can be predicted. Even though some γ-ray emissions usually accompany rapid beta decays, a steady state of emissions from these fragments would have reached at the time of commissioning as the rate of spontaneous decay matches the formation of stable nuclei. Table 9 lists the relevant specifications of the ^{252}Cf source utilized at commissioning and at the time of use (19/05/2017).

Table 9: Californium-252 commissioning and in-use specifications

Parameter	**Commissioning Specifications (19/02/2014)**	**In-use (19/05/2017)**
Activity / Bq	7.48×10^{7}	3.18×10^{7}
Effective Half-Life / years [286]	2.65	2.65
Point source neutron fluence rate / neutrons s^{-1}	-	3.71×10^{6}
Gamma fluence rate / γ rays s^{-1}	-	8.20×10^{6}
Average neutron energy / MeV	2	2
Average gamma energy / MeV	1.2	1.2

The ^{252}Cf source is comprised of a 5 µg of active ^{252}Cf content which is incorporated in a ceramic material and encapsulated inside two welded stainless steel capsules. The source is mounted to a hydraulic system inside a 1 m^3 stainless steel container filled with water and a steel wall thickness of ~33 mm. Radiations of organic samples were achieved by operating a hydraulic arm to move the source from the centre of the tank towards one of the internal faces of its water-filled container, as per Figure 15a. Organic samples were set up next to this face before source exposure. For dosimetry estimates, samples were approximately 20 cm away from the source. Figure 15b shows the irradiation setup for sealed neat glycerol and ethylene glycol samples. The samples were positioned next to the face of the tank where the ^{252}Cf source will be in its exposed position.

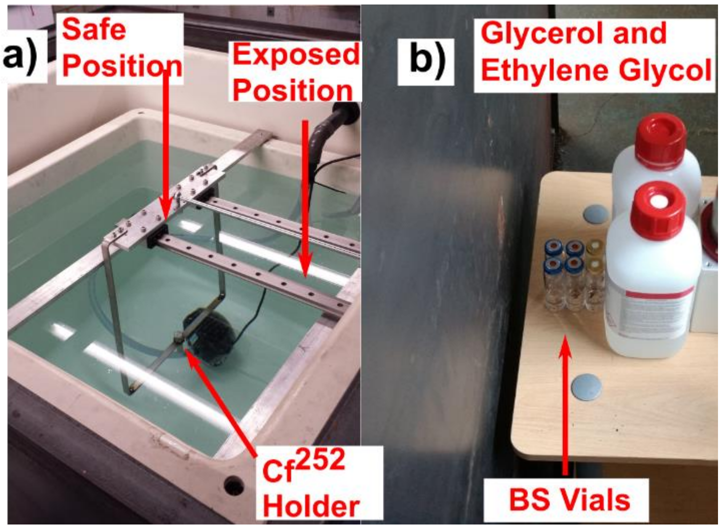

Figure 15: a The steel cubic tank filled with water showing the ^{252}Cf source holder, the support frame, and the hydraulic system showing the safe and exposed positions. **b** Organic samples setup situated to the closest cubic face of the tank as to the ^{252}Cf exposed position: BS vials containing neat ethylene glycol or glycerol and corresponding bulk bottles for the ^{252}Cf exposures.

3.4.1.1 Californium-252 Dosimetry

To determine the suitability of ^{252}Cf as a radiation source for radiolytic conversion, neutron dosimetry calculations were conducted for a hypothetical water sample substitute. Neutron dosimetry was achieved by extrapolating to the ^{252}Cf source's current activity, and subsequently the γ-ray fluence and neutron point source fluence as shown in Table 9 for the current activity. To calculate the absorbed dose into a sample, several assumptions were made for an overestimate of the absorbed dose due to neutrons as follows:

1) KERMA-absorbed dose approximation.
2) Average neutron energy for interactions of 2 MeV.
3) No moderation due to the steel or water in the containment tank.
4) Uniform dispersion of neutron emissions from a point source.
5) ~50% of the neutron fluence rate is thermalized in a sample of a depth of 2.5 cm [287].

It is worth noting that the above approximations are rudimentary, and this calculation is primarily here to serve as an estimate of the absorbed dose for an assessment of the feasibility of ^{252}Cf for supplying a sufficient dose to the organic samples. Due to these approximations, neutron backscatter, the attenuation of neutrons due to steel or water, and the different kerma values across the energy spectrum range have not been considered. Therefore, the estimated absorbed dose may be inaccurate but will offer an estimate of the order of magnitude of the dose rate.

Estimating the absorbed dose used the KERMA-absorbed dose approximate (as detailed in 2.10) together with equation (43) which estimates kerma from the ^{252}Cf neutrons. A KERMA coefficient of 3.31×10^{-11} Gy cm^2 corresponding with an average neutron energy of 2 MeV and interacting with water was utilized [181]. The neutron fluence rate through a sample was calculated through the area of a sphere with a radius of 20 cm away from the point source, resulting in a fluence rate of 739 n cm^{-2} s^{-1}. The fluence rate was then reduced further by 50% to 370 n cm^{-2} s^{-1} based on the neutron fluence drop through 2.5 cm of water [287]. This provided an estimate of 0.044 mGy hr^{-1} for the achievable kerma dose rate due to neutrons from the ^{252}Cf source. Foreseeing a potential limitation regarding regards generating a suitable analyte concentration for the detection of radiolysis products, samples were irradiated semi-continuously for a total of

25 days (600 hrs), resulting in an estimated absorbed dose due to neutrons of 0.026 Gy. The corresponding dose from γ rays is estimated to be 30% of the total absorbed dose (neutrons and γ ray combined) from a ^{252}Cf source assuming a water target [288, 289], achieving a total combined absorbed dose of ~0.038 Gy with γ-ray absorbed dose constituting ~0.011 Gy. While these calculations constitute an overestimation, the long irradiation times were necessary when using this source to achieve suitable doses to potentially detect radiolytic product concentrations.

As described later (results and discussion), the low neutron fluence and consequently low dose rate of the ^{252}Cf proved to be insufficient for experimental radiolysis work. A more active radioactive source was required to generate sufficient concentrations of radiolytic products and to achieve comparable doses to those of an operational fission reactor or a spent fuel pool.

3.4.2 250 kW TRIGA Fission Reactor, JSI Slovenia.

The TRIGA (Training, Research, Isotopes and General Atomics) Mark II, 250 kW research fission reactor at the Jožef Stefan Institute (JSI), in Slovenia was utilized. This reactor was built in the ’50s and ’60s and was used initially for the production of radioactive isotopes but is used today for a range of purposes including training and research [290]. It is a light-water-cooled, pool-type reactor using solid fuel rods which are a homogeneous composite of 20% enriched uranium with a zirconium hydride moderator; this composite fuel system was designed to create an intrinsically safe reactor for all TRIGA-purposed reactors. The reactor core contains 70 individual fuel rods, arranged in a lattice pattern together with several core-irradiation positions shown in Figure 16. Two main types of experiments were conducted using the JSI reactor: 1) The irradiation of organic samples for radiolytic organic component generation (and subsequent *G*-value calculations) using the large triangular irradiation channel (TriC indicated by the red arrow), or 2) the irradiation of organic samples for instrumental neutron activation analysis (INAA) for radioactivity determination using the JSI carousel facility (blue arrow).

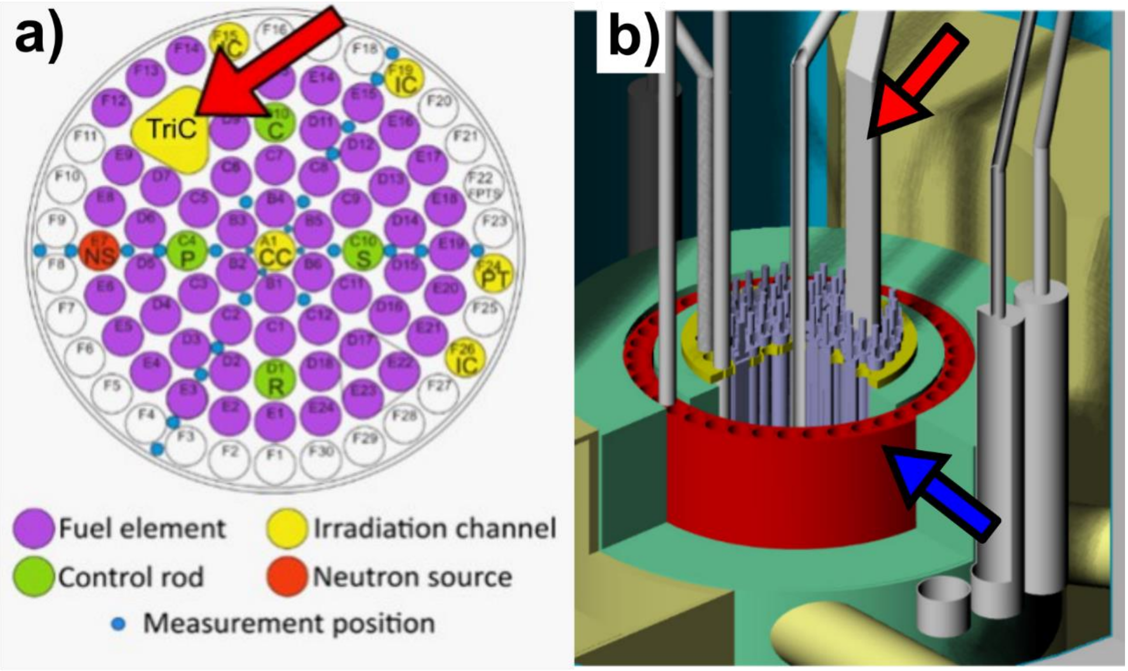

Figure 16: a A schematic of the TRIGA Reactor Core: showing the large triangular channel (TriC) indicated by the red arrow. **b** CAD schematic of the reactor showing the TriC access pipe (red arrow) used for *G*-value determination and the surrounding carousel facility (indicated by the blue arrow) used for INAA testing. Images were used with permission from Anže Jazbec [291].

The large triangular channel was installed to accommodate larger-sized samples, this channel position has a diameter of ≈ 4 cm allowing the irradiation of entire silicon detectors [292]. This large TriC proved to be useful for the irradiation of numerous vials for radiolytic organic component synthesis. Furthermore, this reactor is often utilized as an unofficial reference centre due to the thorough characterization and modelling of the neutron and γ-ray fluences within all the irradiation channels. The characteristics and specifications of the TriC at 250 kW power are shown in Table 10 [291].

Table 10: Neutron Flux Specifications of the Triangular Irradiation Channel (TriC).

Specification	**Max. Neutron Flux [cm^{-2} s^{-1}]**
Thermal (<0.625 eV)	4.5×10^{12}
Epithermal (0.625 - 10^5 eV)	3.5×10^{12}
Fast (>10^5 eV)	3.8×10^{12}
Total	1.2×10^{13}
1 MeV Equivalent	3.6×10^{12}

The Triangular channel offered the best irradiation position for the following reasons:

i) **Large volume for irradiations.** Four headspace vials or twelve polypropylene vials could fit within the TriC for single irradiation, allowing multiple sample parameters to be explored during a single exposure. Vials could also be stacked – increasing this number.

ii) **High % fast neutron flux.** The TriC offered a relatively high percentage of fast neutron flux (≈ 33%) compared with the other irradiation positions. This was important to determine the feasibility and efficacy of neutrons for radiolytic chemical production, without high radioactivity.

iii) **High relative dose rates.** At full power, samples in the TriC are irradiated with 2.1×10^5 Gy h^{-1} and 3.4×10^5 Gy h^{-1} neutron air kerma and γ-ray air kerma, respectively [199]. These dose rates offer a similar radiation environment to the fields generated within a working commercial NPP.

Figure 17a displays a top-view photo of the TRIGA pool reactor, looking down into the core. Figure 17b shows the lowering of several samples into the TriC. The samples are contained within several layers of polyethene bags to prevent contamination from or to the sample vials (and the TriC irradiation position). Figure 17c shows diagrams of the vials used in this research.

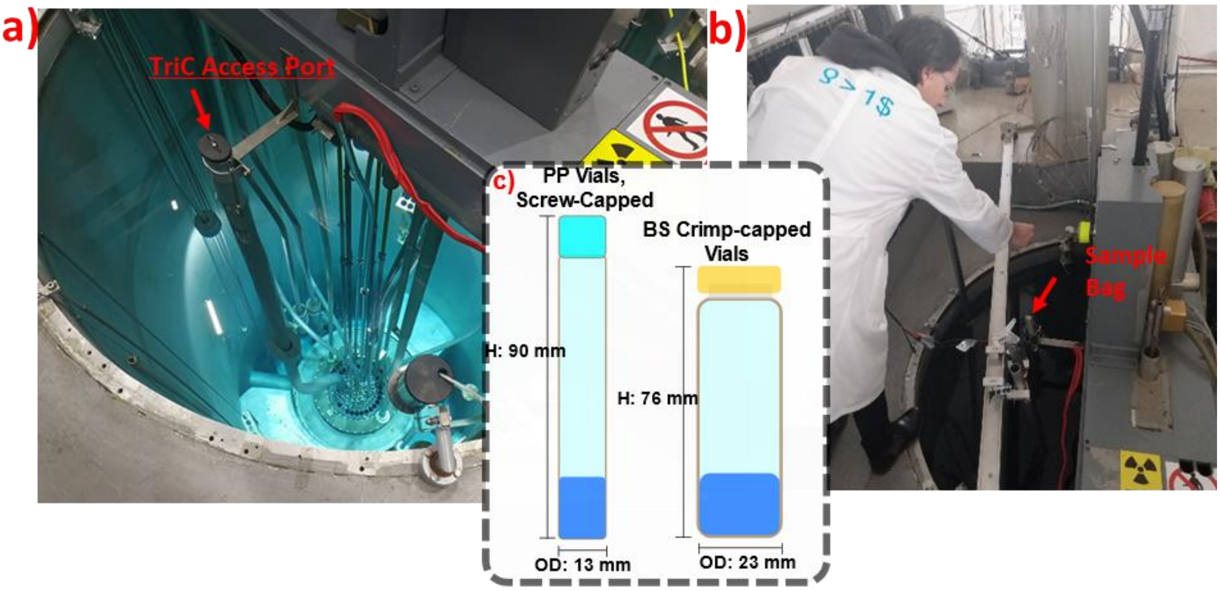

Figure 17: a Top view of the 250 kW TRIGA pool reactor at JSI (2018). The red arrow indicates the larger Triangular Irradiation Channel (TriC) access port for samples. **b** Organic vials being lowered into the TriC access port (Dr Anže Jazbec pictured). **c** diagram of the polypropylene (PP) and the borosilicate vessels (BS) used.

Once samples are lowered down the TriC access port and into the reactor's core, the reactor can be operated in either of two different modes of operation:

i) **Operational mode** – Where the control rods are elevated, and the reactor is brought to steady-state criticality in which a specific power output is maintained between 10 kW and 250 kW. This mode irradiates in-core samples with a consistent mixed-field spectrum of neutron + γ rays. During this mode, the neutron flux within the TriC can reach 1.18×10^{13} n cm^{-2} s^{-1}, with γ-ray flux simultaneously reaching 1.21×10^{13} cm^{-2} s^{-1} [201].

ii) **Shutdown mode –** Where the control rods are fully lowered, stopping critically within the core. This mode irradiates samples in the TriC with delayed γ rays from radioactive fission products (^{140}Cs, ^{90}Sr etc.) generated within the UrZnH fuel rods. When the reactor power is <1 kW, the delayed γ-ray flux can be as high as $<3.75 \times 10^{12}$ cm^{-2} s^{-1} but decays exponentially with time [185]. Any dose from subcritical neutrons is thought to be negligible.

For radiolytic organic component production, these two different modes of irradiation allow a comparison between a majority neutron dose from high-fluence mixed-field irradiations and delayed γ-ray only irradiations when identical sample mixtures are considered. Since reports of γ-ray irradiations are common in the radiolysis literature, this γ-ray only mode also allows comparisons with existing literature data. Figure 26c shows examples of irradiated BS and PP vials.

3.4.2.1 In-core Dosimetry

For the determination of the dose rate in Gy min^{-1} and consequently the absorbed dose in kGy into the organic samples, different calculation methods were employed for the two different radiation modes.

For operational mode (mixed-field neutron + γ rays) and the corresponding dosimetry, the existing spatial MNCP model of the JSI 250 kW reactor [199, 293] utilized the MCNP code, version 6.1 [294]. This model, in combination with the ENDF/B-VIL.0 nuclear data library [295] was used to calculate the particle flux, spectra and dose rate values of both neutrons and γ rays within channels of the core. In previous research, various values for particle fluences, air KERMA and silicon equivalent have been calculated and then confirmed against values derived from experimental studies [185, 193], with MCNP calculations being within an excellent agreement. This in-core dosimetry through the utilization of the MCNP model was performed by Luka Snoj, informing the JSI reactor operator (Anže Jazbec) irradiation time required for the desired dose for the organic samples.

Utilizing this existing MCNP model and substituting the sample for an ICRU human tissue analogue, allowed the calculation of the mixed-field neutron + γ-ray KERMA dose-rate factors related to the reactor power. These were calculated using the track length estimates of volume average energy deposition (F6 tally mode). Due to similar compositions and KERMA factors, the ICRU tissue was deemed to be a good analogue to the various organic glycol mixtures. A factor of 5.44×10^{-4} Gy s^{-1} W^{-1} was determined for the total mixed-field dose rate from the MCNP model for the JSI reactor [199, 293]. Individual factors of 3.51×10^{-4} Gy s^{-1} W^{-1} and 1.93×10^{-4} Gy s^{-1} W^{-1} were determined for neutrons and γ rays, respectively [296]. This resulted in a dose contribution of ≈64% and ≈36% from neutrons and γ rays, respectively (for human tissue KERMA). For example, a total of 50 kGy mixed-field irradiation would have 32 kGy and 18 kGy doses from neutrons and γ rays, respectively with an estimated error of 10% due to uncertainties in the MCNP model's neutron fluence and dose rate with that extended over the period for irradiation [198, 199].

For shutdown mode (γ-ray only) and its corresponding dosimetry, values for absorbed dose rates were calculated based on the power reading on the reactor instrumentation for a specific time. The delayed γ-ray only absorbed dose rate in Gy s^{-1} is directly proportional to the reactor power output readings in Watts, as measured in the linear channel located outside the core and graphite reflector [185, 297]. Within this linear channel is the compensated ionization chamber (IC) which is sensitive to delayed γ rays and allows the determination of dose rate. Using the calibrated ionization chamber, a γ-ray only dose rate factor of 14250 Gy s^{-1} W^{-1} for the triangular irradiation channel was determined with an accuracy of 10% [194].

Due to the exponential decay of the reactor power (in Watts), the dose rate was measured in regular intervals by the reactor operator (Anže Jazbec) with a compensated ionization chamber located in the linear channel (which is sensitive to γ rays) for a direct readout. The reactor power was averaged across several minutes, with the average dose rate and subsequent absorbed doses over the period tabulated until the required dose was reached. A sample analogue of light water (H_2O) was used for these calibrations [298] to determine the absorbed dose.

3.4.2.2 Radioactivity Testing: Instrumental Neutron Activation Analysis (INAA)

To detect and quantify radionuclides that might arise in the samples as a result of irradiation, samples of ethylene glycol and glycerol were tested according to the O2-K0-instrumental neutron activation analysis (INAA) standard working procedure [299], as described here. This INAA service was conducted by Dr Radojko Jaćimović at the JSI reactor facility [300]. The INAA method allows the identification and quantification of impurities with their respective radioactivity induced by neutron exposure. For the INAA method, 1.4 g and 2.4 g samples were loaded into polyethene ampoules for ethylene glycol and glycerol, respectively. The liquid samples were irradiated with thermal neutrons and γ-rays for 12 hours in the carousel facility of the TRIGA reactor at a power of 250 kW, with a thermal neutron flux of 1.1×10^{12} cm^{-2} s^{-1}, as confirmed using the experimentally supported MCNP model [199, 293]. During this time, the samples were exposed to a total absorbed dose of 520 kGy, with 270 kGy of that being from thermal neutrons and 250 kGy from γ rays. A certified reference material of Al-0.1% Au (IRMM-530R) was used to determine neutron dosimetry and k0 method standardization.

Following irradiation, the liquid samples were transferred to a new polypropylene vial and the γ-ray spectrum of the irradiated liquid was measured at intervals of 0.5, 4, 11 and 22 days after irradiation using a High-Purity Germanium (HPGe) detector. Peak area evaluation was achieved using Hyperlab 2002. For the determination of elemental concentrations, the following values for thermal-to-epithermal flux ratio and epithermal flux deviation, $f= 28.74$ and $\alpha= -0.0023$, were derived, respectively. To determine the induced radioactivity within the samples after time, t from irradiations, the empirical data (section 4.4) were extrapolated using known radionuclide half-lives. The radioactivity of activated impurities is calculated at: 0 hrs, 24 hrs, 62 hrs, 168 hrs and 240 hrs after the completed irradiation. These radioactivity calculations for the impurities after irradiations were conducted by Plant A. G.

3.4.3 Radiation Sample Plans and Variables

As detailed in chapter 2.13.6, many parameters can be explored for the radiolysis of aqueous samples. A list of 8 samples irradiated with the ^{252}Cf source are given in Table 13. A total of 28 ethylene glycol sample vials and 72 glycerol-based mixture sample vials were irradiated with the JSI reactor which are listed in Table 15 to Table 19 with associated radiation and sample parameters. The irradiated samples were returned to the University of Lancaster for GC-MS analysis, along with 10 unirradiated control samples of all vial and mixture types. The explored parameters of the irradiated samples have been collated with the measured concentration, the following *G*-value, and mass productivity data in Appendix A, Table A4 to Table A17. Using the 250 kW JSI TRIGA reactor, the radiolytic products were generated and studied against the following parameters:

3.4.3.1 Radiation Types

To compare the radiolytic effectiveness of neutrons with γ rays, organic samples were exposed to either a mixed-field neutron + γ rays or γ rays only via operational mode or shutdown mode, respectively. For a quantitative comparison, samples of equivalent absorbed doses were compared. For mixed-field irradiations, approximately 65% of the total absorbed dose is due to neutron interactions with the remaining 35% due to γ rays.

3.4.3.2 Absorbed Dose Dependency

To determine the radiation-induced effects across a range of large, absorbed doses (>20 kGy), organic samples were irradiated with either 20, 40, 50, 60, 80 or 100 kGy of absorbed dose of the respective radiation type.

3.4.3.3 Dose Rate Dependency

With the JSI reactor in operational mode, the mixed-field neutron + γ-ray dose rate could be controlled by regulating the reactor power via control rod positions. Four dose rates (0.52, 1.31, 3.27 and 8.17 kGy min.$^{-1}$) were explored for neat ethylene glycol and glycerol samples, all with a total absorbed dose of 50 kGy. γ-ray only irradiations were limited to lower dose rates of up to ~40 Gy min.$^{-1}$ based on the emissions from the activated elements in the nuclear fuel rods.

3.4.3.4 Liquid Sample Type and Solute Concentration

To maximise the conversion of glycerol and increase the efficiency of GC-MS detection, high % mass solutes were focussed upon. Both neat ethylene glycol and glycerol samples were irradiated across the absorbed dose range. Samples of various high solute %, aqueous glycerol mixtures were also irradiated, as indicated by Table 11.

Table 11: Mass compositions of the glycerol mixtures irradiated with the indicated doses from the JSI TRIGA reactor using both operational and shutdown irradiation modes.

Mixture Name	**Mixture Components, wt.%**			**Mixture Density, g cm^{-3}**	**Absorbed Dose(s), kGy**
	Glycerol	**Acetone**	**Water**		
Binary Mix 1	70	0	30	1.169	20, 40, 50, 60, 80, 100
Binary Mix 2	63	0	37	1.126	
Binary Mix 3	50	0	50	1.115	
Ternary Mix 1	46	28	26	1.018	50
Ternary Mix 2	34	34	32	0.977	
Ternary Mix 3	26	48	26	0.928	
Neat	100	0	0	1.26	20, 40, 50, 60, 80, 100

3.4.3.5 Radiation Vessels

For a comparison between different sample vessels, 20 ml borosilicate headspace crimp-capped (BS) and polypropylene vials (PP) of the same neat organic samples were irradiated. Their leak susceptibility, visual differences and radiolytic product differences have been compared to determine the most suitable vial type for in-core, high dose rate, and high dose irradiations. All aqueous-based glycerol mixtures were irradiated in the polypropylene vials. A full list of all the organic samples used within this study is listed in Table 15 to Table 19Table 20 at the start of the results in chapter 4.2. Table 20 lists the two empty irradiated BS vials used for compression testing, compared against unirradiated BS vials.

3.5 Sample Work-up and Gas Chromatography-Mass Spectrometry Analysis at Lancaster, UK.

Organic samples were prepped at Lancaster, UK and sent via DPD express to the reactor facility at the Jožef Stefan Institute. Irradiated organic samples were stored in a temperature-controlled freezer at -18°C until transport back to the UK. The samples (including unirradiated controls) were shipped with dry ice via DPD express back to Lancaster, UK for analysis. On arrival, the samples were then immediately placed back into another -18 °C freezer and taken out for analysis when required. Chemical analysis of the samples was conducted using a Shimadzu TQ-8040 NX GC-MS at a maximum of 40 days after their initial irradiations. To limit volatile losses via sample work-up methodology, several different sampling and sample work-up techniques were explored during this stage: i) direct headspace GC sampling of the irradiated, 20 ml borosilicate sample vials, and ii) external solvent dilution with liquid GC sampling.

3.5.1 Dilution Method

For reproducible direct liquid sampling, the irradiated samples were diluted in a polar solvent of ethanol, with a mass ratio of ≈15:1 (or ≈0.25 g in a 5 ml volumetric flask). This was done to reduce the viscosity of neat ethylene glycol (0.016 mPa s) and glycerol (1.412 Pa s) at ambient temperatures, which had several desired effects for GC analysis: i) decreased degradation of the stationary phase of the GC column and, ii) reliable, consistent volume injection due to less viscosity-induced bubbles of the sample within the injection needle caused by the sample matrix. Propan-1-ol was also used as a solvent to confirm the synthesis of acetone from neat glycerol samples.

Due to the relatively high viscosity of glycerol, the first extraction of the irradiated glycerol samples was done gravimetrically (rather than volumetrically). The extracted irradiated sample was then diluted volumetrically with ethanol in 5 ml volumetric flasks. A known mass of the diluted internal standard stock (2-butanol) was added to each flask.

3.5.2 Gas Chromatography Methodology

Samples were analysed using a Shimadzu TQ-8040 gas chromatography-mass spectrometry (GC-MS) equipped with an AOC 6000 autosampler, as shown in Figure 18. Shimadzu’s LabSolutions GC-MS software (version 4.45) was utilized for data capture, analyte confirmation using analytical standards, and further quantification analysis. The same software was used as an interface for comparisons between the measured mass-charge fragmentation patterns and the NIST 11 reference database. Data from a GC-MS is normally displayed as a Total Ion Chromatogram (TIC). The x-axis of the chromatogram represents the time since injection (minutes) and the y-axis is the integral of all the individual charged mass fragment peaks to result in a value for the total signal intensity (arbitrary units). If measured across the entire mass-charge fragment range, this will ideally be able to identify the small fragments of any molecule. TICs are given in the results chapters for ethylene glycol and glycerol, respectively.

3.5.2.1 Headspace (HS) Sampling

Preliminary direct headspace sampling of the irradiated borosilicate vials was conducted to attempt to quantify volatiles. This sampling used a 30m Zebron ZB-5 analytical column, an injection gas volume of 1 ml, heating agitation time of 6 mins at a temperature of 60°C. This method proved insufficient for direct sampling from reactor-irradiated BS vials due to the viscous properties of the organics and shipping method, rotating during shipping and sticking to the septa, coating the gas needle in viscous glycol during sampling, resulting in carryover for the next ~20 injections and column degradation. Additionally, headspace sampling with gas chromatography-mass spectrometry (HSGC-MS) did not present a sufficiently low detection limit and missed out on non-volatile components that could have been generated using the ^{252}Cf source or JSI reactor.

3.5.2.2 Diluted Liquid Sampling

Liquid sampling separations were performed using a 10 m column guard and a Zebron 624-Plus analytical column: with a length of 30 m × 0.25 mm i.d. and a film thickness of 1.4 μm. The fused silica Zebron Z-Guard was found to be necessary to protect the analytical column's stationary phase. All columns, fittings and GC sample vials were purchased from Phenomenex.

For liquid injections, the injector temperature was set to 300 °C and the oven program was set as follows: 40 °C (10 min.); ramp of 25°C min.$^{-1}$ to hold at 300 °C (2.6 min). Split injections were used with an injection volume of 1 μl, with a split ratio of 20:1 with a constant column flow of 1.71 ml min.$^{-1}$ during a run. The carrier gas used was helium with a purity of 99.999%. The detector and interface temperatures were set to 250 °C and 300 °C, respectively. The MS detector was set to scan at 1000 scans per second between the mass-charge ratio (m/z) range initially of 30 to 500 for identification but then a scan range of 30 to 300 for quantification.

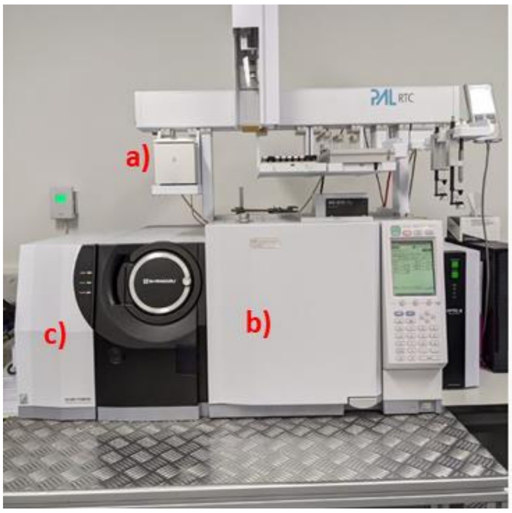

Figure 18: Shimadzu TQ-8040 triple-quadrupole GC-MS with AOC 6000 autosampler. **a** Headspace heated agitator. **b** GC oven. **c** Mass spectrometer with vacuum pump.

For accurate identifications of the radiolytic analytes, mass-fragmentation patterns of analyte peaks were firstly compared against the NIST 11 spectral database [301], giving a % similarity match to the closest matching chemical in the database. To confirm this identification labelling, analytical standards were purchased and analysed with the same GC method parameters to match against the analyte retention times and fragmentation patterns. Several criteria were used to determine the suitability of the analytes for confirmation and subsequent quantification:

1) A reliable peak shape for detection and assessment across the absorbed dose range (>20 kGy).
2) The largest peak areas which suggested large relative concentrations and superior *G*-values.
3) (>90%) MS fragmentation pattern similarity match to NIST 11 pattern database.

The analyte standards of radiolytic products from ethylene glycol and glycerol are listed in Table 12. The concentration ranges for the internal calibration curves are also given. An internal standard of 2-butanol was used in all standard and irradiated samples, with a concentration of ≈34 ± 2 μg ml^{-1} inside the samples.

Table 12: Analyte standard concentrations for the calibration curve range. Full examples of the calibration curves are given in Figure A6 and Figure A7.

Feedstock	**Analyte Standard**	**Calibration Curve Concentration Range**	
		Low / µg ml^{-1}	**High / µg ml^{-1}**
Ethylene Glycol	Acetaldehyde	44.1	964.3
	Methanol	15.8	488.3
	Ethyl Acetate	10.3	226.2
Glycerol	Acetaldehyde	0.99	117.75
	Methanol	4.47	536.78
	Glyceraldehyde Dimer	0.4	48.58
	Acetol	3.23	387.09
	Solketal	2.87	344.43

The calibration curves for each analyte were generated using Shimadzu's LabSolutions software [302], with examples listed in Appendix A, Figure A6 and Figure A7. The following concentrations of analytes in the diluted samples (in µg ml^{-1}) were also determined using the software, giving root mean square % (RMS%'s) errors for all concentrations. Due to vacuum pressure shifts and MS sensitively drift with possible MS quadrupole saturations during analysis, MS detector calibrations were repeated regularly.

3.6 Radiation Chemical Yield (*G*-value) and Mass Productivity Calculations

For the determination of radiation chemical yields (*G*-values) in the irradiated sample in SI units µmol J^{-1}, as specified by equation (44) in chapter 2.12.1, the following calculation method was conducted using the diluted analyte concentration data as measured via the GC-MS technique. However, several gravimetric and volumetric sample preparation steps were necessary due to the high viscosities of both neat ethylene glycol and glycerol, leading to a more complicated dilution process than routine volumetric dilution methods. Figure 19 shows the various components and quantities used in the method. For the calculation of mass productivity equation (46), the same calculation steps need to be followed to determine the total mass of the analyte ($Mass_{A,V1}$).

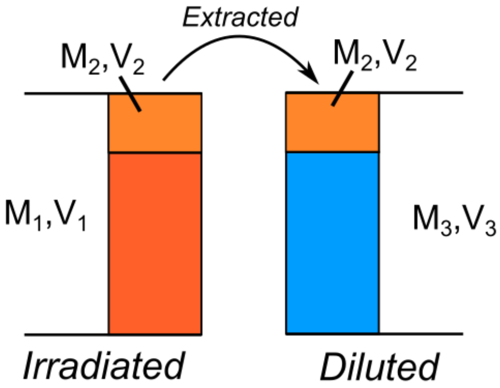

Figure 19: A schematic diagram of the sample work-up quantities for irradiated viscous samples. M, Mass and V, Volume. Subscripts defining the volume or mass partition of the: **1** total irradiated sample, **2** extracted irradiated sample, and **3** the diluted sample.

Referring to Figure 19, the concentration of analyte A in the irradiated extracted sample, $Conc_{A,V2}$ is calculated using the following equation,

$$Conc_{A,V2} = Conc_{A,V3} \times D_R \tag{54}$$

where $Conc_{A,V3}$ is the measured concentration in the diluted sample (in µg ml^{-1}) and D_R is the dilution ratio, as per,

$$D_R = \frac{V_3}{V_2} \text{ and } V_2 = \frac{M_2}{\rho_{av.irrad}} \qquad \text{(55) and (56)}$$

Where V_3 is the volume of the volumetric flask in ml, V_2 and M_2 are the extracted irradiated sample's volume and mass, respectively, and $\rho_{av.irrad}$ is the density of the irradiated sample in g ml^{-1}. As the concentration of the analyte in V_2 would be equivalent to the concentration in V_1, the following equation was used for the calculation of analyte mass within the whole irradiated sample,

$$Mass_{A,V1} = Conc_{A,V2} \times V_1 \tag{57}$$

Where $Mass_{A,V1}$ is the mass of analyte, A, in the whole irradiated sample (in µg) and $V_1 = M_1/\rho_{av,irrad,}$ for the sample. Using the quantity for analyte mass, the mass productivity can then be calculated as defined by equation (46).

The moles of the analyte, A generated in the irradiated sample can be calculated via the following equation:

$$Moles_{A,V1} = Mass_{A,V1}/\ Mr_A \tag{58}$$

Where $Moles_{A,V1}$ is the moles of analyte A in the irradiated sample (in µmol) and Mr_A is the molecular mass of analyte, A. This quantity for moles of the analyte can be used for the calculation of % molar yield as previously given by equation (45).

The radiation chemical yield (G-value) than then be calculated for the analyte in the irradiated mixture using the following equation,

$$G - value_{A,V1} = \frac{Moles_{A,V1}}{Energy\ into\ the\ Sample} \tag{59}$$

Where G-value is in units µmol J^{-1} with the energy into the sample calculated by dividing the specific absorbed dose in J kg^{-1} by the starting mass of the irradiated organic sample in kg.

3.7 Modelling, Economic and Feasibility

To examine the scale-up potential and feasibility of the radiolytic production of acetol or solketal with existing nuclear fission facilities, several particle transport simulations have been performed with the Monte Carlo N-Particle transport code (MCNP) to determine γ-ray dose rates on a specified volume of organics for a variety of production scenarios. The MCNP methodology has been validated on benchmark experiments in the field of reactor physics, radiation shielding, particle accelerators, medical applications, etc. For these simulations, MCNP version 6.1.1 was used on one node of a modern computer cluster with 40 cores/80 threads (Intel Xeon Gold 6148). Construction of the specific MCNP radiolysis models for the determination of dose rates and reaction volumes was kindly conducted by Bor. K. at JSI. MCNP models were utilized for the following production capacity scenarios:

1) 250 kW JSI TRIGA fission reactor mark II model (with in-core loop).
2) Typical PWR MCNP model (within reactor vessel loops) - (specifically for the Krško 2 GWhr Thermal/ 688 MW electrical).
3) Spent Fuel Pool (SFP) with 5 × 2 matrix of spent fuel elements within storage cells.

The MCNP code for the JSI TRIGA model utilized existing accurate models [196, 199, 293]. Figure 20a shows the top view of the JSI reactor core, Figure 20b shows the top view of the MCNP model for the JSI reactor and Figure 20c shows the schematic view of the JSI reactor with all core and carousel positions. The organic carrying pipe (volume = 157 cm^3) for this model was situated through the core Triangular Channel (TriC).

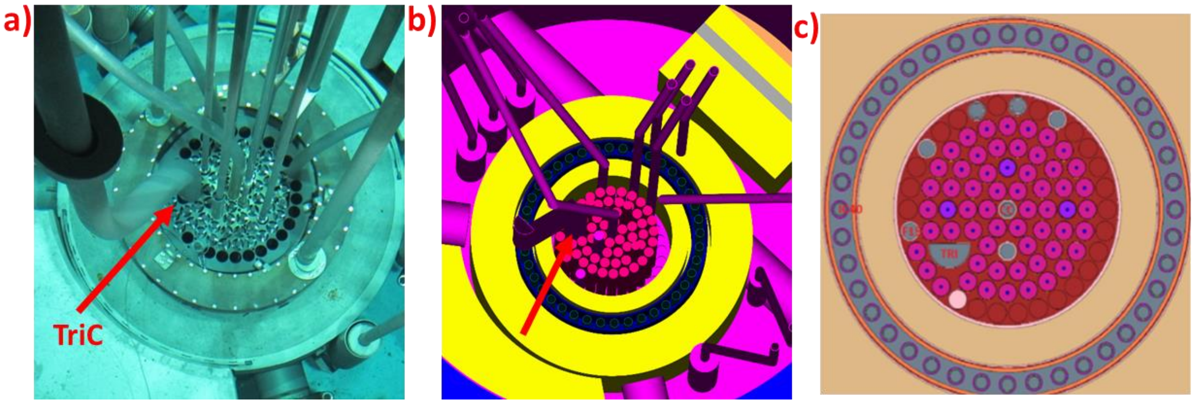

Figure 20: **250 kW TRIGA reactor and MCNP model at JSI, Slovenia modified by B. Kos. a** Top view photo of the JSI pool reactor, with the red arrow showing the Triangular (TriC) channel. **b** Equivalent spatial MCNP model of the JSI reactor. **c** MCNP top-view of JSI reactor showing possible radiation positions. Images kindly provided by B. Kos.

Figure 21a and b show some 3D perspectives of the MCNP model of the Krško NPP reactor in Slovenia with organic carrying vertical pipes. Figure 21c shows the vertical cross-section of the MCNP model, showing subsections for the organic-carrying pipes.

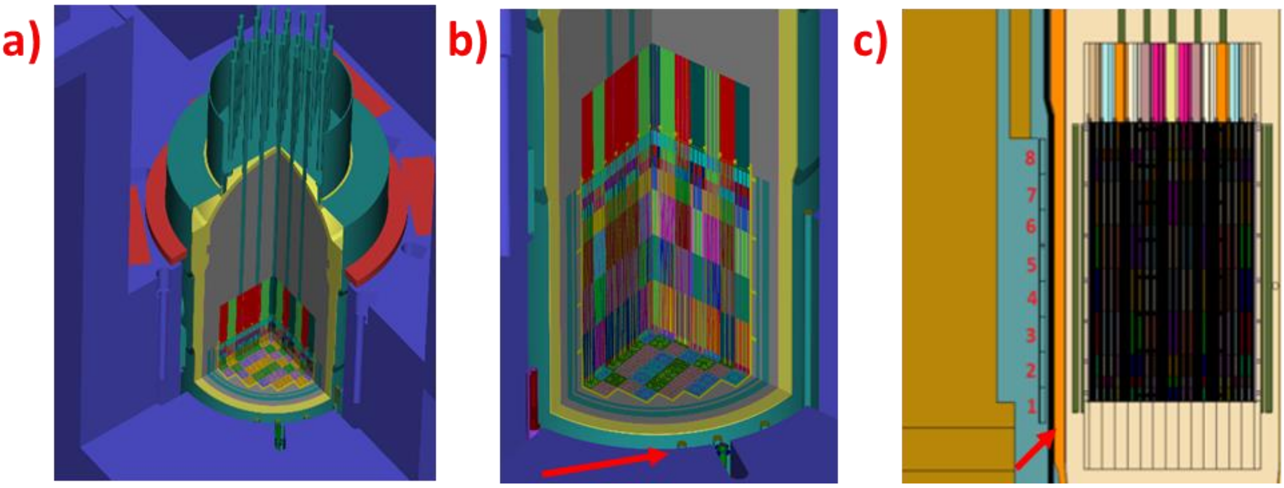

Figure 21: **Spatial Images of the Krško PWR MCNP model, modified by B. Kos.** The red arrow indicates the organic-carrying pipes (totalling 50) within the steel reactor containment vessel, travelling the vertical dimension of the containment vessel. **a** and **b** segmented cross-sections of the reactor with the red arrow indicating an organic-carrying pipe. **c** vertical cross-section showing sections for organic-carrying pipes.

These pipes were positioned in the model in the reactor cavity between the pressure vessel and the biological shield, which could accommodate 50 pipes. A 2 mm indium (In) layer on the outside of the pipe was included to decrease the neutron flux through the stainless-steel pipe but increase the γ-ray fluence [303]. The decision to include an indium layer was informed by the data described in chapter 4.6 which suggested a higher *G*-value preference using low-LET irradiations (for acetol and solketal). Here, the neutrons interact with indium via the following neutron capture reaction: $^{115}\mathrm{In}\,(n, \gamma)^{116}\mathrm{In}$. This neutron capture reaction emits a prompt γ-ray with one of 42 possible discrete energies [303]. Each 4.8 cm diameter, 4 m height pipe was segmented into eight 50 cm vertical sections for dose-rate determination along the reactor core's vertical y-axis. The total dose rate for the entire length of the organic-carrying pipes was calculated using simulations for the case of an operational reactor emitting a mixed neutron and γ-ray field.

Figure 22 details the 5 × 2 spent fuel rod matrix MCNP model (developed by Bor Kos) where a and b show the horizontal and vertical cross-sections of a spent fuel element. Figure 22c provides the dimensions of the 5 × 2 matrix fuel model with an organic pipe depicted passing between the rows. Figure 22d shows an isometric view of the model highlighting the organic-carrying pipe.

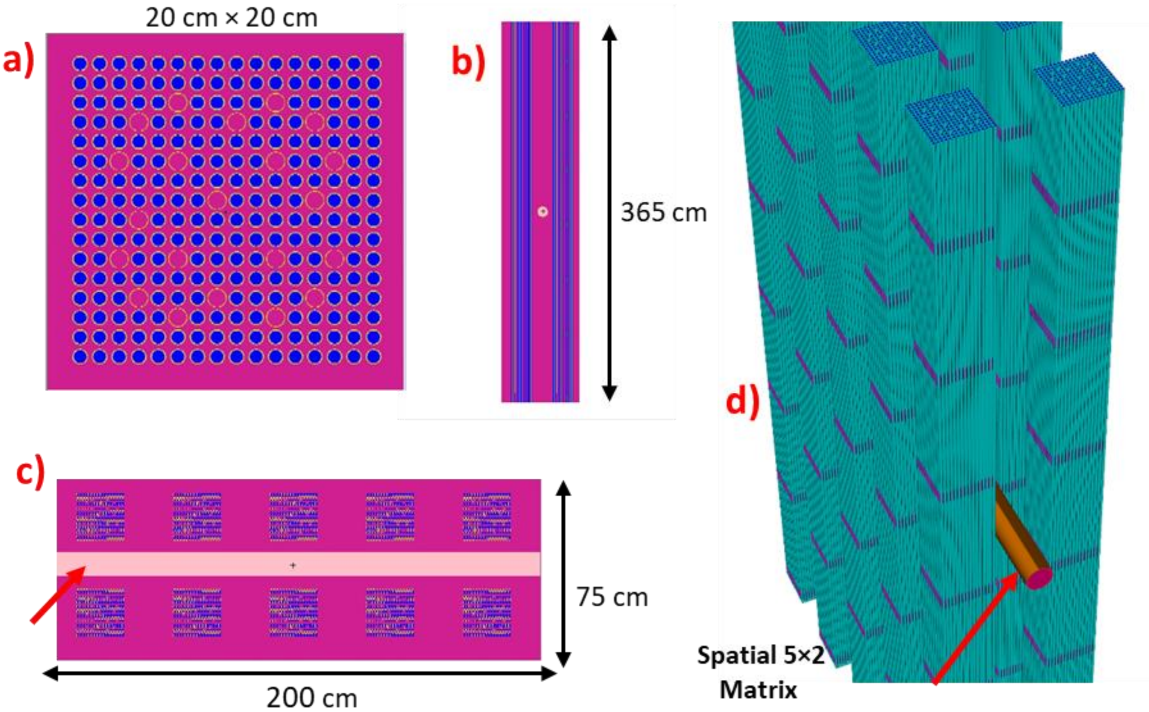

Figure 22: Krško Spent Fuel Pool (SFP) 5 × 2 model developed by Bor Kos. a and **b** spent fuel element cross-section: blue circles= Ur fuel rods, purple circles = absorbing rods. **c** Top-view of the MCNP Model expansion to a 5 × 2 matrix. **d** Isometric Spatial MCNP Spent Fuel Pool (SFP) facility model with a 5 × 2 grid of spent fuel elements. Orange pipe and red arrows indicate the organic-liquid carrying pipes.

Figure 23 shows the expansion of the 5 × 2 model to a potential ~1710 elements as per the approximate maximum capacity of the spent fuel pool based at Krško SFP [304]. This expansion included 10 organic pipes in the *z*-axis between two rows of elements, assuming an equivalent dose rate for all pipes. The 10 organic carrying pipes are then extended along the *x*-axis for a 30 × 2 matrix of fuel elements, then extended in the *y*-axis for 57 rows of elements with organic-carrying pipes between every row of elements for maximum volume.

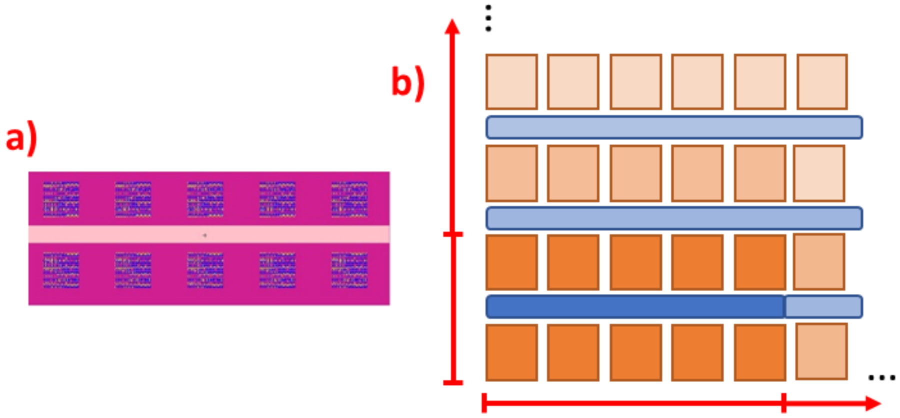

Figure 23: Scaling up of the 5 × 2 fuel element SFP model by Plant A. G. a 5 × 2 matrix model **b** extrapolation to a 30 × 57 matrix of fuel elements with 10 organic-carrying pipes (blue) in between each row of elements, giving a total of 560 pipes. Spent fuel elements are described by the squares with the pipes

The γ-ray dose rate, maximum organic volume for irradiation and the radiolytic product masses for glycerol-related mixtures was then calculated for each model, giving a value for maximum production capacity per year.

3.7.1 Scaling Up for a European Production Network

To assess the scale-up production capacity potential corresponding to all possible nuclear facilities within Europe. The data obtained from the Krško SFP model (described in chapter 4.7) were extrapolated to comparable facilities within continental Europe, totalling 180 operating nuclear reactors [305], as shown by country in Figure **24**. These 180 EU-based NPPs correspond to a net electrical capacity of 159.4 GW(e). The total organic product mass was calculated to assess the throughput and real-world impact of such an extended network, extrapolating from the spent fuel pool facility connected to the 688 MW(e) Krško (NEK) reactor. This assumes that other NPPs throughout Europe have comparable SFP facilities to Krško and that the spent fuel produced is proportional to their net electrical capacity. For radiolytically-produced solketal and its application as a petroleum fuel additive, the maximum capacity volume of petroleum-solketal fuel blends from the proposed Europe network was calculated (section 4.8). The radiation-directed production of solketal using the possible 180 equivalent SPFs was evaluated against the total volume of transport petrol consumed per year in the EU (section 5.7). The radiochemical production of solketal from glycerol was also compared against other proposed radiation-chemical systems that are quoted in the literature as candidates for industrial implementation.

Figure 24: The locations of the 180 operational nuclear reactors within continental Europe by country. The number of operational reactors in each country was obtained from [305], Last accessed 11/03/21]. The area of each circle is proportional to the number of reactors in each case. Grey indicates countries outside geographical Europe and black indicates countries within Europe with no commercial nuclear capacity. Base map altered from ©MapRoom, modified by Plant A. G., Table A20 lists the reactor numbers by country with their respective total electrical capacity.

4 Results

This chapter presents the data from the irradiation experiments described in the preceding methods chapter, for the range of ethylene glycol samples and glycerol samples and radiation conditions. *G*-values and mass productivities are detailed for each chosen radiolytic analyte as well as data for sample radioactivity and vial compression results. Later sections detail the results from the production capacity calculations for each radiation facility scenario. The most effective scenario has been expanded to a theoretical production network within similar facilities within Europe and the impact of radiolytic biofuel additive production has been projected.

4.1 Research with Californium-252

The following table lists the samples irradiated using the ^{252}Cf source for a semi-continuous 25 days of irradiation.

Table 13: Organic sample list for Cf^{252} irradiations for samples shown in Figure 15.

Sample Number	Neat Organic Sample	Vessel	Estimated Dose / Gy	Dose Rate / mGy hr^{-1}
1	Ethylene Glycol	20ml BS Vial with Al/Silicone Septa	0.038	0.044
2	Ethylene Glycol	20ml BS Vial with Al/Silicone Septa	0.038	0.044
3	Ethylene Glycol	20ml BS Vial with PTFE/Silicone Septa	0.038	0.044
4	Glycerol	20ml BS Vial with Al/Silicone Septa	0.038	0.044
5	Glycerol	20ml BS Vial with Al/Silicone Septa	0.038	0.044
6	Glycerol	20ml BS Vial with PTFE/Silicone Septa	0.038	0.044
7	Ethylene Glycol	1L Plastic Bottle	0.038	0.044
8	Glycerol	1L Plastic Bottle	0.038	0.044

After 25 days of semi-continuous exposure to the ^{252}Cf source, routine full-range ion scanning via headspace GC-MS sampling (described in section 3.5.2.1) showed was unable to detect any unique radiolytic products from neat ethylene glycol. Due to different analytes fragmenting differently, they exhibit different detection limits. Extrapolating from existing radiolytic *G*-value data for ethylene glycol [244], it was hypothesised that an estimated concentration of ~0.05 ppm of acetaldehyde could have been generated. This assumed an estimated absorbed dose of 0.038 Gy (as per chapter 3.4.2.1) with the synthesised mass of acetaldehyde not escaping from the sample, despite being extremely volatile. Likewise, extrapolating from existing radiolytic *G*-value data for glycerol [3], a hypothetical acetol concentration of ~0.6 ppb was anticipated within the irradiated glycerol sample. Both these extrapolations assume similar *G*-value responses for neat samples than for the diluted samples in the literature. Both these calculations used equation (59) to determine the moles produced, used literature *G*-values of 18.13 μmol J^{-1} and 0.23 μmol J^{-1} for acetaldehyde and acetol [3, 244], and assumed 0.037 J of energy into a 1 kg sample. The remaining calculations used the molecular masses of each respective analyte to determine the mass (i.e. $Mass{=}Mr{\times}Moles$). Mass of 50 μg and 0.64 μg was estimated for acetaldehyde and acetol, respectively with the concentration in ppm calculated as a mass ratio against the 1 kg bulk sample as per the following equation:

$$Conc, ppm = \frac{mass\ of\ analyte, g}{mass\ of\ bulk\ sample, g} \times 10^6 \qquad (60)$$

Additionally, GC headspace analysis of neat ethylene glycol samples spiked with ~100 ppm of acetone showed a small acetone peak compared with the TIC baseline (as per Appendix A, Figure A8), suggesting a relatively high limit of quantitation (LOQ) and corresponding limit of detection (LOD) for HS analysis of similar volatile carbonyls. For acetone, the limit of quantitation and detection was estimated to be ~80 ppm and ~20 ppm, respectively based on the signal-to-noise ratio. In chromatography, the LOD and LOQ have typically been estimated as 3:1 and 10:1 signal-to-noise (S/N) ratios, respectively where the noise is measured from the normal baseline variation [306].

The LOD can be improved via running the GC in selective ion monitoring (SIM) mode, however, for the detection of any new or previously undetected compounds, the MS detector needs to be run across a large m/z range to detect all available possible fragments. Therefore, limiting the method's capabilities for discovering new radiolytic products. Consequently, the flux from the ^{252}Cf source was deemed too low for future experimental considerations due to the limited achievable dose rates.

Figure 25 shows the TIC of a headspace-sampled, Cf-irradiated ethylene glycol sample (sample 1) for a ~0.038 Gy dose and a dose rate of ~0.044 mGy hr^{-1}, compared against an unirradiated organic sample and solvent blank. This figure shows no new detectable analytes compared to the irradiated sample and the unirradiated control.

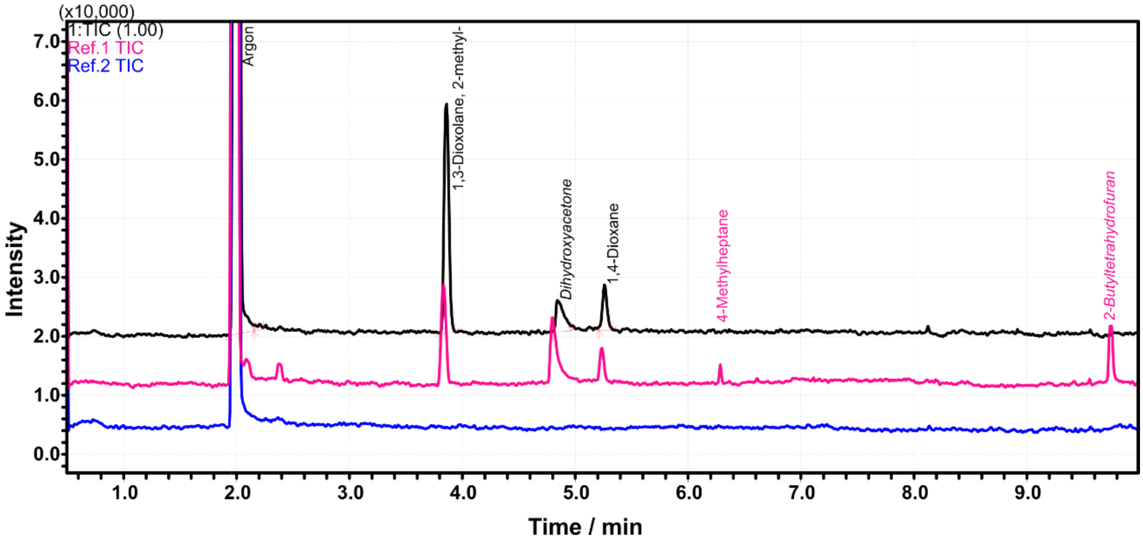

Figure 25: Total ion chromatogram (TIC) of the ^{252}Cf-irradiated, ~25-day semi-continuous exposure, ~0.037 Gy ethylene glycol sample 1 (black) using the headspace sampling method. No new detectable analytes between the unirradiated sample (pink) and blank (blue).

There initially appears to be a relative reduction in height of several existing analytes peaks compared with the unirradiated sample. This reduction could be explained by two reasons: the loss of volatiles from the poor vial crimp seal over >25 days during the summer months (the ^{252}Cf source was not within a temperature-controlled room) or decomposition due to radiation effects. For 1,3-dioxolane, 2-methyl specifically, it has a boiling point of 83°C and a vapour pressure of 42 mmHg at 20°C [307]. Compared with ethanol which has a vapour pressure of 60 mmHg at 25°C [308], this shows that dioxolanes are reasonably volatile and losses during irradiation are quite possible. However, as shown by Table 14, the data indicates a relative increase in peak area for both dioxolanes (as opposed to a reduction in peak area), when normalized to dihydroxyacetone which has a vapour pressure of 0.02 mmHg [309]. Therefore, the relative increases of the dioxolanes are thought to be due to either i) the low-dose radiolytic formation reaction of the dioxolanes or ii) over extended periods at ambient temperatures, the formation of ether bonds is more thermodynamically stable than the free hydroxyl groups of ethylene glycol. The disappearance of methylheptane and butyltetrahydrofuran in the irradiated samples could be explained by either i) a low-dose radiolytic decomposition effect or, ii) analyte loss to vial leaks of the volatiles (vapour pressures listed in Table 14).

Table 14: Peak identification and vapour pressure of impurities within ethylene glycol.

Analyte	**Peak Time / minutes**	**% Similarity**	**Relative increase in peak area normalized to dihydroxyacetone.**	**Vapour Pressure / mmHg @ 25°C**	**Vapour pressure ratio relative to dihydroxyacetone**
1,3-dioxolane, 2-methyl	3.9	97	4.64	42 @ 20 °C [307]	2100
Dihydroxyacetone	4.8	85	1	0.02 [309]	1
1,4-Dioxolane	5.2	98	1.45	38.1 [310]	1905
4-Methylheptane	6.3	95	NA	39.8 @ 37°C [311]	1990
2-Butyltetrahydrofuran (90%)	9.8	90	NA	3.36 [312]	168

While there arguably could be a low-dose radiolytic effect for dioxolane formation, there was a lack of synthesis of any other expected radiolytic products compared to the unirradiated sample that are quoted in literature (acetaldehyde, formaldehyde etc.) via the HSGC-MS method. Samples 2, 3 and 7 of neat ethylene glycol showed little variation to the TIC shown in Figure 25. Even though dihydroxyacetone has been previously reported as a radiolysis product with *G*-values of ~0.016 µmol J^{-1} [3], there is no expected increase in the relative peak sizes (therefore concentration) compared with the dioxolane peaks which are not reported in radiolysis literature. This suggests that any radiation effect from the ^{252}Cf source to produce radiolytic products is negligible. Similarly, HSGC-MS analysis of samples 4, 5, 6 and 7 of ^{252}Cf-irradiated neat glycerol showed no new analyte peaks which would correspond to radiolytic peaks, as shown by example Figure A9 for sample 4, in appendix A. While several existing peaks are missing from the irradiated sample, this is thought also be from volatile losses from the vials over the extended periods of irradiation. Since the single ~0.038 Gy exposures took over 25 semi-continuous days (600 hours) to complete, these long experimental times and low doses were considered unfeasible for a large study on neutronic radiolytic effects.

4.2 JSI 250 kW Reactor

Based on the lack of dose achievable using the ^{252}Cf source, most of the radiolytic empirical data has been obtained with the use of the JSI reactor as the radiation source. The list of organic samples irradiated at the JSI reactor in the TriC position and their associated parameters with ethylene glycol, glycerol, or glycerol-related mixtures are detailed in the following Table 15, Table 16, Table 17, and Table 18. INAA samples are listed in Table 19 and empty vials for compression analysis are listed in Table 20.

The concentration of radiolytically produced analytes has been listed in Appendix A, chapter 8.2.1 with Table A4, Table A5, Table A6, Table A7, Table A8, Table A9, and Table A10. Furthermore, the full radiolytic *G*-value data from these samples are provided in Appendix A, chapter 8.2.2 with Table A11, Table A12, Table A13, Table A14, Table A15, Table A16, and Table A17.

Table 15: List of samples irradiated with neutrons + γ rays from the JSI reactor (in the TriC): containing either neat glycerol, neat ethylene glycol or binary aqueous glycerol mixtures in **PP vials**. Aqueous binary mixtures glycerol wt.%: Mix. 1: 63% Mix. 2: 50% Mix. 3: 70%.

Sample Number	**Organic Sample**	**Absorbed Dose / kGy**	**Dose Type**	**Reactor Power / kW**	**Dose Rate / Gy min^{-1}**	**Vial Type**	**Mass of Organics / g**	**Total Mass before irradiation / g**	**Total mass after irradiation / g**	**% Mass Change related to organic mass**	**Notes**
9	Neat Glycerol	20	Neutron + γ	50	1630	PP	1.258	5.442	5.443	0.040	
10	Neat Glycerol	40	Neutron + γ	100	3270	PP	1.325	5.487	5.487	-0.023	
11	Neat Glycerol	50	Neutron + γ	100	3270	PP	1.254	5.412	5.413	0.048	
12	Neat Glycerol	60	Neutron + γ	200	6530	PP	1.367	5.507	5.502	-0.358	
13	Neat Glycerol	80	Neutron + γ	200	6530	PP	1.346	5.495	5.492	-0.193	
14	Neat Glycerol	100	Neutron + γ	200	6530	PP	1.152	5.336	5.285	-4.392	
15	Binary Glycerol Mixture 1	20	Neutron + γ	50	1630	PP	1.2879	5.2244	5.485	20.242	Slightly melted next to vial 17
16	Binary Glycerol Mixture 1	40	Neutron + γ	100	3270	PP	1.124	5.306	5.307	0.098	
17	Binary Glycerol Mixture 1	50	Neutron + γ	100	3270	PP	1.0718	5.4841	5.226	-24.100	Slightly melted next to vial 15
18	Binary Glycerol Mixture 1	60	Neutron + γ	200	6530	PP	1.1688	5.3224	5.269	-4.543	
19	Binary Glycerol Mixture 1	80	Neutron + γ	200	6530	PP	1.225	5.3774	5.350	-2.212	
20	Binary Glycerol Mixture 1	100	Neutron + γ	200	6530	PP	1.2937	5.4633	NA	NA	Slightly melted with vial 26
21	Binary Glycerol Mixture 2	20	Neutron + γ	50	1630	PP	1.1128	5.306	5.308	0.144	
22	Binary Glycerol Mixture 2	40	Neutron + γ	100	3270	PP	1.2719	5.4514	5.454	0.173	
23	Binary Glycerol Mixture 2	50	Neutron + γ	100	3270	PP	1.2488	5.3815	5.384	0.224	
24	Binary Glycerol Mixture 2	60	Neutron + γ	200	6530	PP	1.1767	5.3601	5.361	0.085	
25	Binary Glycerol Mixture 2	80	Neutron + γ	200	6530	PP	1.1613	5.3668	5.367	0.043	

Table 15: (Continued).

26	Binary Glycerol Mixture 2	100	Neutron + γ	200	6530	PP	1.2705	5.423	NA	NA	Slightly melted with vial 20
27	Binary Glycerol Mixture 3	20	Neutron + γ	50	1630	PP	NA	5.3272	5.329	NA	
28	Binary Glycerol Mixture 3	40	Neutron + γ	100	3270	PP	1.1047	5.2532	5.254	0.063	
29	Binary Glycerol Mixture 3	50	Neutron + γ	100	3270	PP	0.9931	5.1435	5.146	0.282	
30	Binary Glycerol Mixture 3	60	Neutron + γ	200	6530	PP	1.0957	5.2589	5.260	0.091	
31	Binary Glycerol Mixture 3	80	Neutron + γ	200	6530	PP	1.0217	5.1841	5.183	-0.098	
32	Binary Glycerol Mixture 3	100	Neutron + γ	200	6530	PP	1.1675	5.3374	5.256	-6.981	
33	Neat Ethylene Glycol	20	Neutron + γ	50	1630	PP	1.054	5.207	5.212	0.446	
34	Neat Ethylene Glycol	40	Neutron + γ	100	3270	PP	1.013	5.171	5.172	0.128	
35	Neat Ethylene Glycol	50	Neutron + γ	100	3270	PP	1.159	5.314	5.316	0.181	
36	Neat Ethylene Glycol	60	Neutron + γ	200	6530	PP	1.167	5.318	5.310	-0.677	
37	Neat Ethylene Glycol	80	Neutron + γ	200	6530	PP	1.093	5.255	5.265	0.878	
38	Neat Ethylene Glycol	100	Neutron + γ	200	6530	PP	1.111	5.307	NA	NA	
39	Neat Glycerol	50	Neutron + γ	100	3270	PP	1.355	5.564	5.564	0.007	
40	Neat Glycerol	50	Neutron + γ	250	8170	PP	0.992	5.207	5.208	0.141	
41	Neat Glycerol	50	Neutron + γ	40	1310	PP	0.96	5.106	NA	NA	
42	Neat Glycerol	50	Neutron + γ	16	520	PP	1.188	5.372	5.369	-0.278	
43	Neat Ethylene Glycol	50	Neutron + γ	100	3270	PP	1.027	5.198	5.198	-0.010	
44	Neat Ethylene Glycol	50	Neutron + γ	16	520	PP	1.059	5.212	5.213	0.076	
45	Neat Ethylene Glycol	50	Neutron + γ	40	1310	PP	1.168	5.36	5.362	0.205	
46	Neat Ethylene Glycol	50	Neutron + γ	250	8170	PP	1.188	5.373	5.375	0.202	

Table 16: List of samples irradiated with γ rays only from the JSI reactor (in the TriC) containing either: neat glycerol, neat ethylene glycol or binary glycerol mixtures in **PP vials**. Unirradiated control samples are also listed. Aqueous binary mixtures glycerol wt. %: Mix. 1: 63% Mix. 2: 50% Mix. 3: 70%.

Sample Number	**Organic Sample**	**Absorbed Dose / kGy**	**Dose Type**	**Reactor Power / kW**	**Dose Rate / Gy min^{-1}**	**Vial Type**	**Mass of Organics / g**	**Total Mass before irradiation / g**	**Total mass after irradiation / g**	**Mass % Change related to organic mass**	**Notes**
47	Neat Glycerol	20	γ - ray	<1	17.92	PP	1.151	5.311	5.317	0.478	
48	Neat Glycerol	40	γ - ray	<1	15.87	PP	1.261	5.443	5.444	0.111	
49	Neat Glycerol	50	γ - ray	<1	26.21	PP	1.106	5.253	5.218	-3.210	Loose Cap
50	Neat Glycerol	60	γ - ray	<1	27.47	PP	1.106	5.256	5.257	0.090	
51	Neat Glycerol	80	γ - ray	<1	40.53	PP	1.24	5.425	5.426	0.081	
52	Neat Glycerol	100	γ - ray	<1	39.59	PP	1.192	5.372	5.376	0.361	
53	Binary Glycerol Mixture 1	20	γ - ray	<1	17.92	PP	1.2989	5.4705	5.473	0.185	
54	Binary Glycerol Mixture 1	40	γ - ray	<1	15.87	PP	1.3268	5.5101	5.519	0.656	
55	Binary Glycerol Mixture 1	50	γ - ray	<1	26.21	PP	1.1596	5.3364	5.340	0.293	
56	Binary Glycerol Mixture 1	60	γ - ray	<1	27.47	PP	1.1375	5.2879	5.292	0.396	
57	Binary Glycerol Mixture 1	80	γ - ray	<1	40.53	PP	1.3283	5.4876	5.492	0.354	
58	Binary Glycerol Mixture 1	100	γ - ray	<1	39.59	PP	1.2646	5.4158	5.420	0.300	
59	Binary Glycerol Mixture 2	20	γ - ray	<1	17.92	PP	1.2222	5.4081	5.411	0.196	
60	Binary Glycerol Mixture 2	40	γ - ray	<1	15.87	PP	1.2715	5.4401	5.450	0.771	
61	Binary Glycerol Mixture 2	50	γ - ray	<1	26.21	PP	1.1975	5.3697	5.371	0.121	
62	Binary Glycerol Mixture 2	60	γ - ray	<1	27.47	PP	1.1704	5.3567	5.359	0.214	
63	Binary Glycerol Mixture 2	80	γ - ray	<1	40.53	PP	1.2781	5.4535	5.459	0.462	
64	Binary Glycerol Mixture 2	100	γ - ray	<1	39.59	PP	1.0512	5.2323	5.236	0.342	
65	Binary Glycerol Mixture 3	20	γ - ray	<1	17.92	PP	0.9431	5.1039	5.106	0.223	
66	Binary Glycerol Mixture 3	40	γ - ray	<1	15.87	PP	1.045	5.2203	5.231	0.976	
67	Binary Glycerol Mixture 3	50	γ - ray	<1	26.21	PP	1.1888	5.3786	5.381	0.227	
68	Binary Glycerol Mixture 3	60	γ - ray	<1	27.47	PP	1.0551	5.2718	5.276	0.398	

Table 16: (Continued).

69	Binary Glycerol Mixture 3	80	γ - ray	<1	40.53	PP	1.2332	5.4101	5.415	0.357
70	Binary Glycerol Mixture 3	100	γ - ray	<1	39.59	PP	1.3634	5.5264	5.531	0.315
71	Neat Ethylene Glycol	20	γ - ray	<1	17.92	PP	1.228	5.378	5.379	0.090
72	Neat Ethylene Glycol	40	γ - ray	<1	15.87	PP	1.032	5.203	5.205	0.145
73	Neat Ethylene Glycol	50	γ - ray	<1	26.21	PP	0.987	5.168	5.172	0.365
74	Neat Ethylene Glycol	60	γ - ray	<1	27.47	PP	1.205	5.353	5.360	0.573
75	Neat Ethylene Glycol	80	γ - ray	<1	40.53	PP	1.08	5.273	5.295	2.009
76	Neat Ethylene Glycol	100	γ - ray	<1	39.59	PP	1.118	5.317	5.319	0.197
77	Control Neat Glycerol	0	NIL	NIL	NIL	PP	1.357	5.494	5.505	0.796
78	Control Neat Ethylene Glycol	0	NIL	NIL	NIL	PP	0.963	5.17	5.187	1.734
79	Control Binary Glycerol Mixture 1	0	NIL	NIL	NIL	PP	1.2302	5.4056	5.406	0.033
80	Control Binary Glycerol Mixture 2	0	NIL	NIL	NIL	PP	1.0515	5.1947	5.196	0.076
81	Control Binary Glycerol Mixture 3	0	NIL	NIL	NIL	PP	1.1334	5.2645	5.266	0.168

Table 17: List of organic samples irradiated with either neutron + γ – rays or γ – rays only from the JSI reactor (in the TriC) containing either neat glycerol or neat ethylene glycol within **BS vials** with Aluminium/Silicone septa.

Sample Number	**Organic Sample**	**Absorbed Dose / kGy**	**Dose Type**	**Reactor Power / kW**	**Dose Rate / Gy min^{-1}**	**Vial Type**	**Mass of Organics / g**	**Total Mass before irradiation / g**	**Total mass after irradiation / g**	**Mass % Change related to organic mass**	**Notes**
82	Neat Glycerol	20	Neutron + γ	50	1630	BS with Al/Silicone Septa	3.802	20.214	20.221	0.1762	
83	Neat Glycerol	40	Neutron + γ	100	3270	BS with Al/Silicone Septa	5.796	22.325	22.338	0.2157	
84	Neat Glycerol	50	Neutron + γ	100	3270	BS with Al/Silicone Septa	6.019	22.359	22.365	0.0930	
85	Neat Glycerol	60	Neutron + γ	200	6530	BS with Al/Silicone Septa	5.73	22.218	22.227	0.1571	
86	Neat Glycerol	80	Neutron + γ	200	6530	BS with Al/Silicone Septa	5.931	22.523	22.536	0.2192	
87	Neat Glycerol	100	Neutron + γ	200	6530	BS with Al/Silicone Septa	4.709	21.326	21.346	0.4311	
88	Neat Ethylene Glycol	20	Neutron + γ	50	1630	BS with Al/Silicone Septa	4.628	21.122	20.718	-8.7252	Leak
89	Neat Ethylene Glycol	40	Neutron + γ	100	3270	BS with Al/Silicone Septa	4.909	21.474	21.278	-3.9866	Leak
90	Neat Ethylene Glycol	50	Neutron + γ	100	3270	BS with Al/Silicone Septa	5.148	21.753	21.347	-7.8943	Leak
91	Neat Ethylene Glycol	60	Neutron + γ	200	6530	BS with Al/Silicone Septa	5.232	21.767	21.241	-10.0535	Leak
92	Neat Ethylene Glycol	80	Neutron + γ	200	6530	BS with Al/Silicone Septa	4.74	21.325	21.174	-3.1962	Leak

Table 17: (Continued)

93	Neat Ethylene Glycol	100	Neutron + γ	200	6530	BS with Al/Silicone Septa	4.818	21.333	20.740	-12.3039	Leak
94	Neat Glycerol	20	γ - ray	<1	17.9	BS with Al/Silicone Septa	5.436	22.019	22.023	0.0754	
95	Neat Glycerol	40	γ - ray	<1	15.9	BS with Al/Silicone Septa	4.935	21.423	21.427	0.0892	
96	Neat Glycerol	50	γ - ray	<1	26.2	BS with Al/Silicone Septa	5.197	21.756	21.769	0.2444	
97	Neat Glycerol	60	γ - ray	<1	27.5	BS with Al/Silicone Septa	5.722	22.262	22.274	0.2097	
98	Neat Glycerol	80	γ - ray	<1	40.5	BS with Al/Silicone Septa	5.254	21.876	21.888	0.2189	
99	Neat Glycerol	100	γ - ray	<1	39.6	BS with Al/Silicone Septa	5.694	22.344	22.386	0.7376	
100	Neat Ethylene Glycol	20	γ - ray	<1	17.9	BS with Al/Silicone Septa	4.224	20.626	20.242	-9.0980	Leak
101	Neat Ethylene Glycol	40	γ - ray	<1	15.9	BS with Al/Silicone Septa	4.925	20.388	20.078	-6.2985	Leak
102	Neat Ethylene Glycol	50	γ - ray	<1	26.2	BS with Al/Silicone Septa	4.557	21.067	20.521	-11.9882	Leak
103	Neat Ethylene Glycol	60	γ - ray	<1	27.5	BS with Al/Silicone Septa	5.163	21.837	21.009	-16.0353	Leak
104	Neat Ethylene Glycol	80	γ - ray	<1	40.5	BS with Al/Silicone Septa	4.004	20.659	20.529	-3.2418	Leak
105	Neat Ethylene Glycol	100	γ - ray	<1	39.6	BS with Al/Silicone Septa	5.236	22.324	22.161	-3.1207	Leak
106	Glycerol Blank	0	NIL	NIL	NIL	BS with Al/Silicone Septa	5.823	23.024	23.033	0.1460	
107	Neat Ethylene Glycol Blank	0	NIL	NIL	NIL	BS with Al/Silicone Septa	4.9	22.088	21.556	-10.8673	*Leak*

Table 18: List of analysed organic samples irradiated with either neutron + γ rays or γ rays only from the JSI reactor (in the TriC). Organic samples are ternary glycerol: acetone: water mixtures within PP vials.

Sample Number	Organic Sample (Glycerol: Acetone: Water) wt.% ratio	Absorbed Dose / kGy	Dose Type	Reactor Power / kW	Dose Rate / Gy min^{-1}	Vial Type	Mass of Organics / g	Total Mass before irradiation / g	Total mass after irradiation / g	Mass % Change related to organic mass	Notes
108	46:28:26 mix	50	Neutron + γ	100	3270	PP	1.062	5.217	5.215	-0.169	
109	46:28:26 mix	50	γ - ray	<1	26	PP	1.230	5.382	5.366	-1.301	
110	34:34:32 mix	50	Neutron + γ	100	3270	PP	1.087	5.254	5.238	-1.389	
111	34:34:32 mix	50	γ - ray	<1	26	PP	0.917	5.086	5.084	-0.207	
112	26:48:26 mix	50	Neutron + γ	100	3270	PP	1.160	5.317	5.306	-0.897	
113	26:48:26 mix	50	γ - ray	<1	26	PP	1.036	5.206	5.202	-0.309	
114	Control 46:28:26 mix	0	NIL	NIL	NIL	PP	1.213	5.361	5.362	0.091	
115	Control 34:34:32 mix	0	NIL	NIL	NIL	PP	0.960	5.160	5.151	-0.979	
116	Control 26:48:26 mix	0	NIL	NIL	NIL	PP	0.976	5.133	5.118	-1.527	

Table 19: Organic neat samples for instrumental neutron activation analysis (INAA). These samples were irradiated in the JSI carousel facility.

Sample Number	Organic Sample	Absorbed Dose / kGy	Dose Type	Vial Type	Mass of Organics / g
117	Neat Ethylene Glycol	520	Neutron + γ	Polyethylene Ampoule	1.4
118	Neat Glycerol	520	Neutron + γ	Polyethylene Ampoule	2.4

Table 20: Axial compression sample list. Rounded or flat-bottomed, empty, unirradiated BS vials capped with either Aluminium/Silicone or PTFE/Silicone septa with crimp caps are listed. Two 100 kGy γ-ray irradiated BS vials were compressed for comparison. Vial failure forces and pressures have been included.

Group Number	Sample Number	Vial	Septa & Cap Type	Irradiation Type and Dose	Failure Force / N	Failure Pressure / N cm^{-2}
1	119	Rounded	Al/Si	-	936	1192
	120	Rounded	Al/Si	-	1018	1296
	121	Rounded	Al/Si	-	414	527
2	122	Rounded	PTFE/Si	-	824	1049
	123	Rounded	PTFE/Si	-	641	816
	124	Rounded	PTFE/Si	-	1495	1903
	125	Rounded	PTFE/Si	-	1468	1869
3	126	Rounded	PTFE/Si	100 kGy γ-ray	1524	1940
4	127	Flat	Al/Si	-	1819	438
	128	Flat	Al/Si	-	976	235
	129	Flat	Al/Si	-	1836	442
5	130	Flat	PTFE/Si	-	655	158
	131	Flat	PTFE/Si	-	533	128
	132	Flat	PTFE/Si	-	496	119
6	133	Flat	Al/Si	100 kGy γ-ray	1708	411
7	134	Rounded	NA	-	740	942
	135	Rounded	NA	-	721	918
	136	Rounded	NA	-	1083	1379
	137	Rounded	NA	-	941	1198
	138	Rounded	NA	-	1147	1460
8	139	Flat	NA	-	1415	341
	140	Flat	NA	-	2078	500
	141	Flat	NA	-	1600	385
	142	Flat	NA	-	1919	462
	143	Flat	NA	-	1959	472

4.3 Vial Appearance, Compression Testing, and Leaks

Initial observations of the sample vessels after high dose rate (>0.52 kGy min.$^{-1}$) mixed-field irradiations, confirmed that the borosilicate glass vials were discoloured to a tan colour qualitatively proportional to the absorbed dose, as shown by Figure 26a. Additionally, the polypropylene vials under mixed-field exposures showed evidence of melting when placed in contact with adjacent borosilicate vials as shown in Figure 26b, although this only occurred with a few high-dose-rate, mixed-field, high-dose irradiations.

Figure 26: Vial observations after high dose (>20 kGy) irradiations. **a** Discolouration of borosilicate vials due to increasing mixed-field absorbed dose from left to right. **b** Deformation of PP vials during high dose rate (6.54 kGy min.^{-1}) mixed-field irradiations when touching adjacent BS vials. BS crimp caps are made of steel with either a PTFE/ silicone (yellow top) or aluminium/ silicone (blue top) septa.

The melting of the polypropylene vials in contact with the BS vials suggests that the borosilicate vials are reaching a minimum of 121°C during irradiations, as per the manufacturing specifications of polypropylene vials [313]. Boron-10, being an effective thermal neutron absorber would absorb a high proportion of the thermal neutron component than the organic sample for the borosilicate vials, causing a potential difference in dose deposition and additionally may be the cause of the high temperatures observed. Boron could also lead to a discrepancy between the desired and received absorbed doses of the contained organic sample.

4.3.1 Axial Compression Analysis

Table 20 lists the empty borosilicate vials tested as to their axial strength, the type of vial (round or flat-bottomed), crimp cap type, and final failure force. Only two γ-ray 100 kGy irradiated vials were compressed to highlight any embrittlement issues with the glass. Figure 27 and Figure 28 show the axial compression of the empty, capped BS vials over time, with the rapid drop in force indicating the failure point of each vial.

a) Rounded, capped

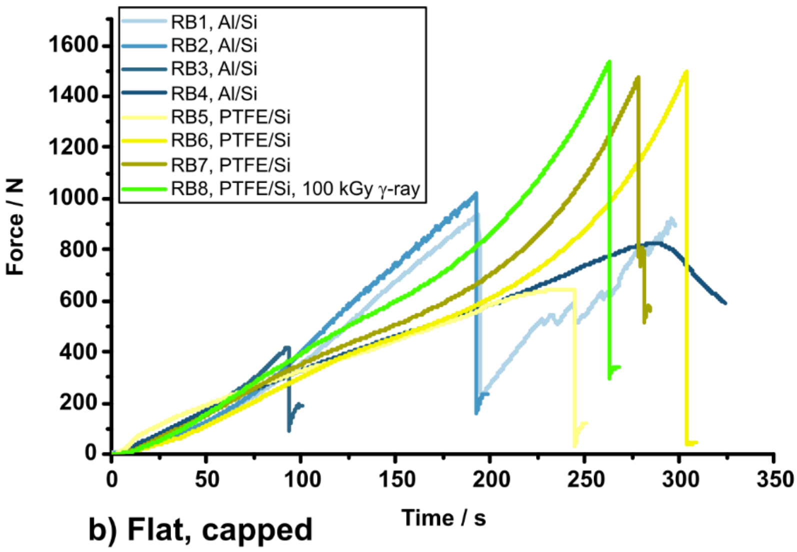

b) Flat, capped

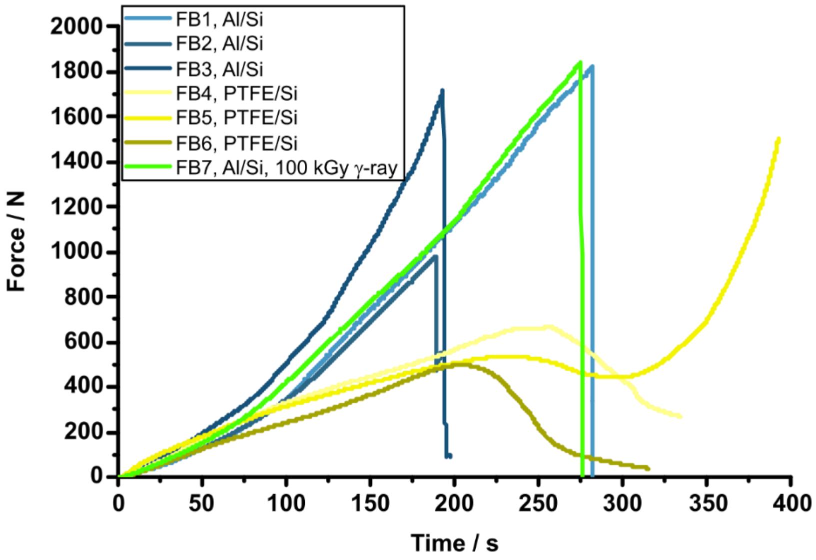

Figure 27: Axial compression force vs time plots of empty, capped **a** round-bottomed (RB) and **b** flat-bottomed headspace vials. Unirradiated BS vials are either shown with yellow (PTFE/Silicone) or blue (Aluminium/Silicone) crimp caps. In **a** and **b** the compression of two 100 kGy γ-ray irradiated vials with the corresponding caps are shown by the green plots.

As shown by Figure 27, there is a large range for the failure force (and corresponding pressures) of the unirradiated BS vials with the caps for each subgroup (vial shape and cap type). The flat-bottomed, PTFE/Si capped (yellow) plots (FB4 to 6) shown in Figure 27b show a slow gradual drop in compression force as opposed to a rapid drop as seen in the other plots. This gradual drop is characteristic of a slow deformation and is thought to be due to the gradual crushing of the crimp cap. The failure force of the capped, 100 kGy γ-ray irradiated vials appears to be within the expected failure range for unirradiated vials. The irradiated vials did seem to crumble into smaller glass shards compared with the unirradiated vials. This could signify the creation of point defects within the BS structure, contributing to the smaller crumb [314].

Due to the observed large range in failure forces with capped vials, uncapped vials were also crushed to remove the potential variable of caps from the axial compression tests. The vial-only tests will gauge a more accurate variation in the borosilicate glass failure force. However, no uncapped vials were irradiated for comparison. Figure 28a and b show the vial compression plots for **a** rounded and **b** flat-bottomed vials, respectively without any caps.

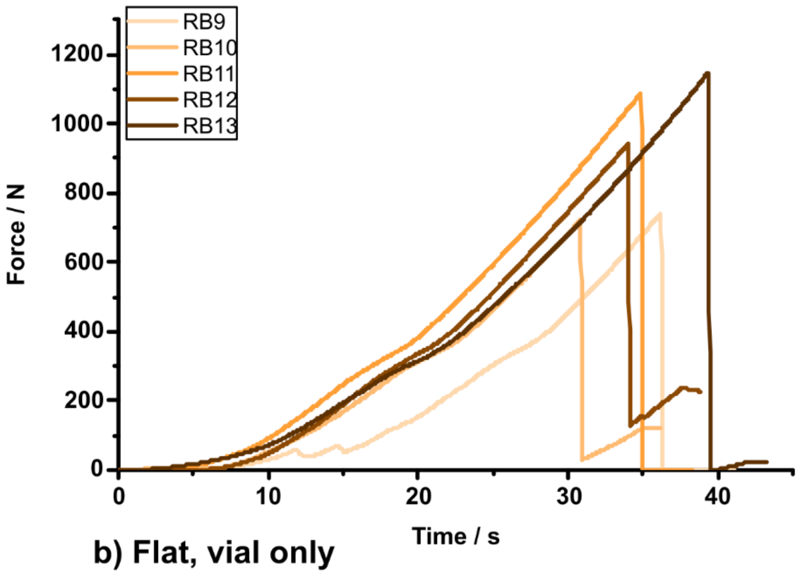

a) Rounded, vial only

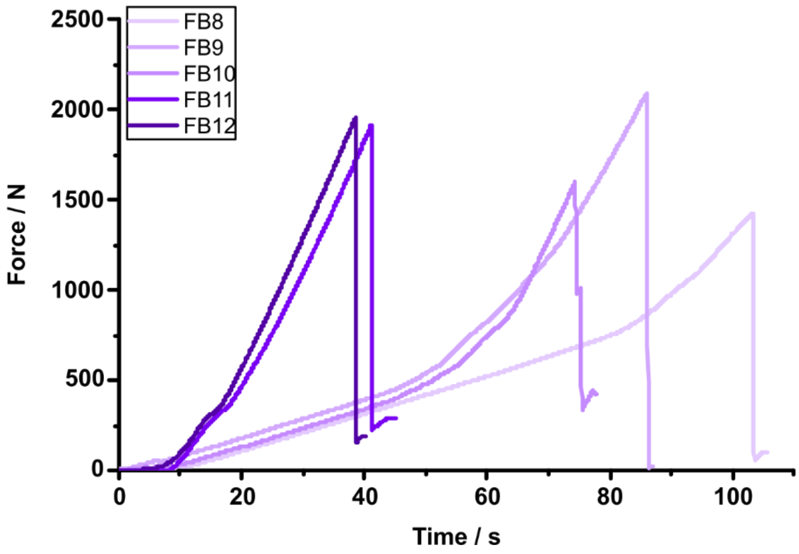

b) Flat, vial only

Figure 28: Axial compression force vs time plots of empty, uncapped **a** round-bottomed (RB) and **b** flat-bottomed headspace vials.

From the above figure, the uncapped vials of either rounded-bottom or flat-bottom type also showed significant variation in the vial failure force. Table 21 lists the failure force statistics and corresponding pressures for each group of vials shown in Figure 27 and Figure 28.

Table 21: Axial compression force and pressure analysis of the borosilicate (BS), headspace rounded or flat-bottomed vials. Vials were capped with either aluminium/silicone (Al/Si), PTFE/Silicone (PTFE/Si) septa crimp caps or left uncapped. Two 100 kGy γ-ray irradiated vials were also compressed as listed in the table.

Group Number	**Vial Type**	**Septa Cap Type**	**Irradiation**	**Average Vial Failure Force / N**	**Average Vial Failure Force Error ±/ N**	**Average Failure Pressure / N cm^{-2}**	**Average Failure Pressure Error ± / N cm^{-2}**
1	Rounded	Al/Si	-	789	328	1005	417
2	Rounded	PTFE/Si	-	1107	380	1409	484
3	Rounded	PTFE/Si	100 kGy γ-ray	1524	-	1940	-
4	Flat	Al/Si	-	1544	401	372	97
5	Flat	PTFE/Si	-	561	68	135	16
6	Flat	Al/Si	100 kGy γ-ray	1708	-	411	-
7	Rounded	-	-	926	150	1180	190
8	Flat	-	-	1794	279	409	67

The average vial failure force for the flat and rounded-bottom vials only were 1794 ± 279 N and 926 ± 150 N, respectively as indicated by vial groups 7 and 8. The corresponding axial fail pressures for the flat and rounded-bottom vials were 409 ± 69 N cm^{-2} and 1180 ± 190 N cm^{-2}, respectively. Due to the large statistical uncertainty for the failure force with only the vials, highlighting any reduction in the vial failure force due to the radiation embrittlement effect becomes unlikely. Table 21 also shows the compression failure statistics for the capped vials of both septum types with average failure pressures of 1005 ± 417 N cm^{-2} and 1409 ± 484 N cm^{-2} for Al/Si and PTFE/Si septa caps, respectively on rounded-bottom vials (with a similar relative variation for flat-bottom vials). Further compression testing may narrow the statistical uncertainties and reveal compressive strength differences between irradiated and unirradiated borosilicate glass given significant numbers of compressed vials.

While these compression tests can give an estimate of the glass embrittlement for irradiated vials, it does not measure the integrity of the cap seal. The cap seal is probably going to be a more regular failure point than the breaking of the borosilicate glass, as long as the vial is handled carefully. A method to determine the integrity of the vial seal and its leaking rate would be more valuable in the future. Polypropylene vials or similar leak-proof, resistant plastic vials that are chemically and irradiation resistant are the suggested vial type for further radiation testing for a couple of reasons. Polypropylene has a more comparable density (ρ_{PP} = 0.9 g cm^{-3}) to the organic samples (ρ_{org} ~ 1.0 to 1.26 g cm^{-3}) whereas borosilicate is significantly denser (ρ_{BS} = 2.21 g cm^{-3}) [278, 279]. This means there is a less significant difference in the phase boundary between the vial and organic sample, ensuring a more uniform dose deposition [127]. Additionally, there would also be fewer heating issues related to thermal neutron absorption with polypropylene vials than with borosilicate glass.

4.3.2 Leaking and Mass Change Analysis

To detect leaks or loss of sample, the mass before and after irradiations was measured and related to the initial organic mass included as indicated in Table 15 to Table 18. A positive value for percentage mass change shows an increase in mass but this is thought to indicate mass balance drift between the before and after mass measurement dates. A negative value indicates a loss of mass from the vials, which is assumed to be from the organic media. For all polypropylene vials, no significant mass changes were recorded for γ-ray only irradiations were observed, above the typical variations. For unirradiated PP controls of glycerol, a % mass change of 0.8% relative to the organic was recorded. For the unirradiated PP vials of ethylene glycol, a % mass change of 1.73% relative to the organic was recorded, suggesting that minor % changes in mass are expected that are not a result of irradiation or heating effects. A threshold of 1% difference in mass before irradiation and after irradiation was chosen to highlight the vials that leaked. Table 22 lists values for mass change from each vial type and organic sample type.

Table 22: Mass change analysis of BS and PP vials for leak identification. Vial mass data was used from Table 15 to Table 18.

Vial Type	Organic Sample Type	Average % Mass Change	% Error (σ)	Leaking Vials or Melted Vials (>+1% difference)	Percentage of Total
PP	EG Unirradiated	1.73	NA	0	0.00%
	EG γ-ray	0.56	0.67	0	0.00%
	EG Neutron	0.16	0.51	0	0.00%
PP	Glycerol Unirradiated	0.80	NA	0	0.00%
	Glycerol γ-ray	-0.35	1.29	1	16.67%
	Glycerol Neutron	-0.81	1.61	1	16.67%
	Glycerol Aqueous Mixes - Unirradiated	0.09	0.06	0	0.00%
	Glycerol Aqueous Mixes - γ-ray	0.38	0.21	0	0.00%
	Glycerol Aqueous. Mixes - Neutron	-1.10	8.35	5	31.25%
	Glycerol Tern. Mixes - Unirradiated	-0.80	0.67	1	33.33%
	Glycerol Tern. Mixes – γ-ray	-0.61	0.22	0	0.00%
	Glycerol Tern. Mixes - Neutron	-0.82	8.35	1	6.25%
BS with Al/Silicone Septa	EG Unirradiated	-10.87	NA	1	100.00%
	EG γ-ray	-8.30	4.66	6	100.00%
	EG Neutron	-7.69	3.21	6	100.00%
	Glycerol Unirradiated	0.15	NA	0	0.00%
	Glycerol γ-ray	0.26	0.22	0	0.00%
	Glycerol Neutron	0.22	0.11	0	0.00%

There seems to be a reasonable variation of sample mass variation across the 105 vials tested. From observing the vials and analysing the mass data, the normal statistical variation of mass from the PP samples that did not leak was 0.31% for gamma-irradiated samples and 0.071% for mixed-field irradiated samples. For γ-ray irradiations, only 1 out of 29 vials displayed a notable mass loss, with the only one showing a loose screw cap (assumed to have been loosened during handling). For mixed-field neutron + γ-ray irradiations, 7 out of 38 PP vials had losses in mass but these involved melted vials (irradiated adjacent to BS vials). Ternary glycerol mixtures (samples 108 to 116) contained in the PP vials showed marginally larger losses, this is thought to be increased minor volatile losses from the more volatile acetone or water components.

There did appear to be significant mass losses (≈-3% to -16%) from all 6 of the borosilicate vials for both mixed-field and γ-ray only irradiations of ethylene glycol (mixed: samples 88 to 93, γ-ray only: 100 to 105). This mass loss appeared to increase with absorbed dose (and dose rate) from 20 kGy up to 100 kGy, indicating the crimp vials and the aluminium/silicone septa are not suitable for high-dose rate NPP environments. Ethylene glycol samples typically showed larger mass losses than glycerol samples which can be explained by the lower boiling point and higher vapour pressure of ethylene glycol compared to glycerol, contributing to the comparably higher volatile losses.

4.4 INAA and γ-ray Spectroscopy

Instrumental Neutron Activation Analysis (INAA) was conducted for both the neat glycerol and neat ethylene glycerol samples using the K0 method (at JSI). Table A18 shows the full list of radioactive elements and their determined concentration within each sample, respectively after their irradiations. Where specific isotopes could not be detected by the INAA method, the method's limit of detection (LOD) for those isotopes has been given. For the detected radionuclides, their radioactivity was quantified for 0 days, 1 day, 3 days, 7 days, and 10 days from irradiation, and these are listed in Table 23.

Table 23: Induced radioactivity of detectable radioisotopes and their decay: Neat glycerol and ethylene glycol were irradiated with a mixed-field absorbed dose of a total of 520 kGy (270 kGy from thermal neutrons and 250 kGy from γ rays) producing the following activation products.

Sample	**Radionuclide**	**Half-life, T$^{1/2}$ / hrs**	**Concentration / mg kg^{-1}**	**Sample Activity / Bq**	**Specific Activity after time, t / Bq g^{-1}**				
				at t=0 (After irradiation)	t=0 days	t= 1 day	t= 3days	t=7 days	t=10 days
Neat Glycerol	As-76	26.24	0.006	117.4	84.0	44.6	12.5	3.5	1.4
	Br-82	35.3	0.011	55.8	39.9	24.9	9.7	3.8	1.9
	Na-24	14.96	0.579	5165.1	3698.6	1216.5	131.6	14.2	2.7
	Sb-124	1444.8	0.002	0.3	0.2	0.2	0.2	0.2	0.2
	W-187	23.72	0.001	33.8	24.2	12.0	3.0	0.7	0.2
Neat Ethylene Glycol	Br-82	35.3	0.027	248.7	104.4	65.2	25.4	9.9	4.9
	Na-24	14.96	1.01	16136.1	6776.4	2228.8	241.1	26.1	4.9
	Sb-124	1444.8	0.001	0.1	0.1	0.1	0.1	0.1	0.1
	Zn-65	5863.2	0.191	0.3	0.1	0.1	0.1	0.1	0.1

The INAA data shows there are only several radioisotopes that could be detected for both ethylene glycol and glycerol but most of these radionuclides show specific activity levels below 105 Bq g^{-1} immediately after irradiations. The exception is sodium-24 with specific activity levels of ~3700 Bq g^{-1} and ~6800 Bq g^{-1} for glycerol and ethylene glycol, respectively. However, after 7 days all radionuclides were observed to decay to negligible levels (<30 Bq g^{-1}) due to their short half-lives. The high sodium content (~1 ppm) in these refined materials is thought to be due to the basic NaOH catalyst used for the biodiesel reaction. The crude glycerol by-product often contains all the residue salts, methanol and water from the biodiesel process, with sodium salts particularly difficult to remove and typically requiring energy-intensive processes such as distillation [315]. For the other radionuclides from glycerol, As-76, Br-82, and Sb-124 are thought to be activated trace elements derived from plant matter that were not completely removed from glycerol during chemical processing. From this INAA study, arsenic, bromine, and antimony are at or below concentrations of 10 ppb for both organics. Studies have shown the uptake of these elements with plants (specifically rapeseed) from soils [316-318] and are observed as trace metals in similar organics [319]. Tungsten and zinc are also thought to be trace metal contaminants in the supplied chemicals at ~1 ppb and 100 ppb levels, respectively. Provided by the manufacturer (Honeywell), the certificate of analysis of glycerol indicates that there are <2 ppm (~2 mg kg^{-1}) of heavy metals (assuming them as Pb) within the glycerol liquid. This manufacturer assay complies with this INAA study as the quantifiable heavy metals add up to 0.60 ppm in glycerol according to the INAA analysis. There is a less detailed manufacturer assay for ethylene glycol with no heavy metal assay available but heavy metals add up to 1.23 ppm according to this INAA analysis. Since the INAA study has shown relatively similar quantities of trace metals to the manufacture's assay range <2 ppb, it is assumed that no additional trace metals were leached into the organics during transport or irradiation.

4.5 Ethylene Glycol

4.5.1 Radiolysis Products: Qualitative

The following section displays the qualitative radiolysis products observed from both mixed-field neutrons + γ-ray and γ-ray only irradiations for ethylene glycol via liquid injection GC-MS analysis. All following data is from samples that have been irradiated using the TriC of the JSI reactor, as described in sections 3.4.2 and 3.4.3. Figure 29a displays the labelled TICs waveforms (black line) for γ-ray only (shutdown mode) and b, mixed field neutron+ γ-ray (operational mode) irradiations. Both figures are compared against similarly diluted unirradiated samples (pink) and ethanol solvent blanks (blue). TICs of samples 35 (neutron+γ), 50 (γ-only) and 78 (control) listed in Table 15 and Table 16 are those used to produce the following figure, along with an ethanol solvent blank.

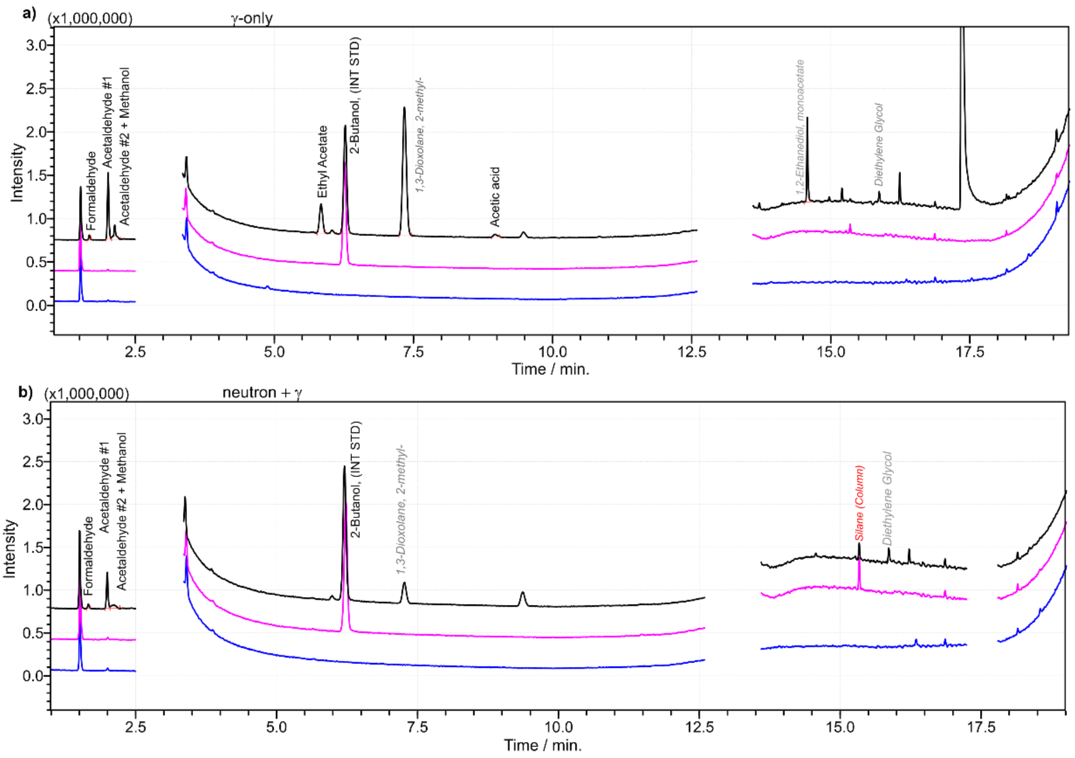

Figure 29: Total Ion Chromatograms of liquid-injected irradiated neat ethylene glycol samples, diluted in ethanol post-irradiation and compared against unirradiated controls and solvent TICs. Samples irradiated in the TriC of the JSI reactor. Black line= 50 kGy irradiated glycerol sample of the specified irradiation type with identified peak labels. Pink = unirradiated glycerol control sample, Blue = ethanol solvent. **a** only γ rays and **b** mixed-field neutron + γ rays.

Comparing both sets of chromatograms, a similar set of detectable radiolytic products is seen for both different types of radiations, although peak area sizes do seem to differ between the irradiation types. Some analyte peaks may be missing from the mixed-field neutron + γ-ray irradiations compared to equivalent-dosage γ-ray only samples (such as ethyl acetate and acetic acid). This may be due to below LOD concentrations for the GC method. Additionally, γ-ray only irradiations produced detectable concentrations of both ethyl acetate and acetic acid. Breaks (or solvent cuts) in the ethylene glycol chromatogram are observed at 2.5 minutes, 12.6 minutes, and 17.3 minutes, corresponding to ethanol, ethylene glycol, and miscellaneous polymeric peaks, respectively. These breaks are periods where the detector is switched off to prevent detector saturation during the elution of high concentrations of compounds such as the solvent or bulk starting material.

Table 24 lists the products detected via MS after γ-ray only irradiations. The table shows the % similarity match with the quoted analyte's EI fragment pattern from the NIST 11 database. Additionally, the table indicates if the analytes have been confirmed using purchased standards and if they have been reported previously.

Table 24: **Ethylene Glycol Radiolysis Products List**: Products from either mixed-field neutron + γ-ray or only γ-ray from neat ethylene glycol. A similarity % match of >90% to an analyte was considered suitable for standard confirmation.

Number	Product	Peak Retention Time (min.)	% Similarity	Confirmed Using Standards (Y/N)	Reported in Literature? Ethyl Glycol or Similar Alcohols (Y/N) [210, 244]
1	Formaldehyde	1.67	97	Y	Y
2	Acetaldehyde	2.10 & 2.15	98	Y	Y
3	Methanol	2.15	98	Y	Y
4	Ethyl Acetate	5.80	98	Y	N
5	Acetaldehyde, hydroxy-	5.95	97	N	Y
6	1,3-Dioxolane, 2-methyl-	7.29	97	N	Y
7	Acetic Acid	8.88	98	Y	Y
8	1,2-Ethanediol, monoacetate	14.57	96	N	N
9	Diethylene Glycol	15.80	94	N	Y
9-23	14 Unidentifiable Products*		<88	-	-

As shown by the chromatograms in Figure 29, some analytes appear in the unirradiated samples. These peaks are O_2 gas (~1.5 min), butan-2-ol (6.3 min) as the internal standard and silane peaks (16 min) which appear due to column degradation. Compared with previous reports on ethylene glycol radiolysis (Table A2), four radiolytic analytes have been detected and matched using this method. These are: formaldehyde, methanol, acetaldehyde, and acetic acid. Additionally, ethyl acetate (5.8 min), a previously unreported product has been observed, although the presence of acetates has been reported [244]. Other acetates, such as (1,2-ethanediol monoacetate), show a high % similarity to their recorded MS fragment patterns on the NIST 11 database but have not been quantified. Large unidentifiable peaks with a similarity % of less than 90% have been given in Table 25, with their electron ionization (EI) fragment patterns shown in Figure A12.

Table 25: Unidentified analyte peaks from neat ethylene glycol radiolysis listing main EI fragments. Full EI fragment patterns are shown in Appendix A, Figure A12.

Unknown #	Retention Time / min.	Suggested Analyte (NIST 11 Database)	% Similarity	Main MS Fragments
1	9.5	Ethyl ethoxy(hydroxy)acetate	84	31, 45, 61, 75
2	16.2	Methyl tetrahydrofurfuryl ether	89	71, 41, 45, 31
3	17.4	2-(Methoxymethoxy) propanoic acid	86	45, 89, 31

The products in Table 24 and Table 25 show similar moieties of C=O or C-O which show the reduction of the OH groups, leading to ether and acetate formation which aligns with prior reports in the radiolysis literature (e.g., diethylene glycol and acetate ions) [210, 244]. One of the largest unidentifiable peaks compared with the internal standard is 2-(Methoxymethoxy) propanoic acid at 17.4 minutes. From the data, this peak is likely to be a miscellaneous polymeric substance that has several different units of oxygenated monomers, resulting in a mixture of compounds that elute at the same time. Such a polymeric substance from alcohol radiolysis has been reported in similar works [210, 217, 320]. It is also possible that the components in Table 25 are pure but are not registered in the NIST 11 reference database.

4.5.2 Quantitative Analysis

4.5.2.1 Neat Ethylene Glycol with Absorbed Dose, Vial Type and Radiation type.

The four radiolytic analytes of acetaldehyde, methanol, ethyl acetate and acetic acid have been quantified by calibration curves of diluted purchased standards. Due to numerous standard calibration curves utilized over the quantitation process, an example of the curves is shown in Appendix A, Figure A6. Each analyte has been compared against the three variable parameters of vial type, irradiation type, and absorbed dose, as per its figure for concentration, *G*-value, and mass productivity, with molar % yield also described occasionally. Experimental data for neat ethylene glycol samples have been tabulated for concentration (Appendix A, Table A4 and Table A5), *G*-values and mass productivity (Appendix A, Table A11 and Table A12 for reference and future comparisons. The data used to compile Figure 30 to Figure 37 derive from the following samples: 33 to 38 (neutron+γ, PP), 71 to 76 (γ rays, PP), 88 to 93 (neutron+γ, BS), and 100 to 105 (γ rays, BS) listed in Table 15, Table A16, and Table 17.

4.5.2.2 Acetaldehyde

For acetaldehyde quantification, the method described in chapter 3.5.2.1 proved not to be ideal for higher concentration or high-dose samples due to split acetaldehyde peaks at 2.10 and 2.15 minutes, which make routine quantification difficult. Additionally, the co-elution of a broad methanol peak from 2.15 minutes to 2.25 minutes exacerbates routine automated quantification techniques which is not obvious from the TIC in Figure 29 (indicated in detail by Appendix A, Figure A10). While peak splitting and co-eluting analytes are not ideal for peak quantification, it can still be possible to analyse them through MS fragment isolation via post-processing. Calibrating off the 44 m/z mass-charge fragment which is not present in methanol, the second acetaldehyde peak can be quantified using the GC-MS software. Figure 30 shows the concentration of acetaldehyde (combination of both peaks) concerning absorbed dose for *a*) γ-ray only and *b*) neutron + γ-ray mixed field irradiations using the TriC of the JSI reactor.

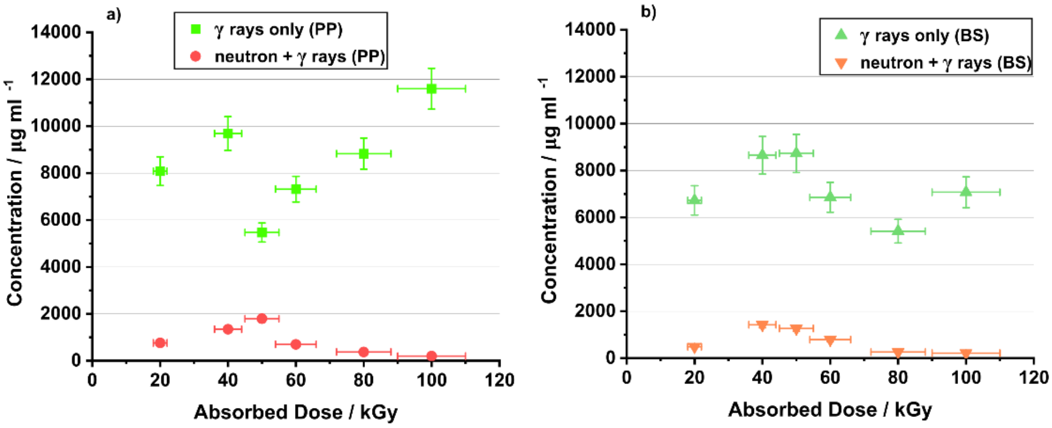

Figure 30: Concentration of acetaldehyde for the specified dose for γ-ray (green) and neutron + γ-ray (red) irradiations of neat ethylene glycol using the JSI reactor and quantified using a GC-MS. **a** Polypropylene vials (PP). **b** Borosilicate vials with Al/Si septa (BS). Y-axis error bars derive from the relative standard deviation from calibration curves with the x-axis indicating the deviation in dose. The data are available in Appendix A, Table A4 and Table A5.

The expected concentration response for primary radiolytic products is for the total accumulated concentration to increase with the total absorbed dose (as Figure 12). However, with acetaldehyde, there appears to be a decrease after 60 kGy for most vial and irradiation types. Secondary radiolytic products are generally expected to increase at a lower rate than primary radiolytic products (as Figure 12). This decrease could refer to a vial leak due to the low boiling point of acetaldehyde, and poor seals of the BS vials. As an example of the calculation processes involved to determine the *G*-values and mass productivities from the GC-MS data, the following paragraph will detail this for sample 35 (50 kGy neutron+γ-ray, PP) as listed in Table 15 as an example. Firstly, the concentration of acetaldehyde from the diluted sample 35 (50 kGy neutron+γ-ray, PP) was measured at 58.9 µg ml^{-1} using the GC-MS and the internal calibration curves for the 44 m/z acetaldehyde fragment (summing up the 44 m/z areas for both acetaldehyde peaks). Accounting for the dilution ratio of 0.0327 for the sample as defined in chapter 3.6 using equations (55) and (56), the concentration of acetaldehyde in the neat sample was determined to be 1796 µg ml^{-1} using equation (54). Using equation (57), the total mass of acetaldehyde is calculated, by multiplying the concentration of acetaldehyde in the neat sample by the volume of the irradiated sample (organic mass ÷ organic density = 1.159 g ÷ 1.11 g cm^{-3} = 1.04 cm^{3}) to get the total mass of 1875 µg. Using equation (58), the total moles of the analyte is calculated by dividing the total mass by the molecular mass of acetaldehyde (44 g mol^{-1}) to get the total moles of 42.6 µmoles within the irradiated sample. Using equation (59), the *G*-value is calculated by dividing the total moles by the energy into the sample (50 kGy × 1.159g = 57.95 J) to result in a *G*-value of 0.735 µmol J^{-1}. Mass productivity % is calculated using equation (46) and the analyte mass from equation 55. For sample 35, the mass of acetaldehyde is divided by the mass of the starting organic sample (0.001875 g ÷ 1.159 g) to result in a mass productivity % of 0.162%. The process to calculate *G*-values and mass productivities of methanol, ethyl acetate, and acetic acid is similar with each process accounting for the different molecular masses of each analyte accordingly. X-axis errors of ±10% were derived from dosimetry accuracy as mentioned in chapter 3.4.2. Y-axis errors for concentration (also mass productivity) were derived from the relative standard deviation percentage (RSD%) of the calibration curve, for sample 35 measuring acetaldehyde, it was 11.2%. For *G*-value errors, the y-axis error for concentration is combined via relative error addition with the 10% error for the absorbed dose (±0.11 µmol J^{-1} for acetol from sample 35). Although the analytical workup errors were also added via relative error addition, they were negligible compared with the RSD% from the calibration curves or the 10% uncertainty for the dosimetry.

Figure 31 shows the radiation chemical yields (G-values) and mass productivity of acetaldehyde for the range of absorbed doses, vial types and irradiation types.

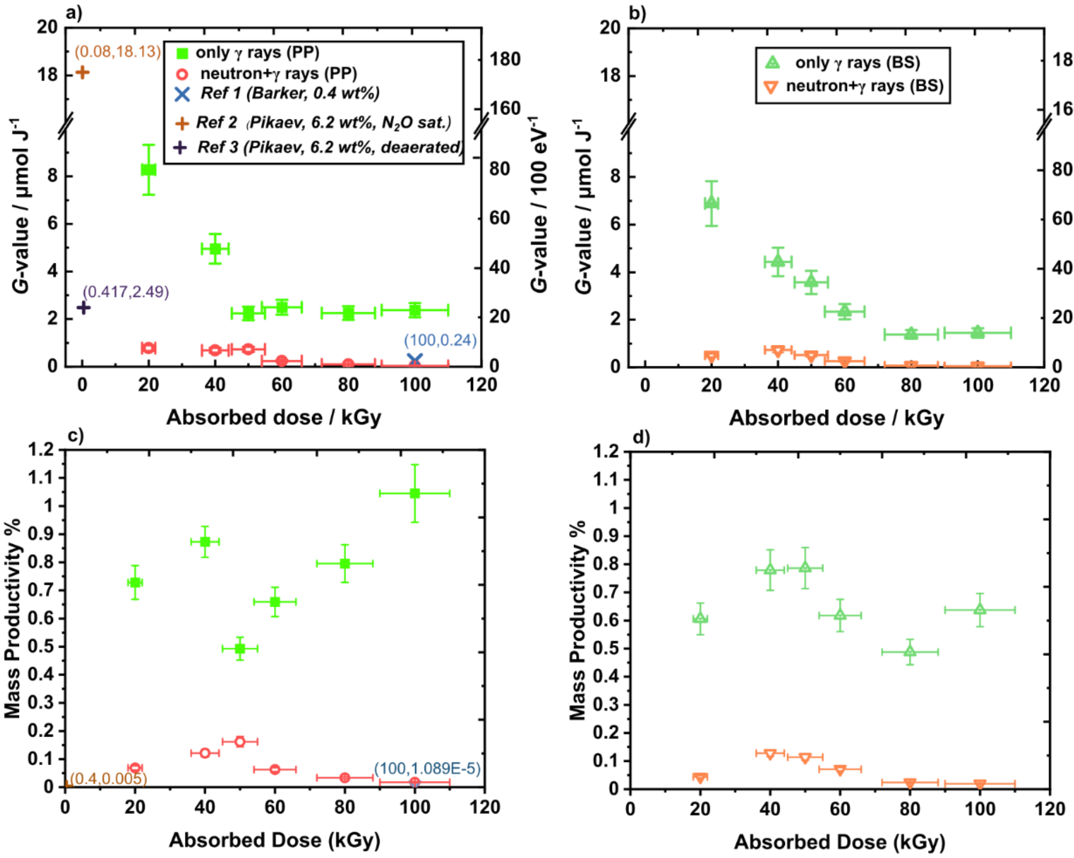

Figure 31: Radiation chemical yields (G-value) and mass productivity values of acetaldehyde for the specified dose for γ-ray (green) and neutron + γ-ray (red) irradiations of neat ethylene glycol. **a** Polypropylene vials (Squares and circles). **b** Borosilicate vials with Al/Si septa (Triangles). **c** and **d** Mass productivity percentages of acetaldehyde in PP and BS vials, respectively. Error bars indicate the combination of instrumental, calibration and dose errors for G-values. Data tabulated in Appendix A, Table A11 and Table A12. G-value references quoted are from Barker with 0.4 wt.% glycerol [210] and Pikaev with samples of 6.2 wt.% [244]**.**

As expected from most of the radiolysis literature, and specifically the ethylene glycol literature [244], the G-value of acetaldehyde decreases with an increased absorbed dose for both irradiation types. There is a noticeable contrast between different irradiation types for lower doses (<50 kGy); γ-ray only irradiations have superior G-values at low doses compared with neutron+ γ-ray irradiations. For acetaldehyde, extrapolating towards 0 kGy, a *zero-dose* G-value of (22.1 ± 9.3) µmol J^{-1} and (1.7 ± 0.8) µmol J^{-1} can be determined for γ-ray only irradiations and mixed-field neutron + γ rays, respectively, from PP sample vials. *Zero-dose* G-values are calculated by appropriately plotting the dose vs G-value trend based on the data and determining the y-axis intercept, as given in section 4.5.2.6. These zero-dose G-values compare well to the literature zero-dose

G-values of 18.1 µmol J^{-1} from lower-dose (0.08 kGy), γ-ray irradiation of 6.2 wt.% diluted aqueous samples as shown in Figure 31a [244].

As expected, mass productivity increases with increased absorbed dose, but not significantly after 20 kGy and only reaching a maximum of ~1.1 % for 100 kGy of γ-ray only absorbed dose. Even with high initial *G*-values of ≈8 µmol J^{-1} or ≈80 molecules 100eV^{-1}, conversions to acetaldehyde with larger absorbed doses γ-ray only are not high. For neutron + γ-ray samples, *G*-values and mass productivity are relatively much lower than corresponding γ-ray only samples. Decreases in *G*-value and mass productivity are observed after 50 kGy which possibly signifies a competing reaction which exceeds the acetaldehyde synthesis reaction after a threshold absorbed dose.

4.5.2.3 Methanol

Similarly, as for acetaldehyde quantification, methanol quantification was made difficult because of its broad peak and co-elution with acetaldehyde. Post-processing with the 31 m/z fragments (negligible in acetaldehyde) allowed for the reasonable quantification of methanol, based on their respective areas with the same fragments from the calibration curve. An example of the post-processing of the different mass fragments is given in Appendix A, Figure A10 where a comparison between 80 kGy γ-ray and neutron + γ-ray irradiated samples is given. The calculation process for concentration, *G*-values, and mass productivities of methanol are akin to those described in 4.5.2.2 for acetaldehyde, just accounting for the different quantitation fragment (31 m/z), calibration curve and the analyte molecular mass (32 g mol^{-1}). Figure 32 shows the dependence of methanol concentration on absorbed dose for both γ-ray only and mixed field neutron + γ-ray irradiations in both PP and BS vials.

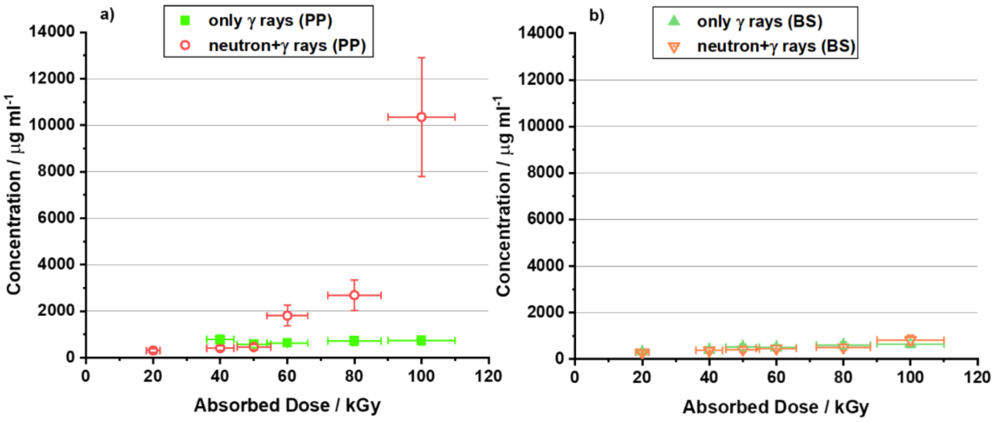

Figure 32: Concentration of methanol for the specified dose for γ-ray (green) and neutron + γ-ray (red) irradiations of neat ethylene glycol. **a** Polypropylene vials (PP). **b** Borosilicate vials with Al/Si septa (BS). Y-axis error bars derive from the relative standard deviation from calibration curves with the x-axis indicating the deviation in dose. The data are available in Appendix A, Table A4 and Table A5.

For PP vials, there is a large increase in methanol concentration above doses of 60 kGy for mixed field irradiations of neat ethylene glycol in PP vials, but it is not observed for BS vials. Appendix A, Figure A11 shows TICs of equivalently irradiated ethylene glycol and glycerol sample vials, focussing on the methanol region. Similar relative concentrations of methanol were not observed from the mixed field irradiations which indicate the methanol derives from the radiolytic decomposition of ethylene glycol and not the PP vial. Figure 33 shows the radiation chemical yields (*G*-value) and mass productivity dependence on absorbed dose for radiolytic methanol from neat ethylene glycol.

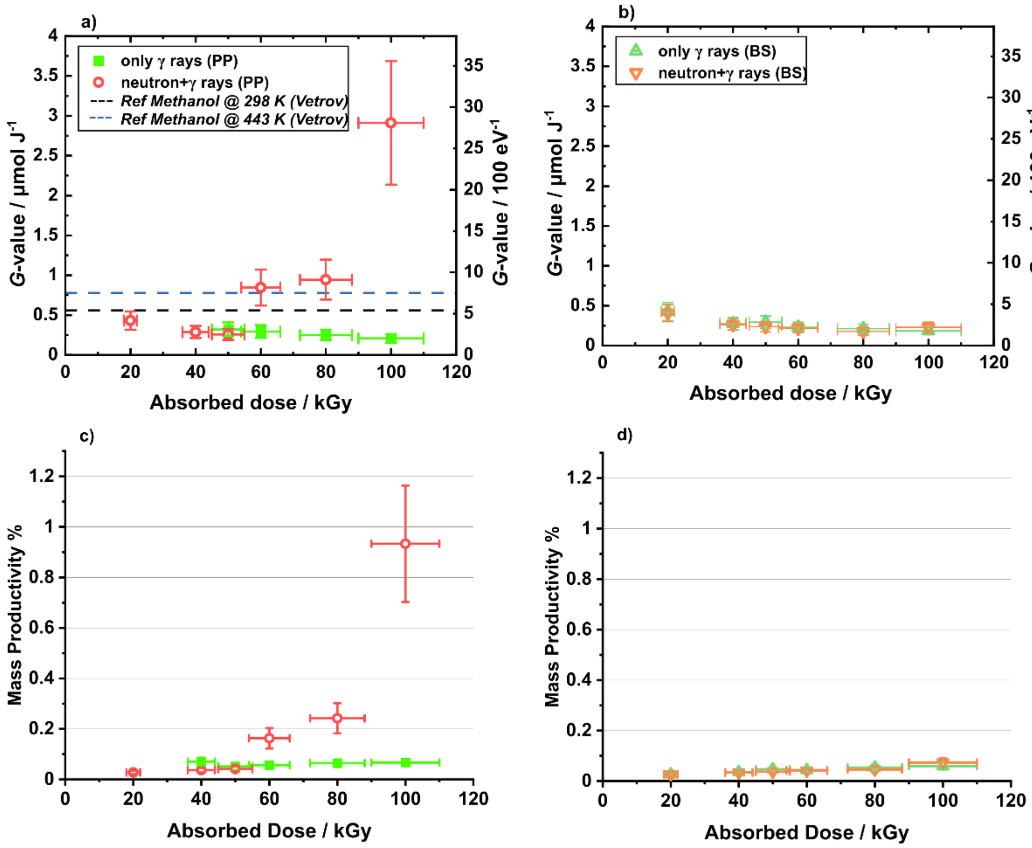

Figure 33: Radiation chemical yields (*G*-value) and mass production % values of methanol for the specified dose for γ-ray (green) and neutron + γ-ray (red) irradiations of neat ethylene glycol**. a** *G*-values with polypropylene vials (PP). **b** *G*-values with borosilicate vials (BS) with Al/Si septa. **c** and **d** Mass productivity percentages for polypropylene and borosilicate vials, respectively. Error bars indicate the combination of instrumental, calibration and dose errors for both values. Datasets can be found in Appendix A, Table A11 and Table A12. *G*-value references for methanol at 298K and 443K quoted are from a report by Vetrov with an undefined dose [277].

In contrast to the acetaldehyde data, Figure 33 shows a significant increase in methanol *G*-values for mixed-field irradiations compared with γ-ray only irradiations, for doses above ~60 kGy. Contrary to expectations, the highest *G*-value observed is 2.91 μmol J^{-1} at 100 kGy of mixed-field dose in polypropylene vials. This suggests a preference for methanol production for higher dose rates or high doses. The observed increases in *G*-value for methanol with increased mixed-field absorbed dose also seem to coincide with the drop of *G*-values observed for acetaldehyde at doses above 60 kGy, suggesting the possibility of competing processes.

The significant differences observed for the concentration and corresponding *G*-values of methanol between PP and BS sample vials of mixed-field irradiations could be explained by temperature and leaks. The increased temperatures reached by the BS vials (due to neutron moderation) and the subsequent leaking of volatile components such as methanol through the poorly-sealed, crimp-capped vials would explain the loss of analytes. Whilst the temperature was not measured in the triangular channel, the occasional melting of a touching PP vial during neutronic mixed-field exposures indicates a possible maximum temperature of 121 °C was reached, according to the PP vial's maximum stable temperature [313]. Additionally, the mass differences of the BS vials measured before and after the irradiations show a loss in organic content and support the theory of poor seals and leaking vials.

4.5.2.4 Ethyl Acetate

As a previously unreported product for ethylene glycol radiolysis, ethyl acetate was an interesting product to quantify. However, it was only quantifiable for lower LET, lower dose rate, γ-ray only irradiations throughout the absorbed dose range and did not reliably appear with high-LET, high dose rate, mixed-field neutron+ γ-ray irradiations. Figure 34 shows the concentration of ethyl acetate dependence on γ-ray only absorbed dose from neat glycerol samples, using data from samples 71 to 76 (γ-ray, PP) and 100 to 105 (γ-ray, BS). Figure 35 shows the radiation chemical yields (*G*-value) and mass productivity dependence on γ-ray only absorbed dose for ethyl acetate from neat ethylene glycol samples in PP and BS vials. The small TIC peaks observed with the GC-MS correspond to small concentrations of ethyl acetate which result in larger uncertainties in *G*-value, especially for lower doses. Similar to the moieties observed for the unidentifiable compounds (ethers, esters, and acetates), ethyl acetate is most likely a secondary product which is supported by the low *G*-values towards zero-dose. The calculation process for concentration, *G*-values, and mass productivities of ethyl acetate is alike to those described in 4.5.2.2 for acetaldehyde, but accounting for the different calibration curves and the analyte molecular mass (88.1 g mol^{-1}).

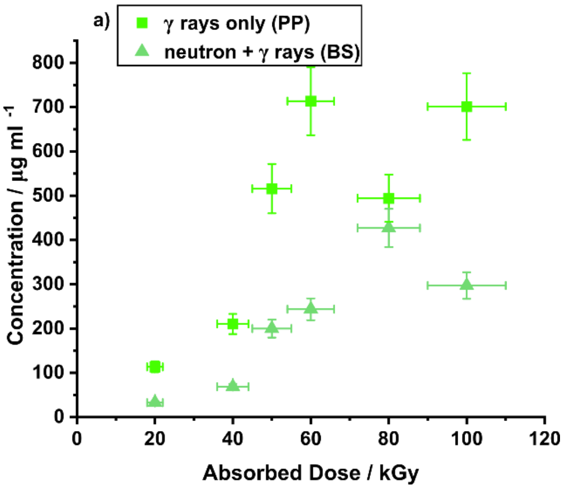

Figure 34: Concentration of ethyl acetate for the specified dose for γ-ray of neat ethylene glycol. From Polypropylene vials (PP, square) and borosilicate vials with Al/Si septa (BS, triangle). No peaks were detected from neutron + γ-ray irradiations. Y-axis error bars derive from the relative standard deviation from calibration curves with the x-axis indicating the deviation in dose. The data are available in Appendix A, Table A4 and Table A5.

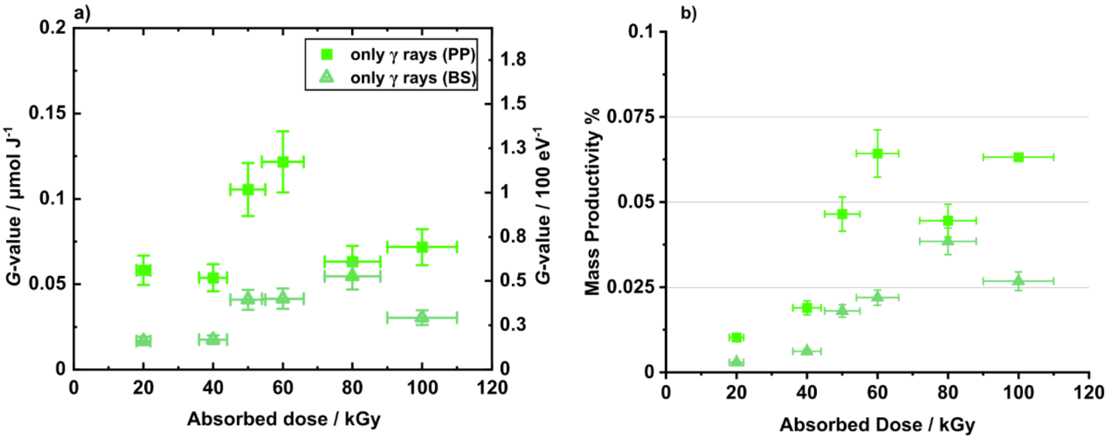

Figure 35: Radiation chemical yields (*G*-value) and mass productivity of ethyl acetate for the specified dose for γ-ray (green) irradiations of neat ethylene glycol. **a** γ-ray for polypropylene vials (Squares) and borosilicate vials with Al/Si septa (Triangles). **b** Mass productivity percentages. Error bars indicate the relative combination of instrumental, calibration and dose errors for both sets of values. The full dataset can be found in Appendix A, Table A11 and Table A12.

Initially, there does not appear to be a clear trend for ethyl acetate production and compared with acetaldehyde due to the high uncertainties involved, the *G*-values observed for ethyl acetate are small. Similar *G*-values are expected for the 1,2-ethanediol monoacetate compound due to similar functional groups and reaction mechanisms involved for ethyl acetate. The lack of detectable ethyl acetate peaks from the mixed-field, neutron + γ-ray exposures indicates that the process is primarily chemical but relies on the concentration of one or several radiolytically produced organic species (predicted to be ethanol and acetic acid).

4.5.2.5 Acetic Acid

While seemingly a minor product with a very small peak area, acetic acid appeared consistently for γ-ray irradiations above 40 kGy. Figure 36 shows the concentration dependence on absorbed dose for acetic acid from γ-ray only irradiations. Figure 37 shows the *G*-values and mass productivity for acetic acid from γ-ray only samples for both vial types, with mixed-field irradiations not producing any detectable concentrations. The calculation process for concentration, *G*-values, and mass productivities of acetic acid is alike to those described in 4.5.2.2 for acetaldehyde, but accounting for the different analyte calibration curves and molecular mass (60.1 g mol^{-1}).

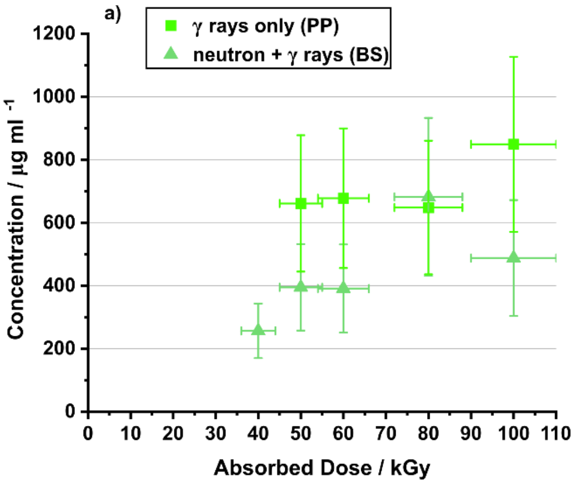

Figure 36: Concentration of acetic acid for the specified dose for γ-ray (green) of neat ethylene glycol. From Polypropylene vials (PP, square) and borosilicate vials with Al/Si septa (BS, triangle). No acetic acid peaks were detected from neutron + γ-ray irradiations. Y-axis error bars derive from the relative standard deviation from calibration curves with the x-axis indicating the deviation in dose. The data are available in Appendix A, Table A4 and Table A5.

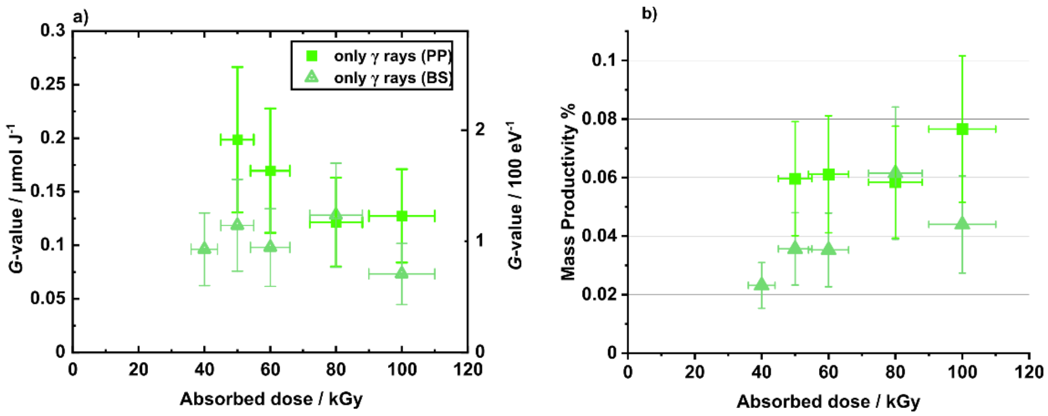

Figure 37: Radiation chemical yields (*G*-value) and mass productivity of acetic acid for the specified dose for γ-ray (green) irradiations of neat ethylene glycol. **a** γ-ray for polypropylene vials (squares) and borosilicate vials with Al/Si septa (triangles). **b** Mass productivity percentages. Error bars indicate the relative combination of instrumental, calibration and dose errors for both sets of values. Full datasets can be found in Appendix A, Table A11 and Table A12.

Figure 37 shows comparable *G*-values between the two different vial types. This indicates that despite polypropylene being reported to produce acetic acid in the literature (discussed as per 3.2), the concentration of acetic acid remains statistically comparable to BS vials, accounting for the uncertainties. Therefore, it is thought that any acetic acid generated by the PP degradation is minimal compared with the acetic generated from ethylene glycol. It is also noted that acetic acid is also quite volatile with a vapour pressure of 15.75 mmHg [321] which shows the potential for acetic acid to leak out of an unsecured vial. There seems to be very little dependence on absorbed dose for *G*-values of acetic acid, this could suggest that higher-order processes occur such as those to synthesise acetates and oxygenated polymers which keep concentrations of acetic acid at a semi-steady state situation with low *G*-values. The generation of acetic acid would be required for the synthesis of ethyl acetate, as mentioned previously in section 4.5.2.4.

4.5.2.6 Zero Dose Values

To compare against the *G*-values reported in the literature, Table 26 lists the *zero dose G*-values for the radiolytic products from γ-ray only and neutron + γ-ray mixed-field irradiations.

Table 26: Zero dose *G*-values for radiolytic products from neat ethylene glycol via extrapolation.

		Methanol [a]		**Acetaldehyde** [a]		**Ethyl Acetate** [c]		**Acetic Acid** [c]	
Irradiation Type	**Mixture Type & Vial**	**Zero-dose *G*-value / μmol J^{-1}**	**± Error**	**Zero-dose *G*-value / μmol J^{-1}**	**± Error**	**Zero-dose *G*-value / μmol J^{-1}**	**± Error**	**Zero-dose *G*-value / μmol J^{-1}**	**± Error**
γ rays only	Neat PP	0.5	0.6	22	9	0.06	0.02	0.3	0.1
	Neat BS	0.7	0.2	14	5	0.02	0.05	0.13	0.04
Mixed Neutron + γ rays	Neat PP	0.3[b]	0.1	1.7	0.8	NA	NA	NA	NA
	Neat BS	0.9	0.4	1.1	0.8	NA	NA	NA	NA

[a] Best fit line with exponential decay
[b] Best fit line with exponential growth
[c] Best fit line with linear relationships

The γ-ray zero dose *G*-value of (22 ± 9) μmol J^{-1} for acetaldehyde shown in Table 26 aligns well with the data reported in lower-dose, γ-ray, radiolysis literature with dilute ethylene glycol, as reported by Pikaev (>13 μmol J^{-1}) [244]. For methanol, the zero dose *G*-value aligns well (range between 0.2 and 0.9 μmol J^{-1}) with the radiolysis literature data of diluted samples reported by Barker [210] and Vetrov [277] of 0.2 μmol J^{-1} and ~0.56 μmol J^{-1}, respectively. The zero-dose *G*-value determination of ethyl acetate and acetic acid is likely to be uncertain due to the lack of a clear trend in *G*-value with absorbed dose and large uncertainties, as seen in Figure 35 and Figure 37.

4.5.3 Dose Rate

For comparison against variable mixed-field neutron + γ-ray dose rates, only acetaldehyde and methanol were quantifiable for the specified dose of 50 kGy across the dose rate range from 0.52 to 8.12 kGy min^{-1}. Figure 38 shows the concentration as a function of the dose rate for a) acetaldehyde and b) methanol, respectively. Figure 38 shows the *G*-value as a function of the dose rate for c) acetaldehyde and d) methanol, respectively. The data used to compile Figure 38 derive from the following samples: 39 to 42 (neutron+γ, PP) listed in Table 15.

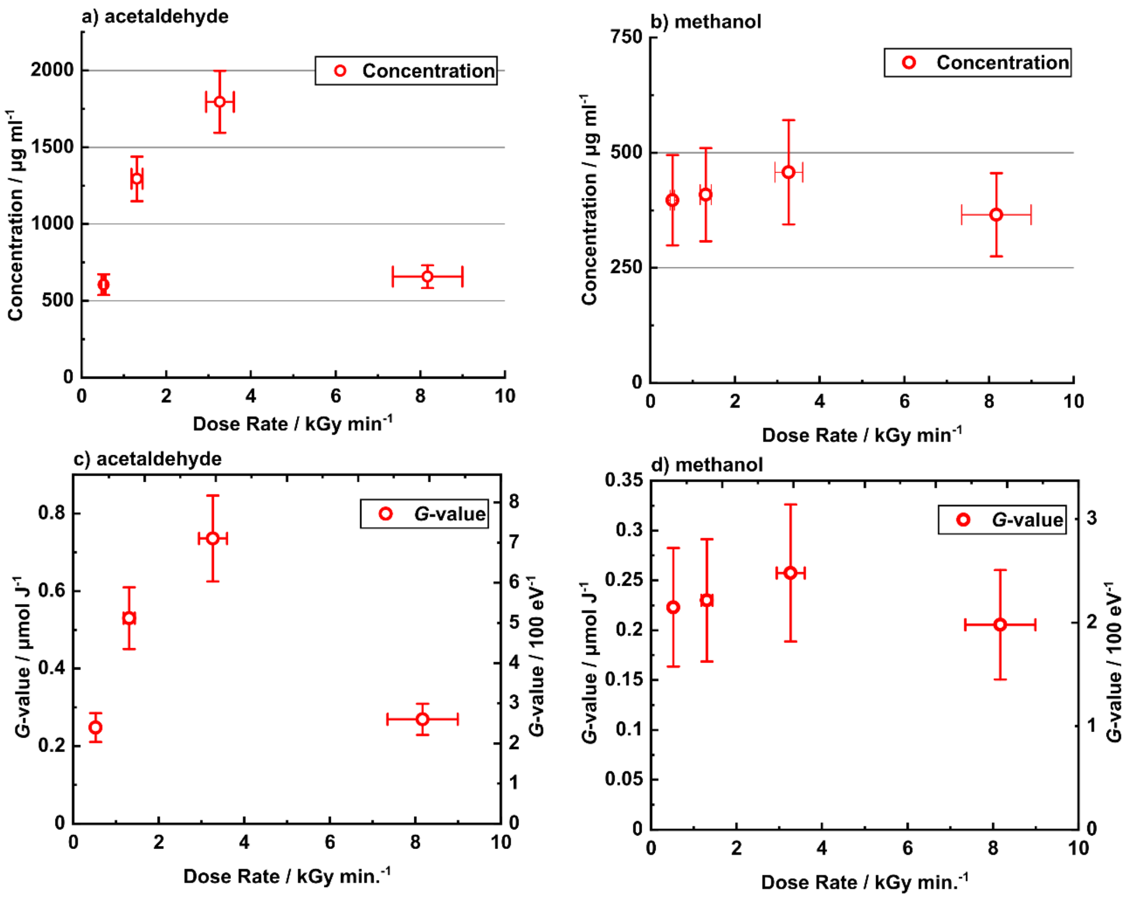

Figure 38: Concentration and radiation chemical yields (*G*-value) as a function of neutron + γ-ray dose rate. From neat ethylene glycol samples, **a** and **b** display the concentration data for acetaldehyde and methanol, respectively. **c** and **d** display the *G*-value for acetaldehyde and methanol, respectively. All samples were irradiated with a total dose of 50 kGy. Error bars indicate the relative combination of instrumental, calibration, and dose errors for *G*-values with concentration errors deriving from calibration curve standard deviations. The datasets are available in Appendix A, Table A4 and Table A11.

For acetaldehyde, there appears to be a preference in *G*-value for neutron + γ-ray dose rate at 3.27 kGy min^{-1} (whilst still lower than corresponding γ-ray only irradiations). These data could explain the trends indicated in Figure 31 with the corresponding drop in *G*-value from absorbed doses above 50 kGy; rather than the absorbed dose causing the drop in *G*-value, the data here indicate that the accompanying increase in dose rate is at minimum, contributing to the observed drop in *G*-value. The high dose rate data, (~8.17 kGy min^{-1}) possibly indicates the increased overlapping of energetic spurs and reduction of the require acidic and radical species for acetaldehyde production, as discussed later in chapter 5.6.1.

For methanol, the data indicates no clear variation of *G*-value between different mixed-field dose rates explored. Therefore, the preference for methanol production as seen previously in Figure 33 is thought to be a result of the total absorbed dose and the cumulative temperature rise estimated in the sample as described in the literature [277]. The reactions for both acetaldehyde and methanol are discussed in chapter 5.6.1. For both ethyl acetate and acetic acid, their peaks were neither detectable nor quantifiable for the neutron + γ-ray 50 kGy irradiations for varying dose rates.

4.6 Glycerol

4.6.1 Radiolysis Products: Qualitative

The following section qualitatively describes the radiolysis products observed from both mixed-field neutrons + γ-ray and γ-ray only irradiations for neat glycerol via liquid injection GC-MS analysis. All following data is from samples that have been irradiated using the TriC of the JSI reactor, as described in sections 3.4.2 and 3.4.3. Figure 39 displays the labelled TICs spectra (black line) for: a) γ-ray only (shutdown mode), and b) mixed field neutron+ γ-ray (operational mode) irradiations for neat glycerol. Both figures are compared against similarly diluted unirradiated samples (pink) and ethanol solvent blanks (blue). TICs of samples 11 (neutron+γ), 49 (γ-only) and 77 (control) listed in Table 15 and Table 16 are those used to produce the following figure, along with an ethanol solvent blank.

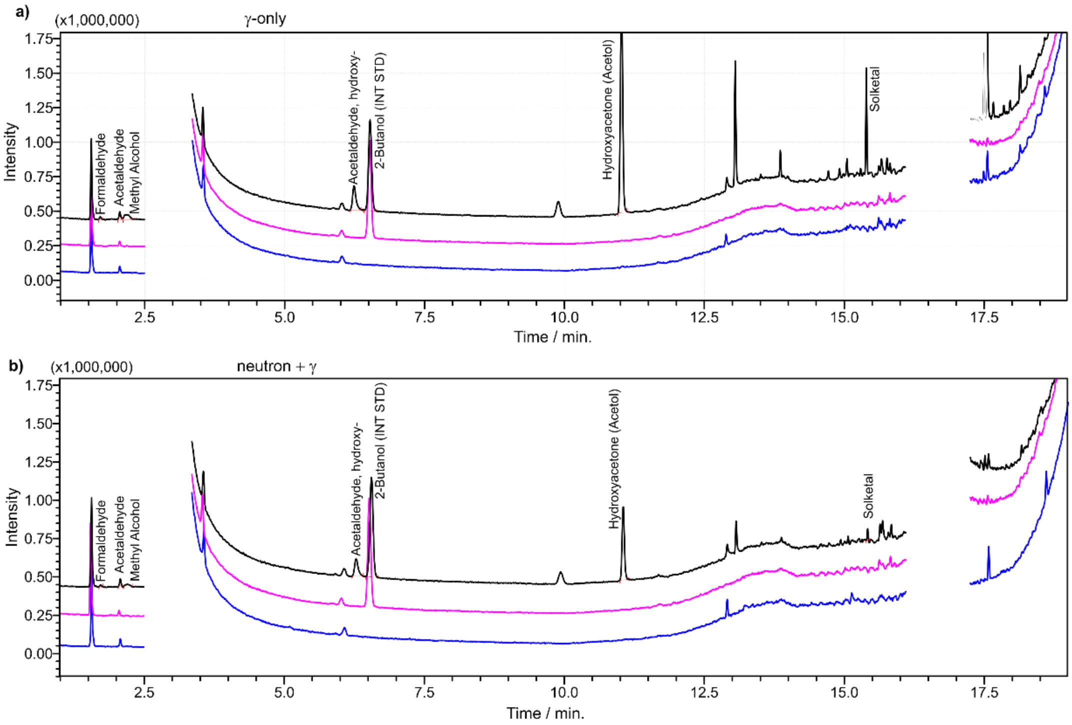

Figure 39: Total Ion Chromatograms of liquid-injected irradiated neat glycerol samples within PP vials, diluted in ethanol post-irradiation and compared against unirradiated controls and solvent TICs. Black line = 50 kGy irradiated glycerol sample of the specified irradiation type with identified peak labels. Pink = unirradiated glycerol control sample, Blue = Ethanol. **a** γ-ray only and, **b** mixed field neutron + γ-ray irradiations.

Solvent cuts are observed at 2.5 minutes and 16.1 minutes for ethanol and glycerol, respectively to prevent detector saturation. As for ethylene glycol with different irradiation types, both irradiation types with glycerol samples produce a similar set of radiolytic products. Any missing peaks in the mixed-field spectra are thought to be related to concentrations below the LOD of the MS method. Table 27 lists the products detected via full scan range monitoring after both types of irradiations. The table shows the % similarity match with the quoted analyte and indicates if the analytes have been confirmed using purchased standards. Ethanol and acetone as radiolytic products were also observed within the retention time window for ethanol solvent, using a different dilution solvent of propan-1-ol but were not quantified.

Table 27: Qualitative radiolysis products of glycerol from either mixed-field neutron + γ-ray or only γ-ray irradiation using liquid sampling GC-MS. Displayed products are for γ-ray absorbed doses above 20 kGy. Molecule similarity comparison against the NIST11 MS spectrum patterns, products were confirmed with analytical standards where applicable.

Number	**Product**	**Peak Retention Time (min.)**	**% Similarity**	**Confirmed Using Standards (Y/N)**	**Reported in Literature? Of Glycerol or Similar Alcohols (Y/N) with Ref.** [3, 52, 240]
1	Formaldehyde	1.7	95	N	Y
2	Acetaldehyde	2.1	96	Y	Y
3	Methanol	2.2	90	Y	Y
4	Ethanol	3.0	96	N	Y
5	Acetone	3.2	97	Y	Y
6	Glycolaldehyde Dimer	6.2	97	Y	Y
7	Acetol	11.0	98	Y	Y
8	Glyceraldehyde	14.9	92	N	Y
9	Solketal ((2,2-Dimethyl-1,3-dioxolan-4-yl)methanol)	15.4	98	Y	N
10-24	14 Unidentifiable Products*		<88	-	-

*Radiolysis products yet unidentified – The majority are higher-order products, with large Mr’s and longer retention times.

The majority of the radiolytic products listed have been reported in the glycerol-related literature or general alcohol radiolysis literature. As expected, acetol, as one of the highest-yielding products reported [3] and displays one of the largest peak areas amongst all radiolytic products of glycerol.

A particularly notable difference is the observation of solketal. This has not been reported as a radiolytically-formed product from glycerol prior to this work. Similar to ethyl acetate being derived from ethylene glycol, solketal is interesting for two reasons: Firstly, solketal has a larger molecular mass (Mr) than the starting material (glycerol) whereas radiolysis typically promotes bond scissions over bond formations for simple compounds (apart from dimerization). Hence, this is an interesting product to derive radiolysis-related mechanisms. Secondly, solketal has the potential to be used as a fuel additive in petroleum-based transport fuels [109]. Blends with solketal have been shown to prevent irregular fuel combustion, improve octane numbers and to lower particulate emissions [322]. Other reports explore the use of solketal in fuel blends for aviation applications since solketal has excellent ice inhibition properties [323] and improves storage stability [324], specifically with biodiesel-based blends [322, 325].

Several reasons might explain to explain why solketal was not detected previously: i) it is likely to be a secondary product and therefore low *G*-values are expected, resulting in low concentrations that are hard to detect; ii) the low absorbed doses (up to 1.4 kGy) associated with the prior art result in low initial concentrations, and iii) very dilute (<1 M) aqueous glycerol samples again limit the maximum possible concentration.

Some of the radiolytic products in Table 27 were only observable, such as ethanol and acetone using propan-1-ol as the dilution solvent. The irradiated samples shown in the chromatograms of Figure 39 show a few relatively large radiolysis product peaks which have not yet been identified. Consequently, Table 28 lists the retention times, relative peak sizes and the main EI mass fragmentation peaks from unidentifiable peaks in Figure 39.

Table 28: Unidentified large analyte peaks from neat glycerol radiolysis. EI fragment patterns are shown in Appendix A, Figure A13.

Unknown #	Retention Time / min.	Suggested Analyte (NIST 11 Database)	% Similarity	Main MS Fragments
1	9.9	Ethyl hydroyacetate	83	31, 61, 45, 75
2	13.1	1-Butanol	84	46, 43, 56, 31
3	13.8	1,1-Dimethoxyacetone	81	47, 43, 75, 73

Additionally, as observed previously in this work with ethylene glycol (Table 25), a polymeric substance is also detected from the γ-ray radiolysis of glycerol at 17.6 minutes in Figure 39. The closest identified match for this was pentaethylene glycol but it did not match the MS pattern or retention time of the pentaethylene glycol analytical standard. Hence, this large molecular mass (Mr) polymer peak is likely to be a polymer mixture of different oxygenated monomers.

4.6.2 Quantitative Analysis

One of the main products from glycerol radiolysis in this work, acetol has been detected regularly with large relative peak sizes compared to other detected products (via GC-MS analysis and shown in Figure 39). These large chromatography peaks suggest high concentrations and subsequent large chain-reaction level *G*-values. Acetol was chosen as the single radiolysis product in which to focus quantification amongst the changing various parameters for reliable peak quantification. Solketal, as a previously unreported radiolysis product and a potentially useful petroleum fuel blend additive, was also quantified with interest. The following subsections explore the sample and radiation parameters and their effects on the observed radiolysis values of these analytes.

4.6.2.1 Neat Glycerol with Absorbed Dose, Vial Type and Radiation Type

The two radiolytic analytes of acetol and solketal have been quantified by calibration curves of the diluted purchased standards. Due to numerous standard calibration curves utilized over the quantitation process, an example of the curves is shown in Appendix A, Figure A7. The following sections (4.6.2.2 to 4.6.2.4) show the absorbed dose dependence of concentrations, *G*-values, and mass productivity for both acetol and solketal in neat glycerol samples. A zero-dose *G*-value has been determined via extrapolation with the absorbed dose vs *G*-value graphs since a zero-dose *G*-value is commonly stated in the radiolysis literature since it allows for wider comparisons. Each analyte has been compared against the three variable parameters of vial type, irradiation type, and absorbed dose, as per its figure for concentration, *G*-value, and mass productivity, with molar % yield also described occasionally. Experimental data for neat glycerol samples have been tabulated for concentration (Appendix A, Table A6 and Table A7), *G*-values, and mass productivity (Appendix A, Table A13 and Table A14) for referencing and future comparisons. The data used to compile Figure 40, Figure 41, Figure 42 and Figure 43 derive from the following samples: 9 to 14 (neutron+γ, PP), 47 to 52 (γ rays, PP), 82 to 87 (neutron+γ, BS), and 94 to 99 (γ rays, BS) listed in Table 15 to Table 17.

4.6.2.2 Acetol

As shown in Figure 40, the concentration of acetol increases with the absorbed dose and matches the expected linear trend for most radiolytically-produced species from solutes [121, 207-209], up to a certain absorbed dose (as shown in Figure 12). Acetol concentration increases at a faster rate with total absorbed dose from γ-ray only irradiations giving superior radiation chemical yields compared to mixed-field irradiations. Figure 40 shows the concentration obtained for acetol from neat glycerol samples of both vial types.

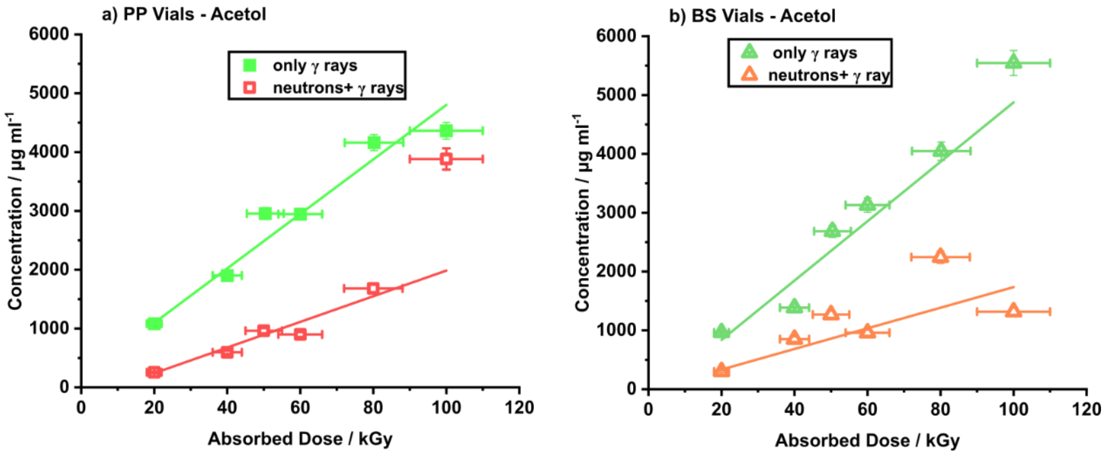

Figure 40: Concentration of radiolytic acetol for the specified absorbed dose for γ-ray (green) and neutron + γ-ray (red) irradiations of neat glycerol. **a** Polypropylene vial, PP (circles and squares). **b** Borosilicate vials, BS with Al/Si septa (triangles). The data are available in Appendix A, Table A6 and Table A7.

As expected, with both modes of irradiation, the concentration of acetol increases linearly with an increased absorbed dose from the origin, suggesting acetol is a primary radiolysis product (as per Figure 12). Figure 41 shows the absorbed dose dependence of *G*-values and mass productivity of acetol from both irradiation types. As with acetaldehyde from ethylene glycol, the calculation process to calculate the *G*-values and mass productivities for acetol from glycerol using the GC-MS data can be described. The following paragraph will detail this calculation process for sample 11 (50 kGy neutron+γ-ray, PP) as listed in Table 15 as an example. Firstly, the concentration of acetaldehyde from the diluted sample 11 (50 kGy neutron+γ-ray, PP) was measured at 36.8 µg ml^{-1} using the GC-MS and the internal calibration curves for acetol. Accounting for the dilution ratio of 0.0383 for the sample as defined in chapter 3.6 using equation (55) and (56), the concentration of acetol in the neat sample was determined to be 963 µg ml^{-1} using equation (54). Using equation (57), the total mass of acetol is calculated, by multiplying the concentration of acetol in the neat sample by the volume of the irradiated sample (organic mass ÷ organic density = 1.254 g ÷ 1.261 g cm^{-3} = 0.994 cm^{3}) to get the total mass of 958 µg. Using equation (58), the total moles of the analyte is calculated by dividing the total mass by the molecular mass of acetol (74 g mol^{-1}) to get the total moles of 12.93 µmoles within the irradiated sample. Using equation (59), the *G*-value is calculated by dividing the total moles by the energy into the sample (50 kGy × 1.254 g = 63.20 J) to result in a *G*-value of 0.20 µmol J^{-1}. Mass productivity % is calculated using equation (46) and the analyte mass from equation (57). For sample 11, the mass of acetaldehyde is divided by the mass of the starting organic sample (0.000958 g ÷ 1.254 g) to result in a mass productivity % of 0.0764%. The process to calculate *G*-values and mass productivities of solketal and acetic acid are similar with each process accounting for the different molecular masses for each analyte accordingly. X-axis errors of ±10% were derived from dosimetry accuracy as mentioned in chapter 3.4.2. Y-axis errors for concentration (also mass productivity) were derived from the relative standard deviation percentage (RSD%) of the calibration curve, for sample 11 measuring acetol, it was 4.64%. For *G*-value errors, the y-axis error for concentration is combined via relative error addition with the 10% error for the absorbed dose (±0.023 µmol J^{-1} for acetol from sample 11). Although the analytical workup errors were also added via relative error addition, they were negligible compared with the RSD% from the calibration curves or the 10% uncertainty for the dosimetry.

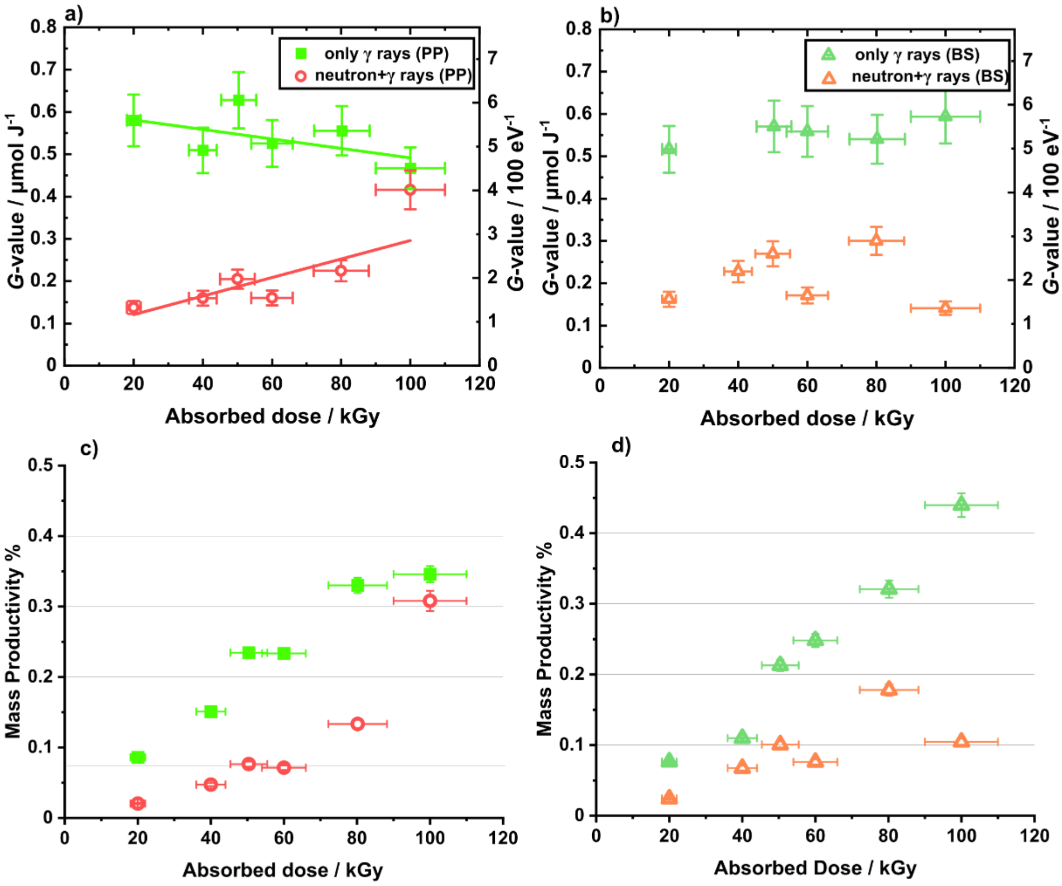

Figure 41: Radiation chemical yields (*G*-value) and mass productivities of acetol for the specified dose for γ-ray only (green) and neutron + γ-ray (red/orange) irradiations of neat glycerol. γ-ray only dose rate ~40 Gy min. $^{-1}$ and neutron + γ-ray dose rate of 1.64 to 6.5 kGy min. $^{-1}$ **a** *G*-values with polypropylene vials (squares and circles). **b** *G*-values with borosilicate vials with Al/Si septa (triangles). **c and d** mass productivity of PP and BS vials, respectively for the two irradiation types. The data are available in Appendix A, Table A13 and Table A14.

There appears to be a significant difference in acetol *G*-values between γ-ray only irradiated and neutron + γ-ray irradiated samples. The data in Figure 41 may also suggest some convergence between the two different irradiation types for higher absorbed doses, although the errors limit the extent to which this can be confirmed. There also appears to be little difference between the *G*-values obtained for borosilicate and polypropylene vials of identical irradiation types. However, the subtle differences in *G*-values do result in different trends of *G*-values being observed between different vials to counter the convergence theory.

4.6.2.3 Solketal

Solketal has been considered further, as per Figure 42 which shows the solketal concentration dependence on absorbed dose for the different vial and irradiation types. The calculation process for concentration, *G*-values, and mass productivities of solketal is alike to those described in 4.6.2.2 for acetol, but accounting for the different calibration curves and the analyte molecular mass (132.2 g mol^{-1}).

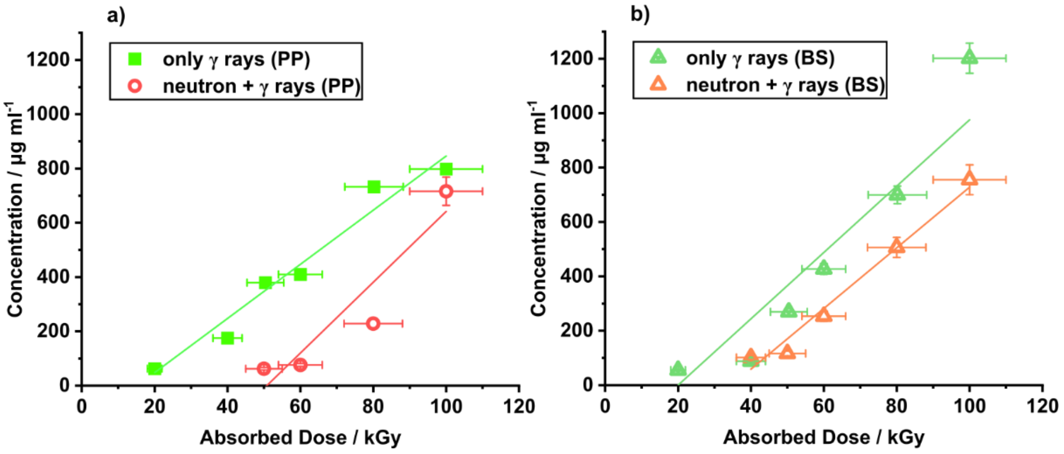

Figure 42: Concentration of radiolytic solketal for the specified absorbed dose for γ-ray only (green) and neutron + γ-ray (red) irradiations of neat glycerol. **a** Polypropylene vials (Squares). **b** Borosilicate vials with Al/Si septa (Triangles) as radiation vessels. The data are available in Appendix A, Table A8 and Table A9.

From Figure 42, the linear best-fit lines for solketal concentrations from all irradiation and vial types show *y*-intercepts significantly below the origin. This implies that solketal is generated as a secondary radiolysis molecular product and that there is a reliance on the concentration of a primary radiolysis species generated first, as described in Figure 12b and chapter 2.12.1. Figure 43 shows the *G*-values and mass productivity of solketal for both irradiation and vial types.

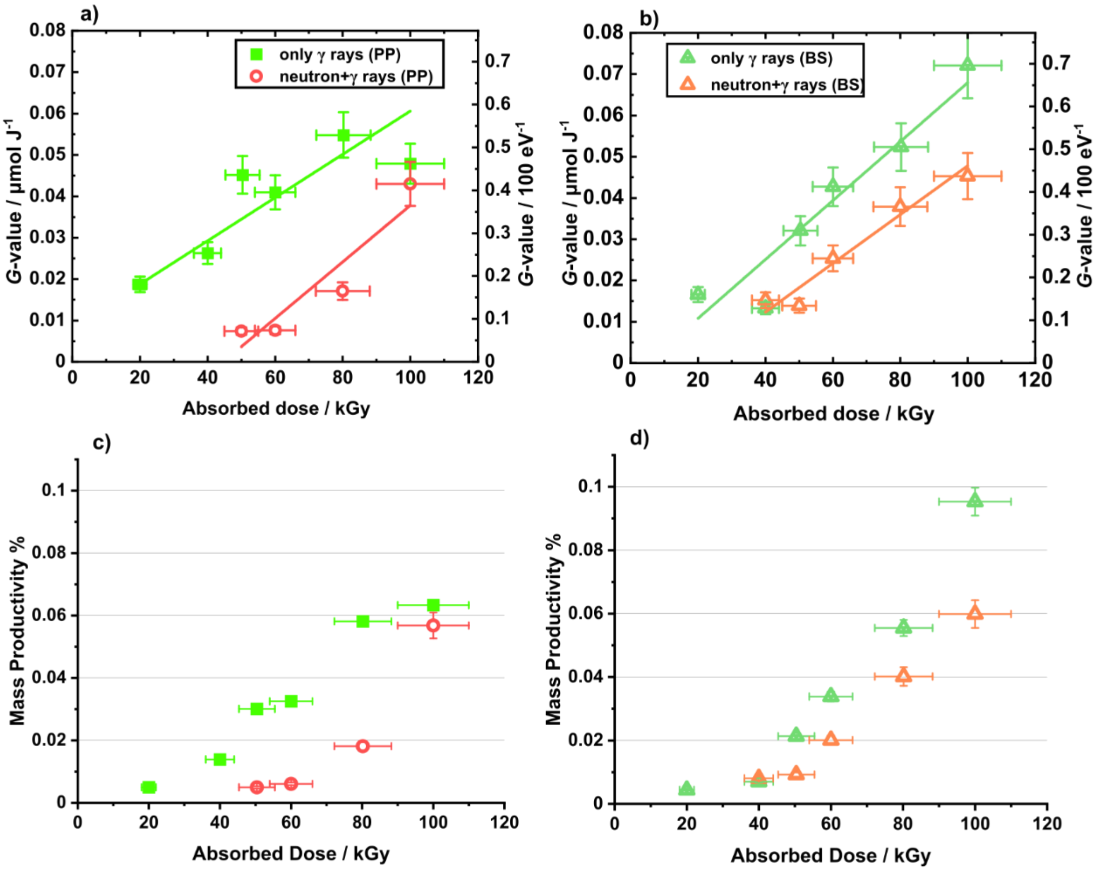

Figure 43: *G*-values and mass productivity of solketal from varying the absorbed dose for γ-ray (green) and neutron + γ-ray (red) irradiations of neat glycerol. **a** Polypropylene vial (squares), **b** Borosilicate vials with Al/Si septa (triangles), **c** and **d** mass productivity of PP and BS vials, respectively for the two irradiation types. The full dataset is available in Appendix A, Table A13 and Table A14.

The linearly increasing *G*-value trend with absorbed dose observed in Figure 43a and b support the theory that solketal is a secondary product. Comparisons between the two irradiation modes show that there is a consistent difference, with γ-ray only irradiation *G*-values superior to mixed-field neutron + γ-ray irradiations. Similarly, with acetol, there are only minor differences in *G*-values between vial types when errors are considered. Compared with the acetol data, the *G*-values of solketal are a factor of approximately ×10 less from neat samples, suggesting a simple radiolysis process that is limited by other primary radiolysis processes and related factors. There does not appear to be a statistical difference in concentration or *G*-value of solketal between the samples in the BS and PP vials across the dose range. This suggests that any trace concentrations of acetone generated from PP vial degradation as suggested in chapter 3.2 is minimal, even as acetone here would be the limiting reagent.

4.6.2.4 Dose Rate

The data used to compile the following Figure 44 derive from the following samples: 39 to 42 (neutron+γ, PP) listed in Table 15. Figure 44 shows the dose rate dependence of concentration and *G*-values for acetol and solketal derived from neat glycerol samples between dose rates of 0.52 to 8.17 kGy min^{-1}, for identical absorbed doses of 50 kGy.

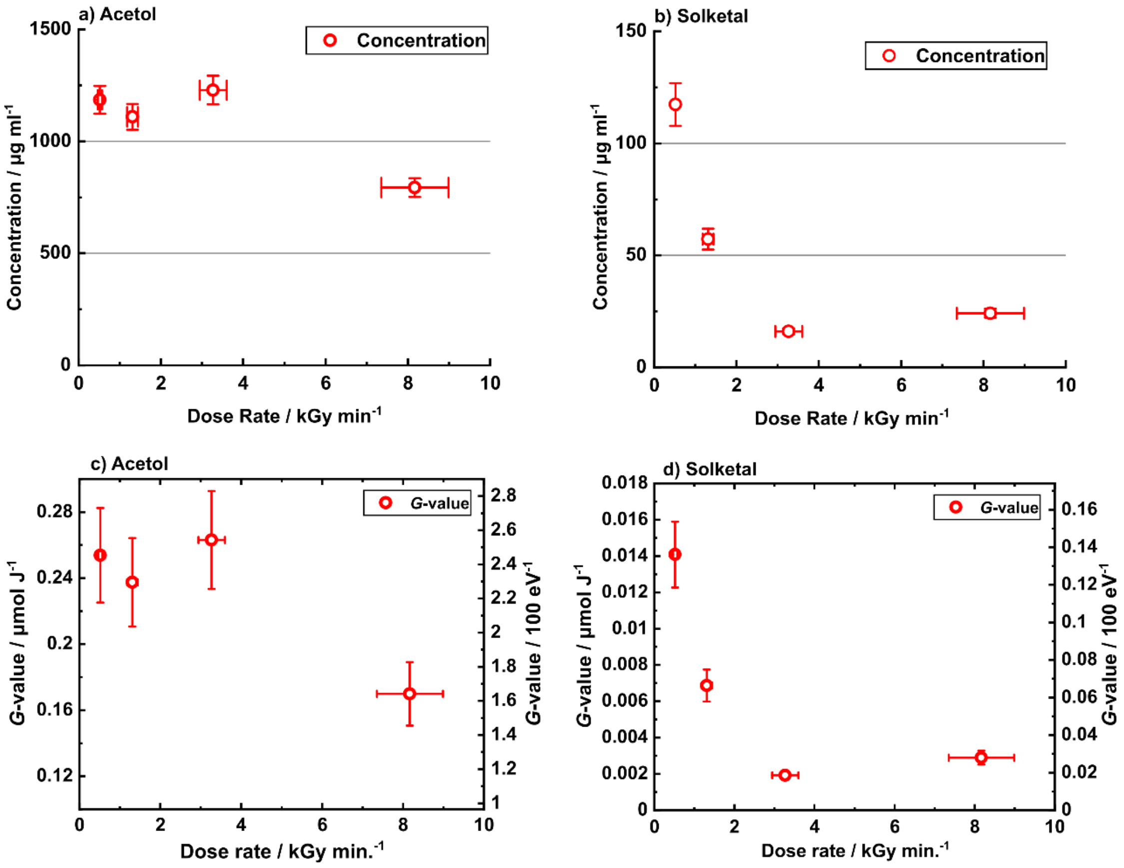

Figure 44: Concentration and *G*-values as a function of neutron + γ-ray dose rate. From neat glycerol sample for; Concentrations of **a** acetol and **b** solketal with corresponding *G*-values of **c** acetol and **d** solketal. All samples were irradiated with a total absorbed dose of 50 kGy. The data are available in Appendix A, Table A6 and Table A13.

Firstly, the dose rates explored here are significantly larger than those quoted in the literature (≈0.008 kGy min^{-1}) for similar dose rate studies [3]. With only 4 data, acetol *G*-values exhibit an inconclusive dependence on mixed-field dose rate, with only one data point to suggest an inverse relationship with increased dose rate. However, the *G*-value dependence on dose rate for solketal is more evident, with a strong logarithmic decay relationship observed in Figure 44b.

4.6.2.5 Binary Mixtures

This section explores the dependence of water and % solute (glycerol) concentration upon the main product, acetol and the newly reported product, solketal for high % solute (glycerol) mixtures. Experimental data for aqueous glycerol samples have been tabulated for concentration (Appendix A, Table A8 and Table A9), *G*-values and mass productivity (Appendix A, Table A15 and

Table A16 Table A16) for reference and future comparisons. The data used to compile the following Figure 45 to Figure 47 derive from the following binary glycerol samples: 15 to 32 (neutron+γ, PP), and 53 to 70 (γ rays, PP) which are listed in Table 15 and Table 16. This is compared against the data previously shown for the neat glycerol samples which derive from the following samples: 9 to 14 (neutron+γ, PP), 47 to 52 (γ rays, PP) which are listed in Table 15 and Table A16.

Figure 45 shows the dependencies of acetol and solketal concentration from irradiated binary mixtures for γ-ray samples and mixed-field neutron γ-ray samples. Figure 46 shows the *G*-values and mass productivity dependencies for acetol and solketal derived from binary mixtures for γ-ray samples, with Figure 47 displaying these trends for mixed-field neutron + γ-ray samples. The calculation processes for concentration, *G*-values, and mass productivities of acetol and solketal in these binary mixtures are alike to those described in 4.6.2.2 and 4.6.2.3 but accounting for the different sample densities of 1.169 g cm^{-3}, 1.018 g cm^{-3}, and 1.115 g cm^{-3} for 70 wt.%, 63 wt.%, and 50 wt.% glycerol mixtures, respectively.

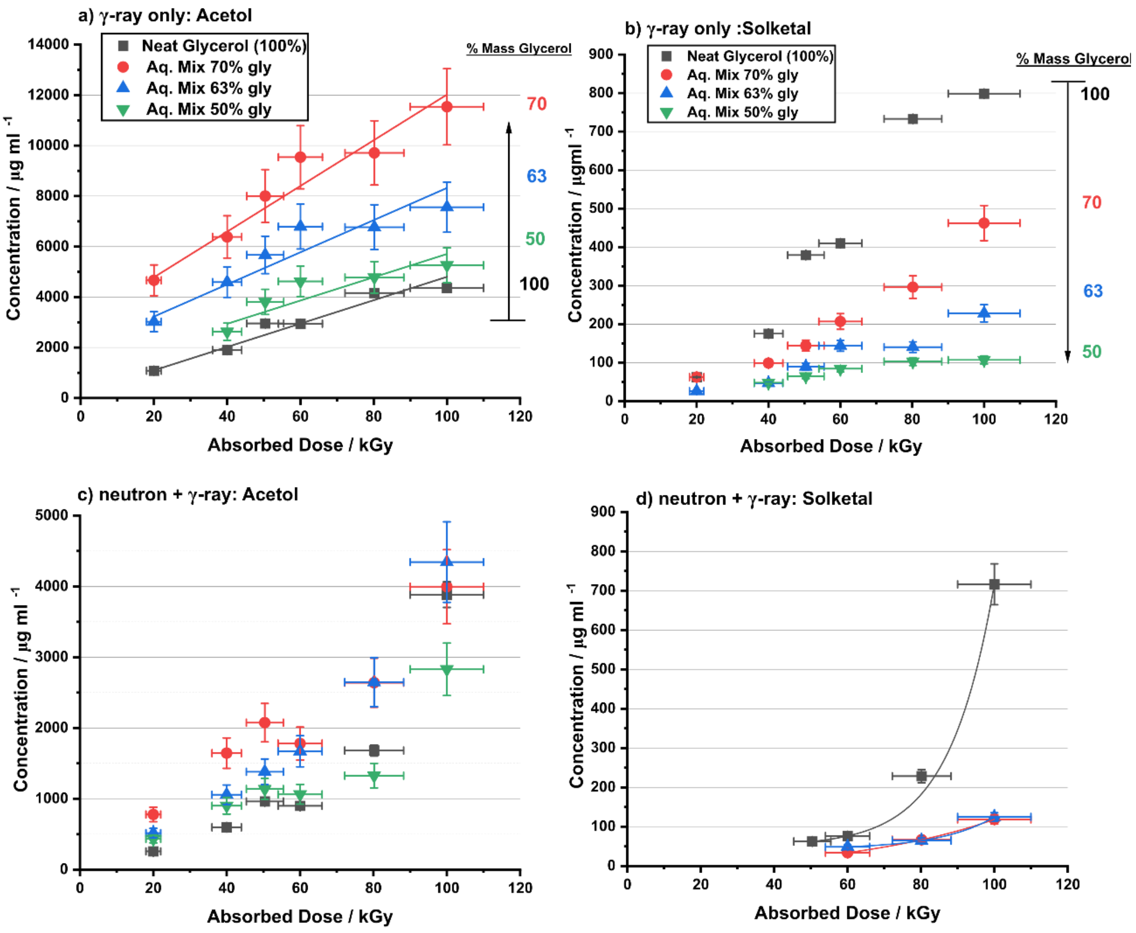

Figure 45: Concentration of radiolytic acetol and solketal for the specified absorbed dose for γ-ray only (**a** and **b**) and neutron + γ-ray (**c** and **d**) irradiations of binary mixtures in PP vials. Different mixtures are as follows: neat glycerol (black squares), glycerol-aqueous mixtures based on wt.%: 70% glycerol (red circles), 63% glycerol (blue upward triangles) and 50% glycerol (green downward triangles). **a** acetol and **b** solketal concentrations from γ-ray only irradiations. **c** acetol and **d** solketal concentrations from neutron + γ-ray irradiations. The data are available in Appendix A, Table A8 and Table A9 (Produced by Plant A. G).

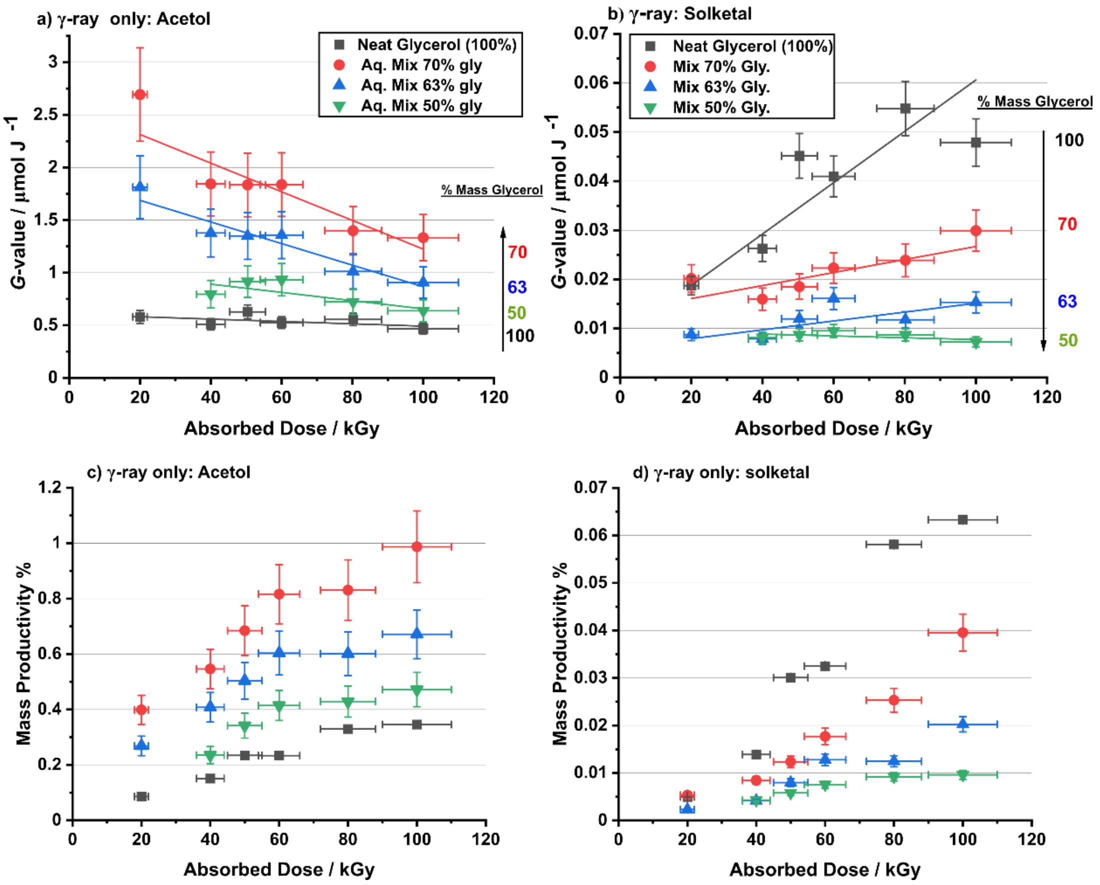

Figure 46: *G*-values and mass productivities of acetol and solketal from aqueous glycerol mixtures of varying concentrations with delayed γ-ray only absorbed doses with **a** and **b** from acetol and solketal *G*-values respectively**,** **c**, and **d**, acetol and solketal mass productivity percentages respectively. Different mixtures are as follows: neat glycerol (black squares), glycerol-aqueous mixtures based on wt.%: 70% glycerol (red circles), 63% glycerol (blue upward triangles) and 50% glycerol (green downward triangles). The data are available in Table A15. (Produced by Plant A. G).

Figure 46a shows that with a small addition of water into the neat samples, the *G*-values of acetol increase, with the highest *G*-value observed for the highest % solute mixture (70 wt.% glycerol: 30 wt.% water) of (2.7 ± 0.4) µmol J^{-1} with 20 kGy. This small addition of water for superior acetol production is explored in chapter 5.5. With further dilution, acetol *G*-values decrease to converge with neat glycerol samples, with the negative trend expected to continue with further dilution. A clear negative trend of acetol *G*-value with the increased absorbed dose for γ-irradiated samples is observed, as expected with the synthesis of a primary radiolytic species. As shown by Figure 46c, the maximum mass productivity for acetol of (1.0 ± 0.1)% is achieved for the 100 kGy-irradiated 70 wt.%-glycerol binary mixture.

As shown by Figure 46b, further dilutions with water progressively decrease the measured *G*-values of solketal, with the neat glycerol samples showing superior solketal *G*-values.

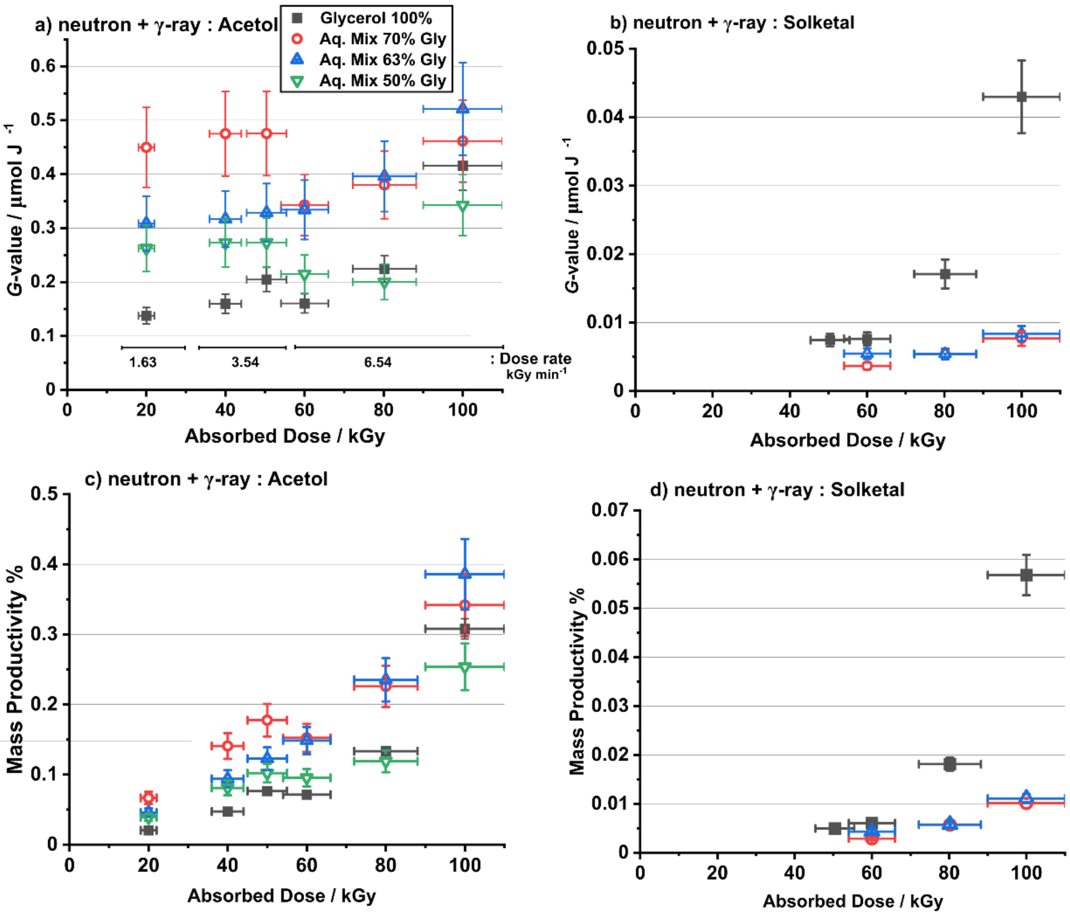

Figure 47: *G*-values and mass productivities of acetol and solketal from varying aqueous glycerol mixtures of varying concentration with mixed neutron + γ-ray absorbed doses; **a** acetol *G*-values and, **b** and solketal *G*-values respectively. **c** and **d** show acetol and solketal mass productivities, respectively. Different mixtures are as follows: Neat glycerol (black squares), glycerol-aqueous mixtures based on wt.%: 70% glycerol (red circles), 63% glycerol (blue upward triangles) and 50% glycerol (green downward triangles). The data are available in Table A16.

As seen previously, in Figure 43 for γ-ray irradiated neat samples, the mixed-field neutron + γ-ray binary mixture samples (Figure 47) also show significantly lower *G*-values compared with γ-ray only samples of comparable absorbed doses; approximately by a factor of 0.38 in terms of *G*-values for the binary mixtures.

Further dilution is also accompanied by significant decreases in the observed *G*-values for solketal, with the 50 wt.% mixtures not having a quantifiable solketal peak across the mixed-field absorbed dose range. Additionally, Figure 47a shows that increasing the neutron + γ-ray dose rate causes a decrease in acetol *G*-value, compared with the projected trend from lower dose rate samples. This fall in *G*-value is evident between samples of 50 kGy and 60 kGy for neat glycerol, 70 wt.% glycerol and 50 wt.% glycerol sample mixtures. Similarly, as with γ-ray irradiated samples, binary mixtures irradiated with a mixed-field dose results in an increase in acetol *G*-values with increasing absorbed dose compared with neat glycerol samples. Comparing the two types of irradiations from Figure 46 and Figure 47, the γ-ray only (shutdown) irradiations produce significantly better *G*-values and mass productivities than mixed-field irradiations (operational) across all sample parameters for binary mixtures.

4.6.2.6 Zero Dose *G*-values

Since the *G*-value dependence on absorbed dose was plotted for acetol and solketal for different mixtures and irradiation types, *zero dose G*-values can be determined for these products. Table 29 indicates the *zero dose G*-values for the different products from different radiation types.

Table 29: Extrapolation to *zero dose G*-values of acetol and solketal from glycerol samples in polypropylene (PP) vials.

		Acetol [a]		**Solketal** [b]	
Irradiation Type	**Mixture Type (wt.%)**	**Zero-dose *G*-value / µmol J^{-1}**	**Error**	**Zero-dose *G*-value / µmol J^{-1}**	**Error**
γ-rays only	Neat Glycerol (100%)	0.60	0.06	0.01	0.05
	70% Glycerol, 30% H_2O	2.6	0.4	0.013	0.003
	63% Glycerol, 37% H_2O	1.9	0.3	0.006	0.002
	50% Glycerol 50% H_2O	1.1	0.2	0.010	0.002
Mixed Neutron + γ rays	Neat Glycerol (100%)	0.15	0.02	0.007	NA
	70% Glycerol, 30% H_2O	0.45	0.08	-0.002	0.003
	63% Glycerol, 37% H_2O	0.302	0.002	0.001	0.004
	50% Glycerol 50% H_2O	0.26	0.06	NA	NA

[a]Acetol: γ-ray plots = linear dependent plots, mixed-field plots = exponential growth fit
[b]Solketal: γ-ray plots = linear dependent plots, mixed-field plots = exponential growth fit

In the literature, the γ-irradiated samples for acetol formation show an increasing *G*-value trend with increased solute concentration with a zero dose *G*-value maximum of 0.23 µmol J^{-1} for a 4.6 wt.% diluted glycerol sample (4.6% the most concentrated sample irradiated). The data here show that the trend extends further for more concentrated glycerol samples, giving a zero dose *G*-value maximum of 2.7 μmol J^{-1} for 70 wt.% glycerol samples. Table 29 also shows that solketal has a zero-dose *G*-value close to 0 for all cases, confirming that it is a secondary product that is dependent on the concentration of primary radiolysis species. As large, absorbed doses were explored in this research (>20 kGy), the *G*-value trend behaviour with smaller doses (<1 kGy) is not known. However, based on the literature, the zero-dose *G*-values for acetol specifically are likely to be higher than the values indicated in Table 29, due to secondary processes reducing the concentration of acetol with larger absorbed doses.

4.6.3 Ternary Mixtures

This section compares the glycerol-water-acetone mixtures against the previously described neat glycerol and binary aqueous mixtures for quantities of acetol and solketal. The data used to compile the following Figure 48 to Figure 51 derive from the following ternary glycerol samples: 108, 110, and 112 (neutron+γ, PP), 109, 111, and 113 (γ rays, PP), 114 to 116 (unirradiated controls) listed in Table 18. This is compared against the data already shown previously for the neat glycerol samples which derive from the following samples: 11 (neutron+γ, PP) and 49 (γ rays, PP), listed in Table 15 and Table 16.

Figure 48 shows the concentration of acetol and solketal produced within the ternary mixtures from 50 kGy irradiations, compared against equivalently irradiated neat glycerol samples and the unirradiated ternary mixtures (blank).

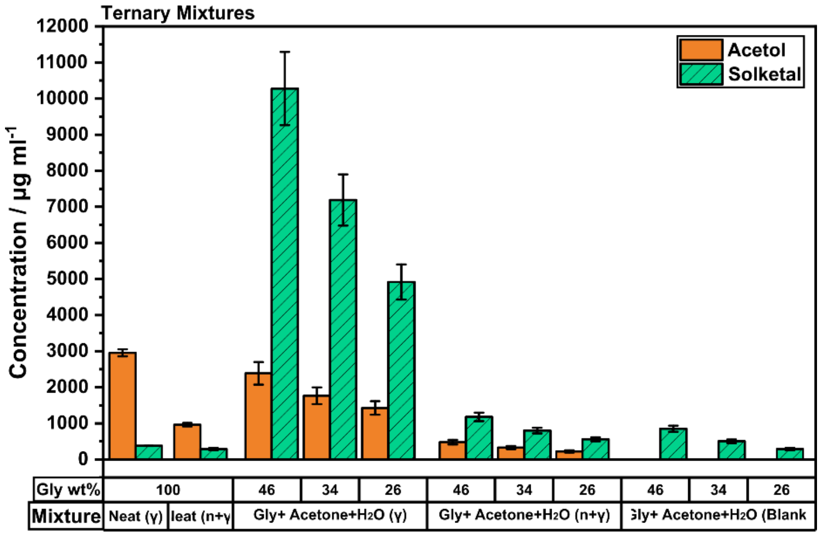

Figure 48: Concentration of acetol and solketal from ternary glycerol mixtures (samples 108 to 116 in Table 18) for 50 kGy of either γ-ray only or mixed-field neutron + γ-ray irradiated, compared against irradiated neat samples and unirradiated ternary mixtures. The indicated ternary mixtures containing glycerol, acetone and water have the following compositions in wt.%: **i)** 46, 28, 26; **ii)** 34, 34, 32; and **iii)** 26, 48, 26, respectively. Error bars represent the relative standard deviation from the calibration curves for each analyte, combined with any dilution work-up errors. Data are available in Appendix A, Table A10.

Figure 49 shows the *G*-values for acetol and solketal across the binary aqueous-glycerol and ternary glycerol-water-acetone mixtures for comparison. The calculation processes for concentration, *G*-values, and mass productivities of acetol and solketal in these ternary mixtures are like to those described in 4.6.2.2 and 4.6.2.3 but accounting for the different sample densities of 1.018 g cm^{-3}, 0.977 g cm^{-3}, and 0.928 g cm^{-3} for 46 wt.%, 34 wt.%, and 26 wt.% glycerol ternary mixtures, respectively as per Table 11. Tabulated data for comparison across all the various parameters explored and for easier comparisons with data from the literature are available in Table A17. Figure 49 displays the *G*-values, molar yields, and mass productivities for ternary mixtures irradiated with 50 kGy of either dose mode. A comparison between previous mixture types, control samples and the literature is given. The data for the ternary glycerol mixtures used in Figure 49, Figure 50, and Figure 51 derive from the following samples: 108, 110, and 122 (neutron+γ, PP), 109, 111, and 113 (γ rays, PP), listed in Table 18.

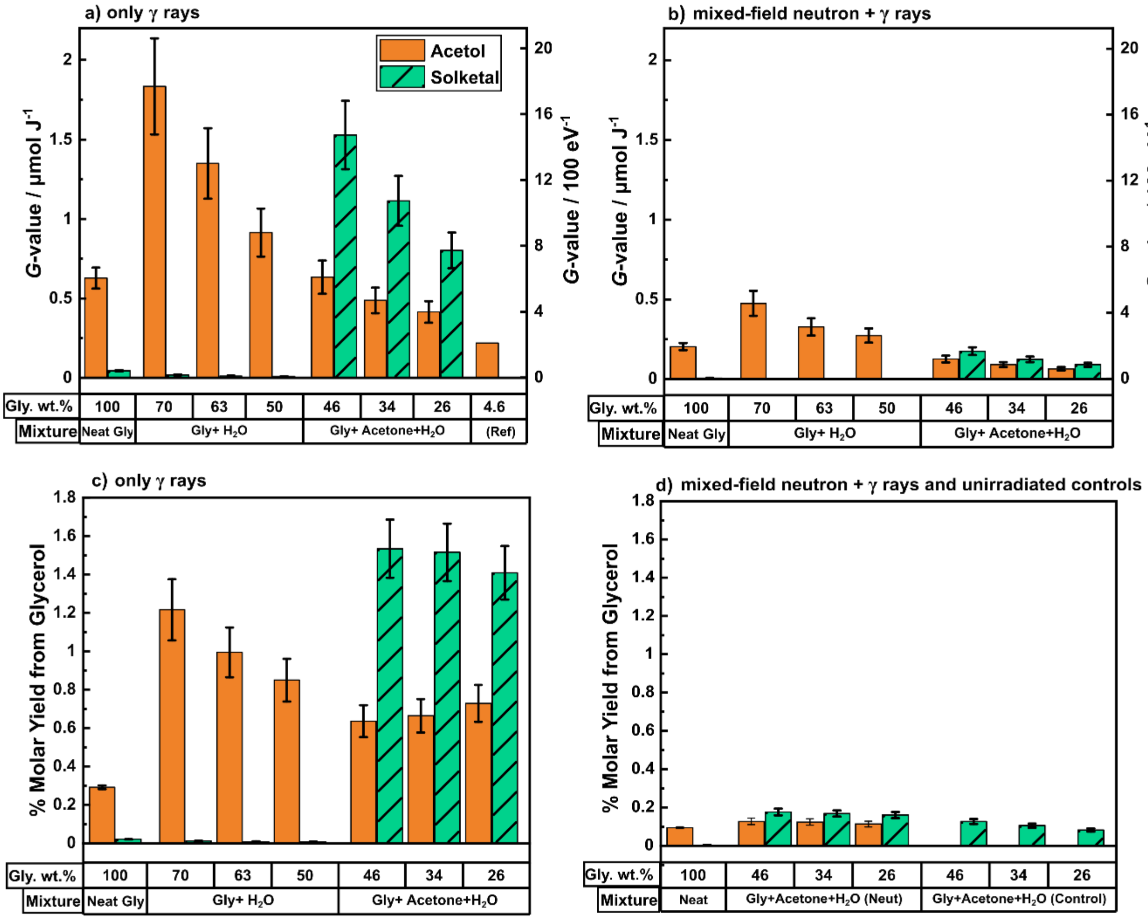

Figure 49: *G*-value and % molar yield of acetol and solketal from ternary (samples 108 to 116 in Table 18) and binary (67, 55, 61 from Table 16 and 29, 17, 23 from Table 15) glycerol mixtures for 50 kGy of either γ-ray only or mixed-field neutron + γ-ray irradiated samples. **a** *G*-values from γ-ray only irradiated samples with an average dose rate of 40 Gy min. $^{-1}$. **b** *G*-values from mixed-field neutron + γ-ray irradiated samples with a dose rate of 3260 Gy min. $^{-1}$. **c** % molar yields for only γ-ray irradiations. **d** % molar yields of mixed-field and unirradiated control samples. The indicated ternary mixtures containing glycerol, acetone and water have the following compositions in wt.%: **i)** 46, 28, 26; **ii)** 34, 34, 32; and **iii)** 26, 48, 26, respectively. (Data are available in Appendix A, Table A17. Error bars represent the combined relative errors from instrumental and dose uncertainties for each sample. Reference data [3] (Ref) for acetol used in **a,** used N_2O-saturated aqueous glycerol samples with a γ-ray dose and dose rate of 1.4 kGy and 8 Gy min. $^{-1}$, respectively.

The data in Figure 49, suggests the acetol *G*-value is strongly dependent on the initial glycerol concentration but the decreasing trend with further dilutions with water shifts persistently lower when also diluted with acetone, suggesting a competing reaction between acetol and solketal formation. Additionally, this extrapolation in trend, based on glycerol % matches the acetol *G*-value data from the literature, as indicated in Figure 49a. Most notably from Figure 49, solketal *G*-values increase significantly (by a factor of ~34 for the γ-ray irradiated ternary samples, relative to the neat glycerol samples. However, the mixed-field neutron + γ-ray irradiations of ternary mixtures only produce minor increases in solketal *G*-value (average factor of ~×1.6) and mass productivities compared with the unirradiated control sample mixtures as shown in Figure 49. Figure 50a and b show the mass productivity of acetol and solketal from the ternary mixtures for 50 kGy γ-ray only irradiated samples, 50 kGy neutron + γ-ray irradiated samples or the unirradiated control samples. Figure 50a, b, c, and d show the dependency on the ternary mixture composition for acetol and solketal as ternary plots.

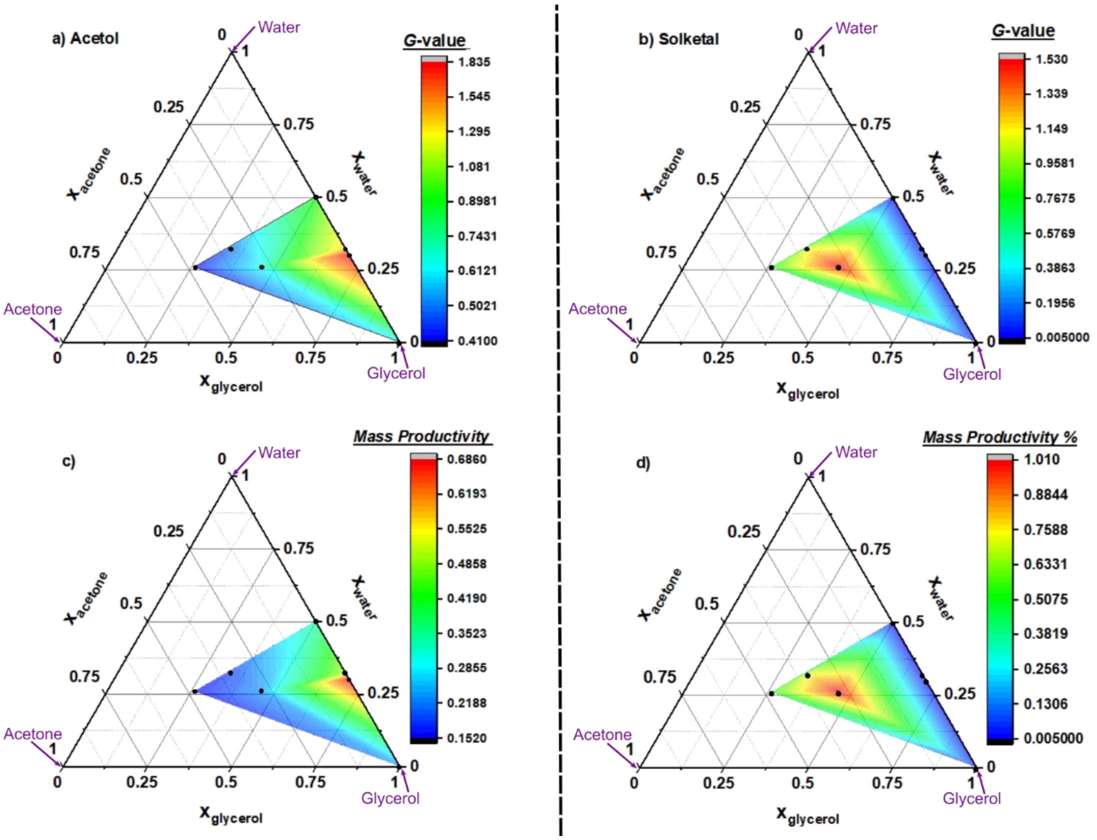

Figure 50: Ternary plots of radiation chemical yields (*G*-value) in µmol J^{-1} for samples of varying starting mixtures containing mass fractions of glycerol, acetone, and water of 50 kGy γ-ray only dose. *G*-values of, **a** acetol and, **b** solketal have been displayed with corresponding values for mass productivities in **c** and **d,** respectively. All mixtures within PP vials that have been irradiated with 50 kGy γ-ray only dose in the TriC. The 7 data points are indicated by black dots. A linear colour gradient is used for both *G*-value and mass productivity plots.

The ternary plots in Figure 50 support the interpretation that higher wt.% glycerol mixtures give higher *G*-values of both acetol and solketal. Further exploration of more aqueous binary and ternary mixtures with acetone will elucidate the optimum mixtures for both acetol and solketal production. It is predicted that the superior *G*-value for acetol may be discovered with binary aqueous mixtures of ≈90% wt.% glycerol due to a significant change in glycerol viscosity of 1414 to 219 mPa s from neat glycerol to 90% wt.% in water at 20°C [326]. This prediction is due to several factors: i) the dependence on the stabilized glycerol acidic species which promotes acetol synthesis and ii) the reliance on the diffusion-controlled mechanisms for acetol synthesis, which is dependent on sample viscosity, as explored in chapter 5.6.2.1.

For high solketal *G*-values, the optimum ternary mixture composition, by mass, is predicted to be mixtures with a low water content but still produce a miscible mixture. Therefore, the optimum mixture is thought to be approximately $X_{glycerol:water:acetone}$= 0.7, 0.15, 0.15 as mass fractions. This reliance on glycerol is again thought to be due to the dependency on the stabilized glycerol acidic species which also promotes solketal synthesis (Figure 56g). Additionally, the lower water concentration mixtures limit the reversible reaction from solketal as described by Le Chatelier's principle, i.e., the lower concentration of water, the slower the reversible reaction, and the higher the solketal concentration. This is explored further in chapter 5.6.2 with the reaction schemes.

4.6.3.1 Acetic Acid

With the addition of acetone into the starting aqueous glycerol mixture, acetic acid was detected in higher concentrations and was able to be quantified. Figure 51a and b show the concentrations and *G*-values for acetic acid, respectively from the ternary samples for both irradiation modes.

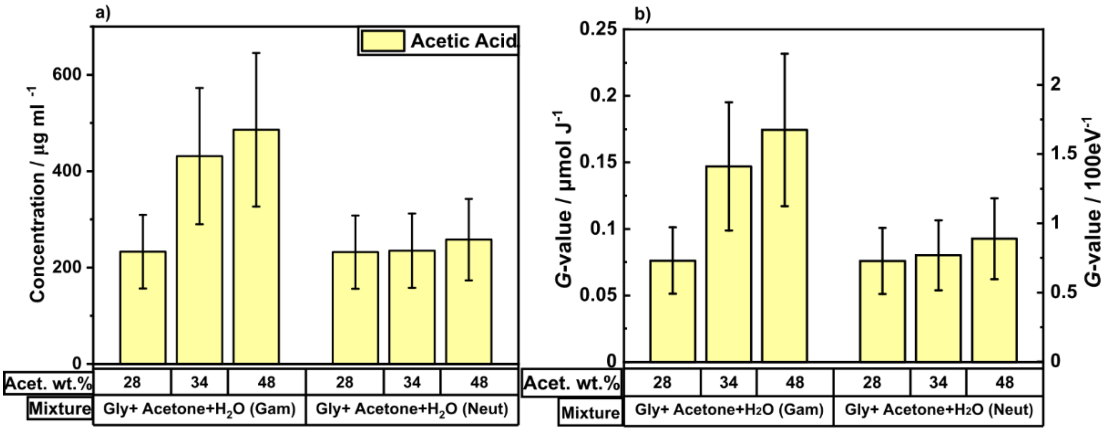

Figure 51: **a** Concentration and **b** *G*-values of acetic acid from the ternary (glycerol + acetone + water) mixtures using only γ-ray and neutron + γ-ray irradiations. Samples have been either irradiated with 50 kGy γ-ray only irradiations with an average dose rate of 40 Gy min^{-1} or 50 kGy neutron + γ-ray mixed field irradiations with dose rates of 3260 Gy min^{-1}.

Figure 51 shows comparable *G*-values of acetic acid between the two irradiation modes, considering the errors involved. The synthesis of acetic acid as a secondary or tertiary radiolysis product is consistent with the radiolysis of acetone [327]. It is theorised that acetone is synthesised as a minor primary or secondary radiolytic product from glycerol radiolysis. The maximum concentration of acetic acid generated in the ternary mixtures is (500 ± 200) µg ml^{-1} generating a calculated pH of 3.46.

4.7 Production Calculations with MCNP models

Using the MCNP models defined in chapter 3.7, the yearly maximum production capacity values of two different glycerol-based starting mixtures for radiolytic acetol and solketal production are given. Table 30 lists the maximum irradiated volume, γ-ray dose rate, acetol capacity and solketal capacity for each different scenario. The starting mixtures used for extrapolation were glycerol mixtures that produced the highest *G*-values for acetol and solketal, respectively.

Table 30: Scale-up values for each MCNP scenario showing the maximum production capacity per year of acetol and solketal. Starting mixtures of **i)** binary glycerol, water composition (70, 30 wt.%) and **ii)** ternary glycerol, acetone, and water composition (46, 28, 26 wt.%).

Scenario	**Radiation Source**	**Dose Rate / Gy min.$^{-1}$**	**Radiolytic organic volume / cm^3**	**Maximum Yearly Production Capacity / t year^{-1}**			
				i) Gly+Acetone+H_2O Mix		**ii) Gly+H_2O Mix**	
				Acetol	**Solketal**	**Acetol**	**Solketal**
1	TRIGA Shutdown	16.7	1.57×10^{2}	5.40×10^{-5}	1.45×10^{-3}	1.81×10^{-4}	2.51×10^{-5}
2	TRIGA at 250kW	3133.3	1.57×10^{2}	1.23×10^{-2}	5.22×10^{-2}	4.14×10^{-2}	9.02×10^{-4}
3	Krško Reactor	20.6	1.45×10^{6}	0.75	3.23	2.51	0.06
4	Krško Spent Fuel Pool	10.1	5.28×10^{7}	13.34	57.41	44.73	1.14

Additionally, Figure 52 shows the highest throughput scenarios for radiolytic acetol and solketal production.

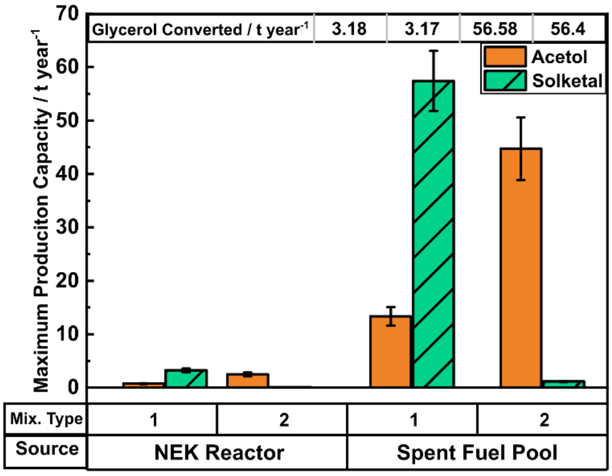

Figure 52: Max production values of acetol and solketal in t year^{-1} using the Krško reactor (50 organic pipes) and the Krško spent fuel pool (~1710 organic pipes) models and highest yielding mixtures. Mix 1= binary aqueous glycerol mixture (data from sample 67) and Mix 2 = ternary glycerol, acetone, and water mixture (data from sample 109).

The Krško spent fuel scenario, utilizing over 1710 spent fuel elements, offered the largest maximum production capacity of any of the radiation sources/scenarios, this is mainly due to the large volume available for irradiations due to the spacious spent pool facility. A maximum of (13 ± 2) and (58 ± 6) tonnes year^{-1} of acetol and solketal, respectively, could feasibly be generated from a theoretical spent fuel radiation-chemical facility with the optimum ternary mixtures used in this research. Additionally, optimum aqueous binary mixtures could produce acetol at (45 ± 6) tonnes year^{-1}. Comparing binary mixtures against ternary mixtures shows similar glycerol converted values, despite the large change in starting material composition and starting glycerol wt.%. This supports the theory of competing processes for acetol and solketal production.

4.8 Expansion to Europe-based Nuclear Facilities

This section details the expansion to a theoretical nuclear-biorefinery production network based in the geographical area of Europe for solketal production, as detailed in chapter 3.7.1. This shows which countries will benefit the most, the maximum production capacity for the current process and how effective radiolysis-derived solketal is as a bio-renewable component in modern fuel blend use in Europe. Extrapolating from the mixture with the highest observed *G*-value for solketal, a theoretical scale-up production network involving nuclear facilities in Europe is conceived. Figure 53 shows a map of countries with geographical Europe and their maximum production capacity of acetol and solketal, respectively, based on their net nuclear electrical capacity as of 2021.

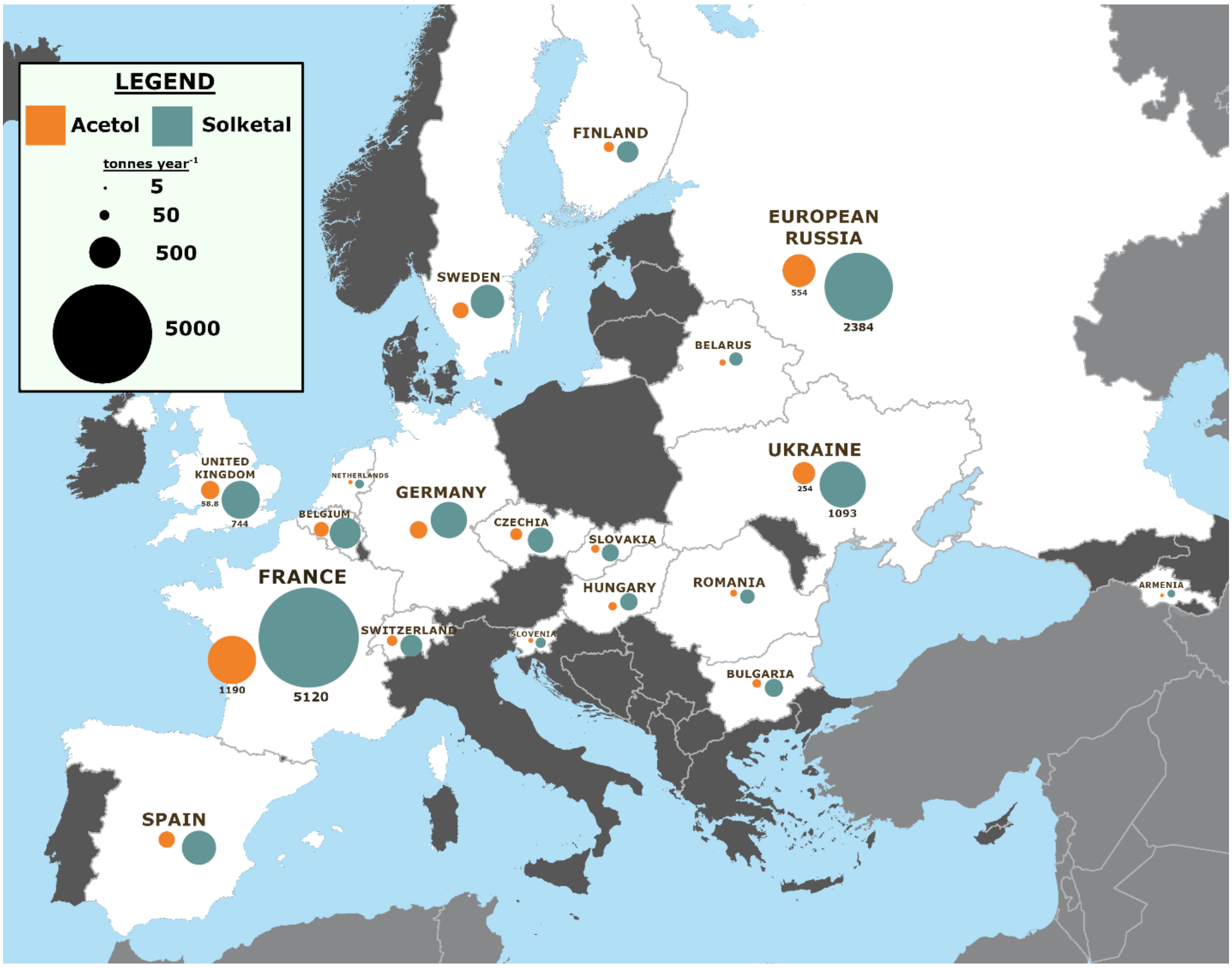

Figure 53: A map of continental Europe showing acetol and solketal maximum production capacity per country (for ternary glycerol, water, acetone mixture of (46, 26, 28 wt.%, sample 109) based on the country's total net electricity capacity GW(e) output. Acetol=orange, solketal=turquoise with the areas of the circles being directly proportional to production values. Top 4: France, European Russia, Ukraine, and the UK. Base map altered from ©MapRoom. Table A20 in Appendix A lists the potential acetol and solketal production for each country.

As shown by Figure 53, the countries which could benefit from radiation-chemical co-production (this process or an alternative) the most would be France, European Russia, Ukraine, and the UK, based on electrical output in GW (which links directly to the rate of spent fuel generation).

Solketal, as a potential renewable fuel additive, could be incorporated into modern transport fuel blends across Europe. As previously mentioned, the renewable component proportion of petroleum fuel blends has been increasing worldwide. The UK's specifically increasing to 10% vol% in 2021, with the current addition of bioethanol as the main renewable component. This renewable proportion volume is expected to increase (to 20% within the EU [68, 69]) due to growing pressures for lower CO_2-producing, more sustainable transport solutions. Table 31 indicates the impact values that a radiation-chemical production network could have on transport fuel blends in which solketal comprises 5% of the total volume.

Table 31: Expansion and impact values of the cogeneration Europe network for EU fuel blends. Extrapolated by total power output from 688 MWe Krško NPP to 180 reactors producing a total power output of 159.3 GW.

Impact Values	**i) PWR spent Fuel Pool** (One NPP= 688 MW)	**ii) Max. Capacity within Europe** (180 NPPs = 159.3 GW)
Annual solketal production (t year^{-1})	57 ± 6	$(1.3 \pm 0.1) \times 10^4$
Annual solketal production (litres year^{-1})	$(5.4 \pm 0.5) \times 10^4$	$(1 \pm 1) \times 10^7$
Total annual petrol blend volume *5% solketal, 95% vol% base petroleum* (litres year^{-1})	$(1.1 \pm 0.1) \times 10^6$	$(2.5 \pm 0.2) \times 10^8$
Percentage of total EU fuel blends in 2019 by volume per year (for the 5% solketal blend) [328]	0.0014 ± 0.0003	0.31 ± 0.03

The maximum production capacity of solketal from the hypothetical use of spent fuel facilities in Europe considered in this work is ~$(1.3 \pm 0.1) \times 10^4$ t year^{-1}, contributing to ~$(2.5 \pm 0.2) \times 10^8$ litres year^{-1} to 5% solketal-petroleum fuel blends. This could alleviate the forecast demand for biomass-derived, sustainable fuel additives which are expensive [329]. However, one clear point here is that despite the potential 180 facilities worth of spent nuclear fuel and the corresponding number of radiation-chemical production facilities, only ~0.3% by volume of total European fuel blends will be contributed with the radiolysis-generated solketal component.

5 Discussion

This chapter describes the production mechanisms and reaction kinetics for the analytes derived from the direct radiolysis of high solute % ethylene glycol and glycerol samples. It will also expand upon the effects of the variable sample and irradiation parameters explored in this research and attempt to explain the trends observed. The potential issue of radioactivity concerning direct ionization radiolysis will be discussed. The current suitability of this system for chemical nuclear cogeneration using spent fuel facilities will be explored and compared with previously proposed systems.

5.1 Induced Radioactivity

The risk of induced radioactivity via neutron activation is often one reason given as to why mixed-field irradiations involving neutrons have not been explored for radiation chemical processing [261]. The data presented here show that significant quantities of only one significant radionuclide (sodium-24) are detected after large-absorbed doses in mixed-field neutron + γ irradiations (>500 kGy). Sodium-24 is a β^- and γ-ray emitter of energies 0.55 MeV (mean) and 2.7 MeV, respectively, but has a short half-life of 14.96 hrs. With refined starting reagents (reagent grade), and after 10 days from irradiations, the induced specific radioactivity of all radionuclides is reduced to negligible levels of <4 Bq g^{-1}, as anticipated based on their short half-lives. This is comparable to the specific radioactivity observed in naturally occurring, unirradiated materials such as coffee or building minerals. Potassium-40, a long-lived radionuclide is the most prominent in coffee and building materials with specific activities of ~1 Bq g^{-1} [330] and ~0.4 Bq g^{-1}, respectively, amongst others [331].

According to the IAEA [332], the specific activity limit for the unrestricted transport of unknown radionuclides or mixtures for β^- and γ-ray emitters is <10 Bq g^{-1}. Within these regulations, the irradiated organic materials from an operational NPP after 10 days as seen here would not be subject to these regulations and can be transported freely. However, the question remains as to whether these organics could be used for further applications, after being purposely exposed to ionizing radiation. Further EU or nation-specific legislation may need to address this in the future. Additionally, it is worth noting that for cheaper, organic feedstocks such as crude glycerol that has not been refined further would have higher concentrations of impurities such as sodium-based salts as well as the trace heavy metals observed in chapter 4.4. This would result in higher specific radioactivity after irradiation which could be a significant issue if mixed-field irradiations are utilized. While the radioactivity data presented here are for glycerol and ethylene glycol specifically, a similar assumption for related radioactivity caused by heavy metal impurities can be made for different liquid reagents with varying grades of quality.

Despite possible radioactivity issues with mixed-field irradiations, superior *G*-values and mass productivities are observed for all radiolytic products using only γ-ray irradiations, except for methanol from ethylene glycol which is temperature-dependent. In terms of potential radioactivity from γ-ray irradiations, photonuclear reactions (γ, n) could produce neutrons that activate nuclei. However, activation with γ rays remains unlikely for organic (low-Z) materials due to a combination of factors. The possible mechanisms for organic materials involve the emission of a neutron from target deuterium or carbon-13 nuclei; $^{2}H(\gamma,n)^{1}H$ and $^{13}C(\gamma,n)^{12}C$, with threshold γ-ray energies of 2.22 MeV and 4.95 MeV [333], respectively. Furthermore, ^{2}H and ^{13}C both have low natural abundance in organic materials within 1-in-6600 hydrogen atoms and 1-in-100 carbon atoms, respectively. Additionally, these (γ,n) photonuclear reactions are made further improbable due to the energy spectrum from ^{235}U fission (and its fission products) as a significant portion of the γ rays are emitted <2.2 MeV in a reactor [334]. For spent fuel specifically, negligible quantities of γ rays from fission products have energies above the 2.2 MeV threshold for the $^{2}H(\gamma,n)^{1}H$ reaction which further improves the proposition for spent fuel usage as an irradiation source [335]. Finally, the cross-sectional areas for photonuclear reactions with deuterium are a factor of ~40 lower than the total cross-sectional areas for all 2 MeV γ-ray interactions with hydrogen [333, 336]. Therefore, in the proposed case of the spent fuel scenario as described in chapter 3.7.1., the induced radioactivity will be negligible and comparable to the specific radioactivity of naturally occurring substances.

5.2 Dependence on Absorbed Dose

With primary radiolytic products, the measured *G*-values are expected to decrease with increased absorbed dose as reported in the radiolysis literature of many solutes [240] (as described in 2.12.1). The same applies in this work to the γ-ray radiolysis of glycerol for acetol production as seen in Figure 41 and Figure 46. Here, the accepted theory for the decrease in *G*-values with increased absorbed dose is that increased concentrations of primary radiolysis products (acetol) react with reactive ions and radicals from irradiations, rather than the starting bulk solute (glycerol). These conflicting reactions (as shown by reactions in Figure 57f,g) on primary radiolysis products may limit the maximum mass productivity for standard radiolytic batch reactions. With increasing absorbed dose, there would be diminishing returns in terms of the energy input into the system for radiolytic synthesis applications. This is supported by the mass productivity trends seen in Figure 41 and Figure 46. The zero-dose *G*-values listed in Table 29 indicate that for primary radiolysis products, the low absorbed doses do result in superior *G*-values but they lack mass conversion which is not suitable for the industrial scale. For secondary products, an increase of *G*-value with absorbed dose is observed (e.g., for solketal), consistent with the increased availability of new primary species which react further under radiolysis (acetone for solketal as an example), as shown in Figure 41.

5.3 Dependence on Vial Types and Vessel Materials

A notable difference has been observed between the two different vial types (PP and BS) in mixed-field irradiations focussing on compounds detectable via liquid GCMS: For higher dose (>60 kGy), higher dose rate (>6.53 kGy min^{-1}) irradiations on ethylene glycol, methanol *G*-values of PP vials have been observed as superior (Figure 33). The difference between the two vial types can be explained by the BS vials reaching higher temperatures during irradiations, increasing the temperature of the organic samples, and increasing the proportion of the high-vapour pressure volatiles (such as methanol) to be in the gas phase, rather than in the liquid. This, coupled with the inferior seal offered by the crimp-capped septa resulting volatile loss out of the vial during irradiation, transport, and storage. This conclusion is supported by the loss of mass observed from mixed-field irradiated, ethylene glycol samples after irradiations.

As for other radiolytic components, there did not seem to be a significant difference between vial types in terms of *G*-values obtained for most radiolytic species, except with methanol from ethylene glycol. Qualitatively comparing the radiolytic products from each vial type, there were no unique products from either vial material. For polypropylene vials, whilst acetone and acetic acid may have been generated in *trace* concentrations from the degradation of the PP vials [280], based on the data comparison with the BS vials there appears to be no discernible quantitative difference for neat ethylene glycol of glycerol between vial material types. Any acetone synthesis from PP degradation would have had a negligible effect as shown by the comparison between BS and PP vials in Figure 42. Additionally, the acetic acid concentrations and *G*-values remain comparable between vial types, as shown by Figure 36 which indicates an insignificant production of acetic acid from radiolytic PP degradation. Any other concentration or *G*-value differences of quantified products between vial types are thought to be due to mixture differences, radiation conditions or volatile losses.

The compression analysis in chapter 4.3.1 did not show any significant embrittlement of the BS glass due to the large statistical uncertainty of the failure force between vials. Other methodologies are suggested to be explored to test the HS vial seal integrity if absorbed doses absorbed 20 kGy are explored. However, based on the mass analysis data presented in chapter 4.3.2 for the PP vials, plastic vials with a good seal such as the polypropylene cryovials are recommended in future testing due to fewer leaks and providing a consequently better seal during irradiations and storage. For industrial applications, suitable materials for the piping system of organics will need to be researched. Given that reactive peroxides and acidic compounds are all generated from the radiolysis of these polyols, the corrosion and flow characteristics all need to be quantified to prevent any possibility of leaking or system failure.

5.4 Dependence on Radiation Type and Dose Rate

Despite the lack of empirical data in the literature on mixed-field neutron + γ-ray irradiations, the data presented here do not suggest any unique products for neutron-related irradiations of glycerol or ethylene glycol samples. Additionally, there is only one occurrence of superior neutron + γ-ray *G*-value for methanol from ethylene glycol compared to γ-ray only samples, which is linked strongly to temperature increases and not the nature of the radiation itself. The data presented here show consistently lower (factor >2) radiation-induced chemical yields of most reported radiolytic products for mixed-field compared with γ-ray only samples. In addition to the poorer yields, there are several reasons to avoid neutron-based irradiations or mixed-field neutron + γ-ray irradiations for the radiolysis of liquids organics, as opposed to strictly using γ-ray only irradiations. In summary, the reasons against using neutron radiolysis are as follows:

i) **No observable unique products.** No observable production of unique or previously unknown organic radiolysis products for neutron-related exposures.

ii) **Significantly lower *G*-values and mass productivities.** Significantly lower yields of organic products than comparable γ-ray doses for most of the detected products. This could be due to the higher LET and higher dose rates that increase recombination rates.

iii) **Neutron activation of metallic impurities.** The activation of metallic impurities to radionuclides within the organic samples. The use of cruder feedstocks would be further susceptible to activation, producing relatively larger quantities of short-lived radioisotopes.

iv) **Neutron flux alterations for operating reactors.** Neutron flux absorption would produce uncertainties in neutron fields and consequently the criticality calculations.

v) **Accumulation of thermal energy due to high neutron dose rates.** High dose-rates and large total absorbed doses typically result in temperature increases of the samples. This could be beneficial or hindering depending on the desired process.

The data presented here prompts the question of why different irradiation types produce consistently different yields? Can any physical, physicochemical, or chemical mechanisms be proposed for these processes that are consistent with the results of differing irradiation types? While γ-ray only radiolysis has been shown here to produce superior *G*-values and mass productivities, the long timescales needed for a suitable dose to accumulate is less desirable for industrial processes, especially when compared against analogous chemoselective processes.

5.5 Dependence on Solute Concentration and Mixtures

Due to the foci of much of the available literature being on dilute aqueous mixtures (typically <1 wt.% solute concentrations), concentrated aqueous mixtures or neat samples have not been explored in-depth. Whilst dilute samples are shown to produce high *G*-values with low doses, the caveat is that the overall change of the whole sample is very little since the majority is water, this is shown by the calculated literature values for mass productivity in Table A2 and Table A3. In this work, neat samples of glycerol produced a *G*-value and an MP % value of 0.47 μmol J^{-1} and 0.35 % for acetol, respectively, for a 100 kGy γ-ray dose. Concentrated aqueous glycerol mixtures (70 wt.% glycerol) produced a notable increase in *G*-value and MP % of 1.33 µmol J^{-1} and 0.99 %, respectively, amongst many other examples of concentrated mixtures presented here. In all cases for acetol, superior *G*-values and MP %s are observed for highly concentrated glycerol aqueous solutions. The dilution with water from 100% wt.% neat glycerol samples to 70% wt.% produced superior acetol *G*-values, this can be attributed to the significant viscosity drop observed from 1414 mPas to ~20 mPas [326], from this the diffusion-controlled physicochemical chain reactions can occur at faster rates to produce acetol, as described in section 5.6.2.1. Further dilutions of glycerol with water produces lower *G*-values compared with more concentrated aqueous solutions which can be explained by a couple of reasons: The further dilutions correspond to a smaller drop in viscosity, with mixtures of 63 wt.% to 50 wt.% glycerol samples corresponding to viscosities of 15 to 6 mPas, respectively. Additionally, further dilution reduces the availability of glycerol molecules for time-sensitive, radical-initiated chain reactions which is more significant than any viscosity drop.

Similarly, the ternary mixtures with the highest starting concentrations of glycerol produced the highest *G*-values and MP %s of radiolytic solketal of 1.53 µmol J^{-1} and 1.0 %, respectively with 50 kGy irradiations (Figure 49). Despite the literature for heterogeneous solketal production reporting an optimum glycerol: acetone mass ratio of 1:1.9 (1:3 moles ratio) to produce superior solketal yields [337], the optimum mixture for the radiolytic production (*G*-value) of solketal relies on mixtures with higher glycerol compositions. Ensuring that the water mass proportion stays comparable across all irradiated ternary mixtures, the optimum acetone: glycerol mass ratio for radiolytic production of solketal is 1:1.6 (samples 108 and 109 in Table 18). This shift in the optimum radiolytic mixture composition is thought to depend on the availability of the stabilized acidic glycerol or hydronium species which promotes the acid-catalyzed reaction and is discussed further in section 5.6.2. Despite the differences in *G*-value, the % molar yields across the ternary mixtures remain comparable as per Figure 49c. This indicates that the reaction kinetics are comparable across the mixtures in terms of their glycerol wt. % and acetone wt. % which suggests that the starting reagents are not the limiting species for the solketal reaction. It can be inferred that the generation (concentration) or efficacy of the catalytic species is the limiting species here.

5.6 Radiolysis Mechanisms – Direct Action

This section will explore the possible physicochemical mechanisms associated with the production of acetol and solketal from the direct action of glycerol, correlating modes of irradiation to the observed data trends seen in this research. A similar mechanistic exploration will be done for ethylene glycol. While not exhaustive, the most prominent and relevant radiolytic mechanisms are described for ethylene glycol and glycerol.

5.6.1 Ethylene Glycol

Initially, direct ionization on neat ethylene glycol would result in the ejection of an electron generating its excited radical cation, $C_2H_6O_2^{\bullet+}$, as per Figure 54a. Here, the formation of methanol is believed to be a result of C-C dissociation from the excited radical cation, as per Figure 54b. With high dose-rate, mixed-field irradiations, the increased temperature causes an increased probability of the radical cation undergoing C-C fragmentation (dissociation) due to the additional thermal energy available [277]. This C-C bond is the weakest in the ethylene glycol structure with a bond dissociation energy (BDE) of 85.5 kcal mol^{-1} [338]. Other fragmentations are less favourable due to stronger C-H and C-O bonds at 95.5 kcal mol^{-1} and 97.1 kcal mol^{-1}, respectively but do occur to produce $H^\bullet$ and $HO^\bullet$ radicals. This fragmentation mechanism explains the superior methanol concentrations and *G*-values observed in PP vials from high dose, high dose rate, mixed-field irradiations of ethylene glycol, as per Figure 32 and Figure 33, respectively.

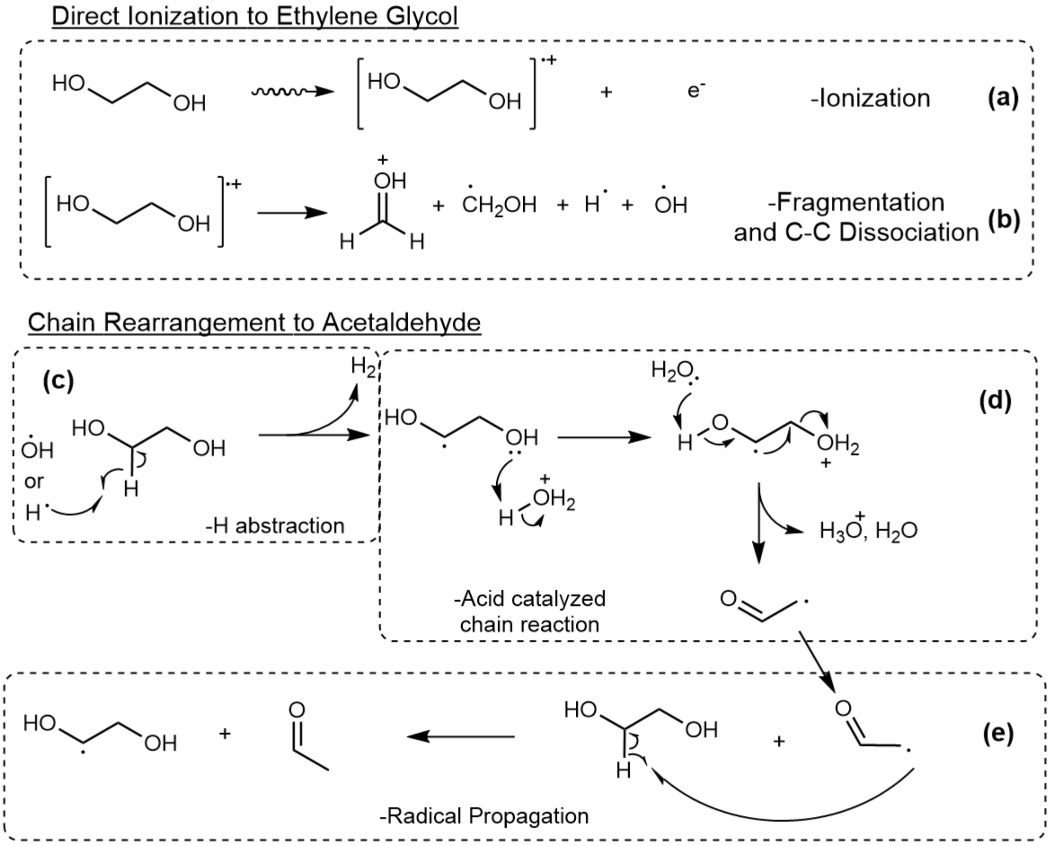

Figure 54: The expanded proposed physical and physicochemical mechanisms involved up to ~10^{-4} s for the radiolysis of neat ethylene glycol. **a** Direct ionization. **b** Fragmentation of the radical cation. **c** Initiating H-abstraction for acetaldehyde production. **d** Acid-catalysed chain reaction. **e** Radical propagation while forming acetaldehyde. Mechanisms have been deduced from the general radiolysis literature for **a** and **b**, the chain rearrangement mechanisms for **c, d** and **e** have been expanded upon by Plant A. G. from the previous literature [244, 246].

The high *G*-values observed from ethylene glycol for acetaldehyde support the theory of a radical-directed chain reaction as mentioned in the prior art [244, 246]. Figure 54 c, d, and e show the expanded acid-catalysed radical chain reaction for acetaldehyde production as suggested previously in the literature [246]. This chain process is initiated with an H-abstraction via $H^•$ or $HO^•$ radicals, propagated by the stabilized acidified ethylene glycol cation, $CH_2OH–CH_2OH_2^+$. As suggested in chapter 4.5.2.3, there is a competition between the thermal fragmentation reaction for methanol and the radical-directed mechanism for acetaldehyde production for the initial excited radical cation species. These competing reactions explain the *G*-value data for acetaldehyde and methanol in Figure 31 and Figure 33, respectively and their dependences on the irradiation type and absorbed dose. For ethyl acetate production, the results suggest that this occurs through a chemical reaction as it requires sufficient concentrations of ethanol to generate.

5.6.2 Glycerol

Extrapolating from simple alcohols and ethylene glycol as summarized in chapter 2.13 as the simplest polyol and methanol as the simplest alcohol described in chapter 2.9, the direct-action radiolysis mechanisms and subsequent reaction kinetics of glycerol can be theorised. Figure 55 shows the theorised physical and physicochemical mechanisms ($<10^{-12}$ s) from direct action upon neat glycerol. These are not extensive but are thought to be the major reactions which relate to acetol and solketal synthesis.

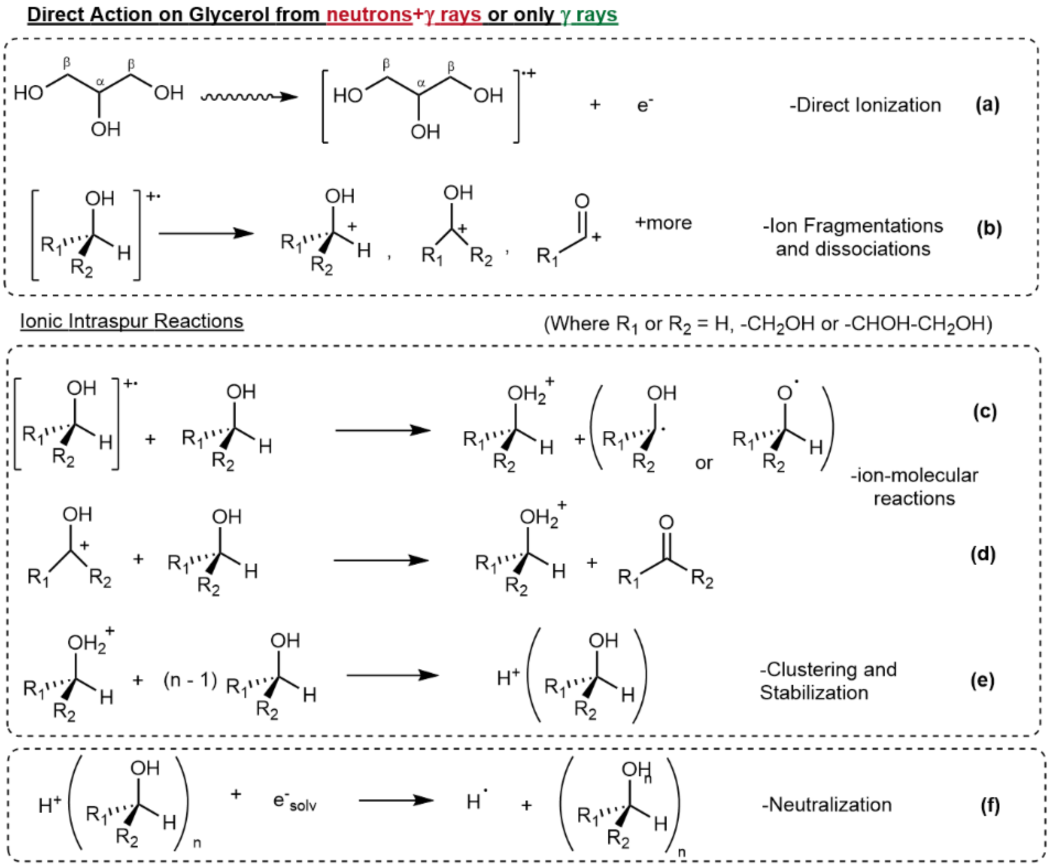

Figure 55: Proposed physical and physicochemical initial mechanisms from the direct action of irradiations upon pure neat glycerol (by Plant A. G.). **a** Direct ionization. **b** Ion fragmentations resulting in most C-C or C-O scissions. **c** and **d** Ion dissociation reactions form acidic glycerol cations with either radicals or carbonyl species. **e** clustering and stabilization of acidic glycerol. **f,** Neutralization of acidic glycerol via solvated electrons. Since H-dissociation could occur at any hydroxyl carbon of glycerol. (R_1 and R_2 = $-CH_2OH$ for α-carbon or -H and $–CHOH-CH_2OH$ for β-carbon species, respectively.) Physical and physicochemical mechanisms have been deduced from generalized literature by Plant A. G.

As shown in Figure 55a, similarly to ethylene glycol, the first step is the direct ionization of glycerol where a non-ionizing electron (e^-) is emitted while also producing an exciting radical cation ($C_3H_8O_3^{\bullet +}$). The radical cations then fragment in several possible ways which contribute to the majority of C-O and C-C cleavage and result in the synthesis of smaller oxygenate compounds such as acetone, ethanol, acetaldehyde, and formaldehyde as per Figure 55b. The non-ionizing electrons typically solvate after $\approx 10^{-12}$ s [130] into the bulk solution. As described in chapters 2.8 and 2.9, expanding energetic volumes called spurs or blobs are created after ionizing particle interactions; these volumes are where there ionic or radical reactions start to occur (typically within 10^{-12}s of the ionization event). In the case of water, specifically, these reactive species can exist in the solution until 10^{-4}s after the irradiation event. Initial intraspur ionic reactions from the ionized glycerol cation are shown in Figure 55c and d if the initial fragmentations of the primary radical cation do not occur. These ionic reactions are thought to produce the acidified glycerol cation which can be stabilised by a clustering mechanism given in Figure 55e.

Within the expanding spurs (intraspur), radical reactions result in C-H cleavages via H-abstraction mechanisms, forming the α-hydroxy ($^\bullet$C-O) or alkoxyl (C-O$^\bullet$) radicals, as generated by the reaction in Figure 55c. Initially formed in comparable quantities within the spurs, the alkoxyl radical converts to the more stable α-hydroxy radical as the spur expands, as indicated by Figure 56a. For glycerol, radical-initiated H-abstraction is most probable from the secondary carbon which produces the α-hydroxy radical as indicated in Figure 56c. This radical can be converted into acetol through the previously mentioned [3] radiation-triggered acid-catalysed water elimination rearrangement and subsequent radical chain-reaction propagation mechanism, as shown in Figure 56d,e. For the direct action on neat glycerol for acetol production, the acid-catalyzed rearrangement mechanism is suggested in this research to be catalysed by the stabilized, acidified glycerol cation ($CH_2OH–CHOH–CH_2OH_2^+$) as generated with spurs via the reactions in Figure 55a-e.

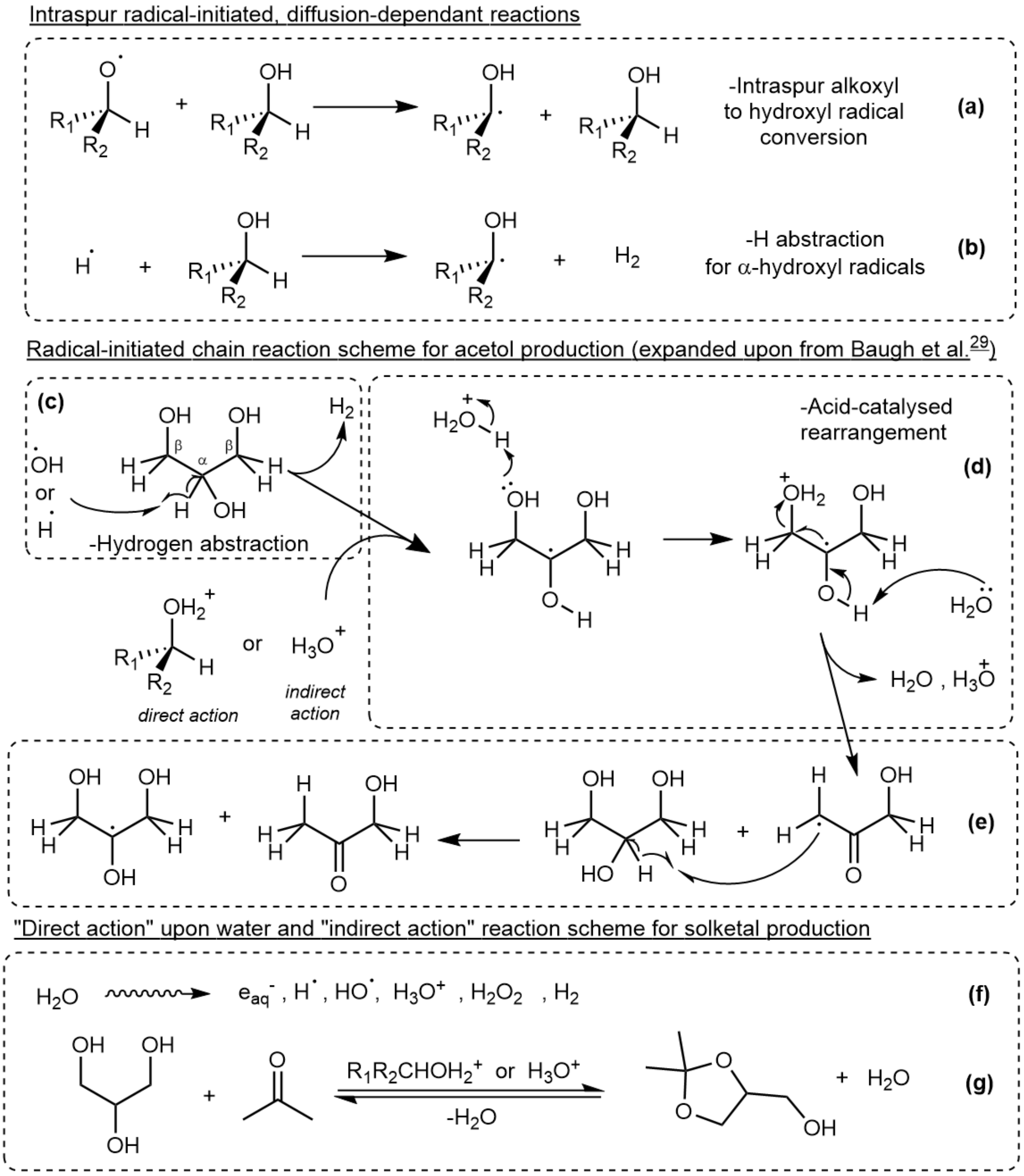

Figure 56: Subsequent proposed radiation-directed, diffusion-controlled reactions up to 10^{-4}s. Radical-directed reactions a-c**.** **a** Intraspur radical conversion to the more stable hydroxy radical. **b** C-H scission dominated by α-hydrogen abstraction. Reactions **c** to **e** is the expanded mechanism for acetol production [3]. **c** Hydrogen abstraction at the weaker α-C-H bond. **d** Acid-catalysed chain re-arrangement via an acidified species. **e** α-H-abstraction and α-hydroxy radical regeneration **f,** Direct action on water producing reactive species such as H_3O^+. **g** Acid-catalysed ketalization reaction scheme for solketal. (R_1 and R_2 = $-CH_2OH$ for α-carbon or H and $–CHOH-CH_2OH$ for β-carbon radicals, respectively.) The chain rearrangement mechanism has been expanded upon by Plant A. G. from previous literature [3].

Similar to other acidic solvent species (such as H_3O^+ from H_2O), the synthesis of the short-lived acidic catalytic species can be influenced by two irradiation factors, i) LET and ii) the dose rate of the irradiation. This dependence can explain the data observed in chapters 4.5.2 and 4.6.2 for the difference in *G*-values between the two irradiation types for all samples.

In terms of the difference in LET, γ-ray (low LET) irradiation creates energetic volumes that are small and well-separated in the sample, as produced by the residual radioactivity of the reactor in shutdown mode. Whereas, with mixed-field neutrons + γ-ray irradiations, the spurs are larger due to higher-energy interactions from the additional fission neutrons (high LET) and more energetic secondary particles. These larger volumes have a greater potential for overlap, increasing the rate of conflicting interspur radical recombination reactions which reduce concentrations of α-hydroxy radicals and the stabilized glycerol cation, as shown in Figure 57a, b, c, d, and e. The differences in radiation-chemical yield of an acidic solvent molecule are evident for H_3O^+ from H_2O with contrasting LET irradiations, with *G*-values for ^{60}Co γ rays (LET = 0.23 keV μm^{-1}) and α-particles (LET:108 keV μm^{-1}) being 0.28 μmol J^{-1} and 0.044 μmol J^{-1}, respectively [339].

A similar dependence on the short-lived acidic species is hypothesised to catalyse the ketalization reaction, provided sufficient availability of acetone in the starting mixture, as indicated by Figure 56g. This reaction proceeds chemically, with any radiolysis-based radical combinations being highly improbable. Acetone, as a limiting reagent, explains the lower yields (a factor of 10 lower) of solketal compared with acetol in the neat samples. The increasing trend in solketal *G*-value observed in Figure 43 with absorbed dose is also explained by the accumulation of acetone for the solketal reaction for higher absorbed doses. Ternary mixtures that are more heavily diluted are shown to produce lower concentrations, *G*-values, and mass productivities of solketal. This can also be explained by le Chatelier's principle and the shifting of the dynamic equilibrium point towards the starting reagents, as opposed to the products of solketal and water.

For the second irradiation factor of dose rate, increasing this by using mixed-field irradiations would have a similar effect to increasing LET [340], due to the increased probability of spurs overlapping and higher recombination rates of the reactive species, limiting acetol production. In combination, dose rate and LET control the *G*-values of the reactive species such as H_3O^+ or the acidified glycerol cation that participate in physicochemical diffusion-controlled mechanisms. The diffusion-controlled mechanisms for acetol and solketal, which require such species would be limited and this conclusion is supported by the data shown in Figure 44a and

Figure 49 for acetol. This is additionally supported by the dose rate data for solketal in Figure 44b.

5.6.2.1 Diffusion-Controlled Mechanisms

As dilutions reduce the starting glycerol concentration with water, the indirect effects begin to become more prominent. After ~10^{-12}s, reactive species from water radiolysis start to interact chemically with the solute, glycerol. Hydroxyl ($HO^{\bullet}$) and hydrogen atoms ($H^{\bullet}$) are reactive towards alcohols, typically interacting via an α-carbon-hydrogen abstraction mechanism as shown in Figure 56c. In dilute samples, the hydronium ion (H_3O^+) is proposed to act as the acidic catalyst in both acetol and solketal mechanisms for a dilute solution similar to the acidified glycerol cation in neat solutions. The solvated electron, e_{solv}^- is unreactive towards alcohol groups and so theoretically does not reduce glycerol but is reactive towards carbonyl (C=O) groups in acetol. Therefore, the decrease in the trend of acetol *G*-values with γ rays with increased absorbed dose can be explained due to the conflicting reaction in Figure 57f. For ternary mixtures, with acetone no longer a limiting reagent for the ketalization reaction, there would be competition kinetics between acetol and solketal mechanisms which both require the acidic species to catalyse. This competition for the acidic catalyst could explain the similar mass productivities between the binary and ternary mixtures, despite the change in the ratio between acetol: solketal *G*-values as indicated by Figure 50.

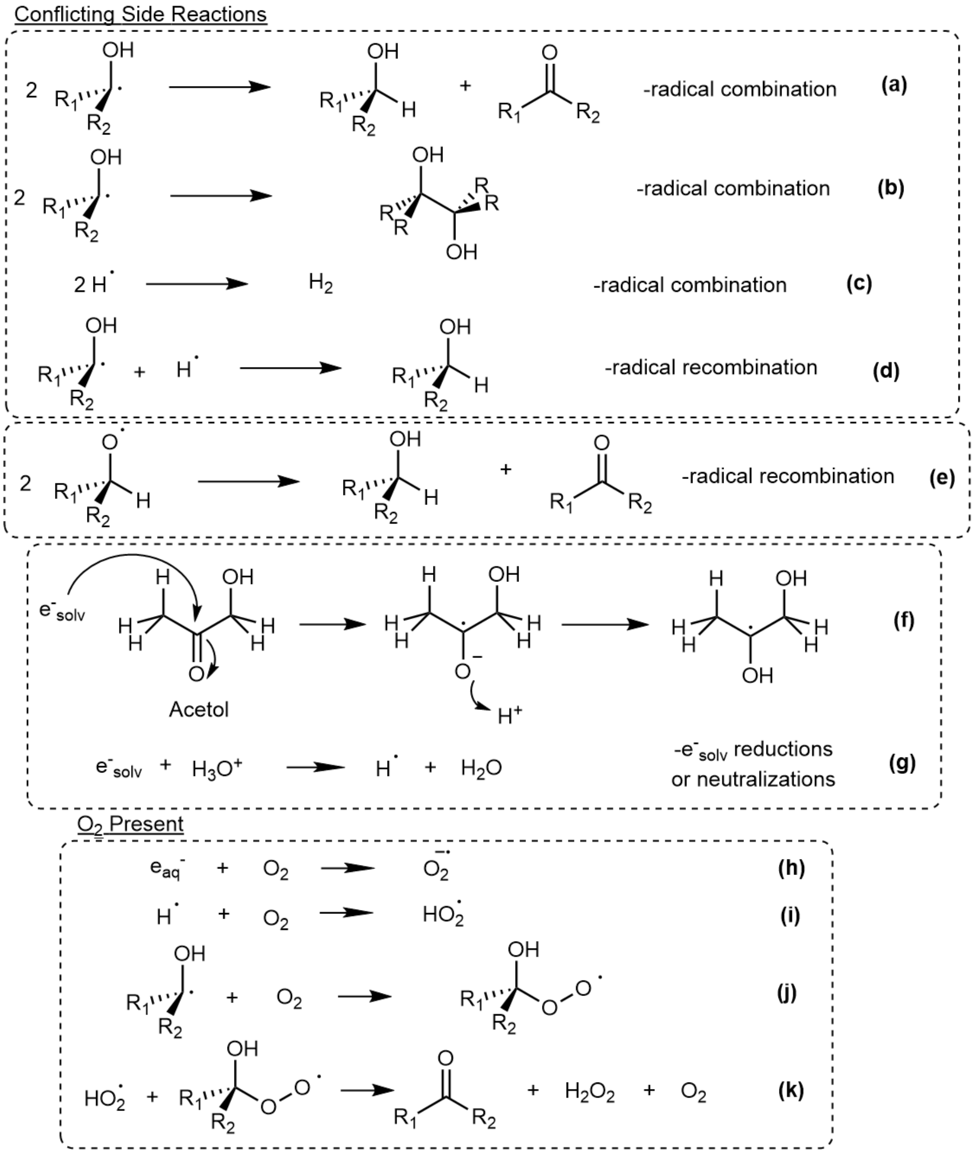

Figure 57: Proposed conflicting reactions affecting acetol production (by Plant A. G): **a** to **e** are interspur radical combinations reactions promoted by the overlapping of spurs with high LET and high dose rates. **f** reduction of acetol via e_{solv}^{-}. **g** neutralization of the hydronium ion. **h** superoxide anion formation. **i** hydroperoxy ($HO_2^{\bullet -}$) radical formation. **j** peroxyl radical ($RO_2^{\bullet}$) formation. **k** radical combination of peroxyl radicals for aldehyde formation). Physicochemical and chemical mechanisms have been deduced from generalized literature by Plant A. G.

For other diffusion-controlled reactions of acetol and solketal, the reaction rates, k_D depends on the diffusion constants, D of the required respective species shown in Figure 56. The diffusion constants are influenced by two factors [341]: a) viscosity, η and b) temperature, T, as indicated by the Stokes-Einstein relationship, as per,

$$k_D \propto D = \frac{kT}{6\pi\eta R} \tag{61}$$

Where k is Boltzmann's constant and R is the species' radii. This dependence can help explain the observed trends between Figure 41 and Figure 50 for acetol and solketal production. The dilution of glycerol will decrease the viscosity of the solution [342], improving diffusion and reaction rates for the reactions listed in Figure 57. As previously mentioned, the additional heating effect caused by increased absorbed doses would raise the temperature of the solution, lower viscosities, increase diffusion constants and increase reaction rates for diffusion-controlled reactions, such as those for acetol and solketal. For water radiolysis, there is an estimated 24ºC temperature increase for a 100 kGy absorbed dose, compared with a 4.8ºC rise at 20 kGy. Thermal energy would be able to dissipate for longer γ-only irradiations, whereas for higher dose rate mixed-field irradiations, the thermal energy would accumulate. Thermal neutron moderation may increase this temperature further as indicated by the melted PP vials (Figure 26b).
These two sample factors explain: i) the increase in *G*-values seen from neat to diluted glycerol samples, and ii) the increasing acetol *G*-values with absorbed dose mixed-field neutron + γ-ray irradiations (Figure 41).

The short-lived acidic catalytic species ($R_1R_2CHOH_2^+$ and H_3O^+) which are required for both acid-catalyzed reactions are neutralized by solvated electrons, as shown by Figure 55f and Figure 57g. Additional conflicting reactions [162, 261], involving molecular oxygen (O_2) are also listed in Figure 57h, i, j, and k where O_2 acts as a scavenger for the $H^\bullet$ and α-hydroxy radicals, reducing their concentrations and inhibiting acetol synthesis. Consequently, the reaction producing the hydroperoxy radical ($HO_2^\bullet$) or the peroxyl radical ($RO_2^\bullet$), respectively, which are both heavily oxidizing are likely to produce aldehydes such as glyceraldehyde or acetone, whilst reducing the availability of necessary $H^\bullet$ radicals for acetol production. Adding an e_{solv}^- scavenger (e.g., N_2O) for future research is thought to increase the *G*-values, production yields and radiolytic process viability of both acetol and solketal. Additionally, the complete removal of O_2 (although difficult) from the samples is predicted to promote concentrations of the necessary radicals that would increase the initiation rate of H-abstractions for the chain process for acetol synthesis.

Based on the data in Chapter 4 and the physicochemical mechanisms discussed here, *G*-values and mass productivities could be improved upon with the following parameters. A low γ-ray dose rate that is feasible for process throughput, removal of O_2 gas, the addition of N_2O gas to promote $^\bullet OH$ or $^\bullet H$ radicals and any further addition of potential co-reagents that can promote these reactions.

5.7 Production Calculations, Feasibility and Comparisons

The data shown in chapters 4.6.3 and 4.7 show that solketal could be generated in significant quantities from the numerous spent fuel facilities throughout geographical Europe. The proposed radiation-chemical refinery can be visually described for acetol and solketal co-production from waste glycerol by the simple schematic as shown in Figure 58 [343], although supporting product refinement and utility systems are not detailed.

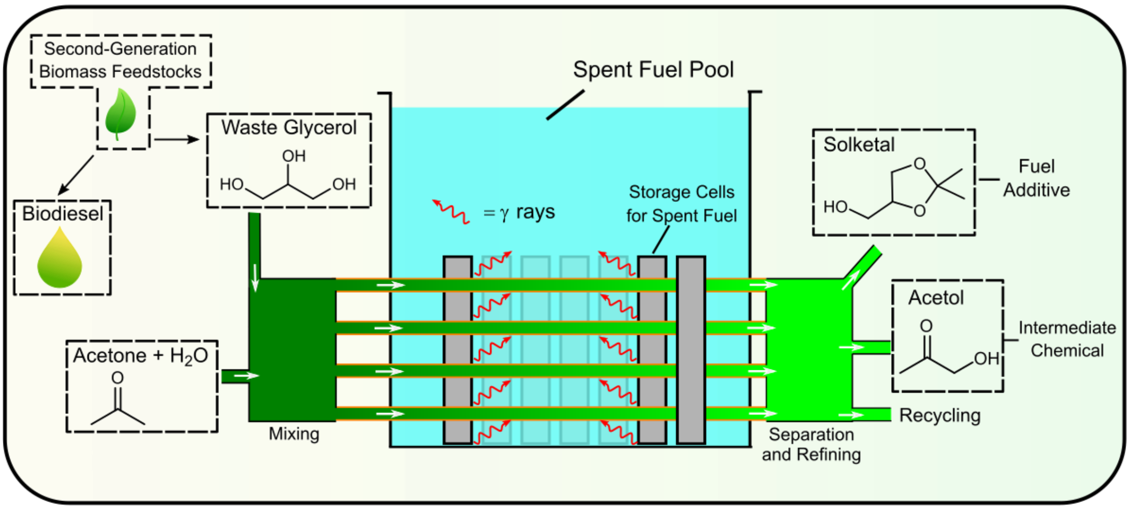

Figure 58: A basic process schematic of the proposed nuclear cogeneration process with the spent fuel pool design (dry cask storage also remains plausible) to produce acetol and solketal.

The synthesis of $(1.3 \pm 0.1) \times 10^4$ t year^{-1} of solketal could alleviate some of the demand for biomass-derived, sustainable fuel additives which can be expensive. Notwithstanding the scarcely available data [329] for solketal prices (3000 \$ tonne^{-1}), it could be produced via irradiations at lower costs than chemoselective methods due to negligible radiation processing costs [162]. However, while this research has shown improved *G*-values from ethylene glycol and glycerol radiolysis, the impact of the proposed glycerol on the solketal process may remain minimal due to low total yields and low throughputs. The glycerol utilization and petroleum fuel offset from solketal would remain at ~0.31%, despite 180 dedicated production facilities. If *G*-values could be increased by a factor of 10 then this could be considered a feasible process to enact, however, with current yields, it is difficult to envisage this process being implemented. On a positive note, many processes that have been previously proposed for nuclear-chemical conversion show comparable or inferior *G*-values to those presented in this work [162, 261]. These processes have been listed in Table 32.

Table 32: Previously explored radiation-chemical processes in literature and *G*-values.

Process	**Phase and Temperature / ºC**	***G*-value range / µmol J^{-1}**	**Reference**
Alkylation reactions: i) propane + ethene to methylbutane and, ii) methane + ethene to methylpropane	Gas, >240 ºC	i) 10 or ii) 120	[261, 344]
Nitrogen Gas Fixation: Formamide to alkenes	Gas	0.3	[345, 346]
Dialkyl phosphates addition to alkenes	Liquid, 20 ºC	6.3	[347]
Direct irradiation of CO_2	Gas	0.01 to 0.1	[162]
CO_2 incorporation into organics: chloroacetic acid + CO_2 to malonic acid	Gas	~9	[348]
Nitrosylation of carbon tetrachloride to trichloronitromethane	Gas	0.47	[162, 349]
Oxidation of hydrocarbons to hydroperoxides	Liquid, 100 ºC	2 to 45	[162]
Oxidation of ethane to acetic acid	Gas, 50 ºC	80, 1000	[162]
Oxidation of benzene to hydroxybenzene	Gas, ~190 ºC	7	[162, 350]
Inorganics CCl_4-P solutions to red phosphorous	Liquid	2.3	[351]
Ethylene glycol to methanol	Liquid	<0.6	[277]
Ethylene + HBr to ethyl bromide	Gas or liquid	<100	[61]
Glycerol to acetol and solketal	Liquid, ~20 ºC	~1.5 to 2.7	Plant. A. G., This work

Compared with direct CO_2 fixation, N_2 gas fixation, nitrosylation, inorganic CCl_4-P to red phosphorus, and even previous methods to synthesise methanol from ethylene glycol, have all shown inferior or comparable yields to those presented here for glycerol utilization. In that instance, this radiation-driven process for acetol and solketal synthesis can be considered a good option compared to other likewise radiation-driven systems. Additionally, glycerol is the exception to all these processes in that it is already manufactured as a waste feedstock and readily available in abundant quantities from renewable materials, offering a unique selling point for this process. While CO_2 can also be considered a notable waste material, extra carbon sequestration processes and supply issues may interfere with future industrial implementation. Some processes involving halogenated reagents do exceed the *G*-values shown in this work, but they lack the added value of a waste organic feedstock as presented here.

5.8 Immediate Suitability of Nuclear Cogeneration

Partly due to the imperative that reactors are reliable and safe, which is enforced by stringent regulations, the practical innovation of nuclear reactor designs has been scant largely since the designs of the popular PWR designs of the 1970s [16], notwithstanding important developments in China and South Korea. While innovation has been conservative, the use of waste heat for co-production projects has shown some success, all of which, do not modify the inner workings of operating reactors. While the direct use of ionization radiation in this research shows the use of a fission reactor which would suggest some reactor modifications to accommodate a co-production process, this is not likely to be attractive to investors.

However, this research highlights the benefit of a γ-ray only scheme with spent fuel, which can be achieved without the integration with an operating reactor, eliminating those concerns. A decay γ-ray only scheme would also remove concerns about sample radioactivity. Furthermore, the nuclear industry has a long history of operating processes at a commercial scale that manages the hazards associated with significant quantities of spent fissile material with flammable compounds (e.g., tri-butyl phosphate), high temperatures and corrosive conditions [352]. These operations achieved a high degree of regulatory compliance over many decades for fuel reprocessing purposes. In comparison, the hazard potential from the γ-ray scheme described in this research would be significantly reduced due to the spent fuel and the organic media being physically separated, with any possible nuclear criticality eliminated by the pre-existing safe design of the spent fuel storage cells. Furthermore, no high temperatures or pH are currently required for this reaction scheme as are for reprocessing procedures. While for a nuclear cogeneration process to be successfully enacted, research into radiation-chemical process modelling, materials corrosion, safety aspects and economic evaluations need to be completed. However, due to potentially limited throughput, limited by low *G*-values and diminishing returns with higher absorbed doses, the economic evaluations of these current processes could be less than appealing for large-scale applications. A continuous radiolytic process in which the product can be easily separated with minimal energy input is suggested to improve the product throughput, reduce secondary side reactions, and keep *G*-values high during exposure. A process such as this may be economically viable and consequently, increase the likelihood of industrial scaling, as seen with the synthesis of ethyl bromide [61]. Additionally, the abundant stockpiles of spent nuclear fuel present an intergenerational societal issue, which requires safe storage and provides no long-term useful purpose, and for which there is not a clear disposal strategy. In response, this research suggests a pioneering application of waste nuclear fuel and advancement on previous radiolysis research which also incorporates the use of waste organic feedstocks to produce useful chemicals. However, the specific reaction scheme presented here could be achieved more easily through recent chemoselective advances. Future reactions with superior *G*-values, mass productivity conversions and more valuable products could have the potential to be implemented in an industrial chemonuclear process involving spent nuclear fuel.

6 Conclusions

This work presents the conversion of waste organic polyols, namely ethylene glycol and glycerol to useful compounds using γ-ray only and mixed neutron + γ-ray irradiation from a 250 kW TRIGA reactor has been presented. The benefit of the lower dose rate, γ-ray only irradiation scheme is made evident from the superior *G*-value and mass productivity data across all variable parameters and products, compared with the higher-dose, higher LET mixed field neutron + γ-ray irradiation, for all but one instance. The exception here is methanol production from ethylene glycol ($G = 2.9 \pm 0.8$ μmol J^{-1}) using the mixed-field neutron + γ-ray irradiations of 100 kGy, in which the preferential production is the result of increased temperatures during high-dose rate, mixed-field reactor operation. The highest *G*-value product from ethylene glycol radiolysis was acetaldehyde at (8.3 ± 1.0) μmol J^{-1} with 20 kGy γ-ray only dose, which it is hypothesised is due to its acid-catalysed radical chain reaction.

Further exploration into the radiolysis of glycerol has yielded more data and, most notably, elucidated the synthesis of solketal (a potential biofuel additive) via low dose rate (<0.04 kGy min.^{-1}), γ-ray only irradiation of ternary glycerol: acetone: water mixtures with a maximum *G*-value of 1.5 ± 0.2 μmol J^{-1} with a dose of 50 kGy. The highest reported *G*-value for acetol synthesis ($G = 2.7 \pm 0.4$ μmol J^{-1}) was with 70 wt.% glycerol aqueous mixtures and 20 kGy γ-ray dose via the acid-catalysed radical chain mechanism. This work suggests that this mechanism is catalysed by either the stabilized acidified glycerol cation ($CH_2OH–CHOH–CH_2OH_2^+$) via direct action on neat samples or the hydronium ion (H_3O^+) with diluted aqueous samples. Instrumental neutron activation analysis of these samples has also shown that the radioactivity decays to levels comparable to natural materials after ~10 days.

For evaluating radiolytic processes for conversions, mass productivity (MP) is shown to be a valuable quantity which demonstrates the importance of concentrated solutions in radiolytic processes in which dose rate into the organic material is a limiting factor for process throughput. Using γ-ray absorbed doses of 100 kGy, the maximum mass productivities towards a single product were measured to be 1.0 ± 0.1 % with acetaldehyde and 1.0 ± 0.1 % with acetol, from ethylene glycol and glycerol, respectively.

Using MCNP models of the JSI 250 kW TRIGA reactor, the Krško NPP and, a 5 × 2 spent fuel cell matrix (extended to 30 × 57 fuel cells), an investigation of possible radiation-chemical production scenarios was completed. The highest yielding production capacity scenario for solketal (57.4 ± 5.6 t year^{-1}) was found to be the spent fuel grid (emulating the Krško SFP) due to the large irradiation volume, lower dose rate, and γ-ray irradiation. Using the collated radiolytic data, a theoretical European production network encompassing ~180 equivalent SFPs was conducted, based on the relative reactor power of the Krško NPP to the ~180 NPPs within geographical Europe. A maximum production capacity of $(1.3 \pm 0.1) \times 10^4$ t year^{-1} of solketal could be collated across these ~180 potential sites, yielding a volume of $(2.5 \pm 0.2) \times 10^8$ litres year^{-1} of a petroleum fuel blend (95% petroleum, 5% solketal). This would account for 0.31% ± 0.03 % of the volume of the petroleum fuel blends consumed yearly within the EU as of 2018. Compared against other radiation-chemical systems quoted in the literature, this proposed system presents a process with comparative *G*-values, converts renewable waste organic feedstocks, pioneers the utilization of waste ionization radiation as catalytic energy from spent fission fuel and produces a renewable, oxygenated additive for transport fuels. Currently, this radiation-directed process may not compete with other chemoselective processes for solketal production specifically. However, if the *G*-values can be improved to ~20 µmol J^{-1} through selected mixtures and additives whilst showing high mass productivity, then this process may become industrially feasible.

6.1 Future Work

While this exploration into the radiolysis of ethylene glycol and glycerol has yielded new empirical data, elucidated the trends of several variables, detailed the mechanistic discussions of direct radiolysis, and evaluated the process scale-up feasibility, further studies could examine the following:

1) Optimization of the ternary glycerol mixtures in terms of starting component wt.%, aiming towards higher wt.% glycerol mixtures to maximise *G*-values and mass productivities of solketal or acetol.
2) Utilization of real spent fuel irradiation sources to evaluate the empirical radiation chemical yields from SFP irradiation sources.
3) Corrosion studies of steel pipes or other suggested materials for organic piping since oxidizing species such as ketones, organic acids and peroxides are generated.
4) An exploration of the feasibility of other radiation-induced processes that display superior *G*-value and higher mass productivities, whilst also using spent fission fuel as a radiation source. Additionally, this could incorporate a traditional heterogeneous co-catalyst which is designed for a specific reaction. This is analogous to microwave-assisted heterogeneous catalysis as explored in recent research [353].
5) An investigation into the feasibility of using low-temperature (<300^{o}C) heated wastewater from PWR NPPs for low-temperature heterogeneous catalysis processes, such as the synthesis of solketal via ion-exchange resin catalysts.

7 References

References: Radiolysis

1. IAEA/iaa, *Opportunities for Cogeneration with Nuclear Energy*. 2017, Vienna: INTERNATIONAL ATOMIC ENERGY AGENCY, https://www.iaea.org/publications/10877/opportunities-for-cogeneration-with-nuclear-energy.

2. Steinberg, M., *CHEMONUCLEAR REACTORS AND CHEMICAL PROCESSING*, in *Advances in Nuclear Science and Technology*, E.J. Henley and H. Kouts, Editors. 1962, Academic Press. p. 247-333, DOI: https://doi.org/10.1016/B978-1-4831-9955-9.50011-8.

3. Baugh, P.J., et al., *γ-Radiolysis of N2O-saturated aqueous glycerol solutions: Product yields and free radical mechanism.* Radiation Physics and Chemistry (1977), 1982. **20**(3): p. 215-222, DOI: https://doi.org/10.1016/0146-5724(82)90082-6.

4. The Royal Society, *Nuclear Cogeneration: civil nuclear in a low-carbon future policy briefing*. 2020: The Royal Society.

5. Schmeda-Lopez, D., T.B. McConnaughy, and E.W. McFarland, *Radiation enhanced chemical production: Improving the value proposition of nuclear power*. Energy, 2018. **162**: p. 491-504, DOI: https://doi.org/10.1016/j.energy.2018.07.208.

6. McConnaughy, T.B., M.R. Shaner, and E.W. McFarland, *A Techno-Economic Analysis of Chemical Processing with Ionizing Radiation.* Chemical Engineering & Technology, 2017. **40**(6): p. 1196-1202, DOI: https://doi.org/10.1002/ceat.201600507.

7. IAEA/iaa. *Nuclear Share of Electricity Generation in 2019*. 2019 [cited 2021 08/02/2021]; Number of Reactors for Each Country Worldwide]. Available from: https://pris.iaea.org/PRIS/WorldStatistics/NuclearShareofElectricityGeneration.aspx.

8. Allardice, C. and E.R. Trapnell, *The first pile*. Vol. 292. 1949: US Atomic Energy Commission. Technical Information Division.

9. IAEA/iaa. *PRIS Database: Nuclear Power Capacity Trend*. 2021 [cited 2021 19/05/2021]; Available from: https://pris.iaea.org/PRIS/WorldStatistics/WorldTrendNuclearPowerCapacity.aspx.

10. INTERNATIONAL ATOMIC ENERGY AGENCY, *Nuclear Power in the World, Reference Data Series No. 2*, in *Reference Data Series No. 2*. 2020, IAEA: Vienna.

11. BP Energy, *BP Energy Outlook 2019 Edition*. 2019.

12. IEA, *World Energy Outlook 2020*. 2020, International Energy Agency,: Paris.

13. IPCC, *In Climate Change 2014: Mitigation of Climate Change: Working Group III Contribution to the IPCC Fifth Assessment Report*. 2015. p. 1329-1356.

14. Great Britain. Department for Business. Energy and Industrial Strategy, *Energy white paper: Powering our net zero future [White Paper]*, E.I.S. Department for Business, Editor. 2020: UK, London, Available from: https://assets.publishing.service.gov.uk/government/uploads/system/uploads/attachment_data/file/945899/201216_BEIS_EWP_Command_Paper_Accessible.pdf .

15. Sepulveda, N.A., et al., *The role of firm low-carbon electricity resources in deep decarbonization of power generation.* Joule, 2018. **2**(11): p. 2403-2420.

16. McFarland, E., *Sustainable Power From Nuclear Reactions: An Imperfect Option Amongst Few*. 2016, Institute for Energy Efficiency: Santa Barbara, USA, Available from: https://iee.ucsb.edu/events/sustainable-power-nuclear-reactions-imperfect-option-amongst-few.

17. IEA, *IEA World Energy Balances 2020*, IEA, Editor. 2020, Available from: https://www.iea.org/subscribe-to-data-services/world-energy-balances-and-statistics.

18. Arlt, D. and J. Wolling, *Fukushima effects in Germany? Changes in media coverage and public opinion on nuclear power.* Public Understanding of Science, 2016. **25**(7): p. 842-857, DOI: 10.1177/0963662515589276.

19. Jarvis, S., O. Deschenes, and A. Jha, *The Private and External Costs of Germany's Nuclear Phase-Out*. 2019, National Bureau of Economic Research.

20. Traber, T. and C. Kemfert, *German Nuclear Phase-Out Policy: Effects on European Electricity Wholesale Prices, Emission Prices, Conventional Power Plant Investments and Eletricity Trade.* SSRN Electronic Journal, 2012, DOI: 10.2139/ssrn.2111325.

21. Grossi, L., S. Heim, and M. Waterson, *The impact of the German response to the Fukushima earthquake.* Energy Economics, 2017. **66**: p. 450-465.

22. (UNSCEAR), U.N.S.C.o.t.E.o.A.R., *Report to the General Assembly and Scientific Annex A: Levels and Effects of Radiation Exposure Due to the Nuclear Accident after the 2011 Great East-Japan Earthquake and Tsunami*. 2013, Available from: http://www.unscear.org/unscear/en/publications/2013_1.html.

23. Kharecha, P.A. and M. Sato, *Implications of energy and CO2 emission changes in Japan and Germany after the Fukushima accident.* Energy Policy, 2019. **132**: p. 647-653, DOI: https://doi.org/10.1016/j.enpol.2019.05.057.

24. Pidgeon, N.F., I. Lorenzoni, and W. Poortinga, *Climate change or nuclear power—No thanks! A quantitative study of public perceptions and risk framing in Britain.* Global Environmental Change, 2008. **18**(1): p. 69-85, DOI: https://doi.org/10.1016/j.gloenvcha.2007.09.005.

25. Markandya, A. and P. Wilkinson, *Electricity generation and health.* The lancet, 2007. **370**(9591): p. 979-990, DOI: https://doi.org/10.1016/S0140-6736(07)61253-7.

26. Wheatley, S., B.K. Sovacool, and D. Sornette, *Reassessing the safety of nuclear power.* Energy Research & Social Science, 2016. **15**: p. 96-100, DOI: https://doi.org/10.1016/j.jclepro.2015.07.059.

27. IEA, *World Energy Model Documentation - 2018*. 2018, International Energy Agency,: Paris.

28. Murphy, D.J. and C.A.S. Hall, *Year in review—EROI or energy return on (energy) invested.* Annals of the New York Academy of Sciences, 2010. **1185**(1): p. 102-118, DOI: https://doi.org/10.1111/j.1749-6632.2009.05282.x.

29. Hall, C.A.S., J.G. Lambert, and S.B. Balogh, *EROI of different fuels and the implications for society*. Energy Policy, 2014. **64**: p. 141-152, DOI: https://doi.org/10.1016/j.enpol.2013.05.049.

30. Lenzen, M., *Life cycle energy and greenhouse gas emissions of nuclear energy: A review*. Energy Conversion and Management, 2008. **49**(8): p. 2178-2199, DOI: https://doi.org/10.1016/j.enconman.2008.01.033.

31. Weißbach, D., et al., *Energy intensities, EROIs (energy returned on invested), and energy payback times of electricity generating power plants.* Energy, 2013. **52**: p. 210-221, DOI: https://doi.org/10.1016/j.energy.2013.01.029.

32. Sovacool, B.K., et al., *Differences in carbon emissions reduction between countries pursuing renewable electricity versus nuclear power.* Nature Energy, 2020. **5**(11): p. 928-935, DOI: 10.1038/s41560-020-00696-3.

33. Harris, G., et al., *Cost estimates for nuclear power in the UK.* Energy Policy, 2013. **62**: p. 431-442.

34. Vaughan, A., *Could rising costs at Hinkley Point C end the UK's nuclear ambitions?*, in *New Scientist*. 2019, New Scientist, Available from: https://www.newscientist.com/article/2217725-could-rising-costs-at-hinkley-point-c-end-the-uks-nuclear-ambitions/#ixzz60jO0O0Fx.

35. Association, W.N., *Nuclear Power Economics and Project Structuring: 2017 Edition.* World Nuclear Association, London, Tech. Rep, 2017.

36. Lipka, M. and A. Rajewski, *Regress in nuclear district heating. The need for rethinking cogeneration.* Progress in Nuclear Energy, 2020. **130**: p. 103518.

37. IAEA/iaa, *Guidance on Nuclear Energy Cogeneration*, in *Nuclear Energy Series No. NP-T-1.17*. 2019, IAEA: Vienna.

38. Leurent, M., et al., *Driving forces and obstacles to nuclear cogeneration in Europe: Lessons learnt from Finland.* Energy Policy, 2017. **107**: p. 138-150, DOI: https://doi.org/10.1016/j.enpol.2017.04.025.

39. Galen Suppes, T.S., *CHAPTER 12 - Nuclear Power Plant Design*, in *Sustainable Nuclear Power*, G.J. Suppes and T.S. Storvick, Editors. 2007, Academic Press: Burlington. p. 319-351, DOI: https://doi.org/10.1016/B978-012370602-7/50029-6.

40. Dawson, J.W. and M. Phillips, *12 - Gas-cooled nuclear reactor designs, operation and fuel cycle*, in *Nuclear Fuel Cycle Science and Engineering*, I. Crossland, Editor. 2012, Woodhead Publishing. p. 300-332, DOI: https://doi.org/10.1533/9780857096388.3.300.

41. Realmonte, G., et al., *An inter-model assessment of the role of direct air capture in deep mitigation pathways.* Nature Communications, 2019. **10**(1): p. 3277, DOI: 10.1038/s41467-019-10842-5.

42. Directorate-General For Energy (European Commision), *Thermal waste recovery at electric power plants in the European Economic Community*. 1991, European Commission: Paris.

43. Yildiz, B. and M.S. Kazimi, *Efficiency of hydrogen production systems using alternative nuclear energy technologies.* International Journal of Hydrogen Energy, 2006. **31**(1): p. 77-92, DOI: https://doi.org/10.1016/j.ijhydene.2005.02.009.

44. Forsberg, C.W., *Hydrogen, nuclear energy, and the advanced high-temperature reactor.* International Journal of Hydrogen Energy, 2003. **28**(10): p. 1073-1081, DOI: https://doi.org/10.1016/S0360-3199(02)00232-X.

45. Megahed, M.M., *Feasibility of nuclear power and desalination on El-Dabaa site.* Desalination, 2009. **246**(1): p. 238-256, DOI: https://doi.org/10.1016/j.desal.2008.03.054.

46. Ewan, B.C.R. and R.W.K. Allen, *A figure of merit assessment of the routes to hydrogen.* International Journal of Hydrogen Energy, 2005. **30**(8): p. 809-819, DOI: https://doi.org/10.1016/j.ijhydene.2005.02.003.

47. Ingersoll, D.T., *4 - Nuclear power 101: Understanding nuclear reactors*, in *Small Modular Reactors*, D.T. Ingersoll, Editor. 2016, Woodhead Publishing: Boston. p. 61-70, DOI: https://doi.org/10.1016/B978-0-08-100252-0.00004-5.

48. National Academies of Sciences, E. and Medicine, *Molybdenum-99 for medical imaging*. 2016: National Academies Press.

49. IAEA/iaa, *Feasibility of Producing Molybdenum-99 on a Small Scale Using Fission of Low Enriched Uranium or Neutron Activation of Natural Molybdenum*, in *Technical Reports Series No. 478*. 2015, IAEA: Vienna

50. Landsman, D. and J. Butterfield, *THE PRODUCTION OF CHEMICALS FROM REACTORS. PART V. ETHYLENE GLYCOL FROM THE PILE (n+ $ gamma $) AND FISSION FRAGMENT IRRADIATION OF LIQUID METHANOL*. 1961, United Kingdom Atomic Energy Authority. Research Group. Atomic Energy ….

51. Long, G., *THE PRODUCTION OF CHEMICALS FROM REACTORS. PART II. DEPOSITION OF ENERGY BY FISSION FRAGMENTS IN TWO-PHASE SYSTEMS*. 1958, United Kingdom Atomic Energy Authority. Research Group. Atomic Energy ….

52. Spinks, J.W.T. and R.J. Woods, *Chapter 9: Organic Compounds*, in *An introduction to radiation chemistry*. 1990.

53. Steinberg, M., *Chemonuclear and Radiation Chemical Process Applications.* Nuclear Applications, 1969. **6**(5): p. 425-433.

54. Hedin, A., *Spent nuclear fuel–how dangerous is it.* SKB Report, 1997: p. 97-13.

55. Lloyd, W., M. Sheaffer, and W. Sutcliffe, *Dose rate estimates from irradiated light-water-reactor fuel assemblies in air*. 1994, Lawrence Livermore National Lab.

56. Harteck, P. and S. Dondes, *Fixation of nitrogen by ionizing radiation as nitrogen dioxide and nitrous oxide.* The Journal of Chemical Physics, 1956. **24**(3): p. 619-619.

57. Harteck, P. and S. Dondes, *Decomposition of Carbon Dioxide by Ionizing Radiation. Part II.* The Journal of Chemical Physics, 1957. **26**(6): p. 1727-1733, DOI: 10.1063/1.1743611.

58. Lichtin, N.N., *Radiolysis of Methanol and Methanolic Solutions by CO60Gamma-Rays and 1.95 x 106Volt de Graaf Electrons.* The Journal of Physical Chemistry, 1959. **63**(9): p. 1449-1454.

59. Krushinskaya, N. and M. Proskurnin, *OXIDATION OF CHLOROBENZENE IN AQUEOUS SOLUTIONS BY THE ACTION OF IRRADIATION.* Zhur. Fiz. Khim., 1959. **33**.

60. Landsman, D., *Hydrazine from a chemonuclear reactor.* Nuclear Eng., 1962. **7**.

61. Harmer, D., et al., *The Dow ethyl bromide process: an industrial application of radiation chemistry*, in *Industrial Uses of Large Radiation Sources. Proceedings of a Conference on the Application of Large Radiation Sources in Industry. Vol. II*. 1963, IAEA.

62. IEA, *The Future of Petrochemicals*. 2018, IEA: Paris, Available from: https://www.iea.org/reports/the-future-of-petrochemicals.

63. Commission, E., *Clean Power for Transport: A European alternative fuels strategy*. 2013, Available from: https://eur-lex.europa.eu/legal-content/EN/ALL/?uri=CELEX%3A52013PC0017.

64. Taylor, R., et al., *From the sugar platform to biofuels and biochemicals: final report for the European Commission Directorate-General Energy*. 2015, E4tech/Re-CORD/Wageningen UR.

65. Spekreijse, J., et al., *Insights into the European market of bio-based chemicals.* Publications Office of the European Union, Luxembourg, 2019.

66. IEA, *Renewables 2019*. 2019, IEA: Paris, Available from: https://www.iea.org/reports/renewables-2019.

67. Union, E., *Directive 2009/28/EC of the European Parliament and of the Council of 23 April 2009 on the promotion of the use of energy from renewable sources and amending and subsequently repealing Directives 2001/77/EC and 2003/30/EC*, in *Official Journal of the European Union*. 2009. p. 2009.

68. E4tech, *ePure - E20 Supply and Demand Study*. 2019: London, UK, Available from: https://www.epure.org/wp-content/uploads/2020/11/191128-def-rep-e4tech-e20-supply-and-demand-study-final-report.pdf.

69. European Commission, D.-G.f.C.A., CE Delft ,ENSYS Energy, Vivideconomics, ICF International, , *Impact of higher levels of bio components in transport fuels in the context of the Directive 98/70/EC of the European Parliament and of the Council of 13 October 1998, relating to the quality of petrol and diesel fuels and amending Council Directive 93/12/EEC [Final Report]*. 2015: Brussels.

70. Shahir, S.A., et al., *Feasibility of diesel–biodiesel–ethanol/bioethanol blend as existing CI engine fuel: An assessment of properties, material compatibility, safety and combustion.* Renewable and Sustainable Energy Reviews, 2014. **32**: p. 379-395, DOI: https://doi.org/10.1016/j.rser.2014.01.029.

71. Joint Research Centre, D.-G.f.M.a.T., European Commission, *State of the Art on Alternative Fuels Transport Systems in the European Union*, J.R. Centre, Editor. 2020, European Commission: Brussels, Available from: https://op.europa.eu/en/publication-detail/-/publication/cfc1b254-cfd6-11ea-adf7-01aa75ed71a1.

72. Jeswani, H.K., A. Chilvers, and A. Azapagic, *Environmental sustainability of biofuels: a review.* Proceedings of the Royal Society A, 2020. **476**(2243): p. 20200351.

73. European Commission, *DIRECTIVE (EU) 2018/2001 OF THE EUROPEAN PARLIAMENT AND OF THE COUNCIL of 11 December 2018 on the promotion of the use of energy from renewable sources*. 2018, EC: Brussels, Available from: https://eur-lex.europa.eu/legal-content/EN/TXT/PDF/?uri=CELEX:32018L2001&from=fr.

74. Parliament, E., *On the promotion of the use of energy from renewable sources*. 2018, EU Parliment: Brussels, Available from: http://data.europa.eu/eli/dir/2018/2001/oj.

75. Knoope, M.M.J., C.H. Balzer, and E. Worrell, *Analysing the water and greenhouse gas effects of soya bean-based biodiesel in five different regions.* GCB Bioenergy, 2019. **11**(2): p. 381-399, DOI: https://doi.org/10.1111/gcbb.12558.

76. Roy, P. and A. Dutta, *Life cycle assessment of ethanol derived from sawdust.* Bioresource Technology, 2013. **150**: p. 407-411, DOI: https://doi.org/10.1016/j.biortech.2013.08.057.

77. Stephenson, A.L., et al., *The environmental and economic sustainability of potential bioethanol from willow in the UK.* Bioresource Technology, 2010. **101**(24): p. 9612-9623, DOI: https://doi.org/10.1016/j.biortech.2010.07.104.

78. Daystar, J., et al., *The NREL Biochemical and Thermochemical Ethanol Conversion Processes: Financial and Environmental Analysis Comparison.* BioResources, 2015. **10**, DOI: 10.15376/biores.10.3.5096-5116.

79. Energy, U.D.o., *Clean Cities: Alternative Fuel Price Report*. 2021, Available from: https://afdc.energy.gov/fuels/prices.html.

80. Karinen, R. and A. Krause, *New biocomponents from glycerol.* Applied Catalysis A: General, 2006. **306**: p. 128-133.

81. National Center for Biotechnology Information. *PubChem Compound Summary for CID 753, Glycerol.* 2021 [cited 2021 4th of May]; Glycerol properties]. Available from: https://pubchem.ncbi.nlm.nih.gov/compound/Glycerol.

82. Abdul Raman, A.A., H.W. Tan, and A. Buthiyappan, *Two-Step Purification of Glycerol as a Value Added by Product From the Biodiesel Production Process.* Frontiers in Chemistry, 2019. **7**(774), DOI: 10.3389/fchem.2019.00774.

83. OECD, Food, and A.O.o.t.U. Nations, *OECD-FAO Agricultural Outlook 2017-2026*. 2017, DOI: doi:https://doi.org/10.1787/agr_outlook-2017-en.

84. Ciriminna, R., et al., *Understanding the glycerol market.* European Journal of Lipid Science and Technology, 2014. **116**(10): p. 1432-1439, DOI: https://doi.org/10.1002/ejlt.201400229.

85. Quispe, C.A.G., C.J.R. Coronado, and J.A. Carvalho Jr, *Glycerol: Production, consumption, prices, characterization and new trends in combustion.* Renewable and Sustainable Energy Reviews, 2013. **27**: p. 475-493, DOI: https://doi.org/10.1016/j.rser.2013.06.017.

86. Liu, C., et al., *Selective electro-oxidation of glycerol to dihydroxyacetone by a non-precious electrocatalyst–CuO.* Applied Catalysis B: Environmental, 2020. **265**: p. 118543, DOI: https://doi.org/10.1016/j.apcatb.2019.118543.

87. B. Flach, K.B., S. Lieberz, *USDA foreign agricultural service global agriculture information network (GAIN) report*, in *EU Biofuels Ann. 25*. 2012.

88. Pagliaro, M., *Chapter 1 - Properties, Applications, History, and Market*, in *Glycerol: The Renewable Platform Chemical*, M. Pagliaro, Editor. 2017, Elsevier. p. 1-21, DOI: https://doi.org/10.1016/B978-0-12-812205-1.00001-1.

89. ICIS. *Spot Europe glycerine prices surge on limited supply, healthy demand*. 2017; Available from: https://www.icis.com/explore/resources/news/2017/03/23/10090697/spot-europe-glycerine-prices-surge-on-limited-supply-healthy-demand/.

90. J., H.L. in *ICIS Asia OleochemicalsConference 2013*. 2013. Kuala Lumpur.

91. Monteiro, M.R., et al., *Glycerol from biodiesel production: Technological paths for sustainability.* Renewable and Sustainable Energy Reviews, 2018. **88**: p. 109-122, DOI: https://doi.org/10.1016/j.rser.2018.02.019.

92. Checa, M., et al., *Recent Advances in Glycerol Catalytic Valorization: A Review.* Catalysts, 2020. **10**(11): p. 1279.

93. Mota, C., B.P. Pinto, and A.L. De Lima, *Glycerol: A Versatile Renewable Feedstock for the Chemical Industry*. 2017: Springer.

94. Santacesaria, E., et al., *New process for producing epichlorohydrin via glycerol chlorination.* Industrial & Engineering Chemistry Research, 2010. **49**(3): p. 964-970.

95. Almena, A. and M. Martín, *Technoeconomic analysis of the production of epichlorohydrin from glycerol.* Industrial & Engineering Chemistry Research, 2016. **55**(12): p. 3226-3238.

96. Crabtree, R.H., *Transfer Hydrogenation with Glycerol as H-Donor: Catalyst Activation, Deactivation and Homogeneity.* ACS Sustainable Chemistry & Engineering, 2019. **7**(19): p. 15845-15853, DOI: 10.1021/acssuschemeng.9b00228.

97. Albonetti, S., R. Mazzoni, and F. Cavani, *Homogeneous, heterogeneous and nanocatalysis*. 2014.

98. Azua, A., et al., *Transfer Hydrogenation from Glycerol: Activity and Recyclability of Iridium and Ruthenium Sulfonate-Functionalized N-Heterocyclic Carbene Catalysts.* ACS Sustainable Chemistry & Engineering, 2017. **5**(5): p. 3963-3972, DOI: 10.1021/acssuschemeng.6b03156.

99. Finn, M., et al., *Next-Generation Water-Soluble Homogeneous Catalysts for Conversion of Glycerol to Lactic Acid.* Organometallics, 2018. **37**(9): p. 1400-1409, DOI: 10.1021/acs.organomet.8b00081.

100. Nakagawa, Y. and K. Tomishige, *Heterogeneous catalysis of the glycerol hydrogenolysis.* Catalysis Science & Technology, 2011. **1**(2): p. 179-190, DOI: 10.1039/C0CY00054J.

101. Nair, D., et al., *Homogeneous catalyst separation and re-use through nanofiltration of organic solvents.* Desalination, 2002. **147**(1-3): p. 301-306.

102. Moulijn, J.A., A.E. van Diepen, and F. Kapteijn, *Catalyst deactivation: is it predictable?: What to do?* Applied Catalysis A: General, 2001. **212**(1): p. 3-16, DOI: https://doi.org/10.1016/S0926-860X(00)00842-5.

103. Hammond, C., *Intensification studies of heterogeneous catalysts: probing and overcoming catalyst deactivation during liquid phase operation.* Green Chemistry, 2017. **19**(12): p. 2711-2728.

104. Mohd Hanif, M., A. Roila, and Y. Wan Md Zin Wan, *A Review of Acetol: Application and Production.* American Journal of Applied Sciences, 2011. **8**(11), DOI: 10.3844/ajassp.2011.1135.1139.

105. Parate, R., et al., *Bioglycerol (C3) upgrading to 2,3-butanediol (C4) by cell-free extracts of Enterobacter aerogenes NCIM 2695.* Journal of Chemical Technology & Biotechnology, 2021. **96**(5): p. 1316-1325, DOI: https://doi.org/10.1002/jctb.6650.

106. Basu, S. and A.K. Sen, *A Review on Catalytic Dehydration of Glycerol to Acetol.* ChemBioEng Reviews, 2021. **8**(6): p. 633-653, DOI: https://doi.org/10.1002/cben.202100009.

107. Dasari, M.A., et al., *Low-pressure hydrogenolysis of glycerol to propylene glycol.* Applied Catalysis A: General, 2005. **281**(1): p. 225-231, DOI: https://doi.org/10.1016/j.apcata.2004.11.033.

108. Célerier, S., et al., *Glycerol dehydration to hydroxyacetone in gas phase over copper supported on magnesium oxide (hydroxide) fluoride catalysts.* Applied Catalysis A: General, 2018. **557**: p. 135-144, DOI: https://doi.org/10.1016/j.apcata.2018.03.022.

109. Mota, C.J.A., et al., *Glycerin Derivatives as Fuel Additives: The Addition of Glycerol/Acetone Ketal (Solketal) in Gasolines.* Energy & Fuels, 2010. **24**(4): p. 2733-2736, DOI: 10.1021/ef9015735.

110. Fatimah, I., et al., *Glycerol to Solketal for Fuel Additive: Recent Progress in Heterogeneous Catalysts.* Energies, 2019. **12**(15): p. 2872, https://www.mdpi.com/1996-1073/12/15/2872.

111. Nanda, M.R., et al., *Thermodynamic and kinetic studies of a catalytic process to convert glycerol into solketal as an oxygenated fuel additive.* Fuel, 2014. **117**: p. 470-477, DOI: https://doi.org/10.1016/j.fuel.2013.09.066.

112. Alibaba. *High Temperature Resistance Catalyst Resin equal to AMBERLYST DT.* 2022 [cited 2022 14/12/2022]; Acid Resin Catalyst Prices]. Available from: https://www.alibaba.com/product-detail/High-Temperature-Resistance-Catalyst-Resin-equal_62530999330.html.

113. Burton, M., *Radiation chemistry.* The Journal of Physical Chemistry, 1947. **51**(2): p. 611-625.

114. Freeman, G.R., *RADIOLYSIS OF ALCOHOLS.* pp 73-134 of Actions Chimiques et Biologiques des Radiations. / Haissinsky, M. Paris Masson et Cie, Editeurs (1970). 1970: p. Medium: X.

115. Shkrob, I.A., M.C. Sauer, and A.D. Trifunac, *Radiation chemistry of organic liquids: Saturated hydrocarbons*, in *Studies in Physical and Theoretical Chemistry*, C.D. Jonah and B.S.M. Rao, Editors. 2001, Elsevier. p. 175-221, DOI: https://doi.org/10.1016/S0167-6881(01)80011-2.

116. Dainton, F.S. and G.A. Salmon, *Primary Products and Processes in the γ-Radiolysis of 2-Methyltetrahydrofuran.* Proceedings of the Royal Society of London. Series A, Mathematical and Physical Sciences, 1965. **285**(1402): p. 319-338, http://www.jstor.org/stable/2415237.

117. Ma, J., et al., *Reactivity of the Strongest Oxidizing Species in Aqueous Solutions: The Short-Lived Radical Cation H2O•+.* The Journal of Physical Chemistry Letters, 2014. **5**(1): p. 258-261, DOI: 10.1021/jz402411x.

118. Morco, R.P., *Gamma-Radiolysis Kinetics and Its Role in the Overall Dynamics of Materials Degradation.* 2020.

119. Wren, J., *Steady-state radiolysis: effects of dissolved additives*, in *Nuclear Energy and the Environment*. 2010, ACS Publications. p. 271-295.

120. Le Caër, S., *Water Radiolysis: Influence of Oxide Surfaces on H2 Production under Ionizing Radiation.* Water, 2011. **3**(1): p. 235-253, https://www.mdpi.com/2073-4441/3/1/235.

121. Donoclift, T.A., *The Radiolytic Steady-State and Factors Controlling H2 Production.* 2017.

122. Chapiro, A., *Chemical Evidence of Track Effects in the Radiolysis of Liquids.* Radiation Research, 1957. **6**(1): p. 11-26, DOI: 10.2307/3570488.

123. ICRU, *ICRU Reports.* Reports of the International Commission on Radiation Units and Measurements, 1973. **os-12**(2): p. 26-29, DOI: 10.1093/jicru_os12.2.26.

124. Attix, F.H., *Introduction to radiological physics and radiation dosimetry*. 1986, New York: John Wiley & Sons.

125. Podgorsak, E.B., *Radiation oncology physics*. 2005: IAEA Vienna.

126. Andreo, P., et al., *Fundamentals of ionizing radiation dosimetry*. 2017: John Wiley & Sons.

127. Attix, F.H., *Introduction to radiological physics and radiation dosimetry*. 2008: John Wiley & Sons.

128. Coderre, J. *Principles of Radiation Interactions*. 2004 [cited 2021 20/05/21]; Available from: https://ocw.mit.edu/courses/nuclear-engineering/22-55j-principles-of-radiation-interactions-fall-2004.

129. Nikjoo, H. and L. Lindborg, *RBE of low energy electrons and photons.* Physics in Medicine & Biology, 2010. **55**(10): p. R65.

130. Choppin, G., J.-O. Liljenzin, and J. Rydberg, *Radiochemistry and nuclear chemistry*. 2002: Butterworth-Heinemann.

131. L'Annunziata, M.F., *Handbook of radioactivity analysis*. 2012: Academic press.

132. Rinard, P., *Neutron interactions with matter.* Passive Nondestructive Assay of Nuclear Materials, 1991(375-377).

133. Prelas, M.A., et al., *A review of nuclear batteries.* Progress in Nuclear Energy, 2014. **75**: p. 117-148.

134. Meyers, R.A., *Encyclopedia of physical science and technology*. 2002: Academic.

135. Bank, O.N.D., *The JEFF-3.2 Nuclear Data Library*. 2014.

136. More, C.V., et al., *Polymeric composite materials for radiation shielding: a review.* Environmental Chemistry Letters, 2021, DOI: 10.1007/s10311-021-01189-9.

137. Soppera, N., M. Bossant, and E. Dupont, *JANIS 4: An Improved Version of the NEA Java-based Nuclear Data Information System.* Nuclear Data Sheets, 2014. **120**: p. 294-296, DOI: https://doi.org/10.1016/j.nds.2014.07.071.

138. Lamarsh, J.R., *Introduction to nuclear reactor theory*. 1966: Addison-Wesley.

139. Rodrigues, C., et al., *Slow-neutron scattering cross-section for methanol, ethanol, propanol, iso-propanol, butanol, ethanediol and propanetriol.* Journal of Nuclear Energy, 1972. **26**(7): p. 379-383, DOI: https://doi.org/10.1016/0022-3107(72)90078-0.

140. Dole, M., C.D. Keeling, and D.G. Rose, *The Pile Irradiation of Polyethylene.* Journal of the American Chemical Society, 1954. **76**(17): p. 4304-4311, DOI: 10.1021/ja01646a015.

141. Nelson, G. and D. Reilly, *Gamma-ray interactions with matter.* Passive nondestructive analysis of nuclear materials, 1991. **2**: p. 27-42.

142. Tavernier, S., *Interactions of particles in matter*, in *Experimental techniques in nuclear and particle physics*. 2009, Springer. p. 23-53.

143. Patrignani, C., et al., *Review of particle physics.* 2016.

144. Ganguly, A. and J. Magee, *Theory of radiation chemistry. III. Radical reaction mechanism in the tracks of ionizing radiations.* The Journal of Chemical Physics, 1956. **25**(1): p. 129-134, DOI: https://doi.org/10.1063/1.1742803.

145. Samuel, A.H. and J.L. Magee, *Theory of Radiation Chemistry. II. Track Effects in Radiolysis of Water.* Journal of Chemical Physics, 1953. **21**: p. 1080, DOI: 10.1063/1.1699113.

146. Mozumder, A. and J. Magee, *Model of tracks of ionizing radiations for radical reaction mechanisms.* Radiation research, 1966. **28**(2): p. 203-214, DOI: https://doi.org/10.2307/3572190.

147. Swallow, A.J., *Radiation Chemistry of Organic Compounds: International Series of Monographs on Radiation Effects in Materials*. Vol. 2. 1960: Elsevier.

148. Morrison, P. *Radiation in living matter: The physical processes*. in *Symposium on Radiobiology: The Basic Aspects of Radiation Effects on Living Systems (Oberlin College, June 14-18, 1950)*. 1952.

149. Murshed, H., *Chapter 3 - Radiation Biology*, in *Fundamentals of Radiation Oncology (Third Edition)*, H. Murshed, Editor. 2019, Academic Press. p. 57-87, DOI: https://doi.org/10.1016/B978-0-12-814128-1.00003-9.

150. Mozumder, A. and Y. Hatano, *Charged particle and photon interactions with matter: chemical, physicochemical, and biological consequences with applications*. 2003: CRC Press.

151. Bewley, D., *Calculated LET distributions of fast neutrons.* Radiation research, 1968. **34**(2): p. 437-445, DOI: https://doi.org/10.2307/3572568.

152. Draganic, I., *The radiation chemistry of water*. Vol. 26. 2012: Elsevier.

153. Tabata, Y., *Pulse radiolysis of irradiated systems*. 1991: CRC Press.

154. Mozumder, A., *Early production of radicals from charged particle tracks in water.* Radiation Research, 1985. **104**(2s): p. S33-S39.

155. Ledingham, K.W.D., et al., *Towards Laser Driven Hadron Cancer Radiotherapy: A Review of Progress.* Applied Sciences, 2014. **4**(3): p. 402-443, https://www.mdpi.com/2076-3417/4/3/402.

156. Magee, J.L., *Theory of Radiation Chemistry. I. Some Effects of Variation in Ionization Density1,2.* Journal of the American Chemical Society, 1951. **73**(7): p. 3270-3275, DOI: 10.1021/ja01151a082.

157. Mozumder, A. and J. Magee, *Theory of radiation chemistry. VII. Structure and reactions in low LET tracks.* The Journal of Chemical Physics, 1966. **45**(9): p. 3332-3341.

158. Buxton, G.V., et al., *Critical Review of rate constants for reactions of hydrated electrons, hydrogen atoms and hydroxyl radicals (·OH/·O− in Aqueous Solution.* Journal of Physical and Chemical Reference Data, 1988. **17**(2): p. 513-886, DOI: 10.1063/1.555805.

159. Swallow, A., *Application of pulse radiolysis to the study of aqueous organic systems*, in *The Study of Fast Processes and Transient Species by Electron Pulse Radiolysis*. 1982, Springer. p. 289-315.

160. Herbert, J.M. and M.P. Coons, *The hydrated electron.* Annual review of physical chemistry, 2017. **68**: p. 447-472.

161. Lai, C.C. and G.R. Freeman, *Solvent effects on the reactivity of solvated electrons with organic solutes in methanol/water and ethanol/water mixed solvents.* Journal of Physical Chemistry, 1990. **94**(1): p. 302-308.

162. Spinks, J.W.T. and R.J. Woods, *An introduction to radiation chemistry.* 1990.

163. Hart, E.J., *Radiation Chemistry of Aqueous Solutions.* Annual Review of Nuclear Science, 1965. **15**(1): p. 125-150, DOI: 10.1146/annurev.ns.15.120165.001013.

164. Nikjoo, P.O.N.D.T.G. and H. M. Terrissol, *Computational modelling of low-energy electron-induced DNA damage by early physical and chemical events.* International Journal of Radiation Biology, 1997. **71**(5): p. 467-483, DOI: 10.1080/095530097143798.

165. Ghoshal, K., et al., *5-Aza-deoxycytidine induces selective degradation of DNA methyltransferase 1 by a proteasomal pathway that requires the KEN box, bromo-adjacent homology domain, and nuclear localization signal.* Mol Cell Biol, 2005. **25**(11): p. 4727-41, DOI: 10.1128/mcb.25.11.4727-4741.2005.

166. Plante I, N. *Radiation chemistry and oxidative stress*. 2010. https://three.jsc.nasa.gov/multimedia/RadiationChemistry2.pdf.

167. Frankenberg, D., et al., *Evidence for DNA double-strand breaks as the critical lesions in yeast cells irradiated with sparsely or densely ionizing radiation under oxic or anoxic conditions.* Radiat Res, 1981. **88**(3): p. 524-32.

168. Getoff, N., et al., *Primary yields of CH3•O and •CH2OH radicals resulting in the radiolysis of high purity methanol.* Radiation Physics and Chemistry, 1993. **41**(6): p. 797-801, DOI: https://doi.org/10.1016/0969-806X(93)90025-P.

169. Baxendale, J.H. and P. Wardman, *The radiolysis of methanol: product yields, rate constants, and spectroscopic parameters of intermediates*. 1975, NATIONAL STANDARD REFERENCE DATA SYSTEM.

170. Ellison, D.H., et al., *Nanosecond pulse radiolysis of methanolic and aqueous solutions of readily oxidizable solutes.* Proceedings of the Royal Society of London. A. Mathematical and Physical Sciences, 1972. **328**(1572): p. 23-36, DOI: doi:10.1098/rspa.1972.0066.

171. Shiotani, M., S. Murabayashi, and J. Sohma, *Spin trapping of the short-lived free radicals formed in γ-irradiated alcohols.* International Journal for Radiation Physics and Chemistry, 1976. **8**(4): p. 483-495, DOI: https://doi.org/10.1016/0020-7055(76)90012-7.

172. Seuntjens, J., W. Strydom, and K. Shortt, *Dosimetric principles, quantities and units.* Radiation oncology physics: a handbook for teachers and students. Podgorsak EB, editor. Vienna, Austria: IAEA, 2005.

173. Attix, F.H., *Charged-Particle and Radiation Equilibria*, in *Introduction to Radiological Physics and Radiation Dosimetry*. 2007, Wiley-VCH Verlag GmbH. p. 61-79, DOI: 10.1002/9783527617135.ch4.

174. NPL. *Quantities, Units, and Ionising Radiation Fundamentals*. [cited 2021 20/05/2021]; NPL document]. Available from: https://www.npl.co.uk/getmedia/5e04a366-0ee0-4df3-9be8-8478ba965dae/Quantities-and-Units-for-Ionising-Radiation.pdf.

175. Rosenberg, I., *Radiation oncology physics: a handbook for teachers and students.* British journal of cancer, 2008. **98**(5): p. 1020.

176. Dance, D., et al., *Diagnostic radiology physics.* International Atomic Energy Agency, 2014. **299**.

177. Knoll, G.F., *Radiation detection and measurement*. 2010: John Wiley & Sons.

178. Moussous, O. and T. Medjadj, *A standard Fricke dosimeter compared to an ionization chamber used for dosimetric characterization of 60Co photon beam.* Polish Journal of Medical Physics and Engineering, 2016. **22**(2): p. 19-24.

179. Uusi-Simola, J., *Finnish Dosimetric Practice for Epithermal Neutron Beam Dosimetry in Boron Neutron Capture Therapy.* 2022.

180. Ma, C.C., *Measurement of radiation.* 2008.

181. Liu, Z. and J. Chen, *New calculations of neutron kerma coefficients and dose equivalent.* Journal of Radiological Protection, 2008. **28**(2): p. 185, DOI: 10.1088/0952-4746/28/2/002.

182. McHale, S.R. and E.R. Walker, *DOSE CONVERSION COEFFICIENTS FROM MONOENERGETIC NEUTRONS COMPUTED WITH THE MCNP6.2 CODE IN THE VIP-MAN PHANTOM.* Radiation Protection Dosimetry, 2021. **193**(2): p. 105-123, DOI: 10.1093/rpd/ncab026.

183. Izewska, J. and G. Rajan, *Radiation dosimeters.* Radiation Oncology Physics: A Handbook for Teachers and Students, 2005: p. 71-99.

184. Zhang, G., *Monte Carlo simulation of mixed neutron-gamma radiation fields and dosimetry devices.* 2011.

185. Ambrožič, K., et al., *Delayed gamma determination at the JSI TRIGA reactor by synchronous measurements with fission and ionization chambers.* Nuclear Instruments and Methods in Physics Research Section A: Accelerators, Spectrometers, Detectors and Associated Equipment, 2018. **911**: p. 94-103, DOI: https://doi.org/10.1016/j.nima.2018.09.103.

186. deAlmeida, C.E., et al., *A Feasibility Study of Fricke Dosimetry as an Absorbed Dose to Water Standard for 192Ir HDR Sources.* PLOS ONE, 2014. **9**(12): p. e115155, DOI: 10.1371/journal.pone.0115155.

187. Verlinden, B., et al., *Dosimetry and methodology of gamma irradiation for degradation studies on solvent extraction systems.* Radiochimica Acta, 2021. **109**(1): p. 61-72, DOI: doi:10.1515/ract-2020-0040.

188. ISO, *Practice for use of the ethanol-chlorobenzene dosimetry system*. 2017, ISO, Available from: https://www.iso.org/standard/72759.html.

189. Jazbec, A., et al., *Dose rate calculations at beam tube no. 5 of the JSI TRIGA mark II research reactor using Monte Carlo method.* Applied Radiation and Isotopes, 2021. **168**: p. 109510, DOI: https://doi.org/10.1016/j.apradiso.2020.109510.

190. McKinney, G., *MCNP - A general Monte Carlo code n-particle transport code, Version 5. X-5 Monte Carlo Team*. 2000.

191. Solberg, T.D., et al., *A review of radiation dosimetry applications using the MCNP Monte Carlo code.* Radiochimica Acta, 2001. **89**(4-5): p. 337-355, DOI: doi:10.1524/ract.2001.89.4-5.337.

192. McKinney, M., *MCNP application for the 21 century*. 2000, Los Alamos National Lab., NM (US).

193. Žerovnik, G., et al., *Validation of the neutron and gamma fields in the JSI TRIGA reactor using in-core fission and ionization chambers.* Applied Radiation and Isotopes, 2015. **96**: p. 27-35, DOI: https://doi.org/10.1016/j.apradiso.2014.10.026.

194. Jazbec, A. and L. Snoj, *Calculation of the gamma and neutron dose field inside JSI TRIGA Mark II reactor hall*. 2020, Available from: https://repozitorij.uni-lj.si/Dokument.php?lang=eng&id=137696&dn=.

195. RUSSELL, D.M. *Validation Suites for MCNP™*. in *Proceedings of the American Nuclear Society Radiation Protection and Shielding Division 12th Biennial Topical Meeting, Santa Fe, New Mexico (April 2002).(LA-UR-02-0878)*. 2002.

196. Goričanec, T., et al., *Evaluation of neutron flux and fission rate distributions inside the JSI TRIGA Mark II reactor using multiple in-core fission chambers.* Annals of Nuclear Energy, 2018. **111**: p. 407-440.

197. Kelm, R.S., *In-water neutron and gamma dose determination for a new Cf-252 brachytherapy source*. 2009, Georgia Institute of Technology.

198. Gruel, A., et al., *Gamma-heating and gamma flux measurements in the JSI TRIGA reactor: results and prospects.* IEEE Transactions on Nuclear Science, 2020. **67**(4): p. 559-567.

199. Ambrožič, K., G. Žerovnik, and L. Snoj, *Computational analysis of the dose rates at JSI TRIGA reactor irradiation facilities.* Applied Radiation and Isotopes, 2017. **130**: p. 140-152, DOI: https://doi.org/10.1016/j.apradiso.2017.09.022.

200. McHale, S.R., A.W. Decker, and B.K. Huff, *APPLICATION OF THE MCNP6.1 CODE TO ESTIMATE THE DIRECTIONAL DEPENDENCE OF RADIATION PROTECTION FACTOR VALUES FOR A SIMPLE SURROGATE VEHICLE.* Radiation Protection Dosimetry, 2020. **189**(1): p. 89-97, DOI: 10.1093/rpd/ncaa017.

201. Ambrožič, K., et al. *Characterization of gamma field in the JSI TRIGA reactor*. in *EPJ Web of Conferences*. 2018. EDP Sciences.

202. Elliot, A.J. and D.M. Bartels, *The reaction set, rate constants and g-values for the simulation of the radiolysis of light water over the range 20 deg to 350 deg C based on information available in 2008*. 2009: Canada. p. 162, Available from: http://inis.iaea.org/search/search.aspx?orig_q=RN:41057263.

203. Fiona Hunter, et al., *Determination of G-values for use in SMOGG gas generation calculations*. 2015, AMEC.

204. LaVerne, J.A., Z. Chang, and M.S. Araos, *Heavy ion radiolysis of organic materials.* Radiation Physics and Chemistry, 2001. **60**(4): p. 253-257, DOI: https://doi.org/10.1016/S0969-806X(00)00357-1.

205. Willis, C., A. Boyd, and O. Miller, *Primary yields and mechanism in the radiolysis of gaseous ammonia.* Canadian Journal of Chemistry, 1969. **47**(16): p. 3007-3016.

206. Silaev, M.M., et al., *Radiation-chemical hydroxypropylation of methanol.* High Energy Chemistry, 1986. **20**(3): p. 221-222, http://inis.iaea.org/search/search.aspx?orig_q=RN:18035231.

207. Myron, J. and G. Freeman, *The radiolysis of ethanol: III. Liquid phase.* Canadian Journal of Chemistry, 1965. **43**(2): p. 381-394.

208. Hata, K., et al., *Simulation for radiolytic products of seawater: effects of seawater constituents, dilution rate, and dose rate.* Journal of Nuclear Science and Technology, 2016. **53**(8): p. 1183-1191, DOI: 10.1080/00223131.2015.1096218.

209. Ershov, B.G., et al., *Radiation-induced nitration of organic compounds in aqueous solutions.* Radiochimica Acta, 2012. **100**(12): p. 919-924, DOI: doi:10.1524/ract.2012.1977.

210. Barker, S., J. Brimacombe, and E. Eades, *Action of gamma radiation on liquid ethylene glycol.* Radiation research, 1964. **22**(2): p. 357-367.

211. Bach, N.A., *Oxygen and Peroxide Effects in the Radiation Chemistry of Organic Liquids.* Radiation Research Supplement, 1959. **1**: p. 190-203, DOI: 10.2307/3583639.

212. Phung, P.V. and M. Burton, *Radiolysis of Aqueous Solutions of Hydrocarbons Benzene, <tex-math>$\text{Benzene-}d_{6}$</tex-math>, Cyclohexane.* Radiation Research, 1957. **7**(3): p. 199-216, DOI: 10.2307/3570497.

213. Draganić, Z.D., et al., *Radiation chemistry of overirradiated aqueous solutions of hydrogen cyanide and ammonium cyanide.* Journal of Molecular Evolution, 1985. **21**(4): p. 356-363, DOI: 10.1007/BF02115655.

214. Boujelbane, F., et al., *Decomposition mechanism of hydroxychloroquine in aqueous solution by gamma irradiation.* Chemical Papers, 2022. **76**(3): p. 1777-1787, DOI: 10.1007/s11696-021-01969-1.

215. Zona, R., et al., *Reactivity of OH radicals with chlorobenzoic acids—A pulse radiolysis and steady-state radiolysis study.* Radiation Physics and Chemistry, 2010. **79**(5): p. 626-636, DOI: https://doi.org/10.1016/j.radphyschem.2009.12.005.

216. Meshitsuka, G. and M. Burton, *Hydrogen Iodide Production in Radiolysis of Organic Liquids Containing Dissolved Iodine: Cyclohexane, n-Hexane, Benzene.* Radiation Research, 1959. **10**(5): p. 499-506, DOI: 10.2307/3570784.

217. Van Sickle, D.E. and H.E. Redeker, *Radiolysis of Various Aromatic Alcohols.* Radiation Research, 1964. **21**(2): p. 256-266, DOI: 10.2307/3571564.

218. Sheldon, R.A., *Fundamentals of green chemistry: efficiency in reaction design.* Chemical Society Reviews, 2012. **41**(4): p. 1437-1451.

219. Constable, D.J., A.D. Curzons, and V.L. Cunningham, *Metrics to 'green' chemistry—which are the best?* Green Chemistry, 2002. **4**(6): p. 521-527.

220. Hans-Joachim Hübschmann, *Fundamentals*, in *Handbook of GC-MS*. 2015. p. 7-354, DOI: https://doi.org/10.1002/9783527674305.ch2.

221. Keough, T., et al., *Comparison of the stable products formed by fast atom bombardment and γ-irradiation of glycerol.* Journal of Mass Spectrometry, 1987. **22**(5): p. 241-247.

222. Lux, L., et al., *On the Limit of Detection in Infrared Spectroscopic Imaging.* Applied Spectroscopy, 2022. **76**(1): p. 105-117, DOI: 10.1177/00037028211050961.

223. Chmielewski, A.G. and M. Haji-Saeid, *Radiation technologies: past, present and future.* Radiation Physics and Chemistry, 2004. **71**(1): p. 17-21, DOI: https://doi.org/10.1016/j.radphyschem.2004.05.040.

224. IAEA/iaa, *Advances in Radiation Chemistry of Polymers – Proceedings of a technical meeting held in Notre Dame, Indiana, USA 13–17 September 2003*. 2004, Vienna: INTERNATIONAL ATOMIC ENERGY AGENCY, https://www.iaea.org/publications/7039/advances-in-radiation-chemistry-of-polymers-proceedings-of-a-technical-meeting-held-in-notre-dame-indiana-usa-13-17-september-2003.

225. Markovic, V., *Radiation chemistry: Little known branch of science.* International Atomic Energy Agency Bulletin, 1989. **31**(1): p. 20-23.

226. Dhiman, S.B., et al., *Gamma and heavy ion radiolysis of ionic liquids: A comparative study.* Journal of Nuclear Materials, 2014. **453**(1): p. 182-187, DOI: https://doi.org/10.1016/j.jnucmat.2014.06.056.

227. Galley, M.R., *The fission fragment irradiation of methane.* 1964.

228. Ramirez-Corredores, M.M., et al., *Radiation-Induced Chemistry of Carbon Dioxide: A Pathway to Close the Carbon Loop for a Circular Economy.* Frontiers in Energy Research, 2020. **8**(108), DOI: 10.3389/fenrg.2020.00108.

229. Hummel, A., *Radiation Chemistry of Alkanes and Cycloalkanes.* Alkanes and Cycloalkanes (1992), 1992: p. 743-780.

230. Butler, J., B.M. Hoey, and A.J. Swallow, *Chapter 3. Radiation chemistry.* Annual Reports Section "C" (Physical Chemistry), 1989. **86**(0): p. 49-93, DOI: 10.1039/PC9898600049.

231. Ungar, G., *Radiation effects in polyethylene and n-alkanes.* Journal of Materials Science, 1981. **16**(10): p. 2635-2656, DOI: 10.1007/BF02402826.

232. LaVerne, J.A. and A. Baidak, *Track effects in the radiolysis of aromatic liquids.* Radiation Physics and Chemistry, 2012. **81**(9): p. 1287-1290, DOI: https://doi.org/10.1016/j.radphyschem.2011.11.014.

233. Allen, A.O., *The radiation chemistry of water and aqueous solutions*. 1961: van Nostrand.

234. Garrett, B.C., et al., *Role of water in electron-initiated processes and radical chemistry: Issues and scientific advances.* Chemical reviews, 2005. **105**(1): p. 355-390.

235. Charlesby, A., P. Kopp, and J. Read, *Radiolysis of dilute aqueous thiourea solutions.* Proceedings of the Royal Society of London. Series A. Mathematical and Physical Sciences, 1966. **292**(1428): p. 122-133.

236. Wardman, P., *Radiotherapy Using High-Intensity Pulsed Radiation Beams (FLASH): A Radiation-Chemical Perspective.* Radiation Research, 2020. **194**(6): p. 607-617, DOI: 10.1667/rade-19-00016.

237. Taub, I.A., et al., *Factors affecting radiolytic effects in food.* Radiation Physics and Chemistry (1977), 1979. **14**(3): p. 639-653, DOI: https://doi.org/10.1016/0146-5724(79)90099-2.

238. Gehringer, P., *Radiation processing of aqueous systems.* 1997.

239. Schuler, R.H., L.K. Patterson, and E. Janata, *Yield for the scavenging of hydroxyl radicals in the radiolysis of nitrous oxide-saturated aqueous solutions.* The Journal of Physical Chemistry, 1980. **84**(16): p. 2088-2089, DOI: 10.1021/j100453a020.

240. Freeman, G.R., et al., *Radiation Chemistry of Ethanol: A Review of Data on Yields, Reaction Rate Parameters, and Spectral Properties of Transients*. 1974: National Bureau of Standards, https://books.google.co.uk/books?id=1kYNyAEACAAJ.

241. Sazonov, A., N. Marchenko, and A. Nikitin, *Gamma-radiolysis of the ethanol-water binary system in the presence of oxygen.* High Energy Chemistry, 2015. **49**(4): p. 223-233.

242. Silaev, M., *The Free-Radical Nonbranched-Chain Formation of 1,2-Alkanediols in Alcohol–Formaldehyde Systems.* 2017. **5**: p. 1-8.

243. Novoselov, A., M. Silaev, and L. Bugaenko, *γ-Induced single-step synthesis of ethylene glycol from methanol-formaldehyde solutions.* Theoretical Foundations of Chemical Engineering, 2010. **44**(4): p. 432-435.

244. Pikaev, A. and L. Kartasheva, *Radiolysis of aqueous solutions of ethylene glycol.* International Journal for Radiation Physics and Chemistry, 1975. **7**(2-3): p. 395-415, DOI: https://doi.org/10.1016/0020-7055(75)90079-0.

245. Schulte-Frohlinde, D. and C. Von Sonntag, *Radiation chemistry of ethylene glycol, meso-erythritol, 2-deoxy-D-ribose and alkyl phosphates as DNA model compounds.* Israel Journal of Chemistry, 1972. **10**(6): p. 1139-1150, http://inis.iaea.org/search/search.aspx?orig_q=RN:05133321.

246. Burchill, C. and K. Perron, *Radiation-induced rearrangement of ethylene glycol in aqueous solution.* Canadian Journal of Chemistry, 1971. **49**(14): p. 2382-2389.

247. Venter, P.J., H.J. van der Linde, and R.A. Basson, *Chain formation of acetaldehyde in the γ-radiolysis of deaerated ethylene glycol.* Journal of the Chemical Society, Chemical Communications, 1972(3): p. 187-188, DOI: 10.1039/C39720000187.

248. Schulte-Frohlinde, D. and C. Von Sonntag, *Radiation Chemistry of Ethylene Glycol, Meso-Erythritol, 2-Deoxy-D-Ribose and Alkyl Phosphates as DNA Model Compounds.* Israel Journal of Chemistry, 1972. **10**(6): p. 1139-1150.

249. Eckert, M., et al., *Acetaldehyde*, in *Ullmann's Encyclopedia of Industrial Chemistry*. DOI: https://doi.org/10.1002/14356007.a01_031.pub2.

250. Baugh, P.J., et al., *The radiolysis of glycerol in aqueous solutions*. 1983, Hungary: Akademiai Kiado, http://inis.iaea.org/search/search.aspx?orig_q=RN:16017117.

251. Moore, J.S. and A.F. Norris, *Pulse Radiolysis of Aqueous Glycerol Solutions.* International Journal of Radiation Biology and Related Studies in Physics, Chemistry and Medicine, 1976. **29**(5): p. 489-492, DOI: 10.1080/09553007614550581.

252. Steenken, S., G. Behrens, and D. Schulte-Frohlinde, *Radiation chemistry of DNA model compounds. Part IV. Phosphate ester cleavage in radicals derived*

from glycerol phosphates. International Journal of Radiation Biology and Related Studies in Physics, Chemistry and Medicine, 1974. **25**(2): p. 205-209.

253. Buley, A.L., R.O.C. Norman, and R.J. Pritchett, *Electron spin resonance studies of oxidation. Part VIII. Elimination reactions of some hydroxyalkyl radicals*. Journal of the Chemical Society B: Physical Organic, 1966(0): p. 849-852, DOI: 10.1039/J29660000849.

254. Soucaille, P., F. Voelker, and R. Figge, *Metabolically Engineered Microorganism Useful For The Production Of Acetol*. 2008, METABOLIC EXPLORER SA,: WO, Available from: https://lens.org/173-254-525-880-922.

255. Kim, K., A.V. Zimin, and V.A. Sharpati, *RADIATION PROCESS FOR SYNTHESIS OF ETHYLENE GLYCOL AND FORMALDEHYDE FROM METHANOL*. Khim. Prom., 1963: p. Medium: X; Size: Pages: 12-15.

256. Gal, O., et al., *RADIOLYSIS OF SOLID OXALIC ACID AND AMMONIUM OXALATE INDUCED BY MIXED PILE AND $sup 60$Co GAMMA RADIATION*. Int. J. Appl. Radiat. Isotop., 19: 645-56(Aug. 1968). 1968: p. Medium: X 2009-12-14, DOI: 10.1016/0020-708x(68)90035-5.

257. Sensui, Y., et al., *Phase effects in the pile irradiation radiolysis of cyclohexane and benzene*. The International Journal of Applied Radiation and Isotopes, 1984. **35**(2): p. 135-138, DOI: https://doi.org/10.1016/0020-708X(84)90197-2.

258. Morgan, D.T., *IN-PILE LOOP IRRADIATION STUDIES OF ORGANIC COOLANT MATERIALS. Progress Report, January 1, 1965-September 30, 1965*. 1965, ; Massachusetts Inst. of Tech., Cambridge. Dept. of Nuclear Engineering. p. Medium: ED; Size: Pages: 35, Available from: https://www.osti.gov/servlets/purl/4559289.

259. Vaishnav, Y.N. and C.E. Swenberg, *Radiolysis in Aqueous Solution of Dinucleoside Monophosphates by High-Energy Electrons and Fission Neutrons*. Radiation Research, 1993. **133**(1): p. 12-19, DOI: 10.2307/3578251.

260. Dawson, J.K. and G. Long, *Chemistry of Nuclear Power*. 1959: Philosophical Library.

261. Woods, R.J. and A.K. Pikaev, *Applied radiation chemistry: radiation processing*. 1994: John Wiley & Sons.

262. Anderson, B., M. Sheaffer, and L. Fischer, *Hydrogen generation in tru waste transportation packages*. 2000, Lawrence Livermore National Lab.

263. Tolbert, B.M., et al., *Observations on the Radiation Decomposition of Some C14-Labeled Compounds1*. Journal of the American Chemical Society, 1953. **75**(8): p. 1867-1868, DOI: 10.1021/ja01104a026.

264. Lemmon, R.M., M.A. Parsons, and D.M. Chin, *Effects of Ionizing Radiation on Choline Chloride and its Analogs1*. Journal of the American Chemical Society, 1955. **77**(15): p. 4139-4142.

265. Verdin, D., *The radiolysis of the xylene isomers and ethylbenzene.* The Journal of Physical Chemistry, 1963. **67**(6): p. 1263-1267.

266. Bach, N. *Radiolytic oxidation of organic compounds*. in *Proc. Intern. Conf. Peaceful Uses Atomic Energy, Geneva*. 1955.

267. Silaev, M.M., *Applied Aspects of the γ-Radiolysis of C1–C4 Alcohols and Binary Mixtures on Their Basis.* High Energy Chemistry, 2002. **36**(2): p. 70-75, DOI: 10.1023/A:1014650726821.

268. Haofang, J., et al., *Selecting ethanol as a model organic solvent in radiation chemistry—I. Radiolysis of acetone-ethanol system.* Radiation Physics and Chemistry, 1996. **47**(4): p. 555-558, DOI: https://doi.org/10.1016/0969-806X(95)00064-5.

269. Chen, C., Y. He, and J. Wu, *Selecting ethanol as a model organic solvent in radiation chemistry--3. Radiolysis of glycyrrhetinic acid (GL)-ethanol system and structure modification of GL by γ radiation method.* Radiation Physics and Chemistry, 1998. **53**(2): p. 151-160, DOI: https://doi.org/10.1016/S0969-806X(98)00007-3.

270. Marfak, A., et al., *Mechanisms of Transformation of the Antioxidant Kaempferol into Depsides. Gamma-Radiolysis Study in Methanol and Ethanol.* Radiation Research, 2003. **160**(3): p. 355-365, 11, https://doi.org/10.1667/RR3024.

271. Merklin, J.F. and S. Lipsky, *The Radiation Chemistry of Organic Liquid Mixtures. II1.* The Journal of Physical Chemistry, 1964. **68**(11): p. 3297-3306, DOI: 10.1021/j100793a035.

272. Head, D. and D.C. Walker, *Nitrous Oxide as a Scavenger in the Radiolysis of Water.* Nature, 1965. **207**(4996): p. 517-518, DOI: 10.1038/207517a0.

273. Ferradini, C. and J.-P. Jay-Gerin, *The effect of pH on water radiolysis: A still open question — A minireview.* Research on Chemical Intermediates, 2000. **26**(6): p. 549-565, DOI: 10.1163/156856700X00525.

274. Philipp, W.H., et al., *Use of radiation in preparative chemistry*. 1971: United States. p. 19, Available from: http://inis.iaea.org/search/search.aspx?orig_q=RN:03033847.

275. Hervé du Penhoat, M.-A., et al., *Radiolysis of Liquid Water at Temperatures up to 300 °C: A Monte Carlo Simulation Study.* The Journal of Physical Chemistry A, 2000. **104**(50): p. 11757-11770, DOI: 10.1021/jp001662d.

276. Hochanadel, C.J. and J.A. Ghormley, *Effect of Temperature on the Decomposition of Water by Gamma Rays.* Radiation Research, 1962. **16**(5): p. 653-660, DOI: 10.2307/3571261.

277. Vetrov, V.S., E.P. Kalyazin, and E.P. Petryaev, *On the alcohol formation in radiolysis of water solutions of ethylene glycol.* Vestsi Akadehmii Navuk BSSR Seryya Fizika-Ehnergetychnykh Navuk, 1978(4): p. 63-64, http://inis.iaea.org/search/search.aspx?orig_q=RN:10468983.

278. Engineering ToolBox. *Liquids - Densities*. 2004 [cited 2022 14/11/2022]; Available from: https://www.engineeringtoolbox.com/liquids-densities-d_743.html.

279. Engineering ToolBox. *Solids - Densities*. 2009 [cited 2022 14/11/2022]; Available from: https://www.engineeringtoolbox.com/density-solids-d_1265.html.

280. Buchalla, R., C. Boess, and K.W. Bögl, *Characterization of volatile radiolysis products in radiation-sterilized plastics by thermal desorption–gas chromatography–mass spectrometry: screening of six medical polymers.* Radiation Physics and Chemistry, 1999. **56**(3): p. 353-367, DOI: https://doi.org/10.1016/S0969-806X(99)00311-4.

281. Hegazy, E.-S.A., et al., *Radiation-induced oxidative degradation of isotactic polypropylene.* Journal of Applied Polymer Science, 1981. **26**(4): p. 1361-1372, DOI: https://doi.org/10.1002/app.1981.070260427.

282. Buchalla, R., C. Boess, and K.W. Bögl, *Analysis of volatile radiolysis products in gamma-irradiated LDPE and polypropylene films by thermal desorption-gas chromatography-mass spectrometry.* Appl Radiat Isot, 2000. **52**(2): p. 251-69, DOI: 10.1016/s0969-8043(99)00125-6.

283. White, I., et al., *An Overview of Basic Radiation Effects on Polymers and Glasses.* 2013.

284. Standards, N.I.o., Technology, and N. Simon, *Irradiation damage in inorganic insulation materials for ITER magnets: a review*. 1994.

285. Snyder, J.B., *Shape and Structure of Neutron-Rich from Cf-252 Fission Fragments.* 2014.

286. Spiegel, V., *The Effective Half-Life of Californium-252.* Nuclear Science and Engineering, 1974. **53**(3): p. 326-327, DOI: 10.13182/NSE74-A23358.

287. Lee, Y.-K. *Neutron deep penetration calculations in light water with Monte Carlo tripoli-4® variance reduction techniques*. in *EPJ Web of Conferences*. 2017. EDP Sciences.

288. Yamashita, H., et al., *Physical and biological dosimetries of Cf-252 radiation.* Nucl. Sci. Appl.; (United States), 1986. **2:3**: p. Medium: X; Size: Pages: 345-367 2009-12-17, https://www.osti.gov/biblio/6698835.

289. Rasouli, F.S., H. Bakhshandeh, and S.M. Salehkoutahi, *A simulation study on using 252Cf for the treatment of esophagus tumor in human phantom.* EJNMMI Physics, 2020. **7**(1): p. 71, DOI: 10.1186/s40658-020-00341-8.

290. Smodis, C., et al., *TRIGA 14 MW Research Reactor Status and Utilization: The JSI TRIGA MARK II REACTOR, SLOVENIA*, in *History, Development and Future of TRIGA Research Reactors. Companion CD-ROM*. 2016, JSI, Slovenia. p. 76-89.

291. (JSI), R.I.C. *Triangular Channel*. Properties of Irradiation Channels 2021 [cited 2022 08/02/2022]; Available from: https://ric.ijs.si/en/triangular-channel/.

292. Smodiš, B. and L. Snoj, *Utilization and Application of the Slovenian TRIGA Reactor*. Jozef Stefan" Institute, Ljubljana, Slovenia, Tech. Rep, 2011.

293. Snoj, L., G. Žerovnik, and A. Trkov, *Computational analysis of irradiation facilities at the JSI TRIGA reactor.* Applied Radiation and Isotopes, 2012. **70**(3): p. 483-488, DOI: https://doi.org/10.1016/j.apradiso.2011.11.042.

294. Goorley, T., et al., *Initial MCNP6 release overview.* Nuclear Technology, 2012. **180**(3): p. 298-315.

295. Chadwick, M.B., et al., *ENDF/B-VII.0: Next Generation Evaluated Nuclear Data Library for Nuclear Science and Technology.* Nuclear Data Sheets, 2006. **107**(12): p. 2931-3060, DOI: https://doi.org/10.1016/j.nds.2006.11.001.

296. Jazbec, A., *Neutron and gamma dose rates for the Triangular Channel in the JSI Reactor*, A.G. Plant, Editor. 2020.

297. Kaiba, T., et al., *Validation of neutron flux redistribution factors in JSI TRIGA reactor due to control rod movements.* Appl Radiat Isot, 2015. **104**: p. 34-42, DOI: 10.1016/j.apradiso.2015.06.026.

298. Pychlau, W., *IC Calibration Certificate No. 1801613*. 2018, PTW-Freiburg: Freiburg.

299. Rossbach, M. and M. Blaauw, *Progress in the k0-IAEA program.* Nuclear Instruments and Methods in Physics Research Section A: Accelerators, Spectrometers, Detectors and Associated Equipment, 2006. **564**(2): p. 698-701, DOI: https://doi.org/10.1016/j.nima.2006.04.015.

300. Jacimovic, R., et al., *Application of k0-method of neutron activation analysis for determination of trace elements in various mineral samples: a review.* Macedonian Journal of Chemistry and Chemical Engineering, 2015. **34**(1): p. 169-179.

301. Stein, S.E., *NIST standard reference database 1A (NIST 11).* The National Institute of Standards and Technology NIST, 2011: p. 1-49.

302. Corporation, S., *LabSolutions LC/GC*. 2021, Shimadzu: Japan.

303. Mauerhofer, E., et al., *Prompt and delayed gamma rays induced by epithermal and fast neutrons with indium.* Journal of Radioanalytical and Nuclear Chemistry, 2021: p. 1-12.

304. ARAO, *Third Revision of the Krško NPP Radioactive Waste and Spent Fuel Disposal Program*. 2019: Ljubljana.

305. International Atomic Energy Agency. *PRIS Database: Operational & Long-Term Shutdown Reactors by Country*. 2021 [cited 2021 11/03/2021]; Available

from: https://pris.iaea.org/PRIS/WorldStatistics/OperationalReactorsByCountry.aspx.

306. Lister, A.S., *7 - Validation of HPLC Methods in Pharmaceutical Analysis*, in *Separation Science and Technology*, S. Ahuja and M.W. Dong, Editors. 2005, Academic Press. p. 191-217, DOI: https://doi.org/10.1016/S0149-6395(05)80051-0.

307. Aesar, A. *2-Methyl-1,3-dioxolane Safety Data Sheet*. 2021 [cited 2022 22/11/2022]; Available from: https://www.alfa.com/en/catalog/A12824/.

308. Engineering ToolBox. *Ethanol - Thermophysical properties*. 2018 [cited 2022 26/11/2022]; Available from: https://www.engineeringtoolbox.com/ethanol-ethyl-alcohol-properties-C2H6O-d_2027.html.

309. Information, N.C.f.B. *PubChem Compound Summary for CID 670, Dihydroxyacetone*. 2022 [cited 2022 22/11/2022]; Available from: https://pubchem.ncbi.nlm.nih.gov/compound/Dihydroxyacetone.

310. Daubert, T.E. and R.P. Danner, *Physical and Thermodynamic Properties of Pure Chemicals: Data Compilation*. 1989: Hemisphere Publishing Corporation, https://books.google.co.uk/books?id=tFrgzgEACAAJ.

311. Limited, M.L.S.U. *4-Methylheptane Safety Data Sheet, CAS: 589-53-7, Product Number: 111023*. 2022 [cited 2022 22/112022]; Available from: https://www.sigmaaldrich.com/GB/en/product/aldrich/111023.

312. ChemSrc. *2-butyl tetrahydrofuran Properties*. 2022 [cited 2022 25/11/2022]; Available from: https://www.chemsrc.com/en/cas/1004-29-1_348903.html.

313. Cole-Parmer. *Argos Technologies PolarSafe® Sterile Cryovials, 5 mL, Skirted-Bottom, External Thread*. 2022 [cited 2022 20/11/2022]; Manufacturer specfications]. Available from: https://www.coleparmer.co.uk/i/argos-technologies-polarsafe-sterile-cryovials-5-ml-skirted-bottom-external-thread-50-cs/0439563.

314. Trifunac, A.D., I.A. Shkrob, and D.W. Werst, *Radiation effects on transport and bubble formation in silicate glasses*. 2001, Argonne National Lab., Argonne, IL (US).

315. Demaman Oro, C.E., et al., *A new approach for salts removal from crude glycerin coming from industrial biodiesel production unit.* Journal of Environmental Chemical Engineering, 2019. **7**(1): p. 102883, DOI: https://doi.org/10.1016/j.jece.2019.102883.

316. Robinson, B.H., et al., *The phytomanagement of trace elements in soil.* Critical Reviews in Plant Sciences, 2009. **28**(4): p. 240-266.

317. Funes Pinter, I., et al., *Arsenic and trace elements in soil, water, grapevine and onion in Jáchal, Argentina.* Science of The Total Environment, 2018. **615**: p. 1485-1498, DOI: https://doi.org/10.1016/j.scitotenv.2017.09.114.

318. Gan, J., et al., *Production of methyl bromide by terrestrial higher plants.* Geophysical Research Letters, 1998. **25**(19): p. 3595-3598.

319. Hutton, R.C., *Application of inductively coupled plasma source mass spectrometry (ICP-MS) to the determination of trace metals in organics.* Journal of Analytical Atomic Spectrometry, 1986. **1**(4): p. 259-263, DOI: 10.1039/JA9860100259.

320. McDonell, W.R. and A.S. Newton, *The Radiation Chemistry of the Aliphatic Alcohols1,2.* Journal of the American Chemical Society, 1954. **76**(18): p. 4651-4658, DOI: 10.1021/ja01647a051.

321. Engineering ToolBox. *Liquids - Vapor Pressures.* 2006 [cited 2022 15/12/2022]; Available from: https://www.engineeringtoolbox.com/vapor-pressure-d_312.html.

322. Corrêa, I., R.P.V. Faria, and A.E. Rodrigues, *Continuous Valorization of Glycerol into Solketal: Recent Advances on Catalysts, Processes, and Industrial Perspectives.* Sustainable Chemistry, 2021. **2**(2): p. 286-324, DOI: https://doi.org/10.3390/suschem2020017.

323. Mushrush, G.W., et al., *The synthesis of acetals and ketals of the reduced sugar mannose as fuel system icing inhibitors.* Petroleum science and technology, 1997. **15**(3-4): p. 237-244.

324. Melero, J.A., et al., *Oxygenated compounds derived from glycerol for biodiesel formulation: Influence on EN 14214 quality parameters.* Fuel, 2010. **89**(8): p. 2011-2018.

325. Giraldo, S.Y., L.A. Rios, and N. Suárez, *Comparison of glycerol ketals, glycerol acetates and branched alcohol-derived fatty esters as cold-flow improvers for palm biodiesel.* Fuel, 2013. **108**: p. 709-714.

326. Secur, J.B. and H.E. Oberstak. *Viscosity of Glycerol and Its d J Aqueous So.* 2002.

327. Riesz, P., *The radiolysis of acetone in air-free aqueous solutions.* The Journal of Physical Chemistry, 1965. **69**(4): p. 1366-1373, DOI: https://doi.org/10.1021/j100888a045.

328. Europe, F., *FuelsEurope Statistical Report 2020 Fig. 18*. 2020: Belgium.

329. Al-Saadi, L.S., V.C. Eze, and A.P. Harvey, *Techno-Economic Analysis of Glycerol Valorization via Catalytic Applications of Sulphonic Acid-Functionalized Copolymer Beads.* Frontiers in Chemistry, 2020. **7**(882), DOI: https://doi.org/10.3389/fchem.2019.00882.

330. Roselli, C., et al., *Radioactivity in coffee.* Journal of Radioanalytical and Nuclear Chemistry, 2013. **295**(3): p. 1813-1818, DOI: 10.1007/s10967-012-2101-7.

331. Buzina, D. and I. Engovatov, *Geoecological assessment methods of the radiation hazard of the use of rocks in the building materials industry*. E3S Web Conf., 2019. **97**: p. 03020, https://doi.org/10.1051/e3sconf/20199703020.

332. IAEA/iaa, *Regulations for the Safe Transport of Radioactive Material*. 2018, Vienna: INTERNATIONAL ATOMIC ENERGY AGENCY, https://www.iaea.org/publications/12288/regulations-for-the-safe-transport-of-radioactive-material.

333. IAEA/iaa, *Handbook on Photonuclear Data for Applications Cross-sections and Spectra*. 2000, Vienna: INTERNATIONAL ATOMIC ENERGY AGENCY, https://www.iaea.org/publications/6043/handbook-on-photonuclear-data-for-applications-cross-sections-and-spectra.

334. Litaize, O., O. Serot, and L. Berge, *Fission modelling with FIFRELIN*. The European Physical Journal A, 2015. **51**(12): p. 177, DOI: 10.1140/epja/i2015-15177-9.

335. Karimzadeh, S., R. Khan, and H. Böck, *Gamma spectrometry inspection of TRIGA MARK II fuel using caesium isotopes*. Nuclear Engineering and Design, 2011. **241**(1): p. 118-123, DOI: https://doi.org/10.1016/j.nucengdes.2010.10.031.

336. Hubbell, J., *Photon cross sections, attenuation coefficients and energy absorption coefficients*. National Bureau of Standards Report NSRDS-NBS29, Washington DC, 1969.

337. Sulistyo, H., et al. *Heterogeneous catalytic reaction of glycerol with acetone for solketal production*. in *MATEC Web of Conferences*. 2019. EDP Sciences.

338. St. John, P.C., et al., *Prediction of organic homolytic bond dissociation enthalpies at near chemical accuracy with sub-second computational cost*. Nature Communications, 2020. **11**(1): p. 2328, DOI: 10.1038/s41467-020-16201-z.

339. Baldacchino, G., et al., *Importance of radiolytic reactions during high-LET irradiation modalities: LET effect, role of O 2 and radiosensitization by nanoparticles*. Cancer Nanotechnology, 2019. **10**(1): p. 1-21, DOI: https://doi.org/10.1186/s12645-019-0047-y.

340. Favaudon, V., C. Fouillade, and M. Vozenin, *Ultrahigh dose-rate," flash" irradiation minimizes the side-effects of radiotherapy*. Cancer radiotherapie: journal de la Societe francaise de radiotherapie oncologique, 2015. **19**(6-7): p. 526, DOI: https://doi.org/10.1016/j.canrad.2015.04.006.

341. Meisel, D., et al., *Radiation chemistry of synthetic waste*. 1991, Argonne National Lab., IL (United States).

342. Wagner, M., et al., *Viscosity measurements of antibody solutions by photon correlation spectroscopy: An indirect approach-limitations and applicability for high-concentration liquid protein solutions*. Pharmaceutical development and technology, 2012. **18**, DOI: https://doi.org/10.3109/10837450.2011.649851.

343. Plant, A.G., et al., *Nuclear-driven production of renewable fuel additives from waste organics.* Communications Chemistry, 2021. **4**(1): p. 132, DOI: 10.1038/s42004-021-00572-5.

344. Bartok, W. and P.J. Lucchesi, *The Radiation-induced Chain Alkylation of Ethylene with Propane.* Journal of the American Chemical Society, 1960. **82**(17): p. 4525-4528, DOI: 10.1021/ja01502a019.

345. Vereshchinskii, I.V., *Preparative Aspects of the Radiation Chemistry of Organic Compounds.* Russian Chemical Reviews, 1970. **39**(5): p. 405.

346. Rokach, J., C.H. Krauch, and D. Elad, *Electron and γ-ray induced addition of formamide to olefins.* Tetrahedron Letters, 1966. **7**(28): p. 3253-3257, DOI: https://doi.org/10.1016/S0040-4039(01)82774-X.

347. Inukai, K., T. Ueda, and H. Muramatsu, *The Radiation-Induced Addition Reaction of Dialkyl Phosphonates to Chlorofluoroolefins.* The Journal of Organic Chemistry, 1964. **29**(8): p. 2224-2226, DOI: 10.1021/jo01031a028.

348. Getoff, N., *CO2 and CO utilization: radiation-induced carboxylation of aqueous chloroacetic acid to malonic acid.* Radiation Physics and Chemistry, 2003. **67**(5): p. 617-621.

349. Henglein, A., *Preparative radiation chemistry—I: Reaction of nitric oxide with some organic liquids induced by high-energy electrons.* The International Journal of Applied Radiation and Isotopes, 1960. **8**(4): p. 149-155, DOI: https://doi.org/10.1016/0020-708X(60)90131-9.

350. Barelko, E., L. Kartasheva, and M.A. Proskurnin. *The nature of the insoluble product formed on radiolytic oxidation of benzene in water*. in *Doklady Akademii Nauk*. 1957. Russian Academy of Sciences.

351. Perner, D. and A. Henglein, *THE REACTION OF WHITE PHOSPHORUS WITH CARBON TETRACHLORIDE UNDER THE INFLUENCE OF $gamma$ RADIATION, LIGHT AND HEAT.* Zeitschrift fuer Naturforschung (West Germany) Divided into Z. Nautrforsch., A, and Z. Naturforsch., B: Anorg. Chem., Org. Chem., Biochem., Biophys., 1962. **Vol: 17b**: p. Medium: X; Size: Pages: 703-11 2016-07-04, https://www.osti.gov/biblio/4736884.

352. McKay, H.A.C., *The PUREX process*. 1990, United States: CRC Press, Inc, http://inis.iaea.org/search/search.aspx?orig_q=RN:24021863.

353. Kokel, A., C. Schäfer, and B. Török, *Application of microwave-assisted heterogeneous catalysis in sustainable synthesis design.* Green Chemistry, 2017. **19**(16): p. 3729-3751.

354. Newton, A.S. and W. McDonell, *The radiolysis products from ethyl alcohol; Effect of total energy input on the radiolysis products.* Journal of the American Chemical Society, 1956. **78**(18): p. 4554-4555.

References

8 Appendix A: Supporting Figures and Tables

List of Appendix A Figures

Figure A1: Normalized Fatality Risks (in deaths per TWh) for both fossil fuels and renewable power generation methods. For fossil fuels, mortality statistics include both accidents and air pollution-related illnesses. Data are from the literature [25, 26]. 205

Figure A2: Possible categories of glycerol-derived compounds with related processes [93] (illustrated by Plant A. G.). 206

Figure A3: Parameters for electron interactions with a nucleus, adapted from [124]. 206

Figure A4: Diagrammatic representation of elastic scattering for a neutron-proton collision, producing a recoil proton. (White = Neutron, Red = Proton) where $(\boldsymbol{En} - \boldsymbol{En'}) = \boldsymbol{EQ}$ 207

Figure A5: Total microscopic cross-sections, σ, for ^{1}H, ^{12}C, ^{16}O nuclei [135], data obtained using JANIS software from the JEFF-3.2 nuclear data library [137]. 207

Figure A6: An example of calibration curves (internal standard method) obtained for the analytical standards of acetaldehyde and ethyl acetate for irradiated ethylene glycol samples. Compared against an internal standard of 20 µl or 40 µl of 2-butanol stock standard (~0.01 g ml^{-1}) depending on the run. 228

Figure A7: An example of the calibration curves obtained (for internal standard method) for standards of acetaldehyde, methanol, acetol, solketal and acetic acid for irradiated glycerol samples. Compared against 20 µl or 40 µl of internal standard 2-butanol stock standard (~0.01 g ml^{-1}) depending on the run. 229

Figure A8: Total ion chromatogram of the HSGC-MS analysis of unirradiated glycerol spiked with either 100 ppm (black) or 3 ppm (blue) of acetone. 100 ppm was estimated to be ~13x the signal to noise ratio (S/N). 3 ppm was below the detection limit (~3 S/N). 230

Figure A9: Total ion chromatogram of the HSGC-MS analysis of 0.038 Gy ^{252}Cf-irradiated neat glycerol (black) or unirradiated glycerol (blue). 230

Figure A10: GC-MS ion chromatograms focussing on the acetaldehyde split peaks (2.00 and 2.15 minutes) with the overlapping broad methanol peak (2.10 minutes). Showing ethylene glycol samples irradiated with either 80 kGy of a γ-ray only (sample 75) or b 80 kGy of mixed field neutron + γ-ray (sample 37). Total ion chromatogram trace (black), 31 m/z fragment trace indicating methanol (pink), and the 44 m/z fragment trace indicating acetaldehyde (orange). 231

Figure A11: GC-MS total ion chromatograms of irradiated samples within PP vials for either irradiated a neat ethylene glycol or b neat glycerol. Black traces indicate the samples from 100 kGy γ-ray only irradiations and blue traces indicate 100 kGy mixed field neutron + γ-ray irradiations. 232

Figure A12: Mass fragment patterns of large unidentifiable radiolytic peaks from neat ethylene glycol radiolysis. In order of retention time; #1, Ethyl ethoxy(hydroxy)acetate, #2, Methyl tetrahydrofurfuryl and #3, 2-(Methoxymethyoxy)propanoic acid. 233

Figure A13: Mass fragment patterns of large unidentifiable radiolytic peaks from neat glycerol radiolysis. In order of retention time; #1, ethyl hydroxyacetate, #2, 1-Butanol and #3, 1,1-dimethoxyacetone. 233

List of Appendix A Tables

Table A1: Stable product *G*-values from the γ-ray radiolysis of various aliphatic alcohols from literature. Datasets have been collated and adapted from Baxendale and Freeman reports. 208

Table A2: Stable product *G*-values from the γ-ray radiolysis of ethylene glycol from literature. Datasets have been collated and adapted from Barker, Pikaev, Schulte-Frohlinde and Vetrov. Acetaldehyde and 2-methyl-1,3-dioxolane have been analysed here for chemical processing potential. 209

Table A3: Stable product *G*-values from the γ-ray radiolysis of aqueous glycerol samples from literature. Dataset has been adapted from a) Baugh 1982, and b) Baugh 1983 Conference paper. All samples have been irradiated with ^{60}Co γ-rays and are at a natural pH. Acetol has been evaluated for chemical processing. ... 210

Table A4: Neat ethylene glycol radiolytic products with their concentration values in this work (Plant A. G.). Data collated via liquid GC-MS for polypropylene (PP) irradiation vials capped in an N_2 gaseous environment with <0.5ppm O_2, ~0.7 ppm H_2O. 211

Table A5: Neat ethylene glycol radiolytic products with their concentration values in this work (Plant A. G.). Data collated via liquid GC-MS for borosilicate (BS) irradiation vials capped in an N_2 gaseous environment with <0.5ppm O_2, ~0.7 ppm H_2O. 212

Table A6: Neat glycerol radiolytic products with their concentration values in this work (Plant A. G.). Data collated via liquid GC-MS for polypropylene (PP) irradiation vials capped in an N_2 gaseous environment with <0.5ppm O_2, ~0.7 ppm H_2O. 213

Table A7: Neat glycerol radiolytic products with concentration values in this work (Plant A.G.). Determined via liquid GC-MS analysis of borosilicate (BS) irradiated vials. 214

Table A8: Binary aqueous glycerol mixture radiolytic products from γ-ray only radiolysis with concentration values in this work (Plant A.G.). Determined via liquid GC-MS analysis of polypropylene (PP) irradiated vials. 215

Table A9: Binary aqueous glycerol mixture radiolytic products from mixed field neutron + γ-ray radiolysis with concentration values in this work (Plant A.G.). Determined via liquid GC-MS analysis of polypropylene (PP) irradiated vials. 216

Table A10: Ternary glycerol, acetone, and water mixtures associated radiolytic products with concentration values in this work (Plant A. G.). Determined via liquid GC-MS analysis of polypropylene (PP) irradiated vials. 217

Table A11: Neat ethylene glycol radiolytic products with *G*-values and mass productivity values in this work (Plant A. G.). Data collated via liquid GC-MS for polypropylene (PP) irradiation vials capped in an N_2 gaseous environment with <0.5ppm O_2, ~0.7 ppm H_2O. To be compared against literature data in Table A2. 218

Table A12: Neat ethylene glycol radiolytic products with *G*-values and mass productivity values in this work (Plant A. G.). Data collated via liquid GC-MS for borosilicate (BS) irradiation vials capped in an N_2 gaseous environment with <0.5ppm O_2, ~0.7 ppm H_2O. To be compared against literature data in Table A2. 219

Table A13: Neat glycerol radiolytic products with *G*-values and mass productivity values in this work (Plant A.G.). Determined via liquid GC-MS analysis of polypropylene (PP) irradiated vials. To be compared against literature data in Table A3... 220

Table A14: Neat glycerol radiolytic products with *G*-values and mass productivity values in this work (Plant A.G.). Determined via liquid GC-MS analysis of borosilicate (BS) irradiated vials. To be compared against literature data in Table A3... 221

Table A15: Binary aqueous glycerol mixture radiolytic products from γ-ray only radiolysis with *G*-values and mass productivity values in this work (Plant A.G.). Determined via liquid GC-MS analysis of polypropylene (PP) irradiated vials. To be compared against literature data in Table A3. 222

Table A16: Binary aqueous glycerol mixture radiolytic products from mixed field neutron + γ-ray radiolysis with *G*-values and mass productivity values in this work (Plant A.G.). To be compared against literature data in Table A3. 223

Table A17: Ternary glycerol, acetone, and water mixtures associated radiolytic products with *G*-values and mass productivity values in this work (Plant A. G.). Data are from PP vials. To be compared against literature data in Table A3. 224

Table A18: Elemental composition analysis and impurity identification within purchased solutes via k0-γ spectroscopy. a glycerol (>99.5%). b ethylene glycol (>99%). Results obtained by k0-INAA of Glycerol and Ethylene Glycol Samples. (<LOD= Below limit of detection of the INAA methodology)........................ 226

Table A19: Internal pressure calculations inside the irradiation vials during irradiations at various absorbed doses. Using 20 ml BS vials with 4 ml of organic liquid and a 16 ml gaseous headspace. An estimated *G*-value (mixed gases) of 7.13 molecules 100eV^{-1} from ethanol γ-ray radiolysis was used [240]...................................... 227

Table A20: European reactors by country, with total power output (as of 08/02/2021), and estimated acetol and solketal output using data shown in Figure 48 and Figure 49 with sample 109 (Table 18)[9]... 234

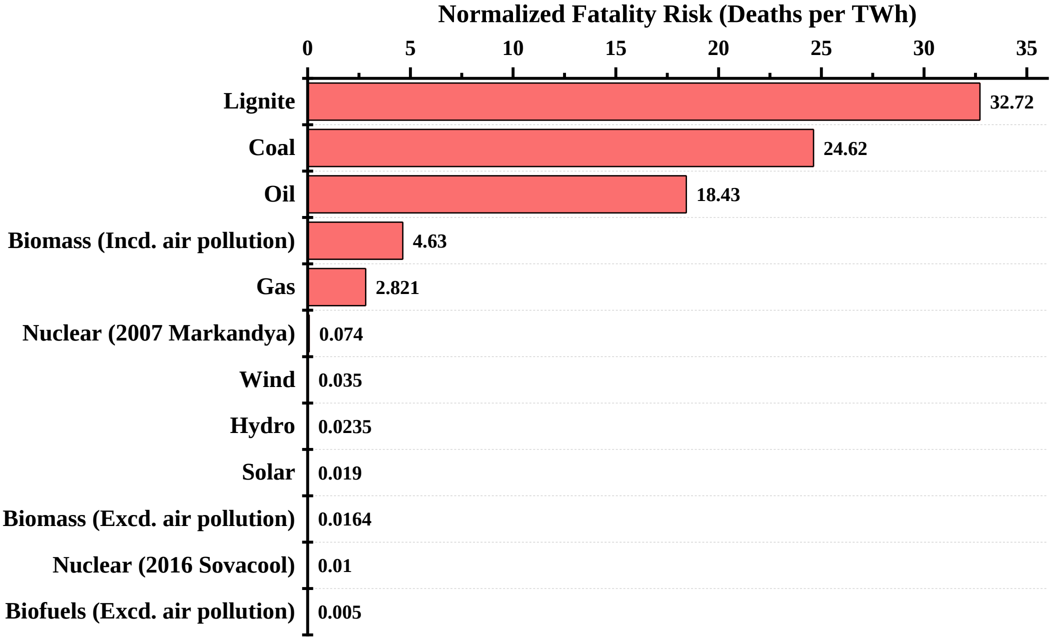

Figure A1: Normalized Fatality Risks (in deaths per TWh) for both fossil fuels and renewable power generation methods. For fossil fuels, mortality statistics include both accidents and air pollution-related illnesses. Data are from the literature [25, 26].

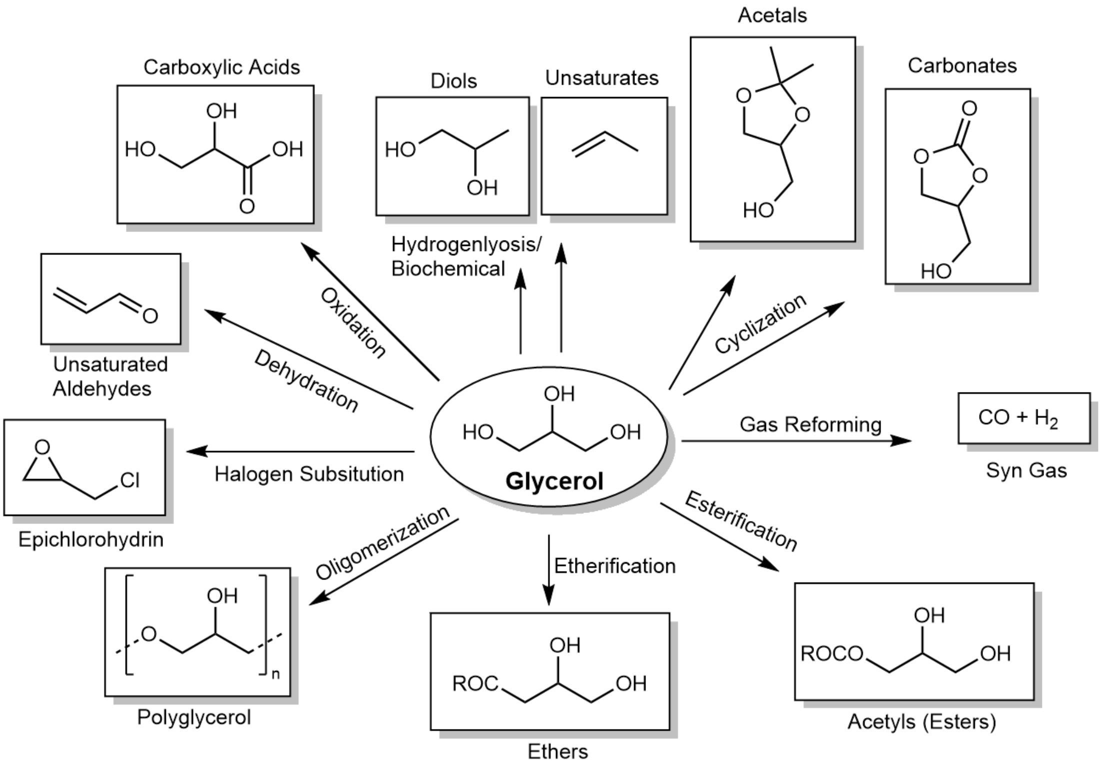

Figure A2: Possible categories of glycerol-derived compounds with related processes [93] (illustrated by Plant A. G.).

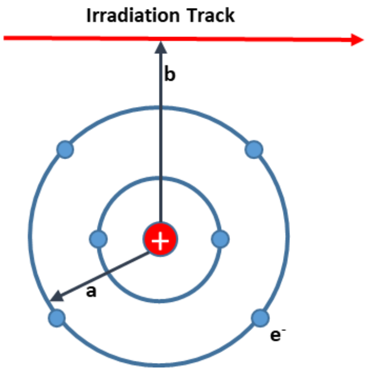

Figure A3: Parameters for electron interactions with a nucleus, adapted from [124].

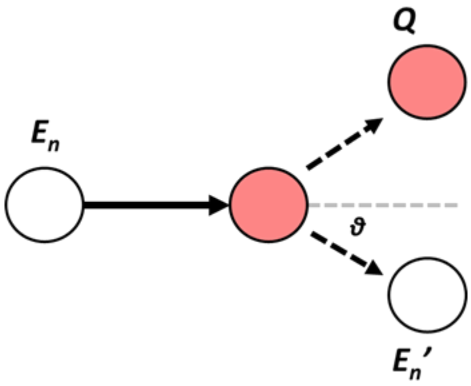

Figure A4: Diagrammatic representation of elastic scattering for a neutron-proton collision, producing a recoil proton. (White = Neutron, Red = Proton) where $(\boldsymbol{E_n} - \boldsymbol{E'_n}) = \boldsymbol{E_Q}$.

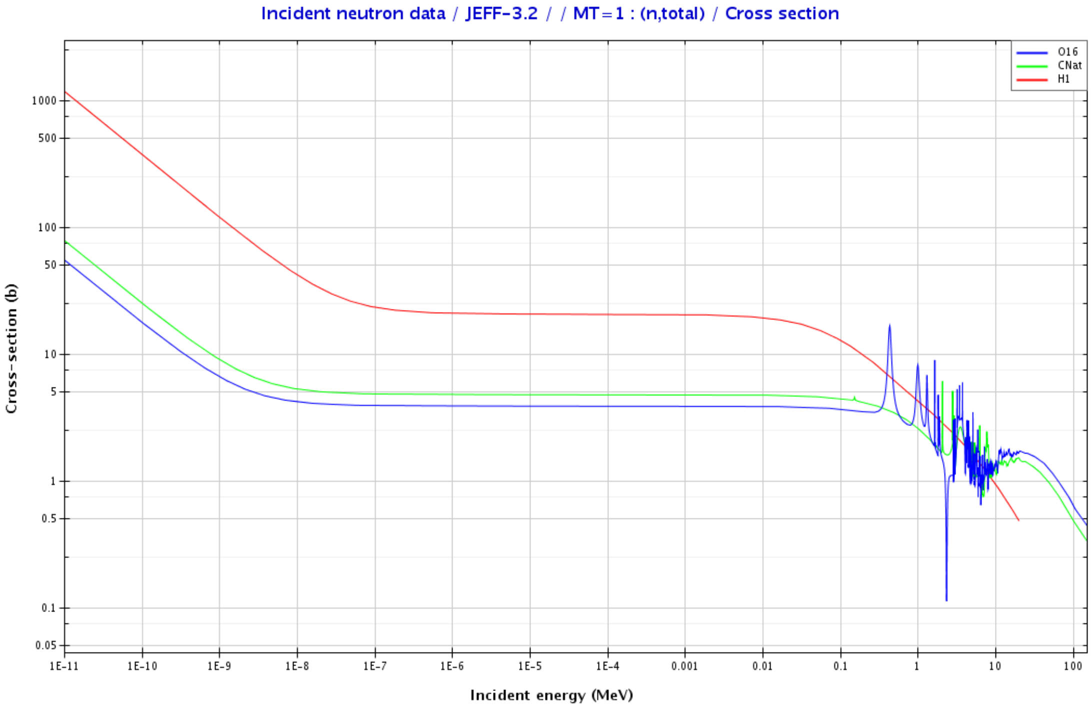

Figure A5: Total microscopic cross-sections, σ, for ^{1}H, ^{12}C, ^{16}O nuclei [135], data obtained using JANIS software from the JEFF-3.2 nuclear data library [137].

8.1 Tabulated Literature data on Alcohols, Ethylene glycol and Glycerol

Table A1: **Stable product *G*-values from the γ-ray radiolysis of various aliphatic alcohols from literature.** Datasets have been collated and adapted from Baxendale and Freeman reports.

		Radiolytic Products *G*-values / μmol J^{-1}						**Sample and Irradiation Parameters**			
Reference	**Alcohol**	**H_2**	**CO**	**CH_4**	**Primary Aldehyde/Ketone**	**Secondary Aldehyde**	**α-Alcohol Dimer**	**Radiation Type**	**Dose / Gy**	**Dose Rate / Gy min^{-1}**	**T / K**
Baxendale "Preferred values": [169]	**Methanol**	0.56	0.01	0.04	G(CH$_2$O)= 0.21		G(CH$_2$OH)$_2$) = 0.33	γ-ray	NA	NA	298 ± 5
Landsman & Baxendale: [50, 169]		0.50	0.03	0.05	0.24		0.26	n,γ (pile)	110,000	480	373
		1.00	0.31	0.09	0.37		0.08	84 MeV Recoil Fission Frag.	120,000	NA	373
Freeman Dataset, "Preferred values" [240]	**Ethanol**	0.60		0.06	G(CH$_3$CHO) = 0.38		G(CH$_3$CHOH)$_2$) = 0.22	γ-ray	<1.6	1 - 1000	295 ± 4
		0.53	0.03	0.06	0.31		= 0.22		160	1 - 1000	295 ± 4
		0.43	0.01	0.06	0.21		= 0.22		16,000	1 - 1000	295 ± 4
Freeman & Newton [240] [354]		0.42	0.01	0.04	0.31		0.15	28 MeV α	48,000	29,000	294
Freeman [114]	**Propan-1-ol**	0.46		0.01	G(C$_2$H$_5$CHO) = 0.3	G(CH$_2$O) = 0.2	0.16	γ-ray	1600	70	293
	Propan-2-ol	0.38	0.02	0.16	G((CH$_3$)$_2$CHO) = 0.16	G(CH$_3$CHO)= 0.03	0.01		1600	NA	298

Table A2: **Stable product *G*-values from the γ-ray radiolysis of ethylene glycol from literature. Datasets have been collated and adapted from Barker, Pikaev, Schulte-Frohlinde and Vetrov.** Acetaldehyde and 2-methyl-1,3-dioxolane have been analysed here for chemical processing potential.

Reference	a) Barker 1964 [210]	b) Pikaev 1975 [244]															c) Schulte [245]	d) Vetrov [277]
Ref. Table (T)/ Figure(F)/ Text	T1,2 and 3	T1					T4							T7			T1	Abstract
Variable Parameter(s)	NA	Gas, pH, Solute Conc.					Solute Conc., Dose							Dose Rate, Gas, pH			Gas	Temp,
Radiolytic Products *G*-values / µmol J^{-1}																		
H_2							0.05*	0.06*				0.09						
Methanol	0.20																	0.78, 0.56
Ethanol	0.08																	
Acetaldehyde	0.24						0.33	1.30	5.39	4.66	3.78	3.42	2.49	18.13	16.58	13.99	0.12	
Formaldehyde	0.51	0.05	0.06	0.10	0.26	0.33	0.07	0.08	0.36	0.22	0.16	0.15	0.11	0.50	0.41	0.30		
Glycolaldehyde	0.18	0.41	0.54	0.77	0.52	0.08											0.1	
Glycerol	0.29																	
Diethylene Glycol (Dimer)	0.03							0.00		0.02				0.07		0.11	0.18	
2-methyl-1,3-dioxolane	1.65																	
Formic acid	0.38																	
Acetic Acid	0.78																	
Sample and Irradiation Parameters																		
Dose / Gy	1.0E+05	160					176	176	32	115	176	224	417	80			NA	NA
Dose Rate / Gy min^{-1}	NA	12													96	433	58	38.4
Ethylene Glycol / (wt.%)	0.0645	0.02	0.1	0.5	0.002	0.1	0.01	0.1	1	1	1	1	1	1	1	1	0.16	0.032
Gas Environment	Deaerated	Air					Deaerated							N_2O			N_2O	Deaerated
pH / additive	Natural	Acid / 0.4 M H_2SO_4		Alkaline/ 0.1 M KOH														Neutral
T / K	Ambient																293	443, 298
Chemical Processing Analysis																		
% Molar Yield (Acetaldehyde)	0.15						0.58	0.23	0.02	0.05	0.07	0.08	0.10	0.15	0.13	0.11		NA
% Mass productivity	0.000						0.000	0.001	0.001	0.002	0.003	0.003	0.005	0.006	0.006	0.005		NA
% Molar Yield (2-methyl-1,3-dioxolane)	1.05																	
% Mass productivity	0.001																	

Table A3: **Stable product *G*-values from the γ-ray radiolysis of aqueous glycerol samples from literature.** Dataset has been adapted from a) Baugh 1982, and b) Baugh 1983 Conference paper. All samples have been irradiated with ^{60}Co γ-rays and are at a natural pH. Acetol has been evaluated for chemical processing.

<u>Reference</u>	a) [3]– Aqueous Glycerol in N_2O gas-only															b) Aqueous Glycerol in O_2 [250]
Ref. Table(T)/Figure(F)/Text	T1			T2				T3								In Text
Variable Parameter	Dose Rate			Temperature				Glycerol Concentration (in wt.%)								Gas Environment
Radiation chemical Yield, *G*-value / μmol J^{-1}																
Glyceraldehyde	0.06	0.08	0.12	0.06	0.08	0.08	0.05	0.08	0.06	0.09	0.07	0.07	0.09	0.08	0.09	0.2
Dihydroxyacetone	0.01	0.01	0.02	0.01	0.01	0.01	0.01	0.01		0.02		0.01		0.02		0.09
3-Hydroxypropanal	0.05	0.04	0.04	0.05	0.04	0.06	0.05	0.04	0.05	0.08	0.09	0.24	0.21	0.27	0.22	
Hydroxyacetone (Acetol)	0.08	0.06	0.05	0.06	0.06	0.07	0.07	0.06	0.08	0.10	0.16	0.16	0.23	0.22	0.23	
1,3-bis(hydroaxymethyl-1,4,butandial	0.04	0.03	0.02	0.01	0.03	0.03	0.03	0.03	0.04	0.03	0.04	0.03	0.04	0.03	0.04	
1,2-bis(glycolyl)ethane	0.02	0.02	0.02	0.01	0.02	0.02	0.01	0.02	0.02	0.02	0.02	0.02	0.01	0.02	0.01	
Trimer	0.02	0.02						0.02	0.02	0.02	0.03	0.02	0.02	0.02	0.03	
Sample Parameters																
Dose / Gy	NA	1142	NA	1442				1442	3124	1442	3124	1442	3124	1440	3124	961
Dose Rate / Gy min^{-1}	1.7	8.0	72.1	8.0				8.0	1.7	8.0	1.7	8.0	1.7	8.0	1.7	NA
Glycerol / (wt.%)	0.1							0.1		0.5		0.9		4.6		0.046
Temperature / K	293			278	293	313	333	293								NA
Chemical Processing Analysis																
% Molar Yield (Acetol)	1.26	1.00	0.83	0.84	0.90	1.08	0.99	0.90	2.46	0.29	1.02	0.32	0.71	0.06	0.14	
Mass Productivity % (Acetol)	0.0009	0.0007	0.0006	0.0006	0.0007	0.0008	0.0007	0.0007	0.0018	0.0011	0.0038	0.0024	0.0053	0.0024	0.0053	

8.2 Tabulated Experimental Radiolysis Data (Plant A. G.) of Ethylene Glycol and Glycerol samples

8.2.1 Concentration Tables

Table A4: Neat ethylene glycol radiolytic products with their concentration values in this work (Plant A. G.). Data collated via liquid sampling GC-MS for polypropylene (PP) irradiation vials capped in an N_2 gaseous environment with <0.5ppm O_2, ~0.7 ppm H_2O.

Reference	Plant A.G.															
Table(T)/Figure(F)/Text	Figure 30, Figure 32, Figure 34, Figure 36												Figure 38			
Variable Parameter (s)	Radiation Type, Vial, Absorbed Dose												Dose Rate			
Concentration / μg ml^{-1}																
Acetaldehyde	8085	9688	5470	7316	8830	11599	761	1345	1796	696	374	197	605	1294	1796	657
Methanol		780	572	629	713	738	306	409	458	1808	2686	10356	397	409	458	365
Ethyl Acetate	114	210	516	713	494	701										
Acetic Acid			662	678	649	850										
Sample Parameters																
Dose / kGy	20	40	50	60	80	100	20	40	50	60	80	100	50	50	50	50
Dose Rate / kGy min^{-1}	0.018	0.016	0.026	0.027	0.041	0.040	1.63	3.27	3.27	6.53	6.53	6.54	0.52	1.31	3.27	8.17
Radiation Type	γ-only						neutrons + γ rays						neutrons + γ rays			
Ethylene Glycol (wt.%)	Neat															
Temperature / K	Ambient						Ambient*						Ambient*			

*Temperature values are thought to be proportional to the dose rate of the operational reactor.

Note: Concentration uncertainties are dependent on the relative standard deviation % (RSD%) outputted but the analyte calibration curves.

Table A5: Neat ethylene glycol radiolytic products with their concentration values in this work (Plant A. G.). Data collated via liquid sampling GC-MS for borosilicate (BS) irradiation vials capped in an N_2 gaseous environment with <0.5ppm O_2, ~0.7 ppm H_2O.

Reference	Plant A.G.											
Table(T)/Figure(F)/Text	Figure 30, Figure 32, Figure 34, Figure 36											
Variable Parameter (s)	Radiation Type, Vial, Absorbed Dose											
Concentration / µg ml^{-1}												
Acetaldehyde	6725	8651	8729	6857	5414	7072	488	1423	1264	788	263	216
Methanol	303	394	523	492	601	659	290	375	417	461	512	819
Ethyl Acetate	33	68	200	244	427	297						
Acetic Acid		257	395	392	683	488						
Sample Parameters												
Dose / kGy	20	40	50	60	80	100	20	40	50	60	80	100
Dose Rate / kGy min^{-1}	0.018	0.016	0.026	0.027	0.041	0.040	1.63	3.27	3.27	6.53	6.53	6.54
Radiation Type	γ-only						neutrons + γ rays					
Ethylene Glycol (wt.%)	Neat											
Temperature / K	Ambient						Ambient*					

*Temperature values are thought to be proportional to the dose rate of the operational reactor.

Note: Concentration uncertainties are dependent on the relative standard deviation % (RSD%) outputted but the analyte calibration curves.

Table A6: Neat glycerol radiolytic products with their concentration values in this work (Plant A. G.). Data collated via liquid sampling GC-MS for polypropylene (PP) irradiation vials capped in an N_2 gaseous environment with <0.5ppm O_2, ~0.7 ppm H_2O.

Reference	Plant A.G. (Thesis)															
Table(T)/Figure(F)/Text	Figure 40, Figure 42												Figure 44			
Variable Parameter (s)	Absorbed Dose, Radiation Type												Dose Rate			
Concentration / μg ml^{-1}																
Hydroxyacetone (Acetol)	1083	1902	2955	2944	4161	4362	257	597	963	899	1681	3883	1185	1109	1229	794
Solketal	62	175	379	410	733	798			62	76	228	716				
Sample Parameters																
Dose / kGy	20	40	50	60	80	100	20	40	50	60	80	100	50			
Dose Rate / kGy min^{-1}	0.018	0.016	0.026	0.027	0.041	0.040	1.63	3.27	3.27	6.53	6.53	6.54	0.52	1.31	3.27	8.17
Radiation Type	γ-ray only (delay)						Neutron + γ rays									
Mixture Type / Glycerol (wt.%)	Neat Glycerol															
Temperature / K	Ambient						Ambient*						Ambient*			

*Temperature values are thought to be proportional to the dose rate of the operational reactor.

Note: Concentration uncertainties are dependent on the relative standard deviation % (RSD%) outputted but the analyte calibration curves.

Table A7: Neat glycerol radiolytic products with concentration values in this work (Plant A.G.). Determined via liquid sampling GC-MS analysis of borosilicate (BS) irradiated vials.

Reference	Plant A.G. (Thesis)											
Table(T)/Figure(F)/Text	Figure 40, Figure 42											
Variable Parameter (s)	Absorbed Dose, Radiation Type											
Concentration / μg ml^{-1}												
Hydroxyacetone (Acetol)	964	1385	2684	3130	4046	5545	303	850	1269	959	2245	1319
Solketal	55	88	269	427	699	1202		101	117	254	506	755
Sample Parameters												
Dose / kGy	20	40	50	60	80	100	20	40	50	60	80	100
Dose Rate / kGy min^{-1}	0.018	0.016	0.026	0.027	0.041	0.040	1.63	3.27	3.27	6.53	6.53	6.54
Radiation Type	γ-ray only (delay)						Neutron + γ rays					
Mixture Type / Glycerol (wt.%)	Neat Glycerol											
Temperature / K	Ambient						Ambient*					

*Temperature values are thought to be proportional to the dose rate of the operational reactor.

Note: Concentration uncertainties are dependent on the relative standard deviation % (RSD%) outputted but the analyte calibration curves.

Table A8: Binary aqueous glycerol mixture radiolytic products from γ-ray only radiolysis with concentration values in this work (Plant A.G.). Determined via liquid sampling GC-MS analysis of polypropylene (PP) irradiated vials.

Reference	Plant A.G. (Thesis)																	
Table(T)/Figure(F)/Text	Figure 45																	
Variable Parameter (s)	Aqueous Mixtures, Radiation Type																	
Concentration / µg ml^{-1}																		
Hydroxyacetone (Acetol)	3022	4593	5670	6793	6769	7562		2626	3808	4622	4780	5262	4662	6383	8002	9540	9713	11540
Solketal	26	47	90	144	140	228		48	65	84	103	107	62	99	144	207	296	462
Sample Parameters																		
Dose / kGy	20	40	50	60	80	100	20	40	50	60	80	100	20	40	50	60	80	100
Dose Rate / kGy min^{-1}	0.018	0.016	0.026	0.027	0.041	0.040	0.018	0.016	0.026	0.027	0.041	0.040	0.018	0.016	0.026	0.027	0.041	0.040
Radiation Type	γ-ray only (delay)																	
Mixture Type (wt.%): Glycerol, Water	Mix 1: 63, 37						Mix 2: 50, 50						Mix 3: 70, 30					
Temperature / K	Ambient																	

*Temperature values are thought to be proportional to the dose rate of the operational reactor.

Note: Concentration uncertainties are dependent on the relative standard deviation % (RSD%) outputted but the analyte calibration curves.

Table A9: Binary aqueous glycerol mixture radiolytic products from mixed field neutron + γ-ray radiolysis with concentration values in this work (Plant A.G.). Determined via liquid sampling GC-MS analysis of polypropylene (PP) irradiated vials.

Reference	Plant A.G. (Thesis)																	
Table(T)/Figure(F)/Text	Figure 45																	
Variable Parameter (s)	Aqueous Mixtures, Absorbed Dose, Radiation Type																	
Concentration / μg ml^{-1}																		
Hydroxyacetone (Acetol)	515	1057	1381	1671	2648	4343	433	902	1138	1063	1326	2829	779	1645	2075	1780	2639	3995
Solketal				49	65	125										34	67	118
Sample Parameters																		
Dose / kGy	20	40	50	60	80	100	20	40	50	60	80	100	20	40	50	60	80	100
Dose Rate / kGy min^{-1}	1.63	3.27	3.27	6.53	6.53	6.54	1.63	3.27	3.27	6.53	6.53	6.54	1.63	3.27	3.27	6.53	6.53	6.54
Radiation Type	Neutron + γ rays																	
Mixture Type (wt.%): Glycerol, Water	Mix1: 63, 37						Mix2: 50, 50						Mix3: 70, 30					
Temperature / K	Ambient*																	

*Temperature values are thought to be proportional to the dose rate of the operational reactor.

Note: Concentration uncertainties are dependent on the relative standard deviation % (RSD%) outputted but the analyte calibration curves.

Table A10: Ternary glycerol, acetone, and water mixtures associated radiolytic products with concentration values in this work (Plant A. G.). Determined via liquid sampling GC-MS analysis of polypropylene (PP) irradiated vials.

Reference	Plant A.G. (Thesis)								
Table(T)/Figure(F)/Text	Figure 48, Figure 51						Figure 48		
Variable Parameter (s)	Ternary Mixture type, Glycerol wt.%, Radiation type						Unirradiated Control		
Concentration / μg ml^{-1}									
Hydroxyacetone (Acetol)	2388	1765	1426	479	331	223			
Solketal	10279	7190	4917	1181	801	560	850	503	288
Acetic Acid	233	431	486	232	235	258			
Sample Parameters									
Dose / kGy	50						-		
Dose Rate / kGy min^{-1}	0.04			3.27			-		
Radiation Type	γ-ray only			Neutron + γ-rays			NA Controls		
Ternary Mixture (wt.%): Glycerol, Acetone, Water	AceMix1: 46, 28, 26	AceMix2: 34, 34, 32	AceMix3: 26, 48, 26	AceMix1: 46, 28, 26	AceMix2: 34, 34, 32	AceMix3: 26, 48, 26	AceMix1: 46, 28, 26	AceMix2: 34, 34, 32	AceMix3: 26, 48, 26
Temperature / K	Ambient			Ambient*			Ambient		

*Temperature values are thought to be proportional to the dose rate of the operational reactor.

Note: Concentration uncertainties are dependent on the relative standard deviation % (RSD%) outputted but the analyte calibration curves.

8.2.2 *G*-value and Mass Productivity % Tables

Table A11: Neat ethylene glycol radiolytic products with *G*-values and mass productivity values in this work (Plant A. G.). Data collated via liquid sampling GC-MS for polypropylene (PP) irradiation vials capped in an N_2 gaseous environment with <0.5ppm O_2, ~0.7 ppm H_2O. To be compared against literature data in Table **A2**.

Reference	Plant A.G.															
Table(T)/Figure(F)/Text	Figure 31, Figure 33, Figure 35 and Figure 37												Figure 38			
Variable Parameter (s)	Radiation Type, Vial, Absorbed Dose												Dose Rate			
Radiation Chemical Yield, *G*-value / μmol J^{-1}																
Acetaldehyde	8.28	4.96	2.24	2.50	2.26	2.37	0.78	0.69	0.74	0.24	0.10	0.04	0.25	0.53	0.74	0.27
Methanol		0.55	0.32	0.29	0.25	0.21	0.43	0.29	0.26	0.85	0.94	2.91	0.22	0.23	0.26	0.21
Ethyl Acetate	0.06	0.05	0.11	0.12	0.06	0.07										
Acetic Acid			0.20	0.17	0.12	0.13										
Sample Parameters																
Dose / kGy	20	40	50	60	80	100	20	40	50	60	80	100	50	50	50	50
Dose Rate / kGy min^{-1}	0.018	0.016	0.026	0.027	0.041	0.040	1.63	3.27	3.27	6.53	6.53	6.54	0.52	1.31	3.27	8.17
Radiation Type	γ-only						neutrons + γ rays						neutrons + γ rays			
Ethylene Glycol (wt.%)	Neat															
Temperature / K	Ambient						Ambient*						Ambient*			
Chemical Processing Analysis																
Mass Productivity % (Acetaldehyde)	0.73	0.87	0.49	0.66	0.80	1.04	0.07	0.12	0.16	0.06	0.03	0.02	0.05	0.12	0.16	0.06
Mass Productivity % (Methanol)		0.07	0.05	0.06	0.06	0.07	0.03	0.04	0.04	0.16	0.24	0.93	0.04	0.04	0.04	0.03
Mass Productivity % (Ethyl Acetate)	0.01	0.02	0.05	0.06	0.04	0.06										

*Temperature values are thought to be proportional to the dose rate of the operational reactor.

Note: Uncertainties for all quoted *G*-values for all products are ~ ± 10%.

Table A12: Neat ethylene glycol radiolytic products with *G*-values and mass productivity values in this work (Plant A. G.). Data collated via liquid sampling GC-MS for borosilicate (BS) irradiation vials capped in an N_2 gaseous environment with <0.5ppm O_2, ~0.7 ppm H_2O. To be compared against literature data in Table A2.

<u>**Reference**</u>	Plant A.G.											
Table(T)/Figure(F)/Text	Figure 31, Figure 33, Figure 35 and Figure 37											
Variable Parameter (s)	Radiation Type, Vial, Absorbed Dose											
Radiation Chemical Yield, *G*-value / μmol J^{-1}												
Acetaldehyde	6.88	4.43	3.57	2.34	1.39	1.45	0.50	0.73	0.52	0.27	0.07	0.04
Methanol	0.43	0.28	0.29	0.23	0.21	0.19	0.41	0.26	0.23	0.22	0.18	0.23
Ethyl Acetate	0.02	0.02	0.04	0.04	0.05	0.03						
Acetic Acid		0.10	0.12	0.10	0.13	0.07						
Sample Parameters												
Dose / kGy	20	40	50	60	80	100	20	40	50	60	80	100
Dose Rate / kGy min^{-1}	0.018	0.016	0.026	0.027	0.041	0.040	1.63	3.27	3.27	6.53	6.53	6.54
Radiation Type	γ-only						neutrons + γ rays					
Ethylene Glycol (wt.%)	Neat											
Temperature / K	Ambient						Ambient*					
Chemical Processing Analysis												
Mass Productivity % (Acetaldehyde)	0.61	0.78	0.79	0.62	0.49	0.64	0.04	0.13	0.11	0.07	0.02	0.02
Mass Productivity % (Methanol)	0.03	0.04	0.05	0.04	0.05	0.06	0.03	0.03	0.04	0.04	0.05	0.07
Mass Productivity % (Ethyl Acetate)	0.00	0.01	0.02	0.02	0.04	0.03						

*Temperature values are thought to be proportional to the dose rate of the operational reactor.

Note: Uncertainties for all quoted *G*-values for all products are ~ ± 10%.

Table A13: Neat glycerol radiolytic products with *G*-values and mass productivity values in this work (Plant A.G.). Determined via liquid sampling GC-MS analysis of polypropylene (PP) irradiated vials. To be compared against literature data in Table A3.

Reference	Plant A.G. (Thesis)															
Table(T)/Figure(F)/Text	Figure 41 and Figure 43												Figure 44			
Variable Parameter (s)	Absorbed Dose, Radiation Type												Dose Rate			
Radiation Chemical Yield, *G*-value / µmol J^{-1}																
Hydroxyacetone (Acetol)	0.58	0.51	0.63	0.53	0.56	0.47	0.14	0.16	0.20	0.16	0.22	0.42	0.25	0.24	0.26	0.17
Solketal	0.02	0.03	0.05	0.04	0.05	0.05			0.01	0.01	0.02	0.04				
Sample Parameters																
Dose / kGy	20	40	50	60	80	100	20	40	50	60	80	100	50			
Dose Rate / kGy min^{-1}	0.018	0.016	0.026	0.027	0.041	0.040	1.63	3.27	3.27	6.53	6.53	6.54	0.52	1.31	3.27	8.17
Radiation Type	γ-ray only (delay)						Neutron + γ rays									
Mixture Type / Glycerol (wt.%)	Neat Glycerol															
Temperature / K	Ambient						Ambient*						Ambient*			
Chemical Processing Analysis																
Mass Productivity % (Acetol)	0.086	0.151	0.234	0.233	0.330	0.346	0.020	0.047	0.076	0.071	0.133	0.308	0.094	0.088	0.097	0.063
Mass Productivity % (Solketal)	0.005	0.014	0.030	0.032	0.058	0.063			0.000	0.000	0.000	0.001	0.009	0.005	0.001	0.002

*Temperature values are thought to be proportional to the dose rate of the operational reactor.

Note: Uncertainties for all quoted *G*-values for all products are ~ ± 10%.

Table A14: Neat glycerol radiolytic products with *G*-values and mass productivity values in this work (Plant A.G.). Determined via liquid sampling GC-MS analysis of borosilicate (BS) irradiated vials. To be compared against literature data in Table A3.

Reference	Plant A.G. (Thesis)											
Table(T)/Figure(F)/Text	Figure 41 and Figure 43											
Variable Parameter (s)	Absorbed Dose, Radiation Type											
Radiation Chemical Yield, *G*-value / μmol J^{-1}												
Hydroxyacetone (Acetol)	0.52	0.37	0.57	0.56	0.54	0.59	0.16	0.23	0.27	0.17	0.30	0.14
Solketal	0.02	0.01	0.03	0.04	0.05	0.07		0.02	0.01	0.03	0.04	0.05
Sample Parameters												
Dose / kGy	20	40	50	60	80	100	20	40	50	60	80	100
Dose Rate / kGy min^{-1}	0.018	0.016	0.026	0.027	0.041	0.040	1.63	3.27	3.27	6.53	6.53	6.54
Radiation Type	γ-ray only (delay)						Neutron + γ rays					
Mixture Type / Glycerol (wt.%)	Neat Glycerol											
Temperature / K	Ambient						Ambient*					
Chemical Processing Analysis												
Mass Productivity % (Acetol)	0.08	0.11	0.21	0.25	0.32	0.44	0.02	0.07	0.10	0.08	0.18	0.10
Mass Productivity % (Solketal)	0.00	0.01	0.02	0.03	0.06	0.10		0.01	0.01	0.02	0.04	0.06

*Temperature values are thought to be proportional to the dose rate of the operational reactor.

Note: Uncertainties for all quoted *G*-values for all products are ~ ± 10%.

Table A15: Binary aqueous glycerol mixture radiolytic products from γ-ray only radiolysis with *G*-values and mass productivity values in this work (Plant A.G.). Determined via liquid sampling GC-MS analysis of polypropylene (PP) irradiated vials. To be compared against literature data in Table A3.

Reference	Plant A.G. (Thesis)																	
Table(T)/Figure(F)/Text	Figure 46																	
Variable Parameter (s)	Aqueous Mixtures, Radiation Type																	
Radiation Chemical Yield, *G*-value / µmol J^{-1}																		
Hydroxyacetone (Acetol)	1.81	1.38	1.35	1.36	1.01	0.91	-	0.79	0.92	0.93	0.72	0.64	2.69	1.84	1.83	1.84	1.40	1.33
Solketal	0.01	0.01	0.01	0.02	0.01	0.02	-	0.01	0.01	0.01	0.01	0.01	0.02	0.02	0.02	0.02	0.02	0.03
Sample Parameters																		
Dose / kGy	20	40	50	60	80	100	20	40	50	60	80	100	20	40	50	60	80	100
Dose Rate / kGy min^{-1}	0.018	0.016	0.026	0.027	0.041	0.040	0.018	0.016	0.026	0.027	0.041	0.040	0.018	0.016	0.026	0.027	0.041	0.040
Radiation Type	γ-ray only (delay)																	
Mixture Type (wt.%): Glycerol, Water	Mix 1: 63, 37						Mix 2: 50, 50						Mix 3: 70, 30					
Temperature / K	Ambient																	
Chemical Processing Analysis																		
Mass Productivity % (Acetol)	0.268	0.408	0.504	0.603	0.601	0.672		0.236	0.342	0.414	0.429	0.472	0.399	0.546	0.685	0.816	0.831	0.987
Mass Productivity % (Solketal)	0.002	0.004	0.008	0.013	0.012	0.020		0.004	0.006	0.008	0.009	0.010	0.005	0.008	0.012	0.018	0.025	0.040

*Temperature values are thought to be proportional to the dose rate of the operational reactor.

Note: Uncertainties for all quoted *G*-values for all products are ~ ± 10%.

Table A16: Binary aqueous glycerol mixture radiolytic products from mixed field neutron + γ-ray radiolysis with *G*-values and mass productivity values in this work (Plant A.G.). To be compared against literature data in Table A3.

Reference	Plant A.G. (Thesis)																	
Table(T)/Figure(F)/Text	Figure 47																	
Variable Parameter (s)	Aqueous Mixtures, Absorbed Dose, Radiation Type																	
Radiation Chemical Yield, *G*-value / µmol J^{-1}																		
Hydroxyacetone (Acetol)	0.31	0.32	0.33	0.33	0.40	0.52	0.26	0.27	0.27	0.21	0.20	0.34	0.45	0.47	0.48	0.34	0.38	0.46
Solketal				0.01	0.01	0.01										0.00	0.01	0.01
Sample Parameters																		
Dose / kGy	20	40	50	60	80	100	20	40	50	60	80	100	20	40	50	60	80	100
Dose Rate / kGy min^{-1}	1.63	3.27	3.27	6.53	6.53	6.54	1.63	3.27	3.27	6.53	6.53	6.54	1.63	3.27	3.27	6.53	6.53	6.54
Radiation Type	Neutron + γ rays																	
Mixture Type (wt.%): Glycerol, Water	Mix1: 63, 37						Mix2: 50, 50						Mix3: 70, 30					
Temperature / K	Ambient*																	
Chemical Processing Analysis																		
Mass Productivity % (Acetol)	0.046	0.094	0.123	0.148	0.235	0.386	0.039	0.081	0.102	0.095	0.119	0.254	0.067	0.141	0.177	0.152	0.226	0.342
Mass Productivity % (Solketal)				0.004	0.006	0.011										0.003	0.006	0.010

*Temperature values are thought to be proportional to the dose rate of the operational reactor.

Note: Uncertainties for all quoted *G*-values for all products are ~ ± 10%.

Table A17: Ternary glycerol, acetone, and water mixtures associated radiolytic products with *G*-values and mass productivity values in this work (Plant A. G.). Data are from PP vials. To be compared against literature data in Table A3.

Reference	Plant A.G. (Thesis)								
Table(T)/Figure(F)/Text	Figure 49, Figure 50, Figure 51						Figure 49		
Variable Parameter (s)	Ternary Mixture type, Glycerol wt.%, Radiation type						Unirradiated Control		
Radiation Chemical Yield, *G*-value / µmol J^{-1}									
Hydroxyacetone (Acetol)	0.63	0.49	0.41	0.13	0.09	0.06			
Solketal	1.53	1.11	0.80	0.18	0.12	0.09	-	-	-
Acetic Acid	0.076	0.15	0.17	0.08	0.08	0.09			
Sample Parameters									
Dose / kGy	50						-		
Dose Rate / kGy min^{-1}	0.04			3.27			-		
Radiation Type	γ-ray only			Neutron + γ-rays			NA Controls		
Ternary Mixture (wt.%): Glycerol, Acetone, Water	AceMix1: 46, 28, 26	AceMix2: 34, 34, 32	AceMix3: 26, 48, 26	AceMix1: 46, 28, 26	AceMix2: 34, 34, 32	AceMix3: 26, 48, 26	AceMix1: 46, 28, 26	AceMix2: 34, 34, 32	AceMix3: 26, 48, 26
Temperature / K	Ambient			Ambient*			Ambient		
Chemical Processing Analysis									
Mass Productivity % (Acetol)	0.235	0.181	0.154	0.047	0.034	0.024			
Mass Productivity % (Solketal)	1.010	0.736	0.530	0.116	0.082	0.060	0.084	0.051	0.031

*Temperature values are thought to be proportional to the dose rate of the operational reactor.

Note: Uncertainties for all quoted *G*-values for all products are ~ ± 10%.

Appendix A: Supporting Figures and Tables

8.2.3 INAA Radionuclide data of Neat Samples

Table A18: Elemental composition analysis and impurity identification within purchased solutes via k0-γ spectroscopy. **a** glycerol (>99.5%). **b** ethylene glycol (>99%). Results obtained by k0-INAA of Glycerol and Ethylene Glycol Samples. (<LOD= Below limit of detection of the INAA methodology)

a) Glycerol			**b) Ethylene Glycol**		
Below LOD?	Element	Concentration / mg kg^{-1}	Below LOD?	Element	Concentration / mg kg^{-1}
<LOD	Ag#	<0.0049	<LOD	Ag#	< 0.0025
	As#	**0.0062**	<LOD	As#	< 0.0003
<LOD	Au#	<0.00001	<LOD	Au#	< 0.00001
<LOD	Ba#	< 0.113	<LOD	Ba#	< 0.058
	Br#	**0.0108**		Br#	**0.0269**
<LOD	Ca#	< 5.8	<LOD	Ca#	< 3.0
<LOD	Cd#	< 0.0067	<LOD	Cd#	< 0.0061
<LOD	Ce#	< 0.0042	<LOD	Ce#	< 0.0020
<LOD	Co#	< 0.0003	<LOD	Co#	< 0.0009
<LOD	Cr#	< 0.0026	<LOD	Cr#	< 0.0039
<LOD	Cs#	< 0.0010	<LOD	Cs#	< 0.0005
<LOD	Cu#	< 0.055	<LOD	Cu#	< 0.061
<LOD	Eu#	< 0.00001	<LOD	Eu#	< 0.00001
<LOD	Fe#	< 0.82	<LOD	Fe#	<0.24
<LOD	Ga#	< 0.0005	<LOD	Ga#	< 0.0005
<LOD	Hf#	< 0.0008	<LOD	Hf#	<0.0004
<LOD	Hg#	< 0.0027	<LOD	Hg#	< 0.0013
<LOD	K#	< 0.010	<LOD	K#	< 0.019
<LOD	La#	< 0.0002	<LOD	La#	< 0.0002
<LOD	Mn#	< 0.0020	<LOD	Mn#	<0.0043
<LOD	Mo#	< 0.0012	<LOD	Mo#	< 0.0035
	Na	**0.579**		Na	**1.01**
<LOD	Nd#	< 0.0077	<LOD	Nd#	< 0.0040
<LOD	Rb#	< 0.028	<LOD	Rb#	< 0.014
	Sb#	**0.0019**		Sb#	**0.00053**
<LOD	Sc#	< 0.0001	<LOD	Sc#	< 0.0000
<LOD	Se#	< 0.0052	<LOD	Se#	< 0.0028
<LOD	Sm#	< 0.0000	<LOD	Sm#	< 0.0000
<LOD	Sr#	< 0.21	<LOD	Sr#	< 0.22
<LOD	Ta#	< 0.0004	<LOD	Ta#	< 0.0002
<LOD	Tb#	< 0.0004	<LOD	Tb#	< 0.0000
<LOD	Th#	< 0.0006	<LOD	Th#	< 0.0002
<LOD	U#	< 0.0002	<LOD	U#	< 0.0002
	W#	**0.0013**	<LOD	W#	< 0.0004
<LOD	Yb#	<0.0005	<LOD	Yb#	< 0.0001
<LOD	Zn#	< 0.038		Zn#	**0.0191**
<LOD	Zr#	< 0.19	<LOD	Zr#	< 0.16

N.B.: # indicates the **non-accredited** concentrations to **non-accredited** activity.

8.2.4 Pressure Calculations, Calibration Curves, and Chromatograms

Table A19: Internal pressure calculations inside the irradiation vials during irradiations at various absorbed doses. Using 20 ml BS vials with 4 ml of organic liquid and a 16 ml gaseous headspace. An estimated *G*-value (mixed gases) of 7.13 molecules 100eV^{-1} from ethanol γ-ray radiolysis was used [240].

	Absorbed Dose / kGy					
	20	**40**	**50**	**60**	**80**	**100**
Estimated Temperature Increase / °C	4.8	9.6	12	14.4	19.2	24
Estimated molecules of mixed gaseous compounds produced (x10^{19})	4.50	8.99	11.2	13.5	18.0	22.5
Moles of mixed gases / µM	75	149	187	224	299	373
Volume of H_2 Gas Produced / cm^3	1.79	3.58	4.48	5.37	7.17	8.96
Absolute Pressure in Headspace Vial after irradiation @ 25°C / atm	1.11	1.23	1.29	1.34	1.46	1.57
Absolute Pressure in Headspace Vial after irradiation @ 100°C / atm	1.39	1.54	1.61	1.68	1.82	1.97

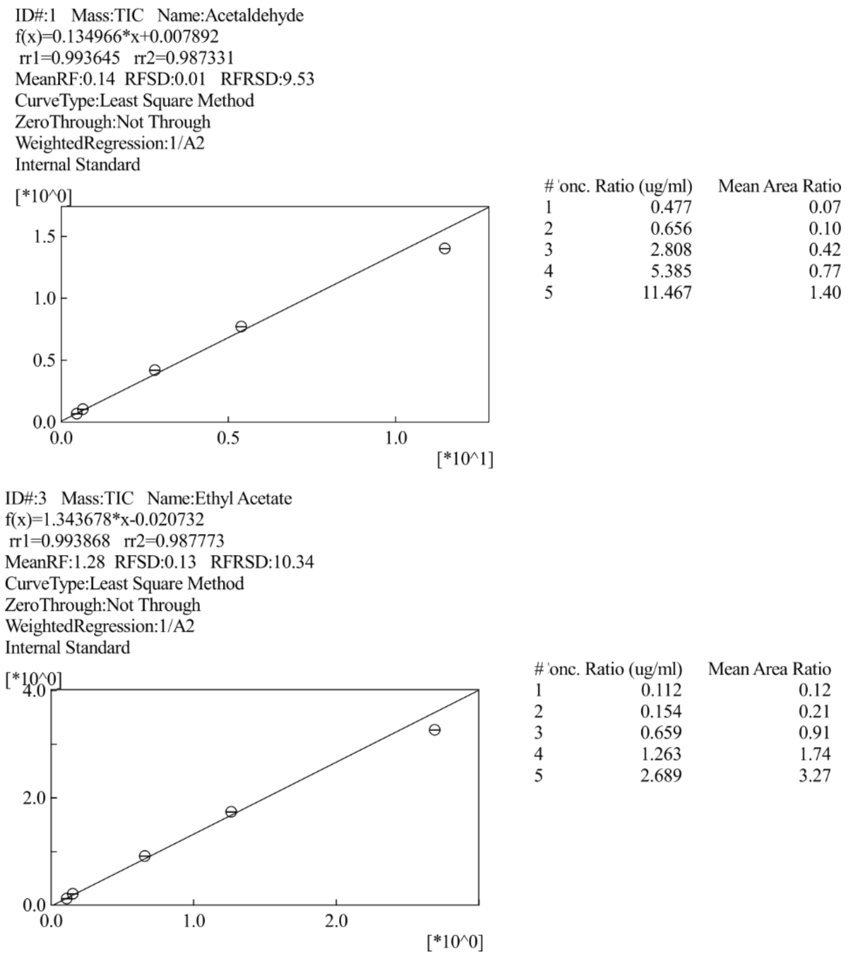

ID#:1 Mass:TIC Name:Acetaldehyde
f(x)=0.134966*x+0.007892
rr1=0.993645 rr2=0.987331
MeanRF:0.14 RFSD:0.01 RFRSD:9.53
CurveType:Least Square Method
ZeroThrough:Not Through
WeightedRegression:1/A2
Internal Standard

#	onc. Ratio (ug/ml)	Mean Area Ratio
1	0.477	0.07
2	0.656	0.10
3	2.808	0.42
4	5.385	0.77
5	11.467	1.40

ID#:3 Mass:TIC Name:Ethyl Acetate
f(x)=1.343678*x-0.020732
rr1=0.993868 rr2=0.987773
MeanRF:1.28 RFSD:0.13 RFRSD:10.34
CurveType:Least Square Method
ZeroThrough:Not Through
WeightedRegression:1/A2
Internal Standard

#	onc. Ratio (ug/ml)	Mean Area Ratio
1	0.112	0.12
2	0.154	0.21
3	0.659	0.91
4	1.263	1.74
5	2.689	3.27

Figure A6: An example of calibration curves (internal standard method) obtained for the analytical standards of acetaldehyde and ethyl acetate for irradiated ethylene glycol samples. Compared against an internal standard of 20 µl or 40 µl of 2-butanol stock standard (~0.01 g ml^{-1}) depending on the run.

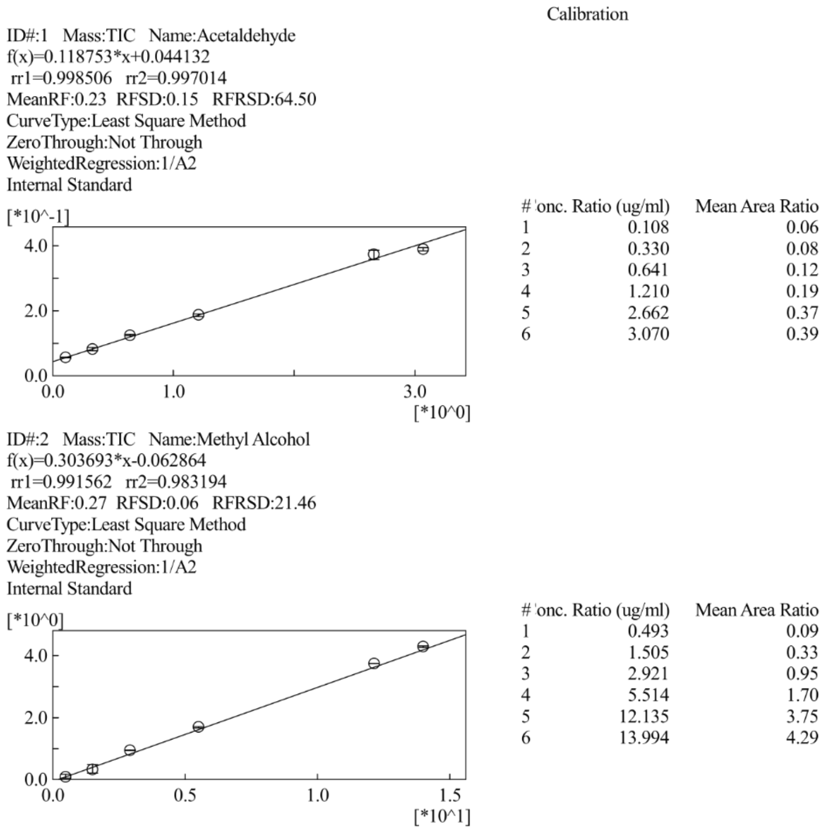

Calibration

ID#:1 Mass:TIC Name:Acetaldehyde
f(x)=0.118753*x+0.044132
rr1=0.998506 rr2=0.997014
MeanRF:0.23 RFSD:0.15 RFRSD:64.50
CurveType:Least Square Method
ZeroThrough:Not Through
WeightedRegression:1/A2
Internal Standard

#	'onc. Ratio (ug/ml)	Mean Area Ratio
1	0.108	0.06
2	0.330	0.08
3	0.641	0.12
4	1.210	0.19
5	2.662	0.37
6	3.070	0.39

ID#:2 Mass:TIC Name:Methyl Alcohol
f(x)=0.303693*x-0.062864
rr1=0.991562 rr2=0.983194
MeanRF:0.27 RFSD:0.06 RFRSD:21.46
CurveType:Least Square Method
ZeroThrough:Not Through
WeightedRegression:1/A2
Internal Standard

#	'onc. Ratio (ug/ml)	Mean Area Ratio
1	0.493	0.09
2	1.505	0.33
3	2.921	0.95
4	5.514	1.70
5	12.135	3.75
6	13.994	4.29

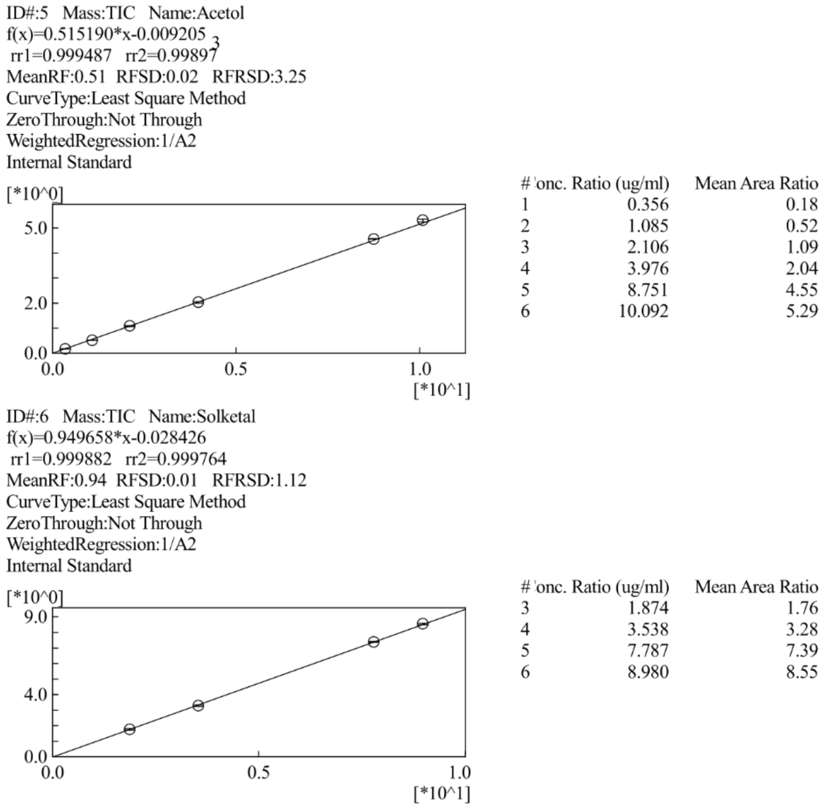

ID#:5 Mass:TIC Name:Acetol
f(x)=0.515190*x-0.009205
rr1=0.999487 rr2=0.998973
MeanRF:0.51 RFSD:0.02 RFRSD:3.25
CurveType:Least Square Method
ZeroThrough:Not Through
WeightedRegression:1/A2
Internal Standard

#	'onc. Ratio (ug/ml)	Mean Area Ratio
1	0.356	0.18
2	1.085	0.52
3	2.106	1.09
4	3.976	2.04
5	8.751	4.55
6	10.092	5.29

ID#:6 Mass:TIC Name:Solketal
f(x)=0.949658*x-0.028426
rr1=0.999882 rr2=0.999764
MeanRF:0.94 RFSD:0.01 RFRSD:1.12
CurveType:Least Square Method
ZeroThrough:Not Through
WeightedRegression:1/A2
Internal Standard

#	'onc. Ratio (ug/ml)	Mean Area Ratio
3	1.874	1.76
4	3.538	3.28
5	7.787	7.39
6	8.980	8.55

Figure A7: An example of the calibration curves obtained (for internal standard method) for standards of acetaldehyde, methanol, acetol, solketal and acetic acid for irradiated glycerol samples. Compared against 20 µl or 40 µl of internal standard 2-butanol stock standard (~0.01 g ml^{-1}) depending on the run.

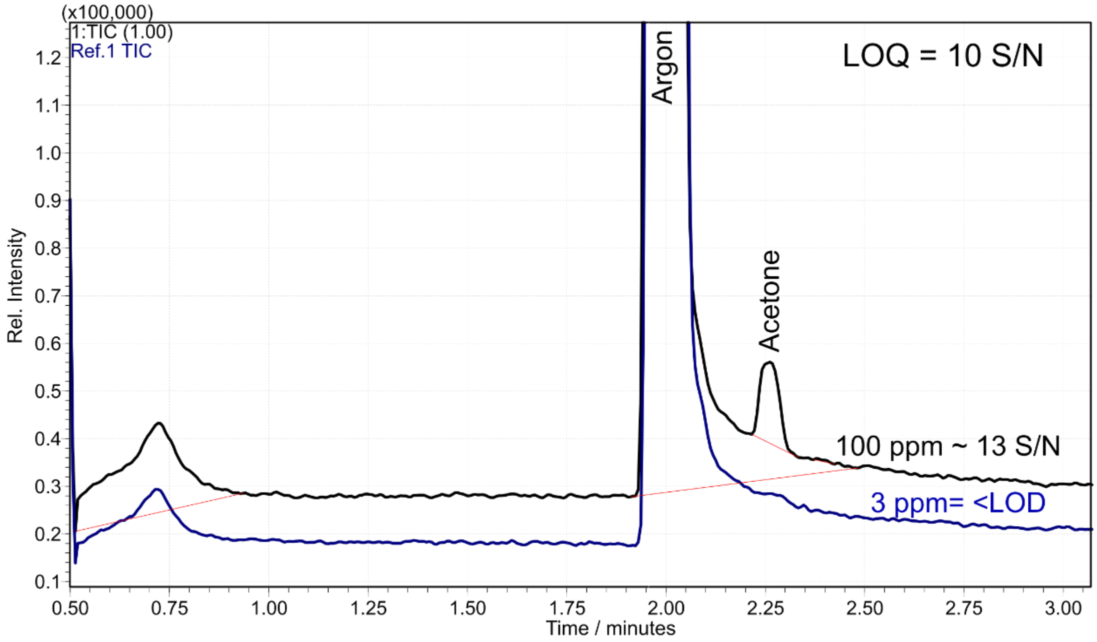

Figure A8: Total ion chromatogram of the HSGC-MS analysis of unirradiated glycerol spiked with either 100 ppm (**black**) or 3 ppm (**blue**) of acetone. 100 ppm was estimated to be ~13x the signal to noise ratio (S/N). 3 ppm was below the detection limit (~3 S/N).

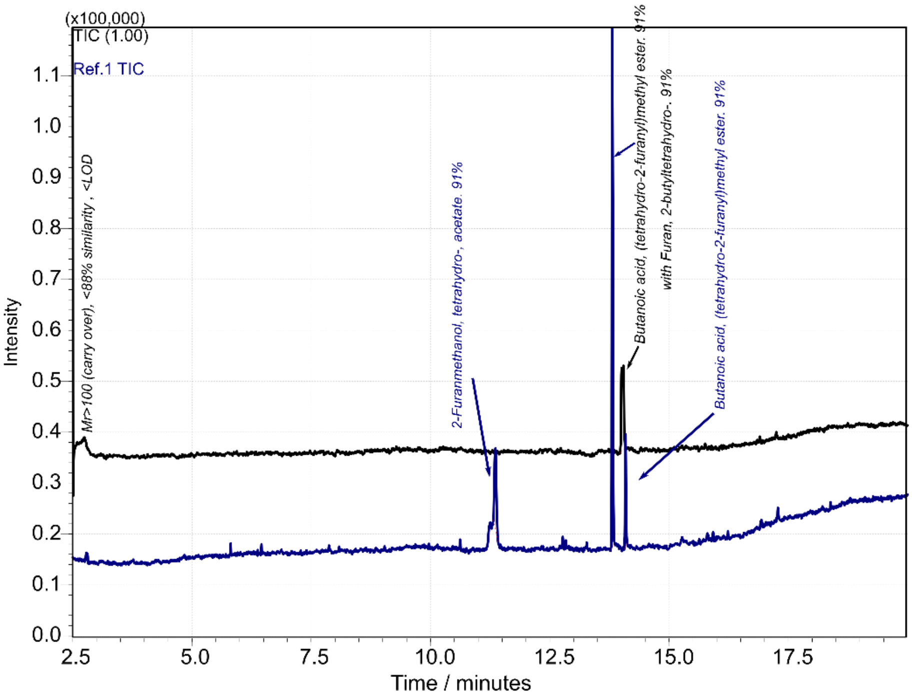

Figure A9: Total ion chromatogram of the HSGC-MS analysis of 0.038 Gy ^{252}Cf-irradiated neat glycerol (**black**) or unirradiated glycerol (**blue**).

a) 80 kGy γ-ray only

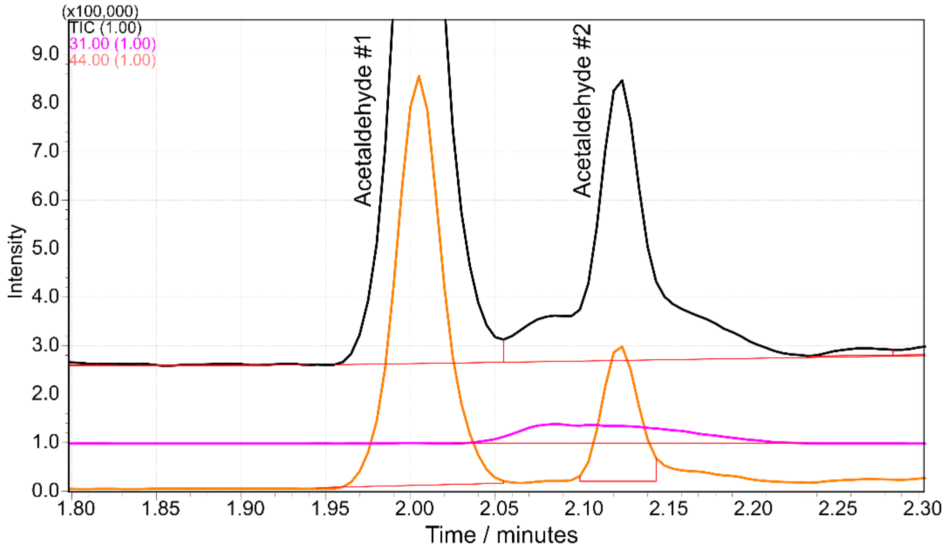

b) 80 kGy neutron+ γ-ray

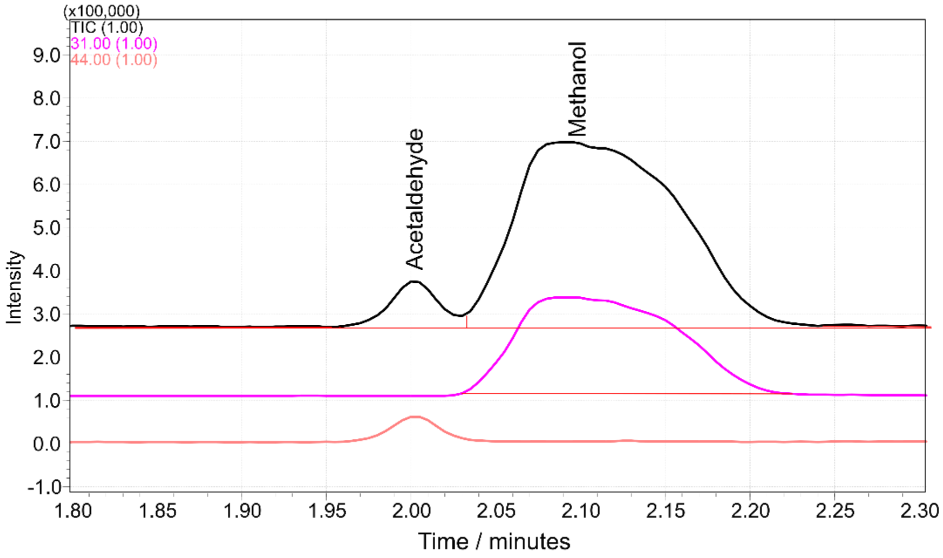

Figure A10: GC-MS ion chromatograms focussing on the acetaldehyde split peaks (2.00 and 2.15 minutes) with the overlapping broad methanol peak (2.10 minutes). Showing ethylene glycol samples irradiated with either 80 kGy of **a** γ-ray only (sample 75) or **b** 80 kGy of mixed field neutron + γ-ray (sample 37). Total ion chromatogram trace (**black**), 31 m/z fragment trace indicating methanol (**pink**), and the 44 m/z fragment trace indicating acetaldehyde (**orange**).

a) 100 kGy Ethylene Glycol, PP Vials

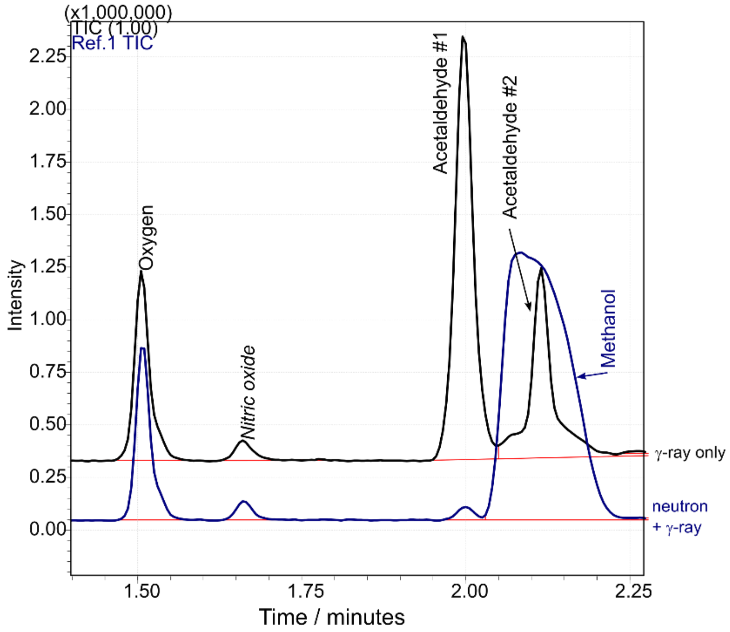

b) 100 kGy Glycerol, PP vials

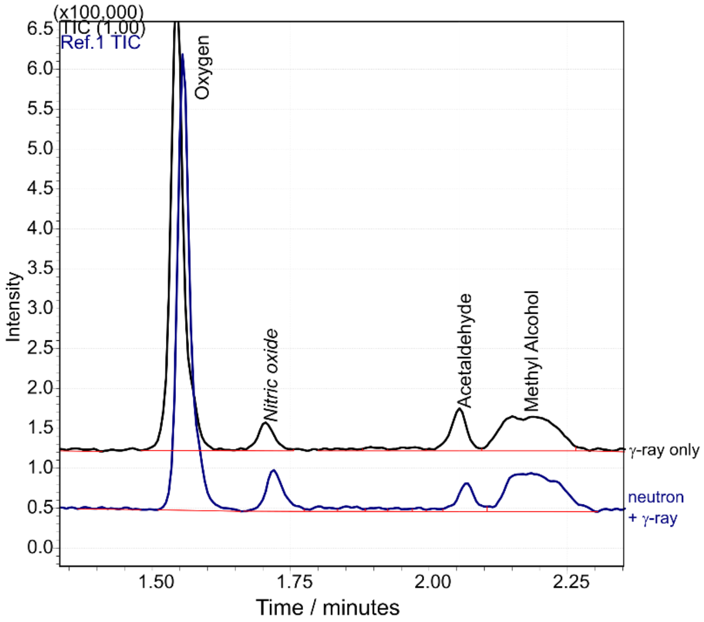

Figure A11: GC-MS total ion chromatograms of irradiated samples within PP vials for either irradiated **a** neat ethylene glycol or **b** neat glycerol. **Black** traces indicate the samples from 100 kGy γ-ray only irradiations and **blue** traces indicate 100 kGy mixed field neutron + γ-ray irradiations.

8.3 MS Fragments Patterns of unidentifiable peaks

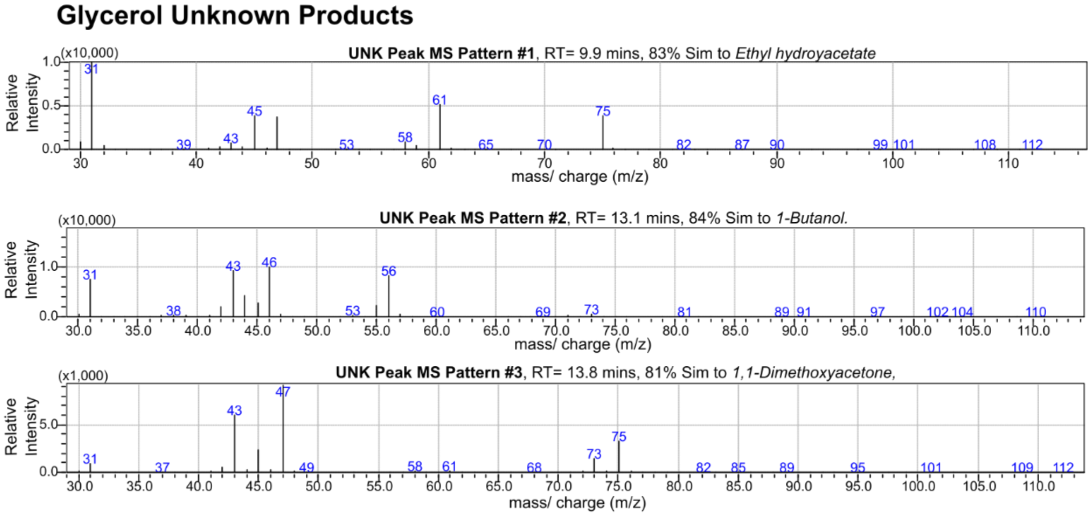

Figure A12: Mass fragment patterns of large unidentifiable radiolytic peaks from neat ethylene glycol radiolysis. In order of retention time; **#1**, Ethyl ethoxy(hydroxy)acetate, **#2**, Methyl tetrahydrofurfuryl and **#3**, 2-(Methoxymethyoxy)propanoic acid.

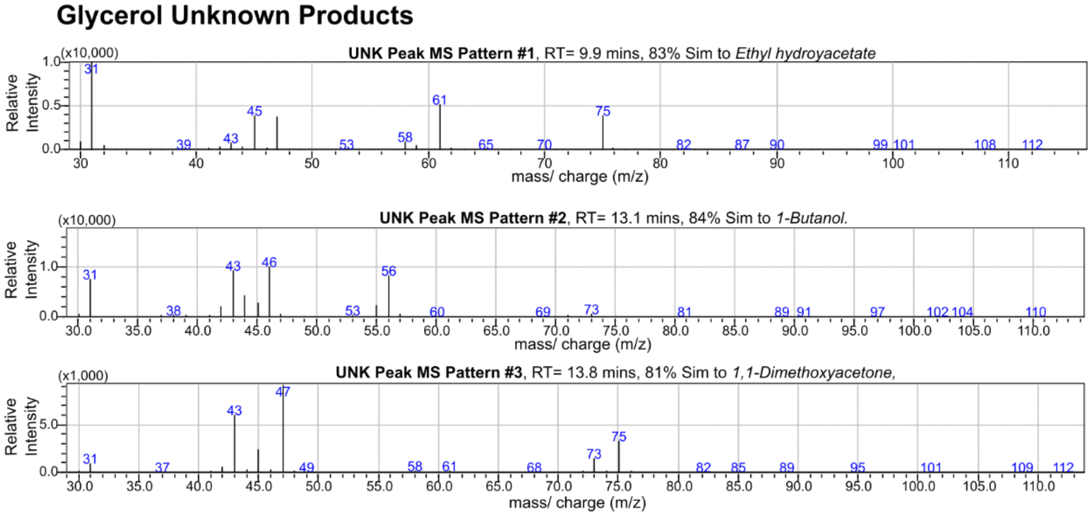

Figure A13: Mass fragment patterns of large unidentifiable radiolytic peaks from neat glycerol radiolysis. In order of retention time; **#1**, ethyl hydroxyacetate, **#2**, 1-Butanol and **#3**, 1,1-dimethoxyacetone.

8.4 European NPPs by country with projected solketal production

Table A20: European reactors by country, with total power output (as of 08/02/2021), and estimated acetol and solketal output using data shown in Figure 48 and Figure 49 with sample 109 (Table 18)[9].

COUNTRY	Number of Reactors	Electrical Power Output / MW(e)	Acetol		Solketal	
			Production / tonnes year^{-1}	Circle Area / arb. unit	Production / tonnes year^{-1}	Circle Area / arb. unit
ARMENIA	1	**375**	7.3	457	31.3	1966
BELARUS	1	**1110**	21.5	1352	92.6	5819
BELGIUM	7	**5930**	115.0	7224	494.7	31086
BULGARIA	2	**2006**	38.9	2444	167.4	10516
CZECH REPUBLIC	6	**3932**	76.2	4790	328.0	20612
FINLAND	4	**2794**	54.2	3404	233.1	14646
FRANCE	56	**61370**	1189.9	74766	5120.1	321706
GERMANY	6	**8113**	157.3	9884	676.9	42529
HUNGARY	4	**1902**	36.9	2317	158.7	9970
NETHERLANDS	1	**482**	9.3	587	40.2	2527
ROMANIA	2	**1300**	25.2	1584	108.5	6815
RUSSIA	38	**28578**	554.1	34816	2384.3	149808
SLOVAKIA	4	**1814**	35.2	2210	151.3	9509
SLOVENIA (Krško)	1	**688**	**13.3**	838	**57.4**	3607
SPAIN	7	**7121**	138.1	8675	594.1	37329
SWEDEN	6	**6859**	133.0	8356	572.2	35955
SWITZERLAND	4	**2960**	57.4	3606	247.0	15517
UKRAINE	15	**13107**	254.1	15968	1093.5	68708
UNITED KINGDOM	15	**8923**	173.0	10871	744.4	46775
TOTAL	**180**	**159364**	**3090.0**		**13295.8**	